Ocean Circulation and Predictive Modeling Study of Two Sea-Disposed Military Munitions Sites in Hawai‘i:

Ordnance Reef (HI-06) and HI-01

U.S. Department of Commerce
National Oceanic and Atmospheric Administration
National Ocean Service
Office of Response and Restoration ● Office of National Marine Sanctuaries

Ocean Circulation and Predictive Modeling Study of Two Sea-Disposed Military Munitions Sites in Hawai‘i: Ordnance Reef (HI-06) and HI-01

Tony Reyer
NOAA Office of National Marine Sanctuaries

Jason Rolfe
Glen Watabayashi
NOAA Office of Response and Restoration

Dr. Melissa Rice
Genwest Systems, Inc.

Dr. Brian Powell
Dr. Margaret McManus
Jeff Sevadjian
Dr. Ivica Janeković
Department of Oceanography, University of Hawai‘i at Manoa

Drew Rak
Dr. Deborah Hunka
NOBLIS, Inc.

U.S. Department of Commerce
Secretary Rebecca Blank (Acting)

National Oceanic and Atmospheric Administration
Dr. Jane Lubchenco
Undersecretary of Commerce for Oceans and Atmosphere

National Ocean Service
David Kennedy, Assistant Administrator

Office of National Marine Sanctuaries
Dan Basta, Director

Office of Response and Restoration
David Westerholm, Director

November 2012

Disclaimer

The content of this report does not necessarily reflect the views and policies of the National Oceanic and Atmospheric Administration (NOAA), NOAA's Office of National Marine Sanctuaries, or NOAA's Office of Response and Restoration, nor does the mention of trade names or commercial products constitute endorsement or recommendation for use.

Contacts

Tony Reyer
NOAA Office of National Marine Sanctuaries
1305 East West Highway
Silver Spring, MD 20910-3278
tony.reyer@noaa.gov

Jason Rolfe
NOAA Office of Response and Restoration
1305 East West Highway
Silver Spring, MD 20910-3278
jason.rolfe@noaa.gov

Abstract

NOAA performed an ocean current and predictive modeling study to support a Department of Defense (DOD) evaluation of the potential human health hazards posed by military munitions present at Military Munitions Sea Disposal Sites HI-01 and Ordnance Reef (HI-06), both offshore of the west coast of Oʻahu, Hawaiʻi. The munitions at the two sites are among many that were sea-disposed (discarded into the ocean) at various times and places until 1970. NOAA reviewed information concerning the munitions constituents believed present at each site, identified the compounds believed to present the greatest potential risk to human health and determined that of the evaluated substances at deepwater site HI-01, hydrogen cyanide presents the greatest potential human health hazard, and ammonium picrate presents the greatest potential human health hazard of any substance at Ordnance Reef (HI-06). NOAA and the University of Hawaiʻi measured ocean currents in the vicinity of the two sites to better characterize ocean circulation, then performed predictive modeling of the "worst-case" release of munitions constituents from each site. Modeling of the worst-case ammonium picrate release from Ordnance Reef (HI-06) indicated that dissolved ammonium picrate concentrations would not exceed hazardous levels at any depth within about 100 meters (330 feet) from shore. Modeling of a worst-case hydrogen cyanide release from deepwater site HI-01 indicated that dissolved hydrogen cyanide concentrations would reach established exposure limits only within 300 meters (984 feet) of the ocean bottom, about 2 km (more than a mile) below the surface, essentially precluding any threat to human health.

Contents

Appendixes

Executive summary

This report presents the results of a National Oceanic and Atmospheric Administration (NOAA) ocean current and predictive modeling study that NOAA performed in support of the Department of Defense (DOD). The DoD requested an evaluation of the potential human health hazards to shoreline communities posed by a potential release of munitions constituent from discarded military munitions located on the sea bottom at two sites off the populated west coast of Oʻahu, Hawaiʻi (locally known as the Waiʻanae Coast). The site closest to shore, locally known as Ordnance Reef, is identified by DOD as Military Munitions Sea Disposal Site Hawaiʻi 06 (HI-06). Its eastern boundary is within 0.5 km (0.25 nautical miles) of the Oʻahu coast. The second site, identified by DOD as Military Munitions Sea Disposal Site HI-01, is approximately 19 km (10 nautical miles) from shore.

NOAA reviewed available information and determined the munitions constituents most likely present at each site. From the munitions constituents present at HI-01, the deepwater site, NOAA determined that hydrogen cyanide posed the greatest potential human health hazard. For Ordnance Reef (HI-06), NOAA determined ammonium picrate posed the greatest potential human health hazard. NOAA's review considered the amount of each of these munitions constituents potentially present at each site, their solubility, and their inherent hazardousness to people. NOAA then performed predictive modeling of a "worst-case" release scenario of hydrogen cyanide at HI-01 and ammonium picrate (HI-06). Although DoD believes the "worst case" scenario was very conservative, it agreed to its use for modeling purposes. NOAA's review found:

- In a worst-case ammonium picrate release from Ordnance Reef (HI-06), dissolved ammonium picrate concentrations in nearshore waters would not exceed approximately 0.3 parts per billion (ppb), which is below established exposure guidelines. Exposure times to the predicted peak concentrations above 0.1 ppb would be less than 3 hours.
- In a worst-case hydrogen cyanide release from deepwater site HI-01, there would be no shoreline or shallow water exposure. Dissolved hydrogen cyanide concentrations would reach hazardous levels too far below the surface and too far offshore to pose a threat to human health.

To conduct the modeling study, a "worst case" release at each site was defined to be the release of the largest possible amount from a single source area of the most hazardous munitions constituent (herein after referred to as chemical) present. NOAA predicted the distance to the point where the concentration of dissolved chemical would drop below 1 ppb. One ppb was selected as the modeling endpoint because it is lower than established human health guidelines and limits; therefore, it is more conservative than those values (i.e., more likely to overestimate than underestimate the potential hazard). A conservative

endpoint was chosen because of the large uncertainty about the health effects of the most hazardous chemicals.

Before beginning the modeling study, NOAA and the University of Hawai'i deployed Acoustic Doppler Current Profilers (ADCPs) in the vicinity of the two disposal sites. These ADCPs, which were left in place for a year, provided NOAA data needed to better characterize ocean circulation in the area and allow modeling to be based on site-specific current data.

At Ordnance Reef (HI-06), previous surveys had found a variety of munitions (e.g., artillery projectiles, mines, mortars, and small arms ammunition). The munitions constituents (chemicals) associated with these munitions that were of particular concern were: 2,4,6-trinitrotoluene (TNT), 2,4-dinitrotoluene (2,4-DNT), hexahydro-1,3,5-trinitro-1,3,5-triazine (RDX), octahydro-1,3,5,7-tetranitro-1,3,5,7-tetrazocine (HMX), and ammonium picrate (Explosive D). Chemical assessment revealed that of these five chemicals, ammonium picrate would pose the greatest potential hazard to the shoreline community if it were to be released, because it dissolves readily in water, is present in significant quantities, and is more toxic than the other chemicals. Because the other four chemicals assessed dissolve much more slowly in water, their maximum concentrations in the water along the shoreline would be below established human health guidelines and limits.

Deepwater site HI-01 was not surveyed because of its great depth (about 1,630 to 2,600 meters [5,300 to 8,500 feet]), but according to military records, approximately 1,800 metric tons (2,000 tons) of chemical warfare agents, including sulfur mustard, cyanogen chloride, lewisite, and hydrogen cyanide, were disposed at this site during the 1940s. A chemical assessment revealed that of these four chemicals, a release of hydrogen cyanide would pose the greatest potential hazard to the shoreline community because of its inherent hazardousness. This is because hydrogen cyanide is highly toxic, dissolves readily in water, persists in solution in a toxic form and a significant quantity (1.8 metric tons [2 tons]) is recorded as having been disposed of at the site. The other chemicals would pose less hazard, primarily because all are significantly less soluble than hydrogen cyanide.

The NOAA study was conducted in support of a larger DOD initiative, under a Special Studies Agreement between NOAA and the U.S. Army and U.S. Navy. The University of Hawai'i, Noblis, Inc., and Genwest Systems, Inc., assisted NOAA.

Acronyms and Abbreviations

ADCP – Acoustic Doppler Current Profiler

°**C** – degree Celsius

cm - centimeter

CWM – Chemical warfare material

d – density

DMM – Disposed military munitions

DOD – Department of Defense

EOD - Explosive ordnance disposal

°**F** - degree Fahrenheit

ft – feet

GNOME – General NOAA Operational Modeling Environment. NOAA pollutant transport model

HI – Hawai‘i

HLC – Hawai‘i Lee Current

HLCC – Hawai‘i Lee Countercurrent

in - inch

kg – kilograms

kt - knots

L – liter

lb – pounds

m – meters

mg - milligram

mi – miles

mL - milliliter

MPRSA - Marine Protection, Research, and Sanctuaries Act of 1972

mt – metric ton

NDBC – National Data Buoy Center (NOAA)

MPRSA - Marine Protection, Research, and Sanctuaries Act

NEC – Northern Equatorial Current

NHRC – North Hawaiian Ridge Current

nm – nautical miles

NOAA – National Oceanic and Atmospheric Administration

PPB – parts per billion

PPM – parts per million

PPT – parts per thousand

ROMS – Regional Ocean Modeling System. University of Hawai‘i computer model

ROUMRS - Remotely Operated Underwater Munitions Recovery System

ROV - Remotely operated vehicle

SAA – Small arms ammunition

s - second

USACE – U.S. Army Corps of Engineers

UXO – Unexploded ordnance

yds – yards

Definitions

Acoustic Doppler Current Profiler (ADCP)	Current measuring device deployed within the water column, which uses sound waves and the "Doppler shift" to measure ocean current velocities (speed and direction).
Booster (Explosive)	An explosive booster acts as a bridge between a low energy explosive and a low sensitivity (but typically high energy) explosive, increases the explosive shockwave from an initiating explosive to the degree sufficient to detonate the secondary charge.
Chemical warfare material (CWM)	Items generally configured as a munition containing a chemical compound that is intended to kill, seriously injure, or incapacitate a person through its physiological effects. CWM also includes chemical agents in bulk containers.
Discarded military munitions (DMM)	"Military munitions that have been abandoned without proper disposal or removed from storage…for the purpose of disposal." (10 U.S.C. 2710(e)(2)). DMM have not experienced the firing sequence normally required to arm their fuzes. Many are not complete, lacking components required for them to function. DMM in general have a significantly lower probability of detonating than UXO.
Hydrolysis	The reaction of a compound with water to form two or more new substances. Generally this means that a bond in the original compound will break, and one half will bind to an H^+ ion from water, while the other half will bind to an HO^- ion from water.
Isobath	A contour line representing water depth.
Level of Concern	The concentration of a pollutant above which a hazard to people may exist or is believed to exist.
Military munitions	"All ammunition products and components produced for or used by the armed forces…including bulk

	explosives, and chemical warfare agents…and devices and components thereof." (10 U.S.C 101(e)(4)(A) through (C))
Munitions constituents	"Any materials originating from unexploded ordnance (UXO), discarded military munitions (DMM), or other military munitions, including explosive and non-explosive materials, and emission, degradation, or breakdown elements of such ordnance or munitions." (10 U.S.C. 2710(e)(3))
Oxidation	An increase in the oxidation state of a chemical, which for organic molecules often involves the addition of one or more oxygen atoms.
Photolysis	The break-up of a molecule due to light energy. This is a significant degradation pathway for compounds found in the photic zone, which extends to a depth of 40m at Ordnance Reef (HI-06). The shallow sites, where the explosives were found, are at a depth of 15 to 40 meters (49 to 131 feet), so they are within this zone. Photolysis will be relevant at these sites.
Sea disposed	Discarded into the ocean.
Thermolysis	The decomposition of a compound due to heat energy. At the water temperatures measured at Ordnance Reef (HI-06) (20 – 27°C) and HI-01 (2°C), thermolysis is not a significant degradation pathway for the compounds of interest.
Unexploded Ordnance (UXO)	"military munitions that …have been primed, fuzed, armed, or otherwise prepared for action;…constitute a hazard…and remain unexploded by malfunction, design, or any other cause." (10 U.S.C 101(e)(5)(A) through (C)). UXO have been through the firing sequence required to arm their fuzes. Although both present potential explosive hazards, DMM in general have a significantly lower probability of detonating than UXO.

Useful conversions

1 kilogram (kg) = 2.2 pounds (lbs)

1 kilometer (km) = 0.62 miles (mi)

1 knot (kt) = 1 nautical mile per hour (nm/hr), or 51 centimeters per second (cm/s)

1 meter (m) = 3.3 feet (ft)

1 metric ton (mt) = 1,000 kilograms (kg) = 1.1 tons

1 microgram/liter (µg/l) = 1 part per billion (ppb)

1 mile (mi) = 0.87 nautical miles (nm) or 1,610 meters (m)

1 milligram/liter (mg/l) = 1 part per million (ppm)

1 nautical mile (nm) = 1.15 miles (mi) = 1.9 kilometers (km)

Introduction

This report presents the results of a long-term study of the ocean currents at two discarded military munitions (DMM) sites offshore of Oʻahu, Hawaiʻi, and the subsequent fate and transport modeling of munitions constituents should a release occur from these same DMM on the sea floor. These munitions are among many that were sea-disposed (discarded into the ocean) by U.S. Department of Defense (DOD) at various times and places until 1970. The study described in this report was conducted by the National Oceanic and Atmospheric Administration (NOAA) in support of a larger DOD initiative to better understand the possible impacts of munitions on human health and the underwater environment.

This report initially describes the two munitions disposal sites, what is known about the munitions disposed at each location, and the general environment in the vicinity of the sites. Findings from three related research efforts are then presented. During the first research effort, the munitions constituents present at each site were analyzed for the purpose of characterizing their inherent hazard to people and their environmental fate, if released into the water. The second research effort was a 1-year study of the ocean currents in the vicinity of the sites, using acoustic sensors stationed adjacent to and within the sites. This research effort was conducted to better understand the ocean currents in the vicinity of the disposal sites and whether and how these currents could possibly bring munitions constituents from either site to nearshore waters frequented by people. The final research effort was a computer modeling analysis, which used the results from the munitions constituents analysis and the improved ocean current information to investigate the potential human health hazards, were there to be a release of munitions constituents from either site.

The study was conducted by NOAA with assistance from the University of Hawaiʻi, Noblis, Inc., and Genwest Systems, Inc.

Project purpose and objectives

The primary purpose of the study was to resolve two data gaps in the 2006 NOAA screening level assessment identified by the Ordnance Reef Coordinating Council established by the Office of the Deputy Assistant Secretary of the Army for the Environment, Safety, and Occupational Health:

> (a) a lack of understanding of the ocean currents in the offshore areas of Ordnance Reef (HI-06)(Oʻahu, Hawaiʻi), and
>
> (b) a need to determine the areas potentially affected should a release of the munitions constituents occur.

In 2006, NOAA entered into a Special Studies Agreement with the U.S. Army (Office of the Deputy Assistant Secretary of the Army for Environment, Safety, and Occupational Health)

and the U.S. Navy (Office of the Deputy Assistant Secretary of the Navy for the Environment) to conduct scientific surveys to evaluate the level of threat sea disposal sites may pose. Under this agreement, NOAA was tasked to collect screening level data to support a DOD evaluation of the potential human health effects of shallow (less than 37 m [120 feet]) and deepwater (deeper than 37 m [120 feet]) sites off O‘ahu, Hawai‘i, where military munitions are known to have been sea-disposed. Under Section 314 of the John Warner National Defense Authorization Act for Fiscal Year 2007 (NDAA, Public Law 109-364), the Secretary of Defense is required to identify sites where military munitions were disposed in coastal waters, and to research the effects on the ocean environment and those who use it. The 2006 study and this ocean circulation and modeling study may be used to meet that requirement.

Both the shallow and deepwater munitions disposal sites are off the west coast of O‘ahu. The nearshore site Ordnance Reef (HI-06) is about 5 km (3 nm) from the town of Wai‘anae, and the deepwater site (HI-01) is about 18.5 km (10 nm) west of the town of Wai‘anae.

Although there was no indication from NOAA’s initial assessment in 2006 that the sea-disposed munitions posed a significant public health or safety risk, one of DOD’s objectives for this study is to model the fate and transport of munitions constituents at both disposal sites. Another objective was to resolve the lack of long-term physical oceanography data for the region by collecting ocean current data, in order to improve predictive modeling.

Sea disposal of military munitions

Sea disposal (offshore dumping) of excess, obsolete, and unserviceable military munitions was practiced by many nations, especially during the years following World Wars I and II. The US DOD ended sea disposal of munitions in 1970. In its 2009 Defense Environmental Programs Annual Report to Congress, the DOD catalogued 65 sea disposal sites created by the U.S. Armed Forces in US coastal waters (DOD, 2010). Sea disposal of munitions became a subject of global concern as awareness grew that potentially dangerous materials have been discarded in most oceans and major seas. Sea-disposed chemical warfare material (CWM) in territorial waters has become a concern for as many as 40 countries, and sea-disposed conventional munitions are a concern for many other countries (Carton and Jagusiewicz, 2009).

Increasing human use of marine resources has prompted action to better understand and manage risks to human health and the environment posed by the munitions and munitions constituents. In 1970, at the recommendation of the National Academy of Sciences, DOD ceased sea-disposal of CWM and began investigating alternative methods for disposing of CWM (Congressional Research Service, 2007). During the 1970s, concerns about sea disposal of CWM and conventional munitions in the United States and Europe led to passage of new regional laws and conventions. In 1972, the U.S. Congress passed the Marine Protection, Research, and Sanctuaries Act of 1972 (MPRSA, Public Law 92-532, commonly

known as the Ocean Dumping Act), which prohibits U.S. disposal of munitions and many other materials at sea unless authorized by a permit. No permits have been issued to DOD for sea disposal of munitions since the MPRSA was enacted (Carton and Jagusiewicz, 2009). Most other nations terminated sea disposal at about the same time (*ibid*.).

Profile of the study area

This study area encompasses two sites containing sea-disposed military munitions. Both sites are off the western, leeward coast of the island of Oʻahu, Hawaiʻi. The study area also includes coastline and waters in the vicinity of the two disposal sites.

Disposal sites

Both disposal sites are off the west coast of Oʻahu (Figure 1). This section of Oʻahu's coastline is commonly known as the Waiʻanae or Leeward Coast.

The site nearest to shore, locally known as Ordnance Reef, is identified by DOD as Military Munitions Sea Disposal Site HI-06. The northern portion of Ordnance Reef (HI-06) extends into Pōkaʻī Bay. The site's western, offshore boundary extends almost to the 300-ft isobath contour, approximately 1.9 to 2.8 km (1 to 1.5 nm) from the shoreline.[1] The eastern, nearshore boundary begins in depths of 6 m (20 ft) within approximately 0.5 km (0.25 nm) of the shoreline. The Ordnance Reef (HI-06) site is roughly 3.7 km (2 nm) long in the north-south direction and 1.9 km (1 nm) wide in the east-west direction. The nearest Hawaiian towns are Waiʻanae, about 5 km (3 mi) to the northeast, Makaha, about 6 km (4 mi) to the northeast, Māʻili, approximately 5 km (3 mi) to the southeast, and Nanakuli, approximately 6 km (4 mi) to the southeast of the site (Table 1).

The second site included in this study is identified by DOD as Military Munitions Sea Disposal Site HI-01. It is located approximately 16.7 km (9 nm) to the west-southwest of Ordnance Reef (HI-06), and roughly 18.5 km (10 nm) from shore. Site HI-01, as shown on NOAA Nautical Chart 19004, covers nearly 165 km^2 (48 nm^2). Its southern extent is at the latitude of Barbers Point Harbor, and its northern extent is at the latitude of Kepuhi Point. It extends westward roughly 16.7 km (9 nm) at its widest point along this northern boundary. Along its southern boundary, HI-01 is approximately 1.9 km (2.5 nm) wide. Water depths at this location range from about 1,630 to 2,600 m (5,300 to 8,500 ft).

[1] An isobath is a contour line representing water depth, so water depths in the westernmost portion of Site HI-06 approach 300 ft (91 m).

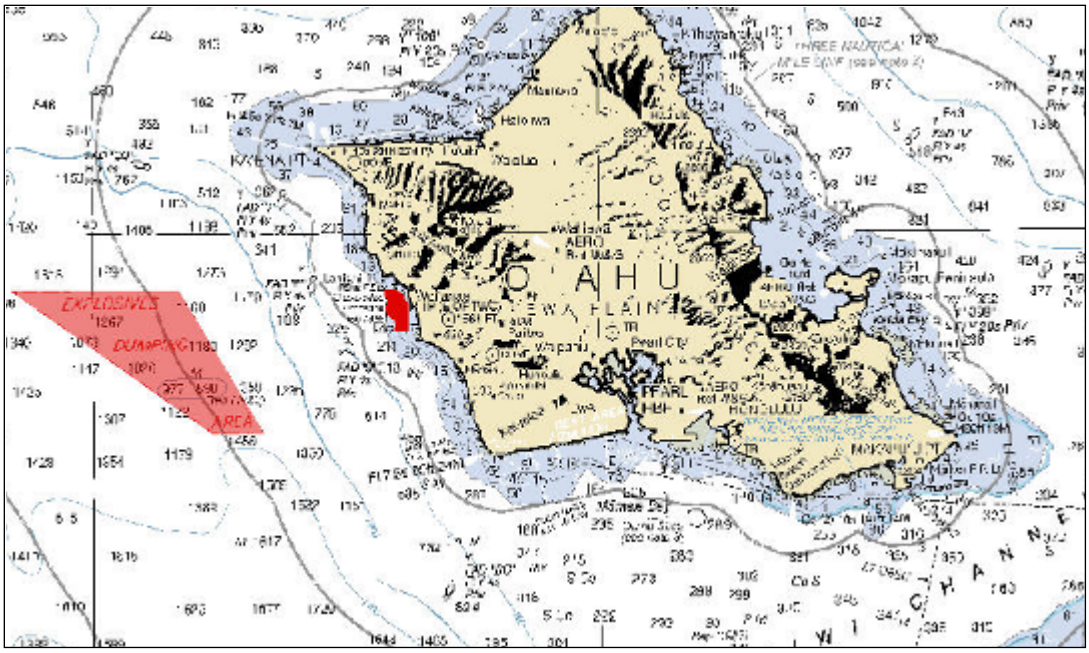

Figure 1. Locations of the sea disposed munitions sites off the west coast of O‘ahu, depicted on NOAA Nautical Chart 19004. Both sites are shaded in red. The deepwater site (HI-01) is to the left; the Ordnance Reef site (HI-06) is to the right, close to the O‘ahu coast.

Adjacent human communities and uses

The Ordnance Reef (HI-06) and deepwater (HI-01) sites are off the populated, largely rural west coast of O‘ahu, a section of coastline commonly known as the Wai‘anae Coast. Table 1 lists the four coastal communities nearest to the sites, their 2010 populations, and their approximate distances from the Ordnance Reef (HI-06) site.

Table 1. Coastal communities near the study area.

Community	2010 population*	Approx. closest distance to Ordnance Reef (HI-06)
Wai‘anae	13,000	4.8 km (3 mi)
Mā‘ili	9,500	4.8 km (3 mi)
Nānākuli	12,700	6.4 km (4 mi)
Makaha	8,000	6.4 km (4 mi)

* Source: US Census Bureau

Public recreation areas and beach parks are numerous along the Wai‘anae Coast, and the nearshore waters and shorelines in this area are popular destinations for outdoor

recreationists. Outdoor activities include recreational fishing, swimming, surfing, snorkeling, diving, kayaking, canoeing, sailing, picnicking, and camping. The largest fishing tournament in Hawai‘i (in terms of number of registrants) is held at Wai‘anae each year, and a popular children’s surfing contest is held annually at Makaha. Fishers come from elsewhere on O‘ahu to fish off the Wai‘anae Coast, generally participating in a small-vessel pelagic troll fishery. Shore casting and spear fishing on the reef also are common along this coast.

General environmental conditions

This section describes the various environmental influences affecting both the ocean current data collection efforts and the ocean circulation and fate/transport modeling work. A consideration of environmental conditions was fundamental for determining the proper location and equipment to be used in collecting ocean current data, and for understanding the possible effects of natural processes on modeling the ocean currents and the potential release of explosives and chemical agents from the disposed munitions into the water.

The information presented below was used by the researchers and is intended to familiarize the reader with the general conditions in the study area as well as the island of O‘ahu and the entire Hawaiian island chain.

Geology and geomorphology

The Hawaiian Islands stretch roughly 2,600 km (1,600 mi) from the island of Hawai‘i to Kure Atoll in the Northwestern Hawaiian Islands. These islands are part of a volcanic chain that runs nearly 6,400 km (4,000 mi) from the Aleutian Islands to the central Pacific Ocean. They were formed from a combination of tectonic plate movement over a volcanic hotspot that now lies beneath the Island of Hawai‘i. They range in age from nearly 30 million years old (Midway Atoll in the northwest) to new land currently being formed by volcanic eruptions on Hawai‘i (Juvik and Juvik, 1998).

As in all regions of the Hawaiian Islands, the geology and geomorphology of the Wai‘anae Coast result from the area’s individual volcanic origins and history. The island of O‘ahu was formed by two volcanoes, the Wai‘anae and Ko‘olau, beginning approximately four million years ago (Stearns and Vaksvik, 1935). Volcanic eruptions deposited lava flows and pyroclastic materials that built the main mass of the Wai‘anae volcano, which has gradually eroded over time to take on its current physical characteristics and appearance.

Winds

A system of persistent winds blows across the Pacific Ocean from the northeast to the southwest in the Northern Hemisphere between 30° north latitude and the Equator. These northeasterly winds became known as trade winds centuries ago when sailing ships

carrying valuable cargo depended on them for fast passage. The trade winds are the predominant winds in Hawai‘i and the most important weather element.

Trade winds prevail most of the summer, but may occur only part of the time in winter. At other times during the winter, Kona winds may blow. “Kona” is a Hawaiian term for stormy, rain-producing winds that blow in from the southwest. Those parts of the islands that are predominantly in the lee of the trade winds—including both the sea disposal sites discussed in this report—are directly in the windward face of the Kona winds when they blow.

In addition, at certain times of the year the trade winds collapse for a few days. At those times, weak diurnal winds occur, with onshore breezes during the day and offshore breezes during the night. These strongly varying wind conditions are especially felt on the western side of the islands.

General ocean processes

This section describes the coastal and ocean processes that shape and define the Wai‘anae Coast's shoreline and nearshore waters, including the currents and tides, water column profile, and water quality.

Currents and Tides

Despite their relatively small size, the Hawaiian Islands strongly affect the atmospheric and oceanic circulations of the northern, subtropical Pacific region. Hawai‘i’s high volcanic mountains, extending from the seafloor (Figure 2), block both the northeast trade winds and the Northern Equatorial Current (NEC), forcing both to squeeze between the islands and creating an ocean/atmosphere wake that extends westward 3,000 km (1,860 mi) across the Pacific. These wind-stress patterns drive the eastward Hawai‘i Lee Countercurrent (HLCC) west of the Big Island, creating a strong shear zone between the NEC and the HLCC.

Figure 2. Two volcanic mountains originating on the seafloor make up the island of Oʻahu (center). Waiʻanae Volcano makes up the northwest section of Oʻahu; Koolau Volcano makes up the eastern section of Oʻahu. The sea disposal sites are off the west coast of Oʻahu, in the area of an ancient undersea landslide (visible in this graphic). Image source: University of Hawaiʻi at Manoa (http://www.soest.hawaii.edu/HMRG/Multibeam/3d.php#hawaii).

The HLCC transports large amounts of heat from the western to the central Pacific and plays an important role in controlling the temperature around the Hawaiian Islands (Xie et al, 2001). As the HLCC approaches the leeward side of the island chain, it bifurcates (splits) and feeds the Hawaiian Lee Current (HLC) that flows to the northwest, thereby returning much of the warm HLCC water westward and preventing much of it from passing between the islands to the east. The North Hawaiian Ridge Current (NHRC) flows to the northwest on the windward side of the island chain, carrying the cooler, subtropical water north of the islands. These currents form the canonical circulation around the Hawaiian Islands, as shown in Figure 3 (below).

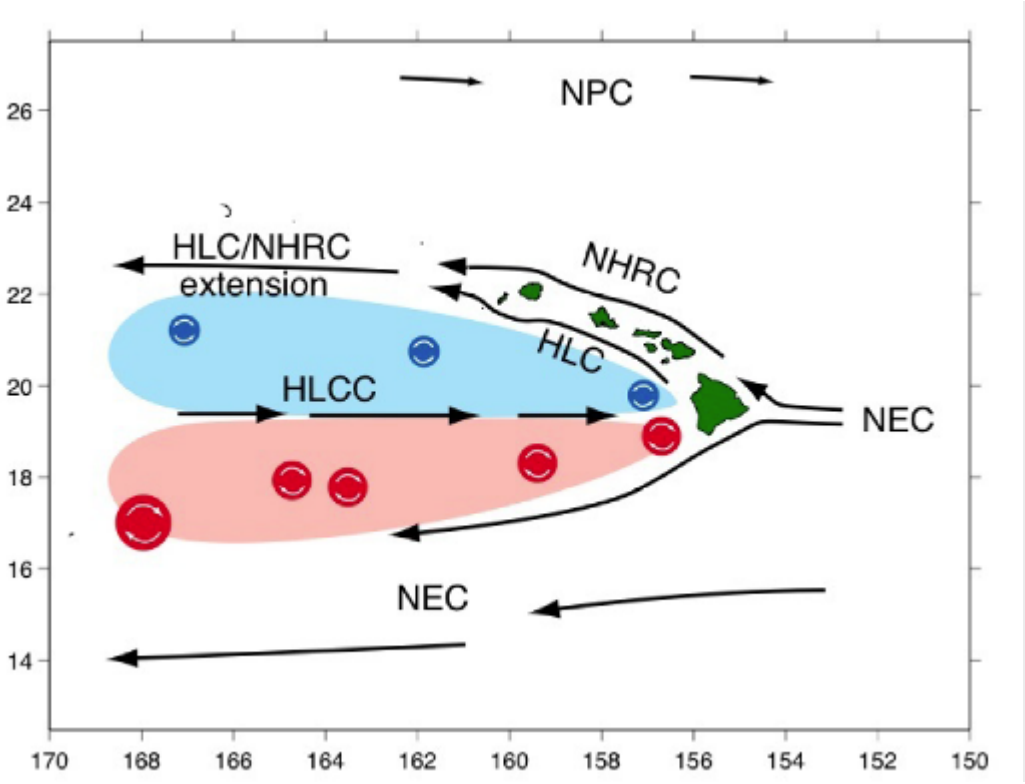

Figure 3. Canonical oceanic circulation around the Hawaiian Islands (Lumpkin, 1998). The blue region is dominated by cyclonic (counter-clockwise-flowing) eddies, and the red region is dominated by anticyclonic (clockwise-flowing) eddies.

The canonical currents are interconnected such that change in the strength of one affects the characteristics of the other currents. The primary region for exchange between the HLC and NHRC is the Kaua'i Channel between the islands of O'ahu and Kaua'i. This channel is composed of the Ka'ena Ridge, a steep sill connecting the two islands. Because cyclonic eddies are prominent in this region (as depicted in Figure 3), they commonly impact the sill and the Wai'anae Coast of O'ahu. In addition to the strong mesoscale activity along the western coast, the Ka'ena Ridge serves as a major generation site of baroclinic tidal energy.

When strong, barotropic tides impact steep ridges, energy is converted into internal or baroclinic waves that propagate along the density structure of the ocean. These tidally induced internal waves can have speeds that are equivalent to the mesoscale, and are a crucial component of the circulation around Hawai'i (Carter et al, 2008). As shown in Figure 4, below, the propagation of these waves follows the Wai'anae coastline. These internal waves alter the density structure of the ocean as they pass. Most noticeably, the thermocline can be heaved by more than 300 m (984 ft) by the strongest internal waves in the area. This change in density depth can displace biological or other particulates in the water column over significant vertical distances. Tidally induced internal waves also can

directly transport matter. As the barotropic tide impacts the slope and the baroclinic internal wave is created, the internal wave can collect matter at the source region (mud, neutrally buoyant biology and particulates) and carry it along the path of the internal wave propagation.

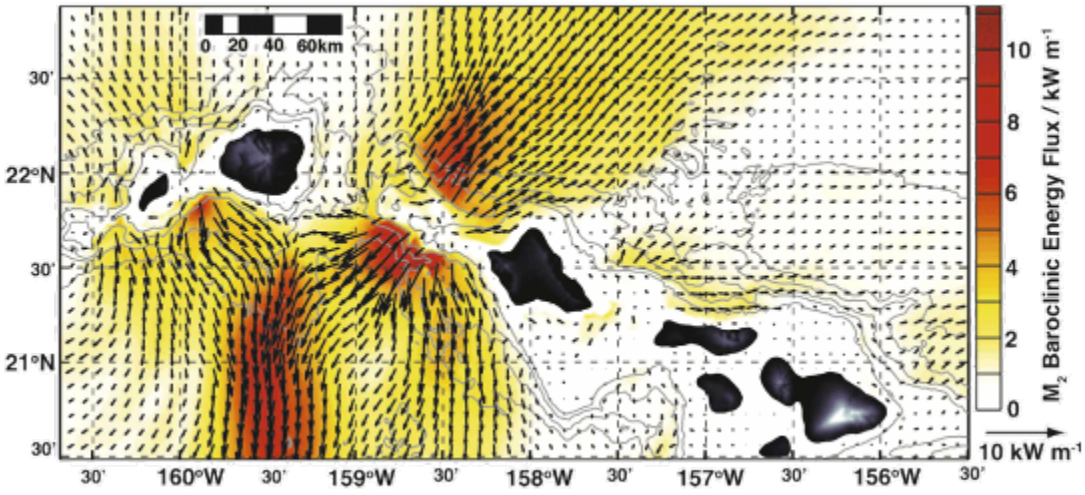

Figure 4. M2 baroclinic energy flux emanating from Ka‘ena Ridge (Carter et al, 2008). Note the strength of baroclinic tidal currents along the Wai‘anae Coast isobaths.

Hawai‘i’s mountainous islands create wakes of weak and variable winds directly in their lee. The Wai‘anae Coast lies directly in the wake of O‘ahu. During normal trade wind conditions, the winds flow around the island, and the Wai‘anae coast is sheltered from those winds in O‘ahu’s wake. For most of the year, these conditions hold, and winds have little impact upon the circulation along the Wai‘anae coast. However, during the winter, the trade winds often collapse (as part of the El Niño-La Niña Southern Oscillation). During these periods, storms traveling from south of the islands can blow strong westerly winds (coming from the west and impacting Wai‘anae). Under some conditions, these winds can affect the circulation along the Wai‘anae coast.

Coral reefs around the Hawaiian Islands significantly protect the islands from the open ocean. Although the coral reefs are exceptionally effective at breaking and dissipating wave energy before it can reach and harm the coast, sustained ocean currents still can impact the islands. Along the Wai‘anae coast, the undersea slope is quite steep, and the waters deepen to 2 km (6,560 ft) within several kilometers of the shore. As a result, the Wai‘anae coast is exposed to the cyclonic eddies present in the HLCC/HLC system. These eddies can impact the island and create significant circulation strengths along the coast.

Tides also affect oceanographic conditions along the leeward sides of the Hawaiian Islands, including the Wai‘anae Coast. Hawai‘i’s semi-diurnal tidal cycle is characterized by two high

waters and two low waters of each tidal day. This tidal regime has been observed to change current patterns along the Wai‘anae Coast. During normal trade wind conditions on a rising or flood tide, strong currents flow from the northwest toward the southeast, parallel to the coastline (Bienfang and Brock, 1980). These currents reverse during falling or ebb tide conditions, flowing from the southeast to northwest.

Water Column Profile

During the 1980s, measurements of temperature, salinity, oxygen, and nutrients were taken at a range of depths from the surface to a depth of 900 m (2,950 ft) and used to characterize the water column profile in the area off Kahe Point (about 11.3 km [7 mi] south of Wai‘anae). The study was conducted by Noda et al (1981). Findings from this study were reported by DBEDT (n. d.), and are summarized below. The water column profile for Kahe Point area is considered representative of the Wai‘anae coast in the vicinity of Ordnance Reef (HI-06).

Temperature and Salinity

Temperature measurements taken during the study period indicated that off Kahe Point, the mixed layer of the ocean (within which temperature changes slowly with depth) extended from the surface down to about 30 to 60 m (100 to 200 ft). Within the ocean’s mixed layer, the properties of the water (including density, temperature, salinity) are essentially uniform, changing little or not at all with depth. Below the mixed layer is the thermocline. Within the thermocline, temperature, and therefore water density, changes relatively quickly with depth. Water density is higher when temperatures are lower. Within the thermocline off Kahe Point, measured temperatures ranged from about 24°C (75°F) at a depth of 60 m (200 ft) to 15°C (59°F) at a depth of about 200 m (650 ft). Below the thermocline, temperature decreased gradually with depth, and at a depth of 900 m (2,950 ft) the measured temperature was about 4°C (39°F).

Off Kahe Point, surface water salinity was about 34.8 parts per thousand (ppt), typical of the Pacific Ocean central water mass. Salinity reached a maximum of 35.1 ppt at 180 m (600 ft), and a minimum of 34.2 ppt at 460 m (1,500 ft). Salinity was 34.4 ppt at a depth of 900 m (2,950 ft) depth.

Dissolved Oxygen

Because warmer water holds less dissolved oxygen, oxygen concentration in Hawaiian waters is lower than in much of the world's oceans. Off Kahe Point, the dissolved oxygen content of the surface water is about 4.8 mL/l of seawater.

Water Quality

Along the Waiʻanae Coast, episodic heavy rainfall events can bring substantial amounts of sediments to nearshore waters. Nevertheless, DBEDT (n. d.) reported that, "temperature and salinity values indicate that the region is well flushed by tidal action and little affected by surface runoff of terrestrial sediments." The tidal flushing means that dissolved pollutants are unlikely to remain long in the waters off the coast.

In general, open ocean surface waters near the Hawaiian Islands are oligotrophic (nutrient poor). This is particularly true of waters off dry leeward sides of the islands such as along the Waiʻanae Coast, where nutrient concentrations are extremely low. Nutrient concentrations in the open ocean off the Waiʻanae Coast are likely to vary depending on the time of year and location. This temporal and spatial variation in nutrient concentrations is also observed in other coastal waters of Hawaiʻi (De Carlo et al., 2004).

The Waiʻanae Wastewater Treatment Plant, a secondary treatment plant located at Waiʻanae, discharges wastewater from the communities along the Waiʻanae Coast into 33 m (108 ft) of water from an outfall pipeline that extends 1.8 km (1.1 mi) offshore. This plant has received several awards, most recently in 2011, recognizing that it has achieved 100 percent compliance with its National Pollutant Discharge Elimination System (NPDES) permit (City and County of Honolulu, 2011).

Marine Ecosystems

DBEDT (n. d.) reported that a variety of ecosystems are found off the Waiʻanae Coast. Vast pelagic and deep sea ecosystems off the Waiʻanae coast support large marine animals such as dolphins, whales, sea turtles, and the occasional endangered Hawaiian monk seal. Near shore, rocky intertidal zones provide habitat for marine invertebrates and plants. Coral reefs are also found near the shoreline along the length of the Waiʻanae Coast. Coral reefs in Hawaiian waters protect shorelines from waves and storm surge, serve as habitat for reef fish and other organisms, and provide snorkeling, diving, surfing, and fishing opportunities.

Explosives and chemical warfare agents at the disposal sites

As part of this study, the explosives and chemical warfare agents of concern known or thought to be present at the two sites were evaluated to:

1. identify their potential human health hazards, physical state (solid, liquid, or gas) under the conditions at the sites, and solubility in water.
2. assess the likelihood that any could be transported to the nearshore zone where people may be present.
3. determine whether any could be present at concentrations high enough to be hazardous to people in the water.

To complete these evaluations, the research team first surveyed the chemical literature to identify the most important chemical reactions that could determine the environmental fate of each of the munitions constituents of concern. The results of these physical and chemical analyses are summarized in this section.

Relevant chemical characteristics and processes

The environmental fate of each munitions constituent is determined by a set of physical properties of the energetics as well as the physical properties of the marine environment. For the energetics, those properties include solubility, density, melting point, vapor pressure, Henry's Law constant, and partitioning coefficients. For the marine environment, physical parameters that determine the chemical fate of the energetics include temperature, pH, salinity, dissolved oxygen, and the ionic strength of seawater. All of these factors in combination determine whether the energetics will be found in the environment as a gas, liquid, or solid and to what extent each compound will react in the environment. The properties are summarized below and are discussed in more detail in Appendices C and D.

The physical state and solubility of a chemical substance are important in part because they determine the location of the substance within the water column. While an insoluble solid substance could be found on the ocean floor, a dissolved solid or a liquid could be in the water column, where it would be more likely to be brought to shore. A liquid that is less dense than seawater could float on the surface, where it would be more likely to come into contact with swimmers.

A key finding from this study is that none of the explosives or chemical warfare agents known or thought to be at either of the two sites would float in seawater, because all are either solids or liquids denser than water. If dissolved in water, the explosives and chemical warfare agents would diffuse and disperse with the water. Not all would readily dissolve in water, and those that would not dissolve would remain on the bottom or associate with

particulate matter. Overall, these characteristics mean a lower potential human health hazard from these chemicals.

Physical state and solubility also affect a compound's availability for biological or chemical degradation. Generally, a more soluble substance is more likely to be degraded than a substance that remains in solid form.

The primary chemical processes that could degrade munitions constituents in the marine environment are thermolysis, oxidation, hydrolysis, and photolysis:

- Thermolysis refers to the decomposition of a compound due to heat energy. At the water temperatures measured at Ordnance Reef (HI-06) (23–25°C [73.4–77°F]) and deepwater site HI-01 (2°C [36°F]), thermolysis is not a significant degradation pathway for the compounds of interest.
- Photolysis refers to the breaking-up of a molecule by light energy. This is a significant degradation pathway for compounds found in the photic zone, which extends to a depth of 40 m (131 ft) at Ordnance Reef (HI-06). The shallow areas at Ordnance Reef (HI-06), where the explosives were found, are at a depth of 15 m (49 ft), within the photic zone. Photolysis could be relevant for the shallow munitions. The deepwater site HI-01, where the CWM was disposed, is at a depth of about 1,630 to 2600 m (5,300 to 8,500 ft), far below the photic zone, so photolysis will not be relevant at these sites.
- Oxidation refers to an increase in the oxidation state of a chemical, which for organic molecules often involves the addition of one or more oxygen atoms.
- Hydrolysis refers to the splitting of a compound due to its interaction with water molecules, with addition of the components of water. Generally this means that a bond in the original compound will break, and one half will bind to an H^+ ion from water, while the other half will bind to an HO^- ion from water.

Oxidation and hydrolysis both depend on pH (a measure of the H^+ ion concentration of the surrounding solution). Under basic (alkaline) conditions, such as those found at Ordnance Reef (HI-06) (pH = 8.12), hydrolysis is favored over oxidation.

Munitions at the Ordnance Reef (HI-06) disposal site

This section describes the characteristics and potential environmental fates of the explosives found at the Ordnance Reef (HI-06) site during past surveys or believed to be present based on the types of munitions found. It also explains why ammonium picrate was selected for fate and transport modeling.

Findings from past surveys of this site

To date, no official records of the military munitions sea-disposed at this site have been found; DOD was alerted to the presence of these munitions by local residents. In 2002, at the request of the Army Corps of Engineers, explosive ordnance disposal (EOD) divers conducted a visual survey of the Ordnance Reef (HI-06) site to determine the amounts and types of munitions present. Munitions located during the survey included naval gun ammunition, 105 mm and 155 mm artillery projectiles, mines, mortars, and small arms ammunition. Munitions found during the diver survey were categorized as DMM rather than UXO.

In 2006, NOAA conducted a screening-level survey of the Ordnance Reef (HI-06) site. The 2006 study confirmed the findings from the 2002 survey, verifying the presence of munitions ranging from small arms projectiles to large-caliber artillery projectiles and naval gun ammunition. The munitions were found in water depths ranging from 7.3 m (24 ft) to the maximum depth of the study area, 91.4 m (300 ft). No explosives or related compounds were detected in fish samples taken during the 2006 survey. The survey was conducted by NOAA, with assistance from the University of Hawai‘i and the Hawai‘i Department of Land and Natural Resources.

ROUMRS (Remotely Operated Underwater Munitions Recovery System)

In fall 2009, the U.S. Army contracted with ARA, Inc., for the design, development, and demonstration of a remote underwater military munitions recovery system at Ordnance Reef (HI-06). The Demonstration’s objective was to develop an integrated remote recovery system that would provide DOD with a variety of options for the safe, cost effective characterization and recovery of various types of military munitions from a variety of water depths and aquatic environments. The integrated recovery system involved a package of technologies consisting of a remotely operated vehicle (ROV), adaptable attachments, specialized tools, and lifting baskets. The Demonstration’s efforts at Ordnance Reef (HI-06) focused on the recovery of DMM from depths of approximately 9 to 37 m (30 to 120 ft) and took place in the summer of 2011.

The US Army requested NOAA’s support prior to the technology demonstration to ensure that best management practices for protection of coral and other benthic habitats were incorporated. In 2010, NOAA began working collaboratively with the Army on a two-year project to assess the corals present within Ordnance Reef (HI-06), develop procedures to avoid and minimize any potential impacts to corals resulting from the Technology Demonstration, and develop an appropriate coral mitigation strategy commensurate with any injuries to corals that occur.

Visual surveys of areas where DMM were present were conducted to identify areas of relative coral injury risks. These surveys were accomplished by NOAA scientific divers

using SCUBA during 78 dives. Dive sites were chosen based on surveys for munitions conducted in 2002 and 2006, as well as from information gained during previous project dives. Munitions were generally found in linear trails, and where concentrations were found, the trails were followed until no additional DMM was observed or divers were forced to surface due to air limitations.

The NOAA staff reviewed all photo documentation obtained during these survey dives and estimated the number and types of munitions as well as habitat types present. DMM were visually identified in the geo-referenced photographs and categorized into three general types: small arms ammunition (SAA) (ammunition without projectiles containing explosives that are .50 caliber or smaller), small to medium caliber munitions (munitions above .50 caliber to and including 105 mm), and large caliber and other munitions (munitions larger than 105 mm and bombs, rockets, etc).

Table 2 summarizes the numbers of DMM documented by NOAA during a 2010 survey of the Ordnance Reef (HI-06) site.

Table 2. Numbers of DMM documented by NOAA at Ordnance Reef (HI-06) prior to the ROUMRS Technology Demonstration Project in 2011.

	SAA[1]	Small to Medium Caliber Munitions[2]	Large Caliber and Other Munitions[3]
Work Area A	14	0	0
Work Area B	229	1,461	0
Work Area C	12,557	6,061	874
Total	12,800	7,525	874

1 Ammunition without projectiles that contain explosives, that is .50 caliber or smaller.

2 Munitions above .50 caliber to and including 105 mm.

3 Munitions larger than 105 mm and bombs, rockets, etc.

Source: http://ordnancereefhawaii.org/EA.htm

During the ROUMRS technology demonstration, it was discovered that most munitions items were covered in a thick layer (upwards of 2.5 cm [1in]) of hard marine growth and concreted to the sea bottom. Almost half the munitions items encountered were so heavily encrusted with hard calcareous growth that they could not be pried from the sea floor and were left in place (Figure 6). Despite this encasement in marine growth, significant

corrosion and loss of metal had occurred for a number of munitions items recovered, but their explosive constituents remained virtually intact (Figure 7). In other instances, loss of metal casings was minimal, and evidence of water infiltration was present. However, none of the recovered munitions items were found to have lost a significant amount of the explosive constituents, be it the slightly soluble TNT or the much more soluble Explosive D (ammonium picrate).

No CWM are known to be located at Ordnance Reef (HI-06). None have been found during the previous site surveys nor would any be expected near shore or in shallow water.

Figure 5 (below) depicts known locations of disposed munitions at the site, as of 2011.

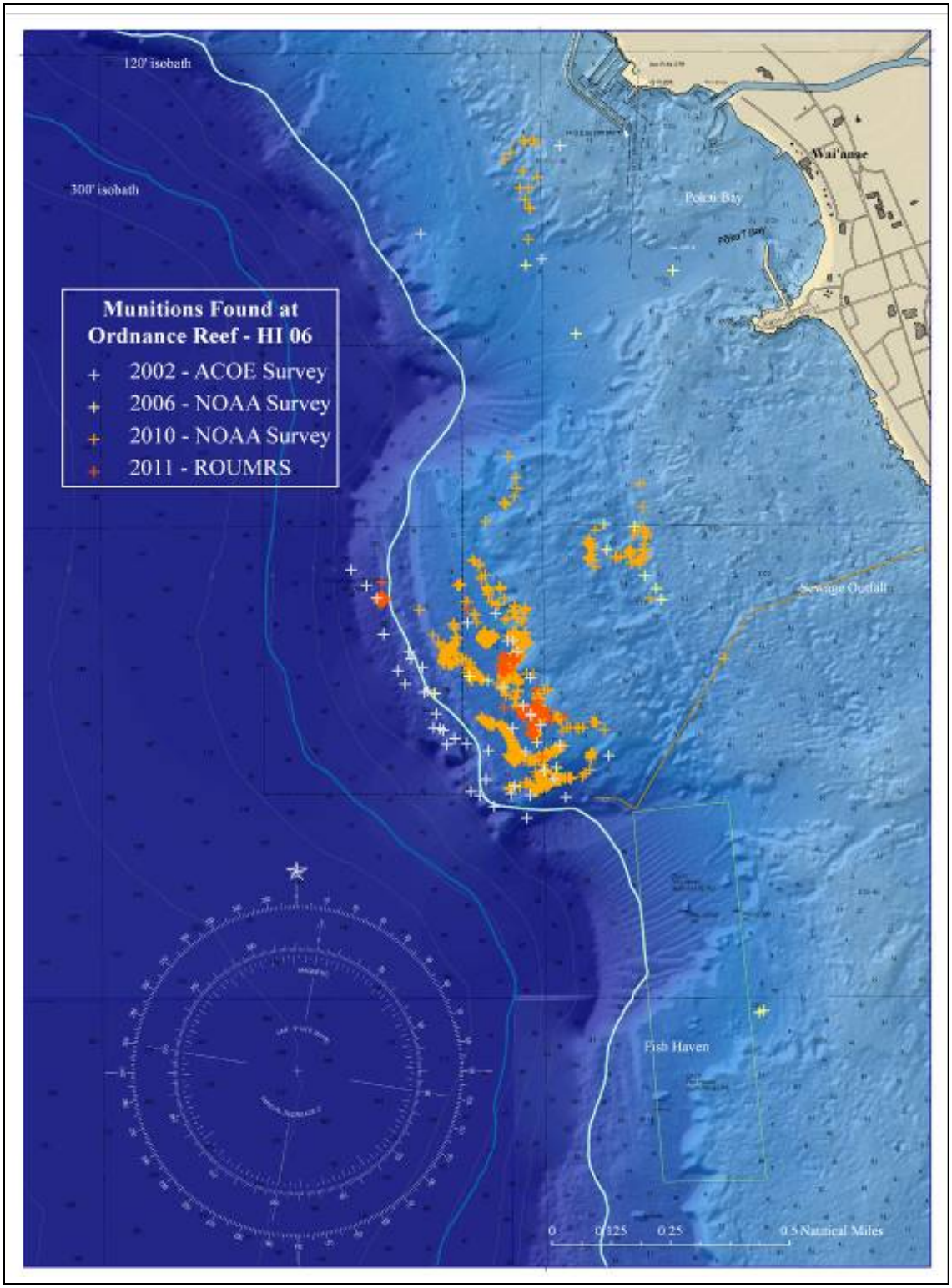

Figure 5. Known locations of munitions at Ordnance Reef (HI-06) (as of mid-2011). Munitions are color-coded by the survey during which they were found. Generally, areas closest to shore have been found to contain relatively small numbers of munitions items, typically small arms ammunition.

Figure 6. Photos showing varying degrees of encrustation on munitions recovered at Ordnance Reef (HI-06). The photo at right shows encrustation on a fragmentation bomb. Some of the encrustation on this bomb was removed during recovery operations, revealing the thickness of this encrustation.

Figure 7. A 100-pound bomb recovered during the ROUMRS technology demonstration. This bomb was cut to expose the main explosive charge (large area with cracks) and booster (at center). Note that much of the metal bomb casing was completely corroded away (and is missing at lower left and center right), although the explosive appears relatively intact. Artillery projectiles, which have thicker shell walls, were largely intact, but many had leaked, allowing water to enter the explosive.

Chemical profiles of the explosives constituents at the Ordnance Reef (HI-06) site

This section summarizes findings discussed in greater detail in Appendix C (Noblis 2011a).

Explosive munitions constituents of concern found at Ordnance Reef (HI-06) include 2,4,6-trinitrotoluene (TNT), 2,4-dinitrotoluene (2,4-DNT), hexahydro-1,3,5-trinitro-1,3,5-triazine (RDX), octahydro-1,3,5,7-tetranitro-1,3,5,7-tetrazocine (HMX), and ammonium picrate (Explosive D). While all shells containing these constituents of concern are assumed to have been intact when disposed, it is possible that some shells have been degraded and compromised over time, in which case, contents may have biodegraded. This report assumes no biodegradation has occurred.

2,4,6-trinitrotoluene (TNT)

Under the conditions at Ordnance Reef (HI-06), TNT is a non-volatile solid which is more dense than water (d = 1.654 g/mL) and only slightly soluble in seawater (solubility at 25°C [77°F] = 94.4 mg/l). These properties mean that any solid TNT released into the environment would sink to the bottom of the water column and reside on the ocean floor, dissolving very slowly.

The organic carbon and octanol-water partition coefficients were estimated, and indicate moderate partitioning into organic carbon and octanol. However, there is very little organic carbon in the sediment at the site, so this is not considered a significant dispersion mechanism.

As mentioned above, thermolysis and chemical oxidation are not significant reactions for the compounds of interest under the conditions at Ordnance Reef (HI-06). For TNT, hydrolysis is not an important reaction either, since hydrolysis of TNT has only been reported at pH ≥ 10, higher than the pH measured at Ordnance Reef (HI-06).

Therefore, the only chemical degradation pathway that is relevant for TNT at Ordnance Reef (HI-06) is photolysis. Any TNT that may have dissolved at the shallow sites could have been photolysed to a number of different compounds (with an estimated photolysis half-life of several hours depending on incoming solar radiation and water clarity). The water-soluble components that have been identified in literature are nitrobenzene, azoxybenzene, and benzisoxazole derivatives with nitro or amine substituents. Some of these compounds are moderately explosive in their own right. Some water-insoluble photolysis products were reported as well, but their specific identities were not determined. However, they are thought to be oligomers of azo and azoxy compounds. See Noblis (2011a) for more details and a list of the specific photolysis products.

2,4-dinitrotoluene (2,4-DNT)

Although 2,4-DNT is not believed to be a large constituent of the munitions at Ordnance Reef (HI-06), it was detected in a few sediment samples taken in 2006. Generally, DNTs are used as stabilizers and ballistic modifiers in propellant, and DNT is a chemical precursor to TNT in the TNT manufacturing process. Hence, it is possible that DNT is present at Ordnance Reef (HI-06) as a manufacturing impurity.

Since 2,4-DNT is structurally similar to TNT, it is not surprising that its physical and chemical properties under the conditions at Ordnance Reef (HI-06) are similar to those of TNT. It is a non-volatile solid which is more dense than water (d = 1.52 g/mL) and sparingly soluble in seawater (solubility at 25°C [77°F] = 127 mg/L). Like TNT, any solid 2,4-DNT released into the environment would sink to the bottom of the water column and reside on the ocean floor, dissolving very slowly.

Hydrolysis is not believed to be a significant reaction for 2,4-DNT. Hydrolysis reactions have only been reported at pH ≥ 10, higher than the pH of the seawater at the site. No literature results on hydrolysis reactions at pH < 10 were found. Thus, photolysis is assumed to be the main chemical degradation pathway for this compound.

Photolysis of 2,4-DNT produces several amino- and nitro-substituted aromatic compounds, including 4-nitrotoluene, 2,4-dinitrobenzaldehyde, and 2,4-dinitrobenzoic acid. Some of these compounds are somewhat explosive in their own right. Some unidentified water-insoluble compounds were formed as well; however, like the insoluble products of TNT photolysis, they are thought to be azo and azoxy polymerization products. See Noblis (2011a) for more details.

Hexahydro-1,3,5-trinitro-1,3,5-triazine (RDX)

Under the conditions at Ordnance Reef (HI-06), RDX is a non-volatile solid that is more dense than water (d = 1.82 g/mL) and even less soluble in seawater than TNT (solubility at 25°C [77°F] = 55.6 mg/L). Like TNT, any solid RDX released into the environment would sink to the ocean floor and dissolve very slowly.

The estimated organic carbon partition coefficient indicates that moderate partitioning into organic carbon can occur, but the octanol-water partition coefficient shows that very little of the compound will partition into non-polar substances. This is not considered a significant dispersion mechanism under the environmental conditions studied.

Thermolysis, chemical oxidation, and hydrolysis are not significant reactions for RDX under the conditions at Ordnance Reef (HI-06), since thermolysis and oxidation are unlikely for any of the compounds, and hydrolysis rates for RDX in seawater were reported to be very low.

Therefore, the only significant degradation pathway for RDX is photolysis, and the possible degradation products reported include azoxy compounds, ammonia, formaldehyde, nitrates, nitrites, nitrous oxide, and N-nitroso-methylenediamine. However, the rates of photolysis would likely be very low even at the shallow sites (15m [49 ft] depth), since reported RDX photolysis rates in river water decrease quickly with increasing water depth, and are very low even at a depth of 3 m (10 ft). There are no reports on the effects of salinity or ionic strength on RDX photolysis, so the effects of salt levels on this chemistry cannot be assessed without further experimentation.

Octahydro-1,3,5,7-tetranitro-1,3,5,7-tetrazocine (HMX)

Like TNT and RDX, HMX is a non-volatile solid that is more dense than water (d = 1.96 g/mL), and essentially insoluble in seawater (solubility at 25˚C [77˚F] = 3.3 mg/L). If released, it will reside on the ocean floor and dissolve extremely slowly.

The aqueous chemistry of HMX under the conditions at Ordnance Reef (HI-06) is nearly identical to that of RDX, except that the rates of photolysis are even lower.

Ammonium picrate (Explosive D)

Unlike the other compounds of interest, ammonium picrate is a non-volatile solid that is soluble in seawater (solubility at 25˚C [77˚F] = 10.2 g/L) and will readily dissolve into ammonium and picrate ions if it is released into the water column.[2] Both the ammonium and picrate would remain in ionic form under the conditions found at Ordnance Reef (HI-06), and would not undergo acid-base chemistry to any significant extent.

None of the four main chemical processes that were analyzed are relevant for the picrate ion. It is not degraded by thermolysis or oxidation, and also does not undergo hydrolysis or photolysis to a significant extent.

However, there is a degradation pathway that is significant for ammonium picrate. Picric acid, the conjugate acid form of the picrate ion, was found to be biologically decomposed by bacteria in marine sediment into several amino- and nitro-substituted phenols. Two studies have identified the toxic and explosive compound picramic acid (2-amino-4,6-dinitrophenol) as the major product of biotransformation of picric acid (Nipper, 2005; Lotufo et al., 2009). Although these researchers were investigating the fate of picric acid and not picrate ion, their findings indicate that biodegradation processes are likely to be relevant for picrate as well.

Another concern regarding ammonium picrate is that even if it is not released into the environment, it could react with the metal casings of the munitions it is stored in, forming

[2] Picrate ion is the conjugate base of picric acid, differing from it only by the absence of one hydrogen ion. In water, picric acid, which has a pKa of about 0.4, is present almost entirely in its anion form as picrate ion.

metal picrate salts which are highly shock-sensitive when dry. These compounds are somewhat less powerful explosives than ammonium picrate or picric acid, but are much more sensitive and therefore much more likely to explode. Because keeping metal picrates wet diminishes their sensitivity, any munitions containing ammonium picrate should be kept wet if brought to the surface.

Selection of ammonium picrate for fate and transport modeling

Of the explosive compounds found at the Ordnance Reef (HI-06) site and surveyed in this study, only ammonium picrate is soluble in seawater. The other compounds are non-volatile solids which are nearly insoluble in seawater and significantly denser than water. If these insoluble, dense compounds were released from containment, they would sink to the bottom of the water column and reside on the ocean floor. Because these compounds dissolve extremely slowly, they would not reach concentrations close to their levels of concern within the marine environment, and so are expected to have no impact on human health under ambient conditions in the area of Ordnance Reef (HI-06).[3]

Ammonium picrate's toxicity[4] and solubility—it is almost 100 times more soluble than any of the other munitions components known to be present at Ordnance Reef (HI-06)—make it the most hazardous of the explosives, if it were to be released. Because of its greater hazard, it was selected for fate and transport modeling (the relevant findings are discussed below in the Fate and Transport Modeling section of this report).

Once dissolved in water, ammonium picrate would separate into ammonium and picrate ions, and would not undergo acid-base chemistry to any significant extent. Because the picrate ion is not degraded by any of the main chemical processes prevalent in the marine environment, it would persist in picrate form unless transformed by bacteria into the toxic and explosive compound picramic acid. Because it is difficult to predict the extent of the biological processing that might occur, it is unknown how much of the picrate ion would be transformed in this way. Therefore, ammonium picrate rather than picramic acid was selected for modeling.

Chemical warfare agents at the deepwater disposal site (HI-01)

This section describes the characteristics and potential environmental fates of the chemical warfare agents recorded as present at deepwater site HI-01, and explains why hydrogen cyanide was selected for fate and transport modeling.

[3] A level of concern is the concentration of a pollutant (in water, air, or other media) above which a hazard to people is believed to exist.

[4] Established human health guidelines and limits for ammonium picrate are shown in Table 5, below.

According to military records, approximately 2,000 tons of chemical warfare agents (including sulfur mustard, cyanogen chloride, lewisite, and hydrogen cyanide) were disposed at this site in the 1940s (Table 3). The disposed chemical warfare agents were packaged as munitions, or in ton containers. The fate of these chemicals in the years since their disposal is not known, and would be difficult to ascertain because of the great depth of this site (about 1,630 to 2600 m [5,300 to 8,500 ft]).

Table 3. Types and amounts of chemical warfare agents present at the deepwater disposal site (HI-01).

Item or Fill	Munition or Container Type	Unit	Quantity	NCAW Per Unit (lbs)	Total NCAW (tons)
Sulfur Mustard	75 mm Projectile	Each	2,440	1.35	2
Sulfur Mustard	105 mm Projectile	Each	21,408	3.17	34
Sulfur Mustard	155 mm Projectile	Each	1,747	11.43	10
Sulfur Mustard	155 mm Projectile	Each	1,949	11.7	11
Sulfur Mustard	155 mm Projectile	Each	595	11.8	4
Sulfur Mustard	4.2 inch Mortar	Each	30,917	6.5	100
Sulfur Mustard	115 lb Bomb	Each	14,956	60.6	453
Sulfur Mustard	Ton Container	Each	1,038	1,885	978
Sulfur Mustard Total					**1,592**
Lewisite	Ton Container	Each	190	2,660	253
Lewisite Total					**253**
Cyanogen Chloride	500 lb Bomb	Each	125	176	11
Cyanogen Chloride	1,000 lb Bomb	Each	1,100	351	193
Cyanogen Chloride Total					**204**
Hydrogen Cyanide	1,000 lb Bomb	Each	20	200	2
Hydrogen Cyanide Total					**2**

NCAW – Net chemical agent weight
Source: Defense Environmental Programs Annual Report to Congress [FY2009] (http://www.denix.osd.mil/arc/upload/10_FY09DEPARC_Sea_Disposal_DENIX.pdf)

Profiles of the chemical warfare agents at the deepwater site (HI-01)

This section describes the characteristics and potential environmental fates of the chemical warfare agents recorded as present at deepwater site HI-01. It summarizes the findings discussed in more detail in Appendix D (Noblis, 2011b). It also explains why hydrogen cyanide was selected for fate and transport modeling.

The chemical warfare agents of concern include sulfur mustard (H/HD), Lewisite (L), cyanogen chloride (CK), and hydrogen cyanide (AC). These compounds are in the munitions

or bulk containers disposed at deepwater site HI-01 16.7 km (9 nm) west-southwest of Ordnance Reef (HI-06).

Sulfur Mustard (HD)

Under the conditions at deepwater site HI-01, sulfur mustard (1,1′-thiobis[2-chloroethane]) is a non-volatile solid that is sparingly soluble in water (solubility at 5°C [41°F] in seawater = 0.3 g/L). It is more dense than water (d = 1.27 g/mL), so any sulfur mustard that is released from munitions will remain on the ocean floor and dissolve very slowly.

Any dissolved sulfur mustard will react with water (hydrolysis) at a significant rate, with an estimated half-life of 3 hours in seawater at 5°C (41°F). If complete hydrolysis occurs, the main product will be thiodiglycol, a non-toxic compound.

However, incomplete hydrolysis and oligomerization (reaction of multiple sulfur mustard molecules with each other) are also possible, and the products of these reactions are charged particles that may be stabilized in the ionic environment present in seawater. It is also possible for these charged particles to form protective bubbles around undissolved sulfur mustard, acting as amphiphilic surfactants to generate stable droplets of sulfur mustard that can persist in the marine environment for years. Since these droplets consist mainly of unreacted sulfur mustard, they will still be denser than water and remain on the sea floor unless they are disturbed.

Lewisite (L)

At 0°C (32°F), Lewisite (primarily 2-chlorovinylarsenous dichloride) will probably be a liquid. Since weapons-grade Lewisite is actually a mixture of related compounds, its melting and boiling points can vary based on the exact composition of the mixture. In any case, all available reports agree that it is both denser than water (d = approx. 1.88 g/mL) and sparingly soluble in water (solubility at 25°C [77°F] in seawater = 0.5 g/L). Therefore, if it is released, it will stay on the sea floor, dissolving very slowly.

Any dissolved Lewisite will react with water quickly, forming chlorovinylarsenous acid (CVAA). Once it is produced, CVAA will quickly reach equilibrium with Lewisite oxide (2-chlorovinylarsenous oxide). Both of these compounds are just as toxic as Lewisite, and they are much more soluble.

CVAA will decompose slowly in cold water at elevated pH, eventually forming arsenous acid ($As[OH]_3$), acetylene, and chloride ion. It is estimated that, under the conditions of the deepwater site (HI-01), the reaction will be complete after several months. The arsenous acid can then enter the inorganic arsenic cycle in the environment and be metabolized by bacteria.

Lewisite oxide will eventually oxidize to the less toxic 2-chlorovinylarsonic acid if left standing in water long enough. This compound can also enter the biological arsenic cycle and be further processed by bacteria.

Cyanogen Chloride (CK)

Cyanogen chloride is a liquid at 0°C (32°F) that is quite soluble in water (solubility at 25°C [77°F] = 69 g/L). Any cyanogen chloride that is released into the environment will quickly dissolve into the surrounding water.

Once it is dissolved, cyanogen chloride will react with water over the course of several months, forming hydrochloric acid and cyanic acid. Both of these acids will be immediately neutralized at seawater pH. Eventually, the cyanate ion that is produced will react with seawater to form ammonium chloride and carbon dioxide, which are not dangerous.

Hydrogen Cyanide (AC)

At 0°C (32°F), hydrogen cyanide is a liquid. It is very soluble in water (miscible in seawater at 0°C), so any hydrogen cyanide that is released will immediately dissolve into the surrounding water.

Unlike the other chemical warfare agents analyzed, hydrogen cyanide does not react with water to any significant degree. It is a weak acid, so a small amount of it will react with hydroxide ions in the water to form cyanide ions. The rest will persist as hydrogen cyanide until processed by bacteria. Some bacteria are known to metabolize hydrogen cyanide to ammonia and carbon dioxide, but it is unknown whether these bacteria are present in the deepwater site (HI-01), or how long it would take them to break down the hydrogen cyanide if they were present.

Oceanographic modeling of chemical warfare agents

Of the four chemical warfare agents analyzed, sulfur mustard and Lewisite are sparingly soluble in water and denser than water, so they would remain on the ocean floor if released from the munitions, dissolving very slowly. While some of the hydrolysis products of Lewisite are soluble, the slow rate at which Lewisite dissolves would limit the concentrations of these products.

Given that both sulfur mustard and Lewisite dissolve very slowly in water, if either ever were to reach a concentration in water at or above a level of concern for humans, that concentration would be reached only within the general vicinity of the source container(s). Given the great distance between the containers on the sea floor and areas frequented by people, these two compounds are expected to have no impact on human health.

The other two compounds, cyanogen chloride and hydrogen cyanide, are significantly more soluble in seawater. Of these two, cyanogen chloride reacts with water to produce several compounds which are not dangerous.

Hydrogen cyanide, on the other hand, is about 2,000 times more soluble than lewisite. It is likely to persist in solution in a toxic form because it does not react with water to any significant extent. Because of this attribute and its toxicity, hydrogen cyanide was chosen for further oceanographic modeling.

Characterizing the ocean currents along the west coast of O‘ahu

This section describes how NOAA and the Department of Oceanography, University of Hawai‘i at Manoa, collected and analyzed information about ocean currents in the vicinity of the two munitions disposal sites, and presents the relevant findings. During the first stage of the ocean currents study, ocean current velocities were measured directly for one year at five locations near the munitions disposal sites. During the second stage, the water velocity data were used to construct and validate models of the ocean currents in the vicinity of the disposal sites. The modeled currents were then used in a fate and transport modeling study (described in the next section of this report) to predict how munitions constituents could be transported through the water, if released from containment.

Observations of the ocean currents along the Wai‘anae Coast

To measure ocean currents in the vicinity of the munitions disposal sites, NOAA and the University of Hawai‘i deployed acoustic sensors near the munitions disposal sites, then compiled and analyzed the data recorded by the instruments.

Deployment of Acoustic Doppler Current Profilers (ADCPs)

From summer 2009 until summer 2010, a total of nine Acoustic Doppler Current Profilers (ADCPs) were deployed at five mooring locations adjacent to the munitions disposal sites, in water depths of approximately 15 m, 90 m, and 2,500 m (49 ft, 295 ft, and 8,200 ft). ADCPs use sound waves and the “Doppler shift” to measure the velocity (speed and direction) of water, and can be used to measure water velocities throughout the entire water column, as was done in this project. The goal of deploying these ADCPs was to collect water velocity data to further and better understand the oceanographic processes occurring in the vicinity of the two disposal sites and to subsequently support the fate and transport modeling study described below.

The nine ADCP sensors were deployed on July 24 and 25, 2009, at the five mooring locations shown in Figure 8, below, and were recovered on August 23 and 25, 2010. They collected ocean current speed and direction data throughout the water column during the 13-month deployment period.

Four of the mooring locations encompassed the nearshore Ordnance Reef (HI-06) disposal site, and one location was adjacent to the deepwater disposal site (HI-01). At the nearshore edge of the deepwater disposal site (HI-01), four Teledyne RD Instruments 75 kHz Workhorse Long Ranger ADCPs and one Teledyne RDI 1200 kHz Workhorse Sentinel ADCP were deployed on a single string. Around the periphery of the Ordnance Reef (HI-06) site, two Teledyne RD Instruments 300 kHz Workhorse Long Ranger ADCPs were deployed at depths of 104 and 72 m (341 and 236 ft), and two Teledyne RDI 300 kHz Workhorse

Sentinel ADCP were deployed at depths of 14 and 17 m (46 and 56 ft). Table 4 (below) provides additional details about the configurations of the deployed ADCPs.

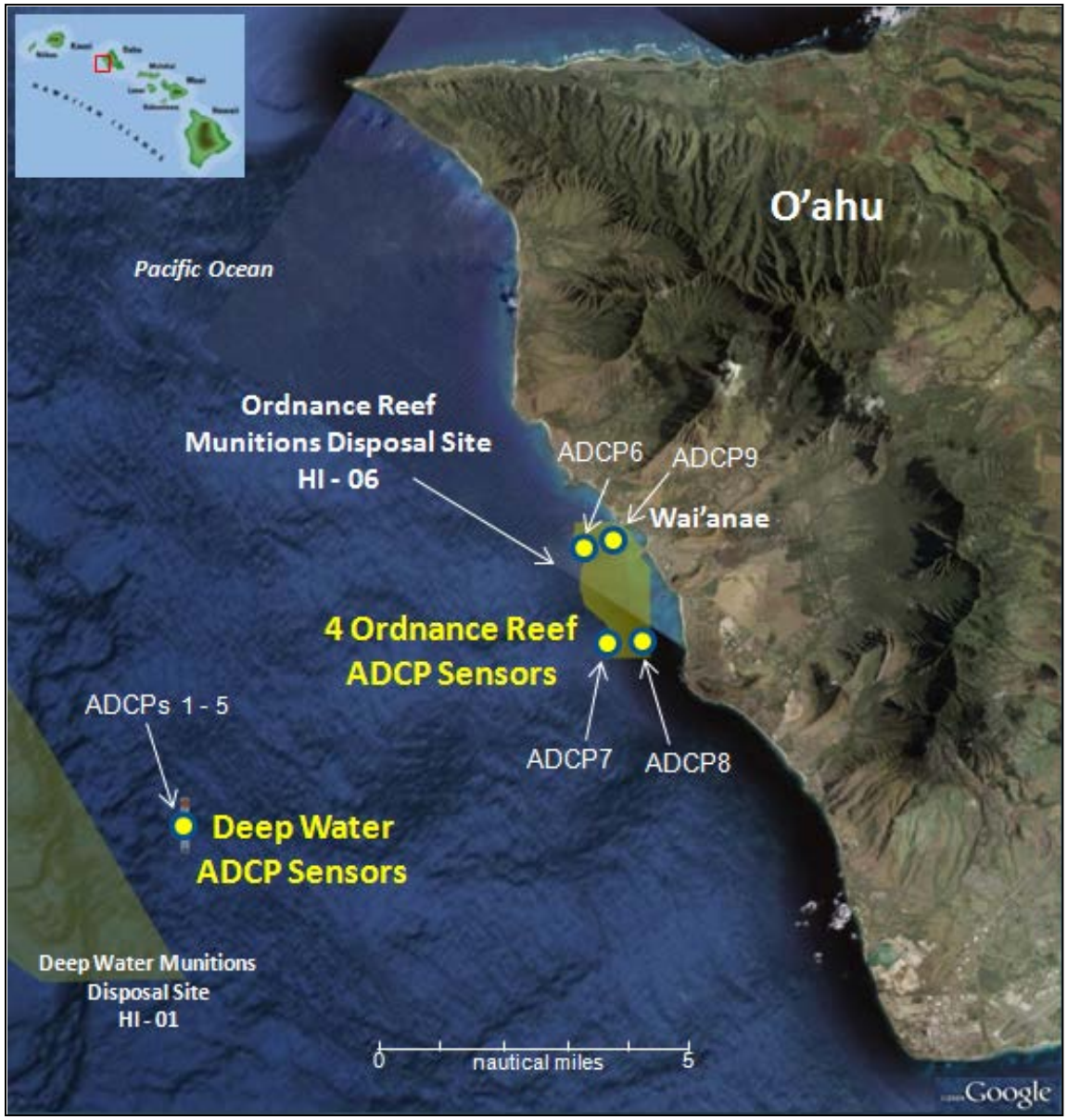

Figure 8. ADCP mooring locations.

Table 4. Descriptions of the ADCPs deployed to measure ocean currents during this project.

	ADCP	Location	Water depth at mooring site (m)	Height above seafloor (m)	Description
Deepwater site	ADCP1	Deepwater disposal site (HI-01)	2,528	450	Upward looking 75 kHz ADCP on the deep string. Collected 2 hr ensembles consisting of 40 pings per ensemble. A total of 8 depth bins of width 20 m each were recorded. Deployed 24 July 2009. Recovered 23 Aug 2010.
	ADCP2	Deepwater disposal site (HI-01)	2,528	450	Downward looking 75 kHz ADCP on the deep string. Collected 2 hr ensembles consisting of 40 pings per ensemble. A total of 8 depth bins of width 20 m each were recorded. Deployed 24 July 2009. Recovered 23 Aug 2010.
	ADCP3	Deepwater disposal site (HI-01)	2,528	150	Upward looking 75 kHz ADCP on the deep string. Collected 2 hr ensembles consisting of 40 pings per ensemble. A total of 8 depth bins of width 20 m each were recorded. Deployed 24 July 2009. Recovered 23 Aug 2010.
	ADCP4	Deepwater disposal site (HI-01)	2,528	150	Downward looking 75 kHz ADCP on the deep string. Collected 2 hr ensembles consisting of 40 pings per ensemble. A total of 8 depth bins of width 20 m each were recorded. Deployed 24 July 2009. Recovered 23 Aug 2010.
	ADCP5	Deepwater disposal site (HI-01)	2,528	12	Downward looking 1200 kHz ADCP at the bottom of the deep string. Collected 15-min ensembles consisting of 60 pings per ensemble. A total of 25 depth bins of width 50 cm each were recorded. Deployed 24 July 2009. Recovered 23 Aug 2010.

	ADCP	Location	Water depth at mooring site (m)	Height above seafloor (m)	Description
Offshore sites	ADCP6	Northwest Ordnance Reef (HI-06) site	94	0	Nearshore 300 kHz ADCP. Collected 10 min ensembles consisting of 12 pings per ensemble. A total of 10 depth bins of width 8 m each were recorded. Deployed 24 July 2009, redeployed (after being flipped) 9 Sept 2009. Recovered 25 Aug 2010.
	ADCP7	Southwest Ordnance Reef (HI-06) site	72	0	Nearshore 300 kHz ADCP. Collected 10 min ensembles consisting of 12 pings per ensemble. A total of 10 depth bins of width 8 m each were recorded. Deployed 24 July 2009. Recovered 25 Aug 2010.
Nearshore sites	ADCP8	Southeast Ordnance Reef (HI-06) site	13.6	0	Nearshore 1,200 kHz ADCP. Collected 3 min ensembles consisting of 12 pings per ensemble. A total of 24 depth bins of width 0.5 m each were recorded. Deployed 25 July 2009. Recovered 25 Aug 2010.
	ADCP9	Northeast Ordnance Reef (HI-06) site	16.9	0	Nearshore 1,200 kHz ADCP. Collected 3 min ensembles consisting of 12 pings per ensemble. A total of 24 depth bins of width 0.5 m each were recorded. Deployed 25 July 2009. Recovered 25 Aug 2010.

ADCPs 6 – 9 measured three-dimensional water velocities and acoustic backscatter throughout the water column. ADCPs 1 – 5 measured three-dimensional water velocities and acoustic backscatter at depths between the seafloor and 620 m (2,030 ft) above the seafloor. The instruments also took single-point measurements of water temperature. Water velocity, backscatter, and temperature data were collected near-continuously between 24 July 2009 and 25 August 2010.

The configuration of the ADCP string adjacent to deepwater site HI-01 is shown in Figure 9 (below). In the figure, deployment heights of ADCPs above the sea floor are shown to the left of the depicted ADCP string.

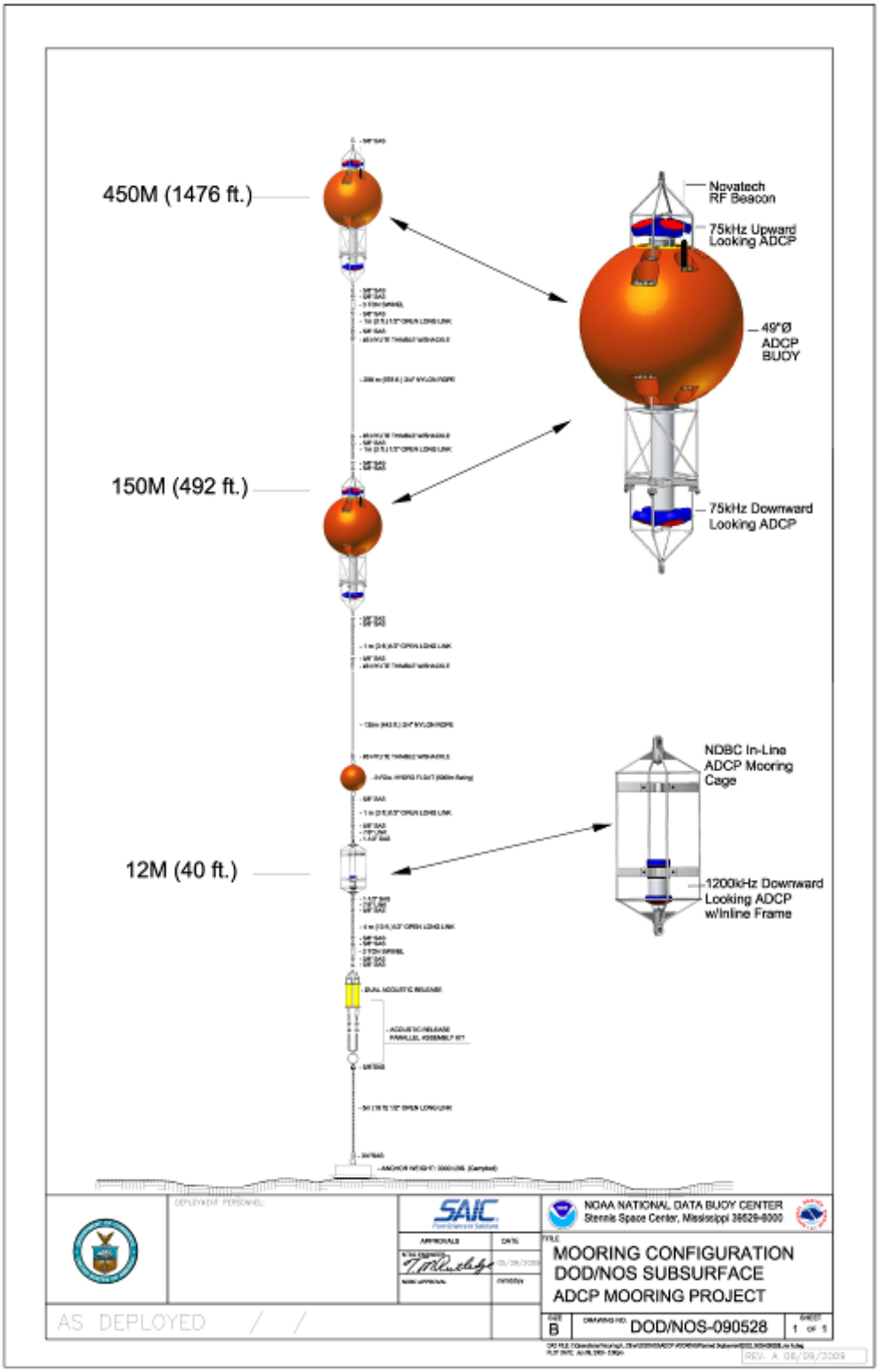

Figure 9. Diagram of the deepwater ADCP string deployed adjacent to site HI-01.

Figure 10. National Data Buoy Center (NDBC) Engineer, Bret Taft, attaching Teledyne 75kHz ADCP and cage to Flotation Technologies 49-in [124-cm] ADCP buoy, July 21, 2009. One of two used at the deepwater mooring.

Figure 11. NDBC engineers aboard the University of Hawai'i Research Vessel *KLAUS WYRTKI* deploying a shallow-water ADCP mounted in a Trawl Resistant Bottom Mount at the Ordnance Reef (HI-06) site, July 25, 2009.

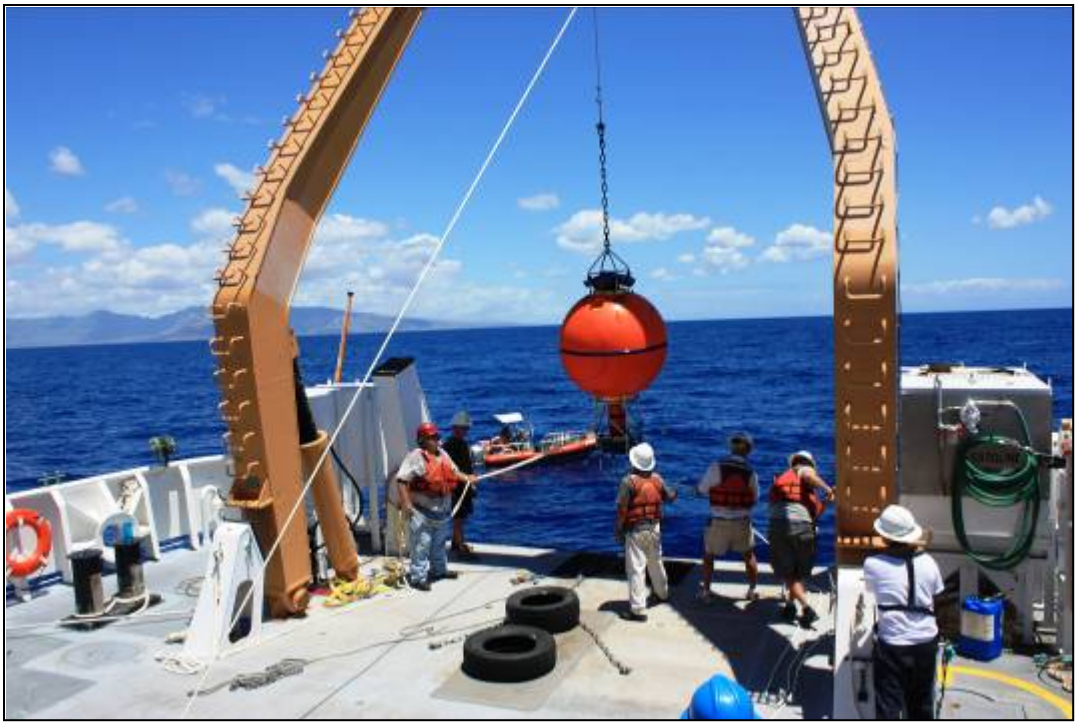

Figure 12. NDBC engineers and NOAA ship HI'IALAKAI crew, recovering deepwater ADCP mooring, August 23, 1010.

Observations of ocean currents at the two disposal sites

Analysis of the data collected by the ADCPs revealed different current regimes at the deepwater site HI-01 and the shallow water Ordnance Reef site (HI-06). Currents in the vicinity of Ordnance Reef (HI-06) were stronger and more focused in the along-shore direction (reversing direction with the tides).

This section summarizes findings discussed in greater detail in Appendixes A and B.

Observations at the deepwater site (HI-01)

Currents at the 2,500-m (8,200-ft) deepwater site (HI-01) were generally weak, most often ranging from 2 to 7 cm/s (0.04 to 0.14 knots), and of varying directionality, with a slight bias towards the along-shore axis (NNW to SSE). A portion of the variability in current orientation occurred at semidiurnal frequencies (indicating tidal influence). Currents at 620 m (2,000 ft) above the seafloor were roughly in phase with currents at the seafloor, indicating little vertical shear or change. Near the seafloor at the deepwater site, northerly currents had an upward vertical component, and southerly currents had a downward vertical component. Small but distinguishable increases in acoustic backscatter near the seafloor (indicative of suspended particulates) occurred most often during periods of upward currents.

At the deepwater site, water temperatures were between 1.6 and 1.8°C (34.9 to 35.2°F) at the deepest ADCP sensor (12 m [39 ft] above the seafloor), and between 2.1 and 2.3°C (35.8 to 36.1°F) at the shallowest sensor (450 m [1,500 ft] above the seafloor).

Observations at the shallow-water sites

Currents at the four shallow ADCP sites at Ordnance Reef (HI-06) (Figure 13) were faster and more focused in the along-shore direction than currents at the deepwater site, reversing direction twice a day with the tides. Velocities at the shallow sites were most often between 15 and 30 cm/s (0.3 and 0.6 knots), oscillating in orientation with flow toward the NNW during ebb tide and toward the SSE during flood tide. Because the ebb phase was generally shorter-lived than the flood phase, currents were oriented toward the SSE a greater percentage of the time.

At the four shallow sites, very low vertical shear throughout the water column was often observed (that is, vertical velocities were nearly identical at all depths), except occasionally during the transition periods in semidiurnal tidal flow.

Water temperature at the two 80-m (260-ft) sites varied between 20 and 26°C (68 to 78.8°F), fluctuating about 3°C (5°F) over each semi-diurnal tidal cycle, while water temperature at the two 15-m (49-ft) sites varied between 23 and 27°C (73.4 to 80.6°F), fluctuating 0.5 to 1°C (1 to 2°F) over each semi-diurnal tidal cycle.

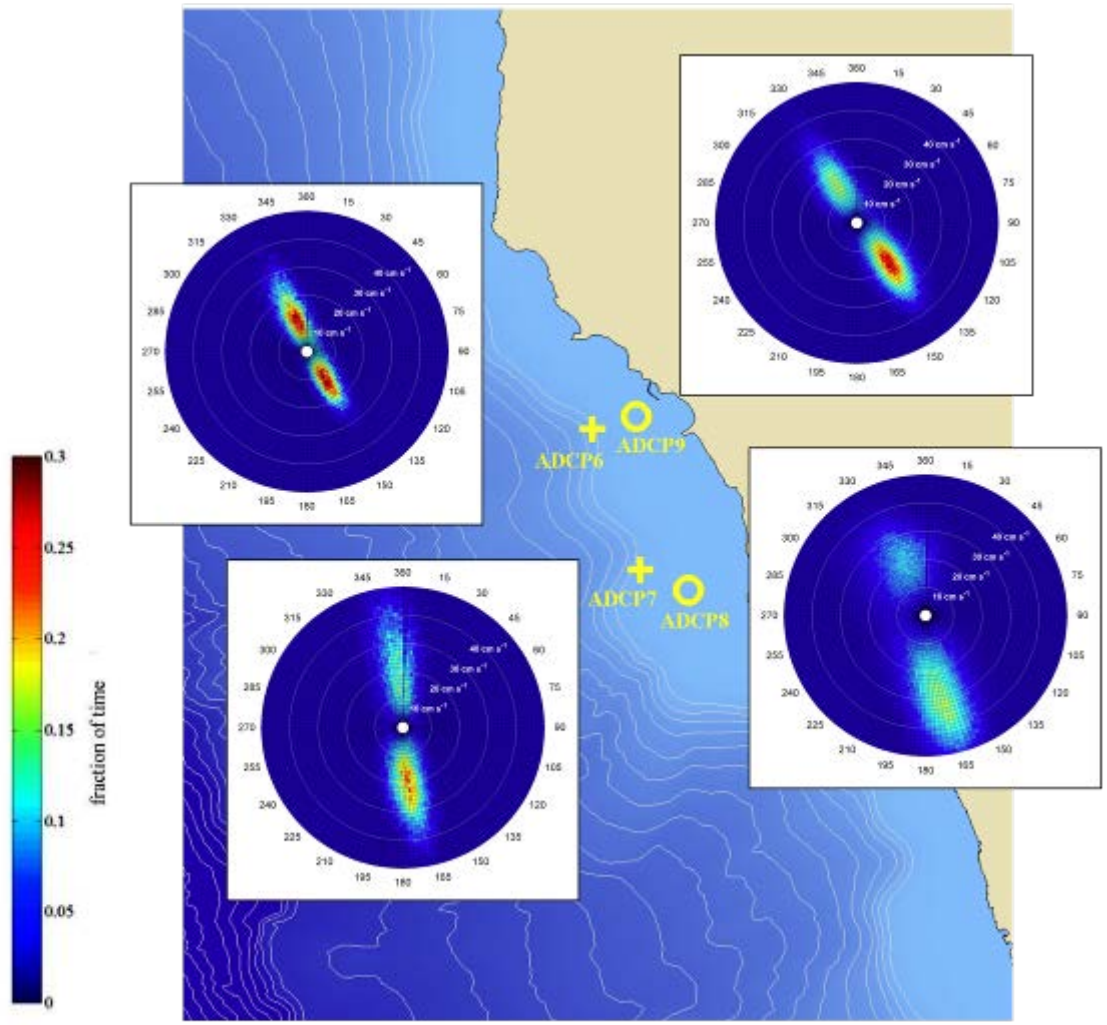

Figure 13. Histograms of current direction and magnitude at the four shallow water sites at Ordnance Reef (HI-06): ADCP6 (80 m [262 ft] depth, top left), ADCP7 (80 m [262 ft] depth, bottom left), ADCP8 (15 m [49 ft] depth, bottom right), and ADCP9 (15 m [49 ft] depth, top right). Yellow, red, and light blue regions within histogram plots represent current directions and magnitudes present during greater percentages of time than dark blue regions, indicating frequent alignment of currents in the along-shore direction. On the background map, white depth contours are shown at 100 m (328 ft) intervals.

Summary of the observed ocean currents off the Wai'anae Coast

As the data collected by the ADCPs indicates (Figure 13, above), the primary circulation along the west coast of O'ahu is along-shore because of the dominance of the semi-diurnal and diurnal tides. Particles in this system are moved north and south along the coast, with weak on- and off-shore motion as the tides change from ebb to flood. During periods of mesoscale activity, current flow is primarily along-shore (anticyclonic [clockwise-flowing] eddies impinging on the shore will push particles along-shore towards the south).

The nearshore ADCPs captured these key characteristics of the regional circulation, as well as along- and cross-shore variance. Further, current modeling revealed that ADCPs 8 and 9 experienced more shoreline effects than the outer ADCPs, because they were closer to the coast. In particular, eddies can shed off the headlands. ADCP 8 was located in the headland wake of Ma'ili Point at the southern extent of the study area. It is in this region that a bifurcation (split) of the on-shore flow occurs.

The following strong episodic current events occurred during the measurement period:

Nov 14 – 18, 2009: Very strong along-shore Spring-tide currents combined with strong persistent winds out of the NE.

Nov 25-Dec 1, 2009: Strong along-shore Spring-tide currents combined with very strong persistent winds out of the NNE.

Jan 27-Feb 5, 2010: Fast currents with a stronger cross-shore component, during a brief shift to strong, diurnal winds.

May 5-29, 2010: Weak currents with very little Spring-Neap modulation, coincident with a brief shift to weak, diurnal winds.

July 19-23, 2010: Neap-tide currents almost entirely to the SSE (instead of diurnal NNW and SSE), coincident with a brief shift to diurnal winds.

In general, currents were strongest between August 2009 and February 2010, and gradually weakened through August 2010. Interestingly, trade winds were strongest between February 10 and April 24, 2010, while current speeds and direction during this period were relatively unchanged.[5]

[5] For more details about the current measurements recorded during this study, see Appendix A, "Physical Circulation along the Western Coast of O'ahu," and Appendix B, "NOAA Ordnance Transport 12-month ADCP data summary." All data collected by the ADCPs during this study are available at http://oos.soest.hawaii.edu/pacioos/data_product/waianae_adcp/

Construction of an ocean current model for the Wai‘anae Coast

The current profile data collected by the ADCPs, along with other relevant data, were used by oceanographers at the University of Hawai‘i to develop a set of modeled currents representing circulation patterns along the Wai‘anae Coast. Other data used to develop the modeled currents included sea surface height and temperature measurements, high frequency radar (HFR) surface current measurements, autonomous glider data, data collected at fixed mooring sites around Hawai‘i and from Argo floats, conductivity, temperature, and depth (CTD) sensor casts from the Hawaiian Ocean Time-Series, and other data of opportunity. The purpose of using as many data sets as possible in developing the model was to ensure that the model best fits the available data. The modeled currents were then used in evaluating the fate and transport of munitions constituents (discussed in the next section of this report).

The University of Hawai‘i’s Regional Ocean Modeling System (ROMS) was used to develop the modeled currents. ROMS has previously been used to model many regions of the world’s oceans, and is used to produce regular ocean current forecasts for the Hawaiian Islands as part of the Pacific Islands Ocean Observing System (PacIOOS). The resolution of ROMS is about 200 m in nearshore waters.

Further details and results from the Wai‘anae Coast current modeling project are in Appendixes A and B.

Fate and transport modeling

A computer modeling study constituted the final phase of this project. The goal of the modeling study was to predict the potential for human health impacts in the event of a chemical release from munitions at either Ordnance Reef (HI-06) or the deepwater site HI-01. The modeling effort focused only on the health risk to people who directly contact water contaminated by a released chemical. It did not address any ecological risk to marine organisms, nor any human health risk associated with ingestion of those organisms by people. Human health or ecological risk associated with the Ordnance Reef (HI-06), including the possible contamination of seafood consumed by the people of the Waiʻanae Coast was evaluated in the 2010-2011 remedial investigation of the munitions at Ordnance Reef (HI-06) performed by the University of Hawaiʻi (De Carlo et al., 2012).

Computer modeling was used to determine whether dissolved chemical concentrations could possibly reach hazardous levels in waters frequented by people, if munitions constituents were released into the water column at either disposal site. The key finding from the modeling study is that if there were to be such an event at either site, chemical concentrations would not reach dangerous levels in human use areas near the coast.

This section of the report describes how the computer modeling was done and the findings that were obtained.

Overall approach

To model potential releases from both disposal sites, a worst-case analysis approach was followed. The research team first identified the worst possible kind of release from each site—such a release is termed the "worst case"—and then used computer models to predict the spatial extent of the contaminant from each worst case scenario, if it were to occur, over a range of time periods. Modeling the worst case scenario is a way to predict the maximum extent of the hazard.

A worst-case release from each site was defined as the release of the largest plausible amount of the most hazardous chemical present. In the case of the Ordnance Reef (HI-06) site, the worst-case release site was taken to be the location of the munitions that potentially contain the most hazardous chemical closest to shore. In the case of the deepwater site (HI-01), the locations of the specific chemicals cannot be precisely determined because that site has not been surveyed and the exact locations of munitions and bulk containers are unknown.

- For each site, the chemical released is the one known to be present at the site that would pose the greatest threat to human health. In the case of the nearshore munitions site (Ordnance Reef (HI-06)), the modeling study focused on ammonium picrate, because it is the most hazardous chemical and is present in relatively large

quantities. In the case of the deepwater site (HI-01), the modeling study focused on hydrogen cyanide because it is highly toxic and persists in toxic form when dissolved in water, and because a substantial amount would be expected to dissolve into the water, if released. Both chemicals are highly soluble in seawater.

- The entire contents of the largest documented source (either a small but reasonable number of shells/projectiles or a single container) are released instantaneously (defined for purposes of computer modeling to be within one minute). Such a rapid release would result in higher concentrations at affected locations than would a longer-duration release. Although such a release is theoretically possible, it is unlikely, and so this scenario is likely to overestimate the hazard.
- In the case of the Ordnance Reef (HI-06) site, the release is from a documented source location that is closest to shore. In the case of the deepwater site (HI-01), the release is from the approximate location of the disposed containers because the exact location of the containers is not known.

When a soluble chemical disperses in the water column, its concentration is highest in the area immediately surrounding the source container. The concentration diminishes with distance from the container as the chemical mixes with the water around it. The goal of the modeling study was to predict the distance to the point where the concentration of dissolved chemical would drop below a pre-determined value, termed the *modeling endpoint*. The research team defined the modeling endpoint to be 1 part per billion (ppb). At points closer to the container, predicted concentrations would be higher than this endpoint for a short time. At more distant points, predicted concentrations would be lower. A longer distance to the endpoint indicates a larger possible hazard zone.

Selecting the modeling endpoint

Because both ammonium picrate and hydrogen cyanide are toxic to people, regulatory agencies have established human exposure limits and recommended guidelines for each chemical. These values are based on available information about how each chemical is believed to affect human health. Such limits and guidelines typically are based on animal toxicity tests and information about the effects of accidental exposures to people. For the modeling study, a modeling endpoint of 1 ppb was selected because it is substantially lower than the established human exposure limits and guidelines for both chemicals, and therefore is more conservative (protective) than those limits. A modeling endpoint is conservative if, when it is used, the hazard zone is more likely to be overestimated than underestimated. The research team chose to use an especially conservative modeling endpoint because of the relatively large uncertainty about the health effects of the chemicals.

Federal and state government agencies have established human exposure guidelines and limits for hydrogen cyanide and ammonium picrate, as well as for cyanide (formed when hydrogen cyanide ionizes in water), picric acid (formed along with the picrate ion when ammonium picrate dissolves in water) and picramic acid (formed when ammonium picrate is biodegraded by bacteria in bottom sediment). Most established guidelines and limits address inhalation hazard. In the context of this study, for which the main concern is exposure to people in the water, the most likely exposure pathways are skin contact with the dissolved chemicals and, to a lesser extent, accidental ingestion of contaminated seawater. Therefore, established contaminant limits for recreational and drinking water are provided in Table 5, below, both for hydrogen cyanide and ammonium picrate as well as for the chemicals produced when those two chemicals dissolve in seawater.

Most drinking water standards assume consumption of 2 liters (1 quart) of water per day. Because consumption of this much seawater is highly unlikely, the selected modeling endpoint of 1 ppb is extremely conservative. In the case of hydrogen cyanide, EPA's maximum contaminant level for cyanide in tap water, a State of Texas water contaminant limit for cyanide, and all established exposure guidelines for hydrogen cyanide are higher than NOAA's 1 ppb modeling endpoint (Table 5).

In the case of ammonium picrate/picric acid/picramic acid, only drinking water standards have been promulgated. Generally, drinking water standards are far more stringent than dermal exposure guidelines such as contaminant limits for recreational waters. The State of Maine drinking water contaminant limit for picric acid and EPA's tap water contaminant level for picramic acid also are higher than the 1 ppb modeling endpoint.

Table 5. Established human exposure limits and guidelines for hydrogen cyanide, cyanide, picric acid, and picramic acid in drinking water and recreational waters.

Contaminant	Guideline or limit	Regulatory body	Value
Hydrogen cyanide	State drinking water guideline[1]	State of Florida	10,000 µg/l [10,000 ppb]
Cyanide	Maximum Contaminant Level (MCL) [drinking water standard][2]	U.S. Environmental Protection Agency	0.2 mg/l [200 ppb]
Cyanide	Tier 1 Contact Recreation Water Protective Concentration Levels (PCL)[3]	State of Texas	16.5 mg/l [16,500 ppb]
Picramic acid	EPA Regional Screening Level tap water standard[4]	U.S. Environmental Protection Agency	1.5 µg/l [1.5 ppb]
Picric acid	State drinking water standard[1]	State of Maine	57 µg/l [57 ppb]

Sources:

[1] U.S. National Library of Medicine, TOXNET hazardous substances database: http://toxnet.nlm.nih.gov/cgi-bin/sis/htmlgen?HSDB

[2] National Primary Drinking Water Regulations: http://www.epa.gov/ogwdw/consumer/pdf/mcl.pdf

[3] Contact Recreation Water PCLs: http://www.tceq.texas.gov/assets/public/remediation/trrp/contactrecpcls.pdf[4] Regional Screening Level (RSL) Summary Table November 2011: http://www.epa.gov/reg3hwmd/risk/human/rb-concentration_table/Generic_Tables/pdf/master_sl_table_run_NOV2011.pdf

Additional modeling assumptions

For purposes of the modeling study, it was assumed that there are no sink terms (factors that would remove the contaminant from the environment) for either ammonium picrate[6] or hydrogen cyanide. That is, it was assumed that neither chemical would be affected by any of the chemical processes of photolysis, thermolysis, hydrolysis, or oxidation, or by the biological process of biodegradation discussed earlier in this report. Because these processes would all act to reduce the concentration of chemical in the water, this assumption is conservative, in that it is more likely to result in an overestimate of the distance to the modeling endpoint than to underestimate that distance.

[6] As discussed in the "Explosives and chemical warfare agents at the disposal sites" section above, because ammonium picrate dissolves readily in water, it is actually the picrate ion, along with some picric acid (and possibly some picramic acid, if biodegradation occurs), that persists in the water column and that was the focus of this study.

The modeling study focused only on waterborne ammonium picrate and hydrogen cyanide, and was based on the 13-month record of currents described in the previous section of this report. Thus the modeling study did not address:

- How heavier-than-water substances could be transported along the bottom or could contaminate bottom sediment. This aspect was not addressed because both sites are distant enough from shore that it is very unlikely that the substances or contaminated sediment could be transported to shore from either location.
- The effects of extreme environmental conditions such as tsunamis and hurricanes.

In addition, the modeling effort did not take into account the effect of wind-produced waves, which can mobilize bottom pollutants in shallow water, producing net shoreward transport within the surf zone. The modeling analysis assumed that the released ammonium picrate or hydrogen cyanide would impact the shoreline if it were to reach the grid box that bounded the shoreline; therefore, no surf dynamics were considered. All ADCP sensors were offshore of the surf zone and sampled stored data at 10-minute intervals, so no surface wave data were collected.

Because different computer models were used for the shallow, nearshore munitions area (Ordnance Reef (HI-06)) and for the deepwater offshore site (HI-01), the modeling methods and results for the two sites are discussed separately below.

Transport modeling for the nearshore munitions site (Ordnance Reef [HI-06])

NOAA's transport model, GNOME (General NOAA Operational Modeling Environment), was used to predict the worst-case spatial and temporal extent of the contaminant, in the event of a release of a munitions constituent from the Ordnance Reef (HI-06) site. GNOME is used by NOAA researchers to predict the trajectory of spilled oil during oil spill responses, and to predict how other spilled substances will spread and move within a water body. It accounts for the bathymetry and shoreline configuration of a particular body of water, and ocean currents, which are the main force that would move a dissolved chemical within the water column. GNOME does not account for the action of surface waves, which tend to move water back and forth over a period of less than 20 seconds.[7]

Method

To predict the trajectory of ammonium picrate from the nearshore Ordnance Reef (HI-06) site, GNOME used the ROMS-modeled ocean currents supplied by the University of Hawai'i. (See Appendix A for details of the University of Hawai'i ocean currents modeling project.)

[7] Further technical details about GNOME are available on the following NOAA webpage: http://response.restoration.noaa.gov/oil-and-chemical-spills/oil-spills/response-tools/gnome.html

For the Ordnance Reef (HI-06) site, modeling focused on ammonium picrate because this chemical readily dissolves in water, is present in significant quantities, is persistent, and is toxic. All the other munitions constituents at the site would dissolve very to extremely slowly in water. Therefore, if any of these chemicals were to be released, their maximum concentrations in the water along the shoreline would be orders of magnitude less than 1 ppb, and below detectable limits. Modeling a slow-dissolving chemical would produce a much shorter distance to the 1-ppb modeling endpoint—that is, a smaller predicted hazard zone, which would not represent the worst case for the shoreline community.

Groups of projectiles containing ammonium picrate have been found at various locations at the Ordnance Reef (HI-06) site. Of these locations, one that is relatively close to shore (at 21° 25.75′ N, 158° 12.13′ W) and known to contain a cluster of closely-grouped large projectiles was selected as the source area and used to initialize the GNOME model run. Figure 14 (below) shows the location of this source area.

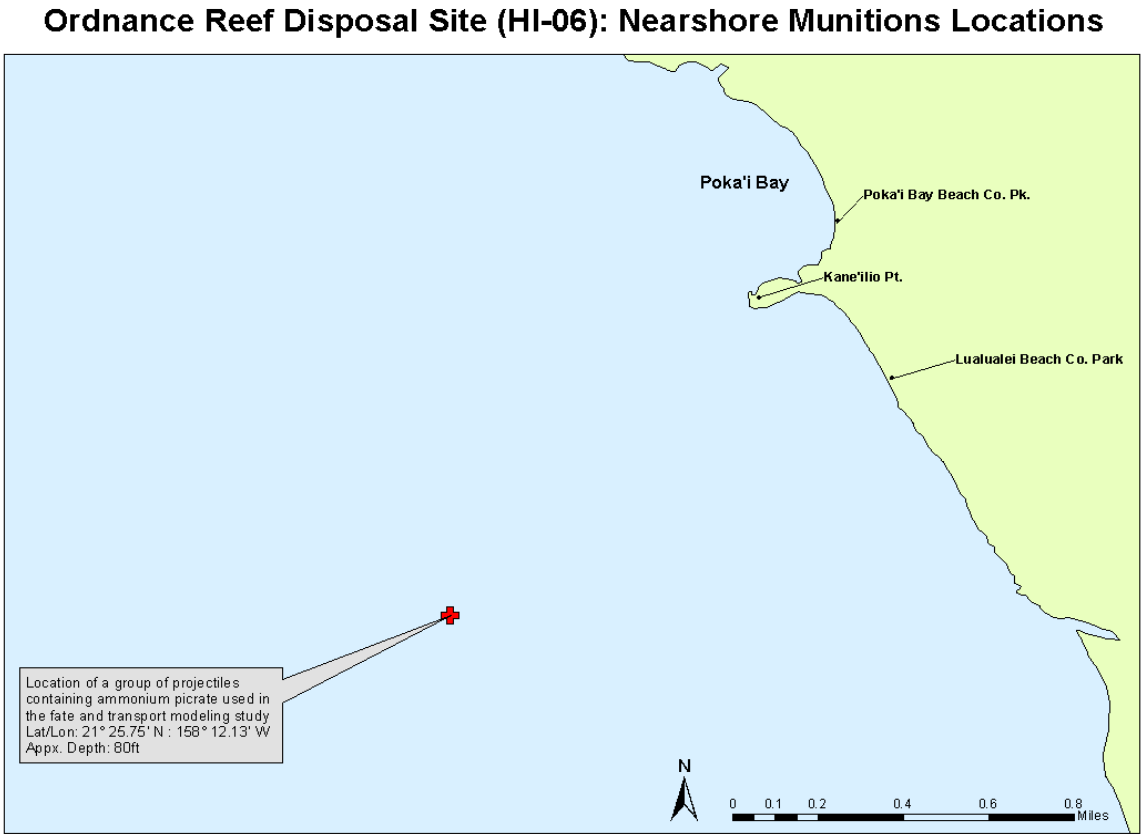

Figure 14. Location of the source area of ammonium picrate selected for the modeling project.

The amount of ammonium picrate in the source area (termed the "source strength") was set to 10 kg (22 lb), based on a "worst-case" but reasonable scenario of a boat anchor striking and rupturing 10 projectiles containing ammonium picrate.

The ADCP data and ROMS modeling results indicated that the ocean currents in the vicinity of Ordnance Reef (HI-06) are dominated by the tides, flowing predominantly along shore (parallel to the shore). During times of along-shore flow, it is very unlikely that munitions constituents released from the source area would impact the surf zone or shoreline. During the 13-month ocean current measurement study (described above), currents were onshore (flowing towards shore) for a sustained period of time only during one 10-day period. When flow is onshore, it is more likely that a released chemical would reach the surf zone or shoreline. The research team defined one onshore event during this 10-day period as the worst-case current flow condition.[8] This event was used for fate and transport modeling.

In GNOME, the ammonium picrate was mathematically represented by 1,000 particles moved by the ROMS-modeled currents. The ROMS 3D current data was provided on a 1-hour model time step. To account for current velocities that were not resolved by the hourly time step, the 10-minute ADCP data was used to provide mean velocity perturbations from the hourly averages along the U (east-west), V (north-south), and W (vertical) axes. For the U and V velocity perturbations, the mean values over several bins in the bottom half of the water column were between 2 and 3 cm/s. In the vertical, the W perturbations were between 0.4 and 0.5 cm/s.

For modeling purposes, GNOME applied a random-motion mixing parameter to particles equivalent to 3 cm/s every hour in the horizontal direction and 0.4 cm/s in the vertical direction. These parameters were effectively mixing coefficients computed from the ADCP data (which reflect the actual degree of random motion), and added to the 1-hour ROMS velocity field at each time step. These mixing values were constant in time and space.

The particles transported in GNOME were exported out every hour and converted into 3D concentrations of dissolved ammonium picrate in the water column by assuming a Gaussian dispersion from each modeled particle over time. (For more details on this step, refer to Appendix B, "Calculating three-dimensional concentrations from particle trajectories modeled via GNOME at Ordnance Reef (HI-06)").

Results

GNOME modeling of the worst-case ammonium picrate release scenario indicated that at all depths within about 100 m (330 ft) of the shoreline, maximum concentrations of dissolved

[8] This onshore flow event occurred on January 27, 2010.

ammonium picrate (and its dissolution products)[9] would not exceed the modeling endpoint of 1 ppb, which is lower than drinking water standards established for this chemical and its dissolution products (Table 5). In this nearshore zone, exposure times to the predicted peak concentrations of just above 0.1 ppb would be less than 3 hours. Peak concentrations in the immediate vicinity of the ruptured containers would likely exceed established standards. Given the speed of ocean currents in this area, for this worst-case release scenario, the duration of exposure to concentrations near the source would be brief.

The implication of these modeling findings is that if 10 projectiles at the Ordnance Reef (HI-06) site rapidly released their full contents of ammonium picrate during an onshore current event, people remaining immersed in the water within the nearshore zone would experience a worst-case exposure to dissolved ammonium picrate of significantly less than 1 ppb for no more than 3 hours. Given that currents are rarely onshore and it is improbable that a number of projectiles would release their entire contents at the same time, it is much more likely that people in nearshore waters would not be exposed to measurable concentrations of dissolved ammonium picrate.

Figure 15 (below) depicts the release scenario.

[9] As discussed above, ammonium picrate dissolves in water to form picrate ion (which differs from ammonium picrate only in the lack of one hydrogen ion), along with some amount of picric acid and possibly some picramic acid (produced by biodegradation).

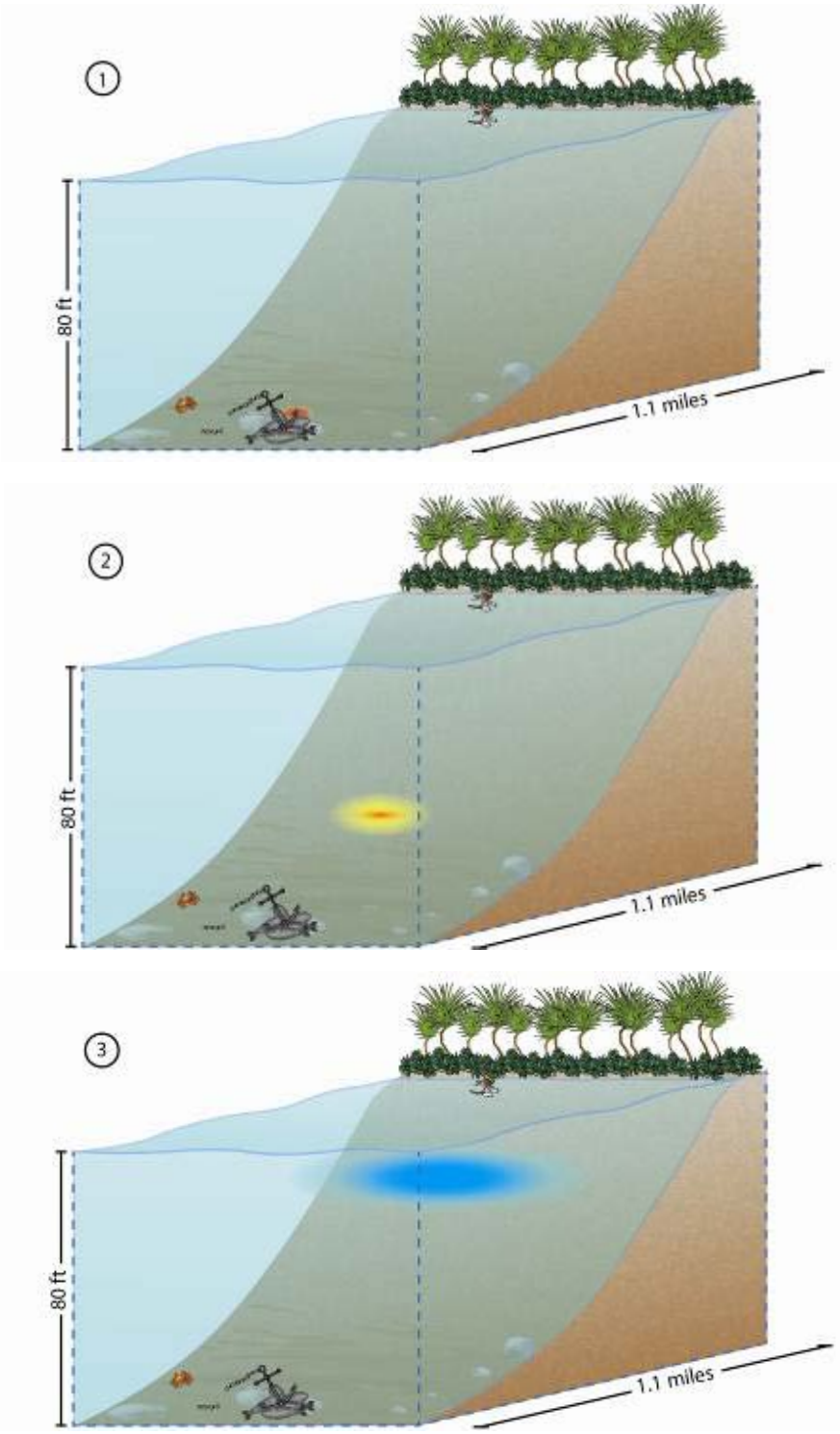

Figure 15. Release of ammonium picrate from a group of projectiles at Ordnance Reef (HI-06): (1) within about an hour of the release, (2) within a few hours to a day of the release, (3) more than a day after the release. Red and yellow color-coding represent picrate concentrations above 1 ppb; blue represents detectable picrate concentrations below 1 ppb.

Figure 16 (below) depicts the relative maximum concentrations of dissolved ammonium picrate predicted to be reached at all water depths and all areas during the first 72 hours after the release begins. In this figure, the dashed line encompasses the area where above-zero concentrations of dissolved ammonium picrate are predicted to exist for some finite period of time after the release begins. Concentrations are predicted to remain below 1 ppb at all depths within the dashed line except within the yellow-, orange-, or red-shaded areas where concentrations are predicted to reach levels higher than 1 ppb, at least briefly. Red areas indicate where the highest concentrations are predicted to be, and orange and yellow areas indicate where somewhat lower concentrations (higher than 1 ppb) are predicted to be.

In some locations, the highest concentrations might be reached deeper in the water column than at other locations. At locations farther from the source container, dissolved ammonium picrate concentrations would peak later than at locations closer to the source. Because the plume of dissolved ammonium picrate would move through the water rather than remaining in place, at any given time after the release, the area impacted would be only a fraction of the area shown in Figure 16, below.

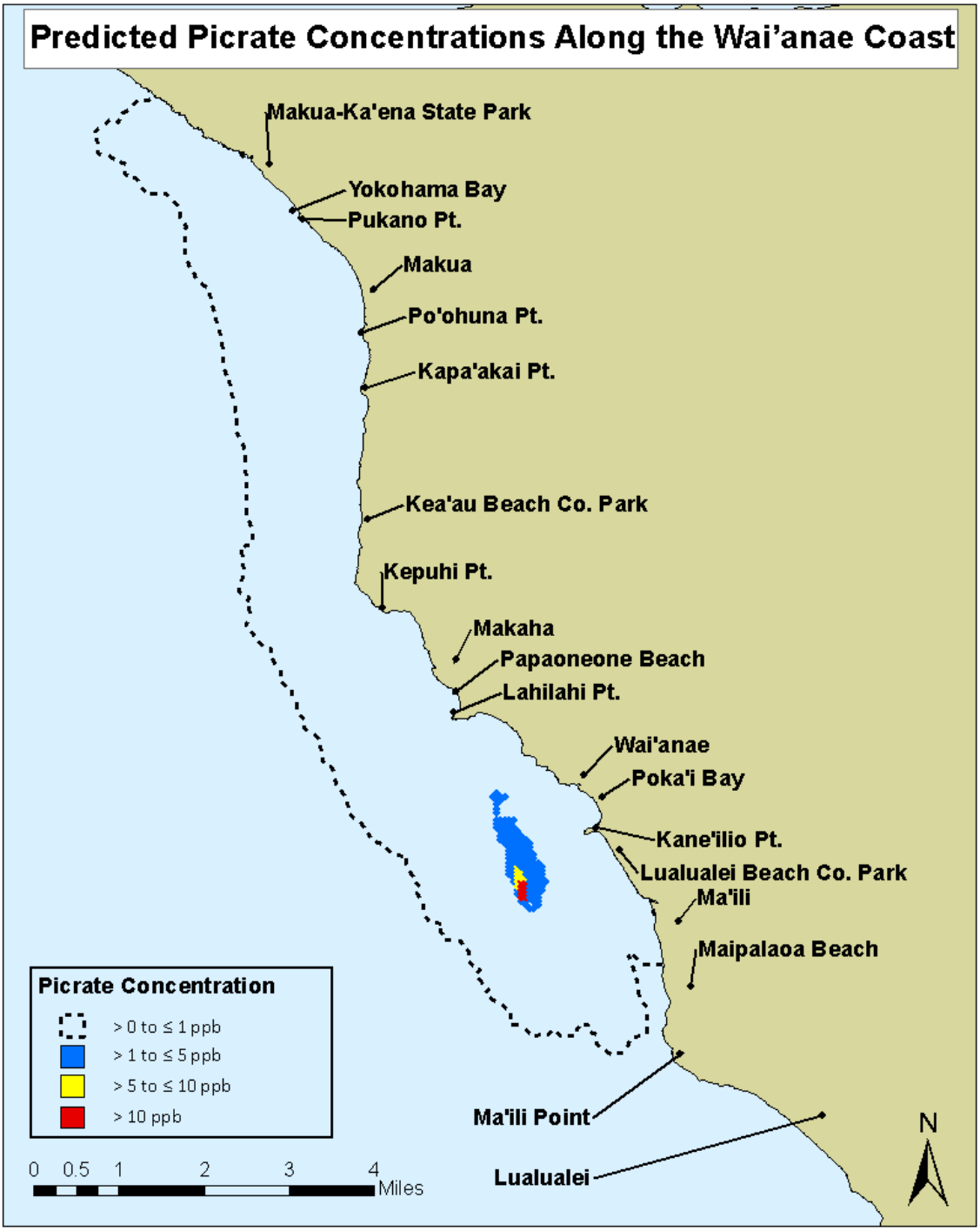

Figure 16. Predicted maximum dissolved picrate concentrations along the Wai'anae coast for the modeled scenario. The red area indicates where the highest concentrations are predicted to be, while the orange and yellow areas indicate where medium concentrations are predicted to be. Predicted concentrations remain below 1 ppb at all depths within the area encompassed by the dashed line, and exceed 1 ppb at some depth in the yellow, orange, and red areas.

Because ocean currents would mix and advect (transport horizontally and, to a lesser extent, vertically) the dissolved ammonium picrate, concentrations near the source area are predicted to drop back to background levels within 3 hours of the release. Figure 17 (below) depicts the predicted average dissolved ammonium picrate concentration at a height of 1 meter above the ocean floor within the model grid cell containing the location of the source area, during the 72 hours following the release.[10] Within this grid cell, the average concentration is predicted to peak at slightly below 35 ppb within about 1 hour, and then to drop to background levels within about 3 hours as ocean currents quickly dilute and disperse the dissolved contaminant.

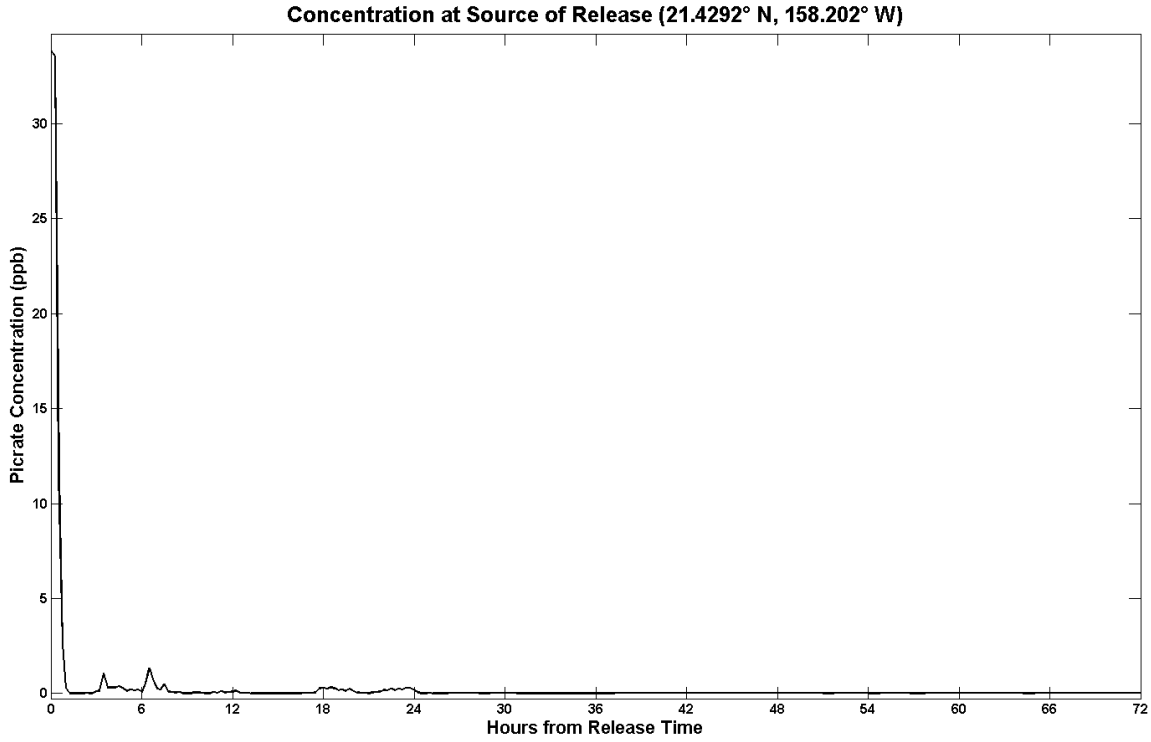

Figure 17. Predicted concentration within the model grid cell containing the source area, during the first 72 hours after the release, at a height of about 1 meter from the bottom.

[10] Averaging is across the volume of the grid cell, 74,000 m^3 (97,000 yd^3). Each grid cell is 72.5 m (238 ft) wide by 72.7 m (239 ft) long by 14 m (46 ft) high.

Figure 18 (below) shows the predicted concentration of dissolved ammonium picrate in a grid cell offshore of Waianae High School. As Figure 16 shows, predicted concentrations at this location remain far below 1 ppb, never exceeding 0.2 ppb. At this location, the cumulative exposure time to concentrations above 0.1 ppb is less than 3 hours (the cumulative duration of the two peaks in the graph that exceed 0.1 ppb). Closer to shore, concentrations would be lower than the concentrations shown on this graph, because alongshore currents and wave action would further mix and dilute the contaminant with the seawater around it.

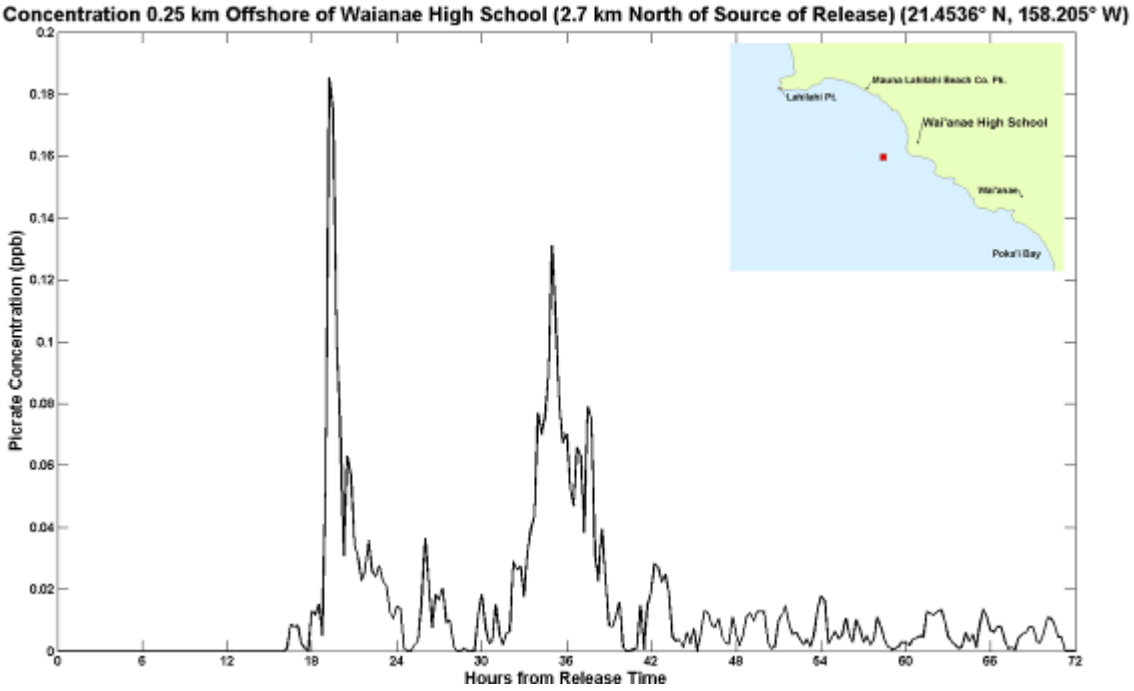

Figure 18. Maximum predicted dissolved ammonium picrate concentration within a nearshore grid cell 0.25 km (270 yds) offshore of Wai‘anae High School, at Wai‘anae, the largest community near the Ordnance Reef (HI-06) site. The two concentration peaks result from the effects of tides.

Figure 19 (below) shows the predicted dissolved ammonium picrate concentration in a model grid cell offshore of Kepuhi Point, about 6.4 km (4 mi) north of Wai‘anae. The predicted concentration at this location reaches a peak of about 0.1 ppb, far below the modeling endpoint of 1 ppb. The peak is reached after about 26 hours (the time taken for the plume to reach this location) and is predicted to last for less than 1 hour. Closer to shore, concentrations would be lower than the concentrations shown on this graph, because alongshore currents and wave action would further mix and dilute the chemical with the seawater around it.

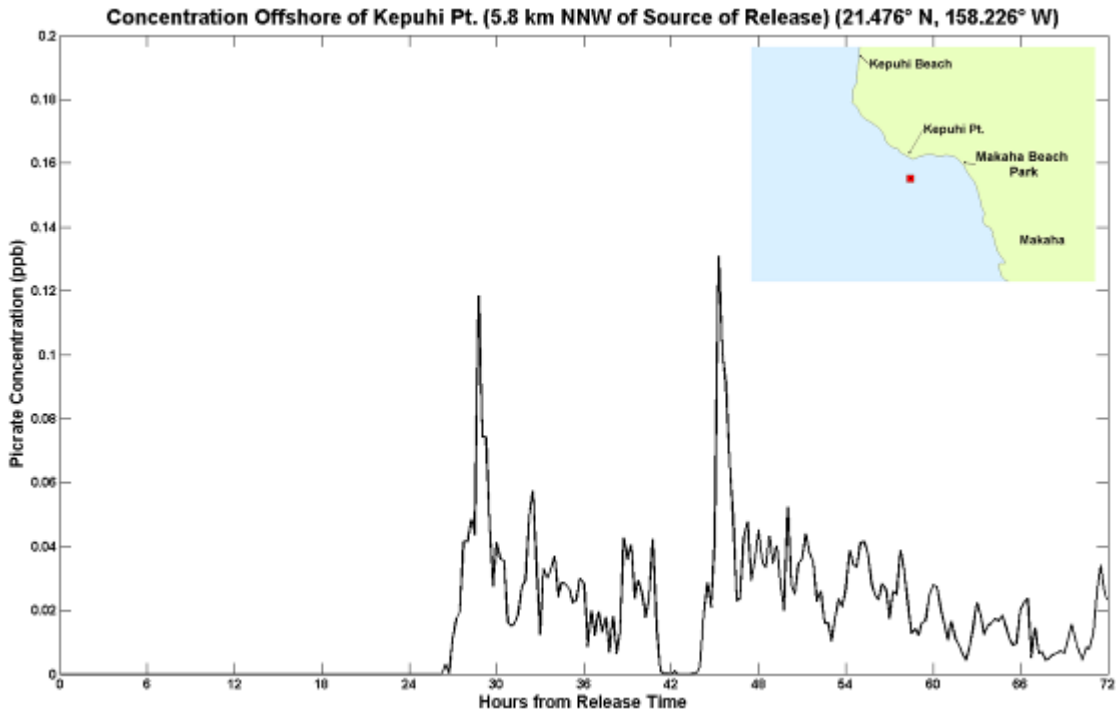

Figure 19. Maximum predicted dissolved ammonium picrate concentration within a nearshore grid cell 0.25 km (270 yds) offshore of Kepuhi Point, 5.8 km (3.6 mi) north of the Ordnance Reef (HI-06) disposal site.

Discussion of modeling uncertainty

There is always some uncertainty about the results of a computer modeling project, since not all relevant factors can be precisely known. The modeling results presented above represent an upper bound on the extent of the human health hazard, as long as all modeled conditions are as described above. That is, if 10 projectiles rupture and release their entire contents as described, it is highly unlikely that the concentration of dissolved ammonium picrate within the surf zone could reach or exceed about 1 ppb for more than a few hours.

Are there foreseeable circumstances when concentrations of dissolved ammonium picrate in the nearshore zone could reach levels much higher than the preceding analysis shows? The following two scenarios show that such an outcome is conceivable, but highly unlikely.

The first scenario would require the overriding of tidal advection[11] by a hurricane or tsunami. As discussed in the previous section of this report, tidal forces are the main factor driving circulation along O‘ahu’s west coast. If currents were to transport dissolved ammonium picrate directly to shore within just a few hours—too quickly for tidal mixing to

[11] The tendency of tidal forces to transport water in the along-shore direction rather than towards shore.

dilute concentrations of the chemical in the water—nearshore concentrations could reach levels 10 to 100 times higher than 1 ppb, depending on how quickly the dissolved ammonium picrate was transported. Under normal conditions, such an event is not possible because tidal currents and tidal mixing are always present. A strong hurricane or tsunami conceivably might transport dissolved ammonium picrate into the nearshore zone so quickly that tidal mixing could not dilute the chemical. However, the powerful currents generated by such an event also would act to dilute the chemical, so that exposure times to the higher concentrations of dissolved ammonium picrate would be short.

The second scenario is one in which more than 10 projectiles release their entire chemical contents at once. It is difficult to conceive of an event other than a powerful earthquake that would produce this scenario. A release from a large number of projectiles would produce higher concentrations nearshore and a larger exposure area. In such a scenario, expect that the chemical concentration would increase linearly with the amount of chemical released. For concentrations to increase 10-fold, at least 100 projectiles would need to release ammonium picrate at once.

What factors might cause lower concentrations of dissolved ammonium picrate in the nearshore zone? One such factor could be biodegradation (discussed earlier in this report in the chemical profile of ammonium picrate). Biodegradation was not accounted for in the modeling study because the study was designed to be somewhat conservative (more likely to overestimate the hazard zone than to underestimate it). As a result, the concentrations predicted by the GNOME model may overestimate actual concentrations. The ultimate fate of the ammonium picrate would be biodegradation. Release rate is another factor that could lower concentrations of dissolved ammonium picrate in the nearshore zone. For the "worst case" scenario above, it was assumed that all containers in a group released their full contents of ammonium picrate within about a minute. It is unlikely that a group of adjacent containers would quickly and simultaneously release their contents. In a more likely scenario, corrosion would create pinholes in one or more of the containers, allowing small amounts of ammonium picrate to slowly escape into the water over a longer period of time. In this scenario, the extent of the hazard zone would be much smaller than for the scenario analyzed.

What about the other chemicals present?

The "Explosives and chemical warfare agents at the disposal sites" section above summarizes the fate of each munitions constituent at Ordnance Reef (HI-06) and lays out the rationale for focusing on an ammonium picrate release as the worst case scenario. Given the properties of the other chemicals present at the site, it also is possible to forecast their fates, if they were to be released.

Because TNT is a solid that would sink and would not dissolve in any significant quantity, the amount of TNT that would dissolve into the water column would not produce

measureable concentrations in the nearshore zone. Further, TNT would degrade if exposed to sunlight. Very little if any TNT would reach shore if released from a munition during an onshore current event.

2, 4-DNT is chemically similar to TNT, and is a sparingly soluble solid. If released from a munition, it would remain on the bottom, and would degrade if exposed to sunlight. It is not likely that 2, 4-DNT would impact the shoreline community in any measureable amounts, if at all.

RDX is a solid, less soluble than TNT and RDX, and less reactive to sunlight than TNT and DNT. Should RDX be released from a munition, it would remain on the bottom and very slowly dissolve over time. We would not expect any impacts to the shoreline community.

HMX, also a solid, is the least soluble of all the contaminants. Like RDX, this chemical would remain on the bottom and very slowly dissolve over time. We would not expect any impacts to the shoreline community.

Transport modeling for the deepwater site (HI-01)

This part of the computer modeling study addressed a release of hydrogen cyanide from a container at the deepwater disposal site (HI-01). Given that this site has never been extensively surveyed because of its great depth (about 1,630 to 2600 m [5,300 to 8,500 ft]), the exact locations and condition of the containers recorded as present at this site are not known. For the purposes of this modeling project, the release location was assumed to be at the nearshore edge of the deepwater site (HI-01), nearly 18.5 km (10.5 nm, 12 mi) off the west coast of O‘ahu, at a depth of more than 2,528 m (1.5 mi, 8,300 ft) below the surface (Figure 20).

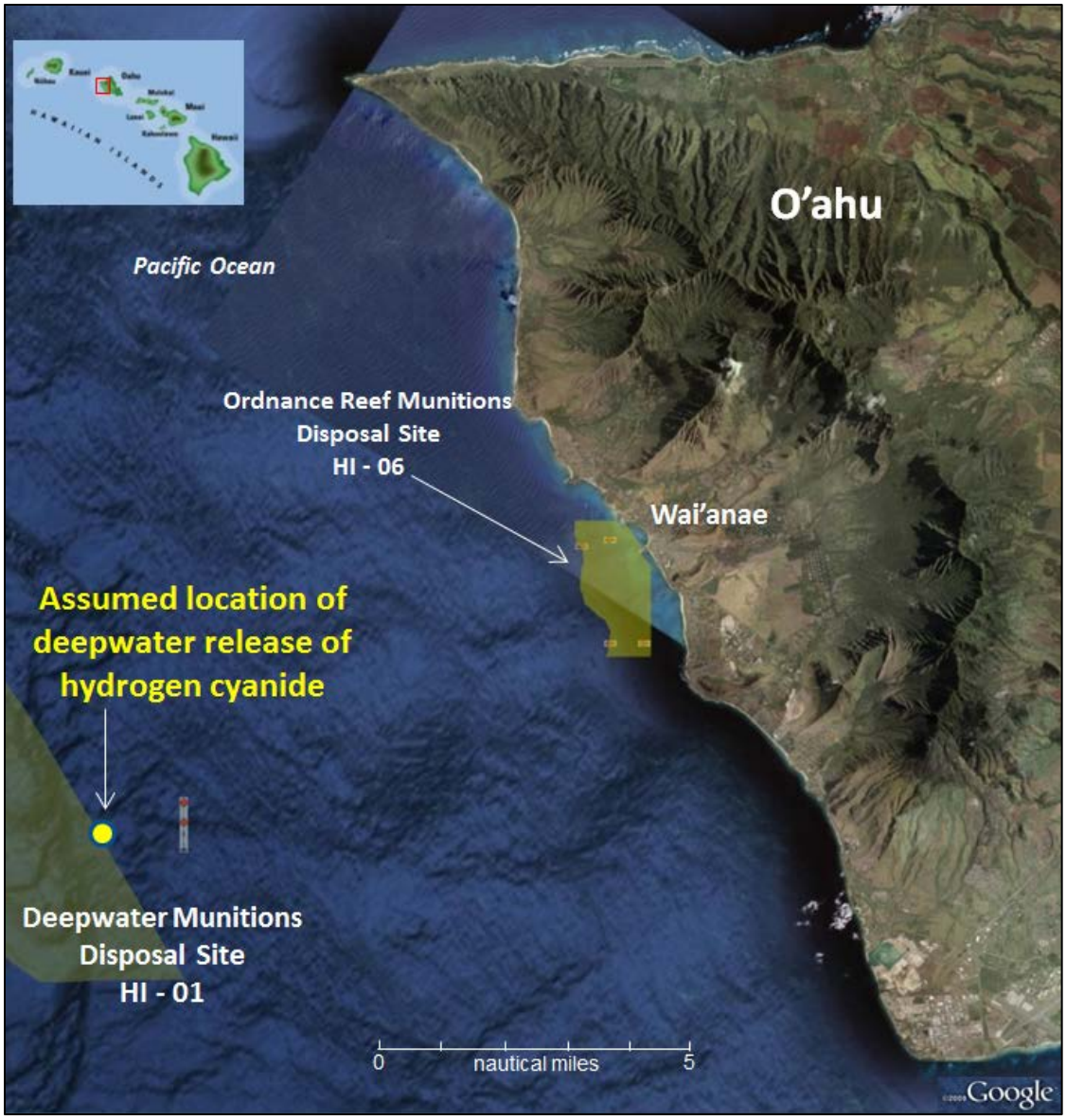

Figure 20. Assumed location of the modeled release of hydrogen cyanide at the nearshore edge of deepwater site HI-01.

For the deepwater site (HI-01), modeling focused on hydrogen cyanide because of its inherent hazardousness—it is highly toxic, dissolves readily in water, and persists in solution in a toxic form—and because a significant quantity is recorded as present at the site. The other chemicals presumed to be at the site would pose less potential hazard if released. Sulfur mustard is denser than water, sparingly soluble, and hydrolyzes to benign compounds. Lewisite also is sparingly soluble and denser than water. While some of its breakdown products are toxic, these compounds would be produced at a slow rate given

the slow dissolution rate of lewisite. Cyanogen chloride is denser than water and is soluble, but reacts with water to form compounds that are not dangerous.

According to military records, a total of twenty 1,000-lb bombs, each containing 91 kg (200 lbs) of hydrogen cyanide, were disposed at the site (Table 3, above). This modeling study assumed that two of these bombs released their contents simultaneously.

The key finding from this phase of the modeling study is that none of the release scenarios modeled would expose the shoreline community or people in nearshore waters to any of the chemicals recorded as having been sea-disposed at the deepwater site (HI-01). In a worst-case scenario of 182 kg (400 lb) of hydrogen cyanide escaping from containment and very quickly dissolving, hydrogen cyanide concentrations would be predicted to reach or exceed the modeling endpoint of 1 ppb only within a layer of water 300 m (984 ft) from the ocean bottom, 1.6 km (1 mi) below the surface. Concentrations reaching or slightly exceeding 1 ppb would be confined to no more than 10 km (6.2 mi, 5.4 nm) from the deepwater site, remaining more than 14 km (8.7 mi, 7.6 nm) from the closest shoreline. Only within 8 km (5 mi, 4.3 nm) from the container would concentrations exceed 1 ppb at any depth for more than about 70 hours. Any comparison to the established human exposure guideline for hydrogen cyanide shown in Table 5 is not relevant as there is no potential for human exposure.

Data and method

Full details of the methodology used and results obtained are discussed in Appendix E. The approach taken was to assume a worst-case source scenario and use measured near-bottom current velocities to model the spread of the dissolved pollutant as a passive tracer with no sink terms. That is, it was assumed that none of the dissolved hydrogen cyanide would be affected by any of the chemical or biological processes that could degrade munitions constituents (i.e., thermolysis, oxidation, hydrolysis, photolysis, or biodegradation). The goal was to predict how far the dissolved hydrogen cyanide would spread in three dimensions before concentrations dropped below the modeling endpoint of 1 ppb.

The source of the hydrogen cyanide was assumed to be two 91-kg (200-lb) containers of hydrogen cyanide, which simultaneously release their full contents (i.e., a total of 182 kg [400 lb] of hydrogen cyanide) into the water within a minute. This release amount is probably an overestimate, because it is unlikely that two containers would release their contents simultaneously, and that the entire contents of both would be released within a minute. Given the great uncertainties regarding the amounts and the current condition of munitions constituents at this site, overestimating the release amount is a conservative choice that is in keeping with the goal of modeling the worst case release from the site.

The container was assumed to be located on the sea floor roughly 11.5 mi (18.5 km) off the west coast of O‘ahu, at about 21° 20′ N latitude and 158° 20′ W longitude, at the location shown on Figure 20. For the purposes of this study, the source location was taken to be a

point on the shoreward boundary of the deepwater CWM disposal area (HI-01), near the mooring location of the ADCP sensors.

To model this release, the 13 months of current data collected at the site were used with a simple chemical transport model. The transport model used the conservative idealization that the hydrogen cyanide would rapidly dissolve in the water and be neutrally buoyant when dissolved. The model also assumed that the hydrogen cyanide, while being mixed and advected by currents, would spread as a 3D Gaussian plume in the X (down-current), Y (cross-current), and Z (vertical) directions. That is, the plume of dissolved hydrogen cyanide within the water column would maintain a normal (Gaussian) shape in the X, Y, and Z directions while being advected.[12] This assumption means that as the plume is advected, (a) concentrations along the plume centerline would remain higher than concentrations out to either side, while (b) overall, concentrations would decline as the plume moves down-current, away from the source (Figure 21).

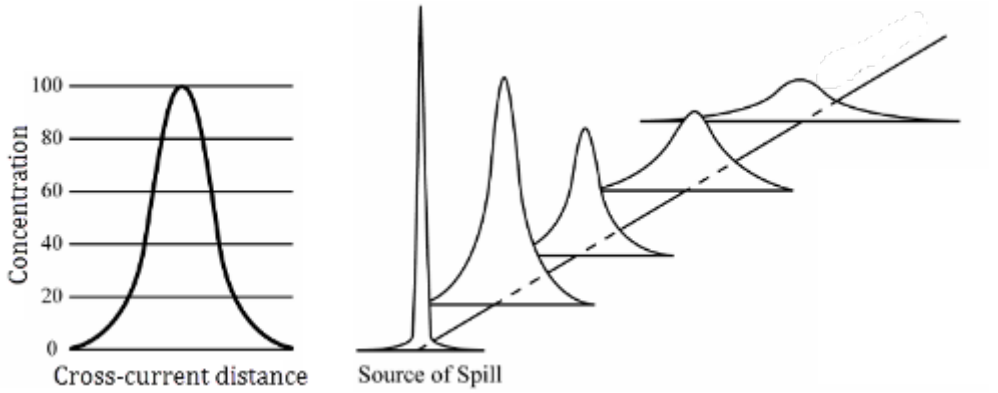

Figure 21. Gaussian dispersion. At left is a graph of the hydrogen cyanide concentration in a cross-current slice of the plume of dissolved hydrogen cyanide, close to the source container. The "bell shape" of this graph is characteristic of a Gaussian distribution. At right is a series of graphs of the hydrogen cyanide concentration, arranged along the travel path of the plume as it is advected by currents. The concentration is highest at the source container at the time of release. As the plume moves down-current, turbulent mixing spreads out the plume and causes concentrations throughout the plume to drop.

Changes in the chemical concentration over time were assumed to result from advection by ocean currents and diffusion (molecular and turbulent). The chemical release was modeled as an instantaneous contaminant point source.

[12] Such a shape is also called a bell curve.

The time-dependent advection velocities were obtained from the ADCP data. The Gaussian mixing parameters were assumed to be constant in time and space. Neither chemical interaction nor breakdown was modeled, and the model did not rely on any chemical properties other than neutral buoyancy.

The transport model used the current velocity data collected by the ADCP sensors at a variety of depths at a single location for the deepwater site (HI-01). The advection currents were assumed not to vary horizontally in the X and Y directions.

From the current velocity dataset, which spanned about 13 months, 58 different release times were randomly selected. The model was run for each of the 58 times. Each model run produced two predictions: the path of the plume center (computationally represented as a single particle) and the pattern of diffusion of dissolved hydrogen cyanide away from the plume center.

The computed pathline concentrations were then summarized out to the horizontal and vertical 1-ppb contours and for exposure times to 1 ppb. Generally, the pathlines trended in a roughly northerly direction, under the influence of an along-shore current strong enough to divert the paths away from the O‘ahu coast.

Results

Figure 22 (below) is a conceptual view of the modeled release.

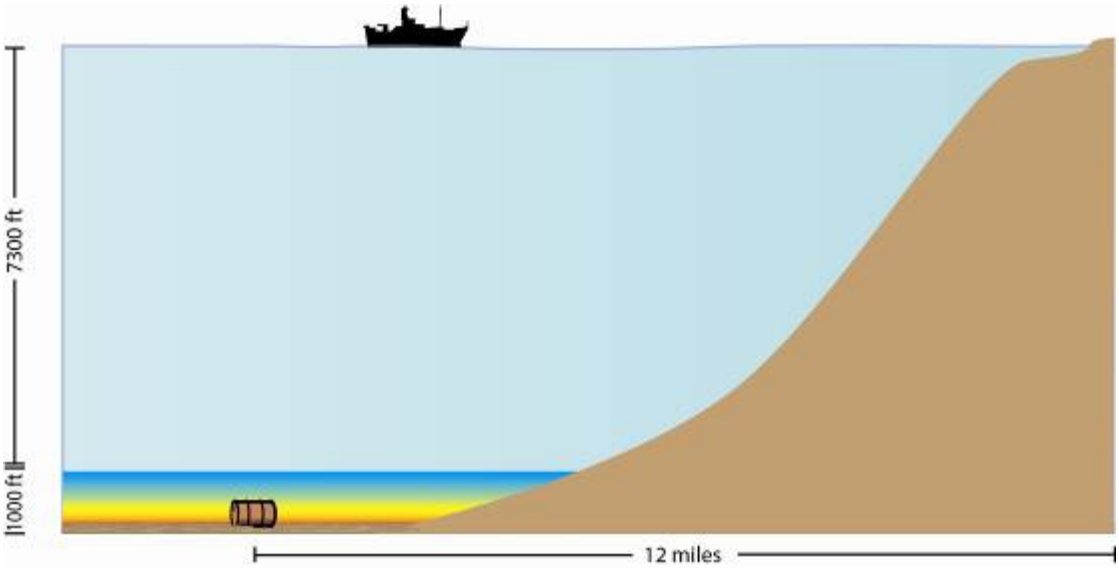

Figure 22. Conceptual view of the release of 182 kg (400 lbs) hydrogen cyanide. Currents have spread and mixed the dissolved hydrogen cyanide into the water column, to form a layer of contaminated water on the sea bottom. The highest hydrogen cyanide concentrations (color-coded red) are closest to the bottom. The predicted top of the contaminated layer is more than a mile (about 2 km) below the ocean surface.

The figures below depict the ensemble results for all 58 model runs. In each figure, colored areas represent locations in the water column where one or more of the 58 model runs predicted that hydrogen cyanide concentrations would reach particular levels (indicated by color coding). Each model run began at a different date and time and encountered different current conditions. In the figures below, color-coding represents the maximum concentration predicted in *any* of the 58 model runs.

Figure 23 (below) represents a side view (or vertical water column view) of the predicted ensemble maximum concentrations for all 58 modeled scenarios, depicted as a vertical profile aligned perpendicular to the adjacent shoreline (cross-shore). The vertical axis of Figure 23 indicates height in meters above the ocean floor. The horizontal axis indicates the cross-shore distance in kilometers from the ensemble plume centerline (roughly east-west). Just above the horizontal axis, a red X marks the horizontal distance from the ensemble plume centerline to Ma'ili Point, the closest point on the O'ahu coastline. The color bar to the right of the figure shows how concentrations of dissolved hydrogen cyanide are color-coded, with black (at the bottom of the bar) representing 0 ppb and white (at the top of the bar) representing concentrations of 1 ppb or greater.

The white zone in Figure 23 represents the region where the maximum predicted concentration (out of all 58 model runs) reached or exceeded 1 ppb, at some time after the release. The white zone extends from the ocean floor up to a height of about 300 m (984 ft). At heights greater than 300 m (984 ft) above the ocean floor, predicted hydrogen cyanide concentrations never reach 1 ppb.

The model, which assumes the ocean floor to be flat, predicts the shortest distance from the nearshore edge of the white zone to Ma'ili Point on the O'ahu coast to be roughly 14 km (8.7 mi, 7.6 nm). In reality, the ocean floor rises steeply from the release location shoreward, as can be seen in Figure 2 (above). This steep rise of the ocean floor would significantly impede shoreward movement of the plume of dissolved hydrogen cyanide. The ocean floor at what otherwise would be the nearshore edge of the white zone lies at a depth of about 3,600 ft (1,100 m), almost a mile (1.6 km) higher than the release location.

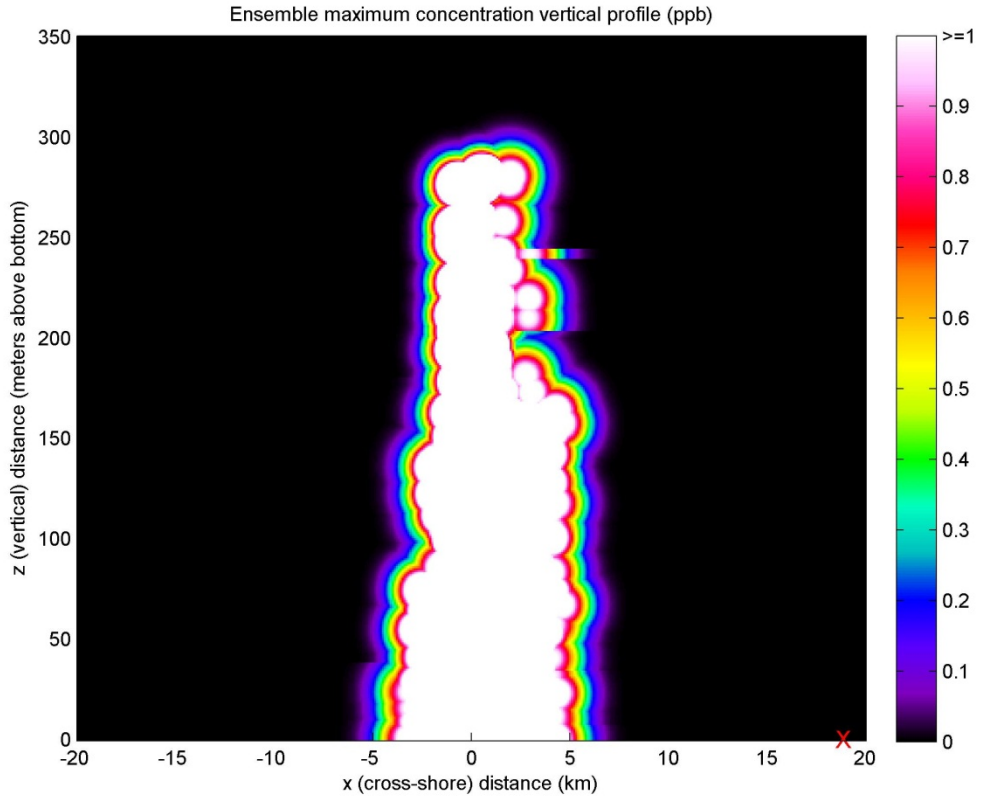

Figure 23. Predicted ensemble maximum concentrations in the vertical plane (incorporating all 58 modeled scenarios). The color bar to the right of the figure indicates how concentrations are color-coded, with black (at the bottom of the bar) representing 0 ppb and white (at the top of the bar) representing concentrations of 1 or more ppb. The red X at the bottom right of the figure marks the horizontal distance from the ensemble plume centerline to the closest point on the Oʻahu coastline. This figure shows that at heights greater than about 300 m (984 ft) above the ocean floor, predicted hydrogen cyanide concentrations never reach 1 ppb.

Figure 24 (below) represents a view from above of the ensemble maximum predicted concentrations, with the horizontal axis oriented in the cross-shore direction (essentially east-west) and the vertical axis oriented in the along-shore direction (essentially north-south). Color-coding represents the maximum concentration predicted for any location, at any depth, in any of the 58 scenarios. As in Figure 23, the white zone encompasses the area where the predicted concentration of dissolved hydrogen cyanide reached or exceeded 1 ppb at some depth. On Figure 24, a red X represents the location of Maʻili Point, the point on the Oʻahu coastline nearest to the disposal site. This point is about 14 km (8.7 mi, 7.6 nm) from the edge of the white zone.

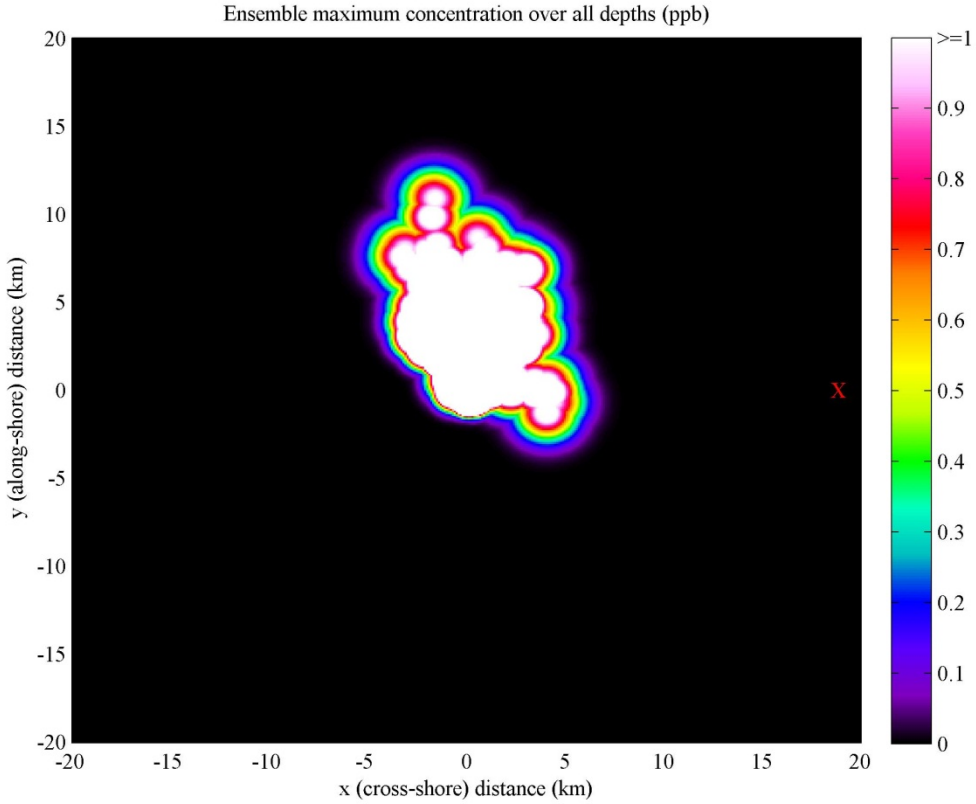

Figure 24. Predicted ensemble maximum concentrations in the horizontal plane (incorporating all 58 modeled scenarios). The color bar to the right of the figure indicates how concentrations are color-coded, with black (at the bottom of the bar) representing 0 ppb and white (at the top of the bar) representing concentrations of 1 or more ppb. The red X marks the horizontal distance from the ensemble plume centerline to the closest point on the Oʻahu coastline.

Figure 25 (below) depicts the overhead view of the ensemble maximum concentrations (over all depths) on a nautical chart.

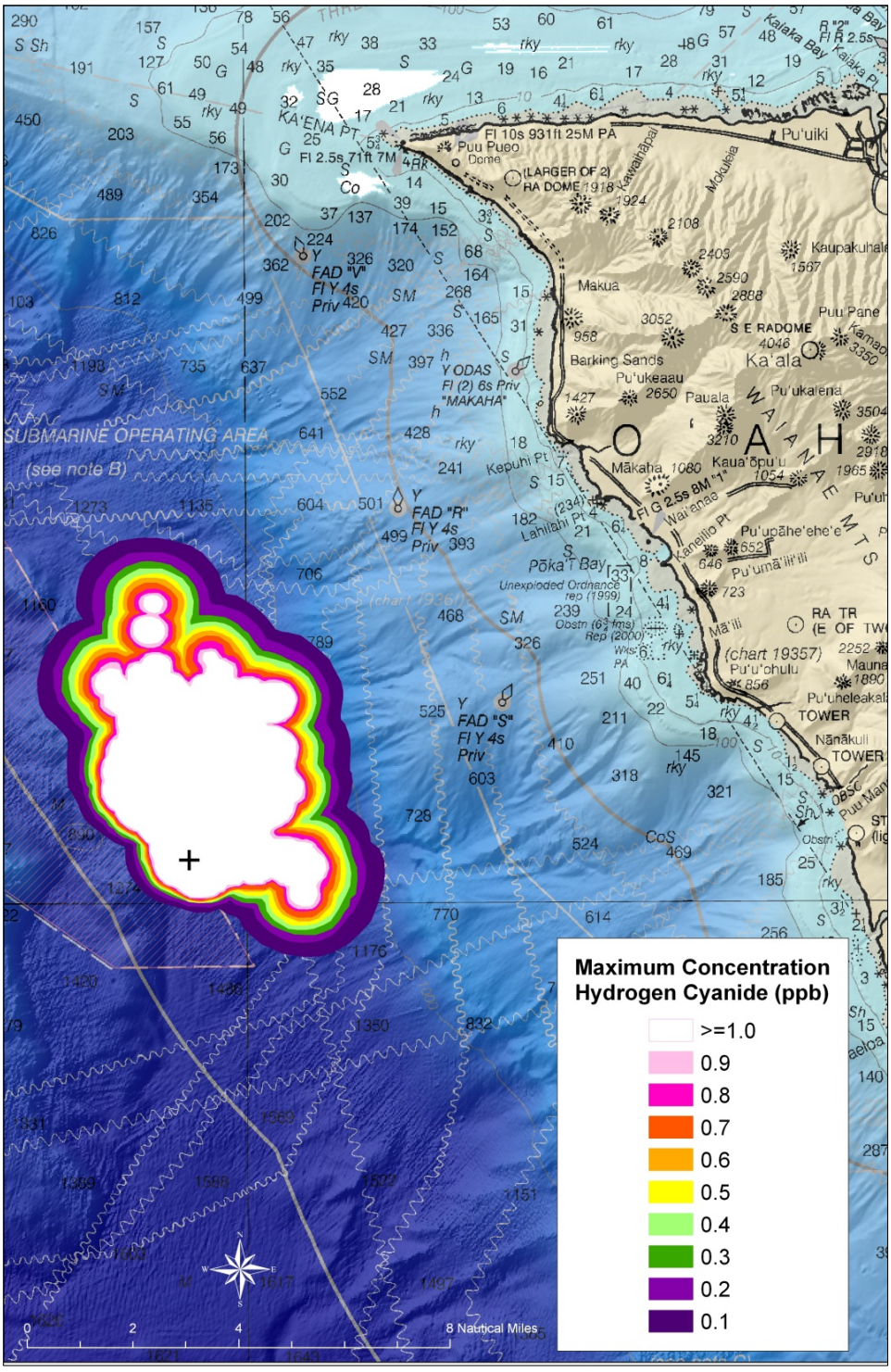

Figure 25. Predicted ensemble maximum concentrations (over all depths) in the horizontal plane, seen on a nautical chart.

Exposure time is the total time that concentration remains at or above the modeling endpoint of 1 ppb at a given point. Figure 26 (below) represents a view from above of the predicted ensemble maximum exposure time (in hours) to concentrations at or above 1 ppb. Color-coding represents the maximum exposure time predicted for any given location, at any depth, in any of the 58 scenarios. The color bar to the right of the figure indicates that white represents locations where the exposure time reaches or exceeds about 70 hours; black represents locations where the modeling endpoint of 1 ppb is never reached (and exposure time is 0). As Figure 26 shows, no location at any depth is exposed to concentrations above 1 ppb for more than about 70 hours.

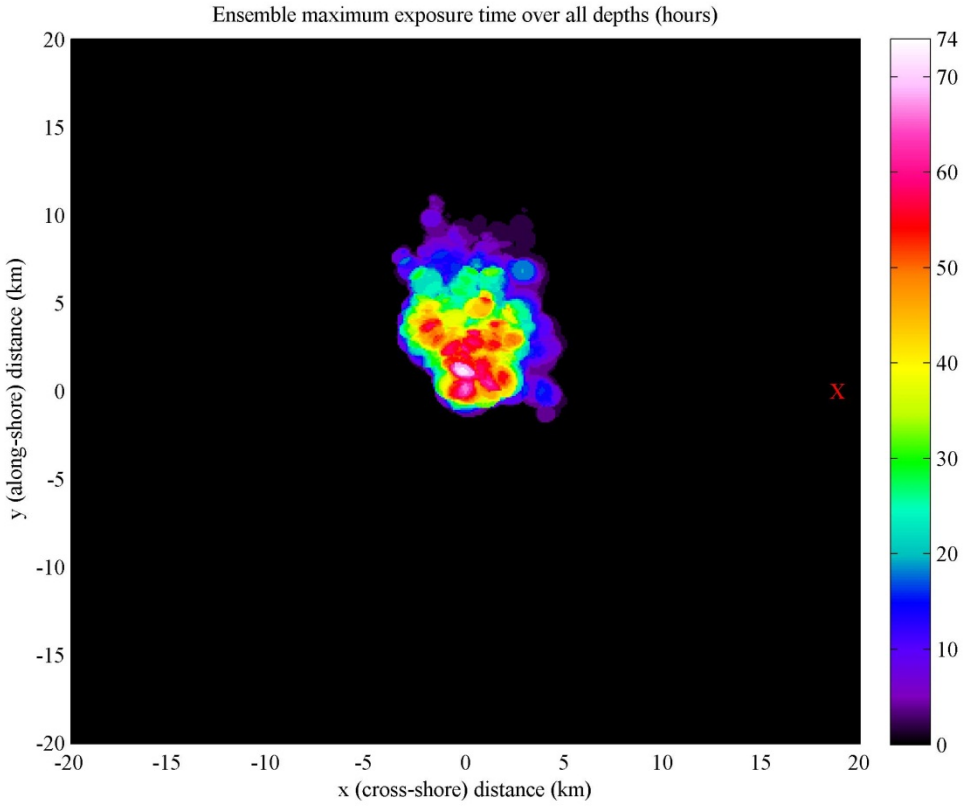

Figure 26. Predicted ensemble maximum exposure time to concentrations at or above 1 ppb (in hours). The color bar to the right of the figure indicates how exposure times are color-coded, with black (at the bottom of the bar) representing 0 hours and white (at the top of the bar) representing 70 hours or longer. The red X marks the horizontal distance from the ensemble plume centerline to the closest point on the O‘ahu coastline.

In summary, the model predicts that in the event of a release of 182 kg (400 lb) of hydrogen cyanide from two containers at the deepwater disposal site (HI-01), concentrations of dissolved hydrogen cyanide would exceed 1 ppb only up to a height of about 300 m (984 ft) above the ocean floor, and out as far as about 5 km (3.1 mi, 2.7 nm) from the source location in the along-shore direction and 10 km (6.2 mi, 5.4 nm) in the cross-shore direction. No location at any depth would be exposed to concentrations above 1 ppb for more than about 70 hours.

These modeling results indicate that concentrations of hydrogen cyanide would not exceed 1 ppb at any time in nearshore waters where people could be present. Furthermore, the results also indicate that at no time would contaminated water from the deepwater site (HI-01) ever reach the nearshore area along the coast.

Discussion of modeling uncertainty

This study also assessed the effects of using different mixing coefficients in the model. Mixing coefficients mathematically represent the degree of diffusion of a dissolved pollutant into the water column produced by turbulent mixing. Higher mixing coefficients (representing stronger turbulent mixing) were found to increase the spread of the dissolved hydrogen cyanide, but they also acted to reduce its concentration over time. Smaller mixing coefficients (representing weaker mixing) were found to increase the exposure time but reduce the spread of the pollutant. Regardless of the mixing coefficients used, dissolved hydrogen cyanide concentrations are not predicted to approach nearshore waters.

The deepwater disposal site (HI-01) lies well below the classic "level of no motion" depth of about 1,000 m (3,300 ft), below which ocean current velocities are assumed to be negligible, and the advected plume would remain below that level. The ADCP data revealed very slow current speeds at this site, as the theory would predict. Therefore any changes to the velocity field over time or space would result in only small changes to the contaminant footprints computed and should not change the overall results or conclusions.

What about the other chemicals that were disposed at this site?

In no realistic scenario would dissolved hydrogen cyanide be transported from the deepwater disposal site (HI-01) to the nearshore zone, if the hydrogen cyanide were released from containment. The other munitions constituents, if released from containment at the site, are even less likely to create a hazard to the shoreline community or people in nearshore waters.

If released, sulfur mustard and lewisite, which are denser than water, would pool on the ocean floor and very slowly dissolve. Sulfur mustard would hydrolyze (react with water). That process, if incomplete, could produce stable droplets of undissolved sulfur mustard that would persist for many years on the ocean floor before eventually dissolving. Lewisite would remain on the bottom, dissolving very slowly and reacting with seawater to produce

toxic byproducts that would slowly decompose ultimately leaving inorganic arsenic. Because the dissolution rates of sulfur mustard and lewisite are very slow, even if a large amount of either chemical was released, the hazard area would be much smaller than the hazard area from hydrogen cyanide.

If released, cyanogen chloride would dissolve because it is quite soluble in water, and then would slowly react with seawater to produce non-toxic byproducts. In a worst-case scenario, released cyanogen chloride could form a plume of about the same dimensions as the predicted hydrogen cyanide plume. The cyanogen chloride plume would persist for a few days, but over time the cyanogen chloride would react with seawater and concentrations would be reduced.

Acknowledgments

The project team would like to acknowledge that this study was funded by the Department of Defense Office of the Deputy Assistant Secretary of the Army for the Environment, Safety and Occupational Health, and was independently performed by NOAA under the 2006 NOAA Special Studies Agreement (MOA-2006-032/7206). The Defense Office of the Deputy Assistant Secretary of the Army for the Environment, Safety and Occupational Health was consulted as to what oceanographic information and modeling analysis were required, but NOAA conducted its work independently as a third party scientific agency providing singularly objective analysis and modeling results.

The authors have benefited from the generous contributions of time made by many people, especially the following:

Reviewers and editors
Mary Evans, Genwest Systems, Inc. (editing)
Diane Wehner, NOAA Office of Response and Restoration (toxicology)

Subject matter advisors
Dr. Adriana Bejarano, Research Planning, Inc. (toxicology)
Dr. George Bizzigotti, NOBLIS (chemical analysis) (deceased)
Aaron Boutwell, NOAA National Data Buoy Center
Richard Burgess, NOAA National Data Buoy Center
Dr. Jim Farr, NOAA Office of Response and Restoration (chemistry)
Ahmed Hafez, NOBLIS (chemical analysis)
Dr. Robert Jones, NOAA Office of Response and Restoration (chemistry)
Lex LeBlanc, NOAA National Data Buoy Center
Dr. Matthew Parry, NOAA Restoration Center (coral biology and ROUMRS project diving)
Brett Taft, NOAA National Data Buoy Center
Dalina Viveros, Genwest Systems, Inc. (chemistry, editing)
Diane Wehner, NOAA Office of Response and Restoration (toxicology)
NOAA Center for Operational Oceanographic Products and Services
NOAA National Data Buoy Center (ADCP mooring design, configuration, deployment, recovery, and data validation)
Ordnance Reef Coordinating Council (data collection planning)
Pacific Islands Ocean Observing System (PacIOOS)
Wai‘anae and Nanakuli Neighborhood Boards and community members

Fate and transport modelers:
Dr. Chris Barker, NOAA Office of Response and Restoration (fate and transport modeling)
Alex Hadjilambris, NOAA Office of Response and Restoration (fate and transport modeling)
Dr. Amy MacFadyen, NOAA Office of Response and Restoration (fate and transport modeling)
Caitlin O'Connor, NOAA Office of Response and Restoration (fate and transport modeling)
Brian Zelenke, NOAA Office of Response and Restoration (fate and transport modeling, report authoring)

Maps and graphics development:
JB Huyett, Genwest Systems, Inc. (mapping and graphics, document management)
Heather Lilly, Genwest Systems, Inc. (document management)
Kristina Worthington, Genwest Systems, Inc. (graphics development)

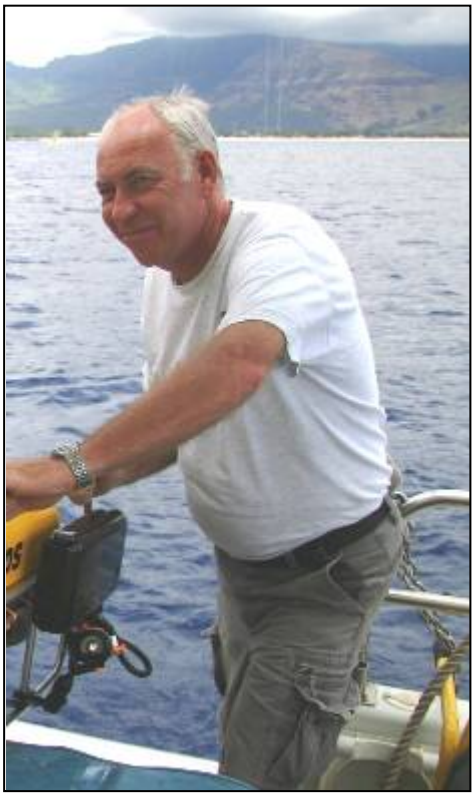

The project team would specifically like to acknowledge the many contributions of the late Mike Overfield. Without Mike's initial vision, undeterred leadership, and dogged determination, NOAA's important work at Ordnance Reef (HI-06) would not have been accomplished. Mike's tireless efforts during a time of personal medical trial were a testament to his dedication to furthering NOAA's role in providing the objective scientific information needed to make important decisions regarding Ordnance Reef (HI-06) and assist the people of the Wai'anae Coast in getting answers to their many concerns about this site. Mike's vision of fostering dialogue between scientists, stakeholders, regulators, and other interested parties has helped each better understand the complex nature of human use of the oceans and provides a model for future engagement.

References cited

Bienfang, P.K., and R.E. Brock. 1980. Predevelopment reconnaissance of the water quality and macrobiota conditions affronting the west beach coastline, Oahu, Hawaii. Technical report. Oceanic Institute, Waimanalo, HI. 118 pp.

Carter, G. S., M. A. Merrifield, J. M. Becker, K. Katsumata, M. C. Gregg, D. S. Luther, M. D. Levine, T. J. Boyd, and Y. L. Firing. 2008. Energetics of M2 barotropic-to baroclinic tidal conversion at the Hawaiian Islands. J. Phys. Oceanogr., 38(10): 2205–2223.

Carton, G., and A. Jagusiewicz. 2009. Historic disposal of munitions in U.S. and European coastal waters, how historic information can be used in characterizing risk. Marine Technology Society Journal 43(4): 16–32.

City and County of Honolulu, Department of Environmental Services. Waianae WWTP heads list of NACWA awards. Retrieved May 16, 2012, from http://www1.honolulu.gov/env/wwm/nacwapeakperformanceawards110805.pdf

Congressional Research Service. 2007. U.S. Disposal of Chemical Weapons in the Ocean: Background and Issues for Congress. Retrieved March 9, 2012, from http://www.fas.org/sgp/crs/natsec/RL33432.pdf

Department of Business, Economic Development, and Tourism (DBEDT), State of Hawaii. Waiʻanae Ecological Characterization. Retrieved March 7, 2012, from http://hawaii.gov/dbedt/czm/initiative/wec/html/sea/ocean/quality.htm

De Carlo, E.H., V. L. Beltran, and M. S. Tomlinson. 2004. Composition of water and suspended sediment in streams of urbanized subtropical watersheds in Hawaiʻi. Applied Geochemistry 19(7):1011-1037.

De Carlo, E. H., E. Cox, and M. Overfield. 2007. Ordnance Reef, Waiʼane, Hawaiʻi: remote sensing survey and sampling at a discarded military munitions sea disposal site. Marine Sanctuaries Conservation Series NMSP-07-01. U.S. Department of Commerce, National Oceanic and Atmospheric Administration, National Marine Sanctuaries Program, Silver Spring, MD. 112 pp.

De Carlo, E.H., S. M. Shjiegstad, S. Koide, and D. H. Dumas. 2012. Remedial Investigation: Ordnance Reef (HI-06), Waianae, Oahu, Hawaii. Dept. of Oceanography, School of Ocean and Earth Science and Technology, University of Hawaii at Manoa.

DOD (Department of Defense). 2010. Defense Environmental Programs Annual Report to Congress Fiscal Year 2009. Chapter 10: Sea Disposal of Military Munitions, pp 85-120.

Garcia, S. S., K. MacDonald, E. H. De Carlo, M. Overfield, T. Reyer, and J. Rolfe. 2009. Discarded military munitions case study: Ordnance Reef (HI-06), Hawaiʻi. In: The

legacy of underwater munitions worldwide: policy and the science of assessment, impacts and potential responses. Marine Technology Society Journal 43(4): 85-99.

Juvik, S. P., and J. O. Juvik. 1998. Atlas of Hawai'i. Hilo, HI: University of Hawai'i Press.

Lotufo, G., M. Nipper, R.S. Carr, and J.M. Conder. 2009. Ecotoxicology of Explosives. Boca Raton, FL: CRC Press.

Lumpkin, C. 1998. Eddies and currents of the Hawaiian Islands Ph.D. dissertation, School of Ocean and Earth Sciences and Technology, University of Hawai'i at Manoa, Manoa, Hawai'i.

McManus, M. A., K. J. Benoit-Bird, C. B. Woodson. 2008. Behavior exceeds physical forcing in the diel horizontal migration of the midwater sound-scattering layer in Hawaiian waters. Mar Evol Prog Ser, 365, 91–101.

Natural Resources Defense Council (NRDC). 2004. Testing the waters: A guide to water quality at vacation beaches. 14th annual report. Current edition available at: http://www.nrdc.org/water/oceans/ttw/ttw2011.pdf

Nipper, M., R.S. Carr, J.M. Biedenback, R.L. Hooten, and K. Miller. 2005. Fate and effects of picric acid and 2, 6-DNT in marine environments: Toxicity of degradation products. Marine Pollution Bulletin 50(110):1205 – 1217.

Noblis. 2011a. Physicochemical Properties for Compounds in Munitions in the Shallow Water Site of Ordnance Reef, O'ahu, Hawaii. Prepared by Noblis for NOAA, Contract GS10F0189T.

Noblis. 2011b. Physicochemical Properties for Compounds in Chemical Munitions in the Deep Water Site of Ordnance Reef, O'ahu, Hawaii. Prepared by Noblis for NOAA, Contract GS10F0189T.

Noda, E. K., P. K. Bienfang, W. J. Kimmerer, and T. W. Walsh. 1981. OTEC Environmental Benchmark Survey, Kahe Point, O'ahu. Final report. DOE/NBM-2016055. Prepared under Contract W-7405-ENG-48 for U. S. Department of Energy.

Rice, M. 2011. Modeling chemical transport at the deep ocean disposed munitions site near O'ahu. Unpublished report.

Stearns and Vaksvik 1935., Geology and ground-water resources of the Island of Oahu, Hawaii: Hawaii Division of Hydrography Bulletin, no. 1, 479 p.

Xie, S-P, W. Liu, Q. Liu, and M. Nonaka. 2001. Far-Reaching Effects of the Hawaiian Islands on the Pacific Ocean-Atmosphere System. Science, 292(5524):2057–2060.

Appendices

Physical Circulation along the Western Coast of Oʻahu

Background

Despite their relatively small size, the Hawaiʻian islands have a significant impact upon the atmospheric and oceanic circulations of the northern, sub-tropical Pacific. High volcanic mountains extending from the seafloor block both the NE trade winds and Northern Equatorial Current (NEC), forcing them to squeeze between the islands creating an ocean/atmosphere wake that extends 3,000 km across the Pacific. These wind-stress patterns drive the eastward Hawaiʻi Lee Countercurrent (HLCC) west of the Big Island, creating a strong shear zone between the NEC and the HLCC. Both cyclonic and anticyclonic eddies are often observed in the lee of the Big Island, which are thought to be generated either through instabilities in this shear zone or directly by the wind-stress curl in the lee of the Big Island. Because the HLCC extends for thousands of kilometers to the west, it transports large amounts of heat from the western to the central Pacific and plays an important role in controlling the temperature around the Hawaiʻian Islands (Xie *et al*, 2001). The system is tightly coupled as the wind stress pattern drives a thermal gradient in the ocean, which --- in turn --- enhances the winds. We have found that the numerical estimation of the winds has a significant impact upon the strength of the HLCC as well as the eddy activity in the lee of the islands, which controls the biological productivity and mesoscale activity (Natarov and Powell, 2011).

As the HLCC approaches the leeward side of the island chain, it bifurcates and feeds the Hawaiʻian Lee Current (HLC) that flows to the northwest. This returns much of the warm HLCC water westward and prevents much of it from passing between the islands to the east. The North Hawaiʻian Ridge Current (NHRC) flows to the northwest on the windward side of the Island chain carrying the cooler, subtropical water to north of the islands. These currents form the canonical circulation around the Hawaiʻian islands as shown in Figure 1.

The canonical currents are interconnected and change in the strength of one affects the characteristics of other currents. The primary region for exchange between the HLC and NHRC is the Kauaʻi Channel between the islands of Oʻahu and Kauaʻi. This channel is composed of the Kaʻena ridge: a steep sill connecting the two islands. As cyclonic eddies are prominent in this

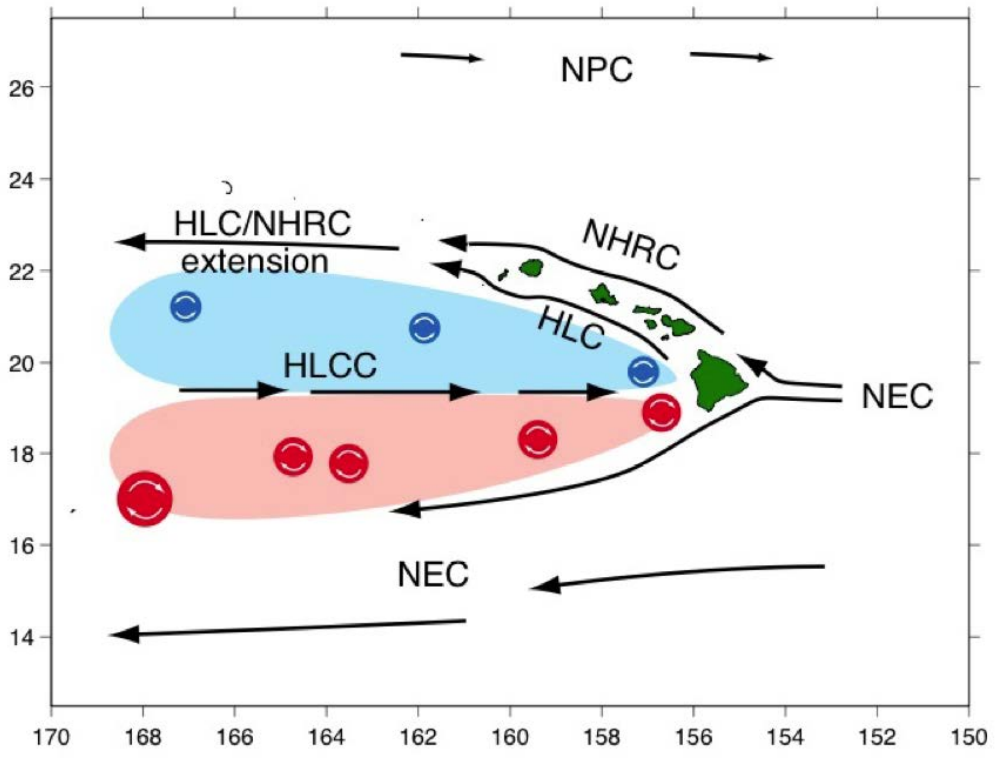

***Figure 1**: Canonical oceanic circulation around the Hawai'ian Islands (Lumpkin, 1998). The blue (red) region is dominated by cyclonic (anticyclonic) eddies.*

region (as shown in Figure 1), they commonly abet against the sill and even against the Waiʻanae coast of Oʻahu. In addition to the strong mesoscale activity that occurs along the western coast, Kaʻena ridge serves as a major generation site of baroclinic tidal energy.

When strong, barotropic tides impact steep ridges, energy is converted into baroclinic waves that propagate along the density structure of the ocean. These tidally induced internal waves can have speeds that are equivalent to the mesoscale, and are a crucial component of the circulation around Hawaiʻi (Carter *et al*, 2008). As shown in Figure 2, the propagation of these waves follows the coastline of the Waiʻanae coast. These internal waves alter the density structure of the ocean as they pass. Most noticeably, the thermocline can be heaved by over 300m by the strongest internal waves in the area. This change in density depth can have an impact upon biological or other particulates in the water column by displacing them over significant vertical distances. Tidally induced internal waves are also capable of transporting matter. As the barotropic tide impacts the slope and the baroclinic interal wave is created, the internal wave can

collect matter at the source region (mud, neutrally buoyant biology and particulates) and carry it along the path of the internal wave propagation.

As discussed, winds are the significant factor in the circulation around Hawai'i, and near the islands, this is also true. Because Hawai'i's islands are mountainous, they create wakes of weak wind directly in their lee. The Wai'anae coast lies directly in the wake of O'ahu. During normal trade-wind conditions, the winds flow around the island, sheltering the Wai'anae coast from the winds. For most of the year, this is the case, and winds have little impact upon the circulation. However, during the winter, the trade winds often collapse (as part of the El Ni o-La Ni a Southern Oscillation). During these periods, storms traveling from South of the islands can blow strong westerly winds (coming from the west and impacting Wai'anae). During these periods, the winds are favorable to impacting the circulation along the Wai'anae coast.

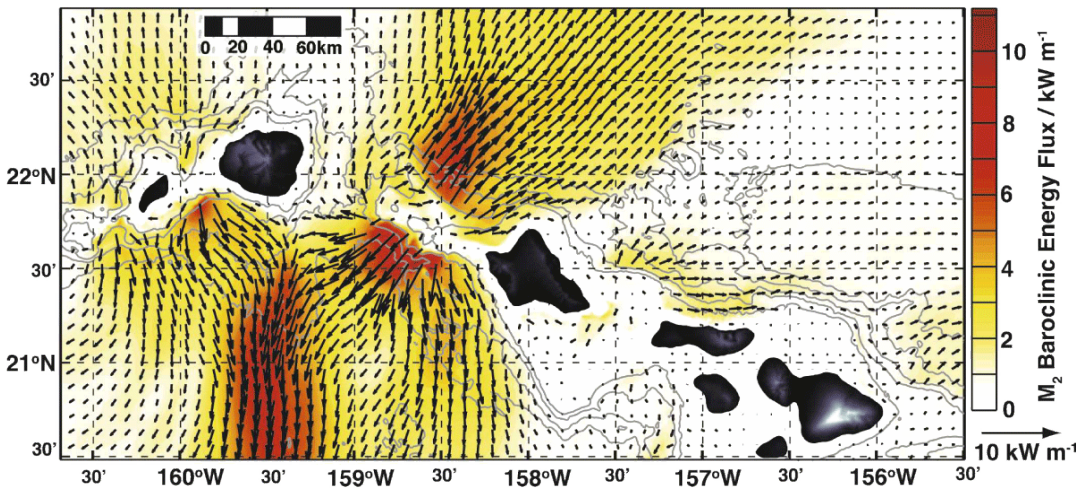

***Figure 2**: M_2 Baroclinic Energy flux emanating from Ka'ena Ridge (Carter et al, 2008). Note the strength of baroclinic tidal currents along the Wai'anae Coast isobaths.*

Finally, the Hawai'ian islands are the largest mountains on the Earth. They are not part of a continental plate system, rather they are volcanic mountains formed at the seafloor and extending upwards of 14,000 ft above sea level. Because of this geographic anomaly, they lack any type of shelf system near the islands. Fortunately, being in oligotrophic waters, they provide a sanctuary

for oceanic life. This life formed coral reefs around the islands, significantly protecting them from the open ocean. The coral reefs are exceptionally effective to breaking and dissipating wave energy (swells, etc.) before it reaches and harms the coast; however, sustained oceanic currents can still impact the islands. Along the Waiʻanae coast, the mountain slope is quite steep and the waters deepen to 2km only several kilometers from the shore. This exposes the Waiʻanae coast to the cyclonic eddies present in the HLCC/HLC system. These eddies can impact right against the island and create significant circulation strengths along the coast.

The Waiʻanae coast is an exceptionally dynamic and interesting region for physical oceanography. The combination of mesoscale energy near the coast, strongly varying wind conditions (from no wind to significant wind forcing), highly energetic baroclinic tides, and a strong mean circulation as the HLC and NHRC exchange waters creates a challenging environment to study and characterize for this project.

Physical Oceanic Observations of the Ocean Currents along the Waiʻanae Coast

Acoustic Doppler Current Profilers (ADCPs) were deployed off the Waiʻanae coast at water depths of 15 m, 80 m, and 2500 m. The ADCPs measured three-dimensional water velocities and acoustic backscatter, throughout the water column at the 15 m and 80 m sites, and between the seafloor and 620 m above the seafloor at the 2500 m site. The instruments also took single-point measurements of water temperature. Water velocity, backscatter and temperature data were collected near-continuously between 24 June 2009 and 25 August 2010.

Currents at the 2500 m site were generally weak, most often between 2 to 7 cm s^{-1}, and of varying directionality, with a slight bias towards the along-shore axis (NNW to SSE). A portion of the variability in current orientation occurred at semidiurnal frequencies. Currents at 620 m above the seafloor were roughly in phase with currents at the seafloor, indicating little vertical shear. Near the seafloor, northerly currents had an upward vertical component, and southerly currents had a downward vertical component. Small, but distinguishable increases in acoustic backscatter near the seafloor (indicative of suspended particulates) occurred most often during periods of upward currents.

Water temperatures at the deep site were between 1.6 and 1.8 °C at the deepest sensor (12 m above the seafloor), and between 2.1 and 2.3 °C at the shallowest sensor (450 m above the seafloor).

Currents at the four shallow sites were faster and more focused in direction than at the deep site (Fig. 3). Velocities at the shallow sites were most often between 15 to 30 cm s^{-1}, oscillating in orientation predictably between NNW (during ebb tide) and SSE (during flood tide). The ebb phase was generally shorter-lived than the flood phase, thus currents were oriented to the SSE a greater percentage of the time. While the majority of variability in the along-shore (NNW to SSE) component of currents occurred at semidiurnal frequencies, variability in the cross-shore (ENE to WSW) component of currents occurred at higher frequencies, and was less predictable within the semi-diurnal tidal phase. There was often very low vertical shear throughout the water column at the four shallow sites, expect occasionally during the transition periods in semidiurnal tidal flow.

Water temperature at the two 80 m sites varied between 20 and 26 °C, fluctuating ~3 °C over each semi-diurnal tidal cycle, while water temperature at the two 15 m sites varied between 23 and 27 °C, fluctuating 0.5 to 1 °C over each semi-diurnal tidal cycle.

Numerical Modeling of the Ocean Currents along the Waiʻanae Coast

The modeling component is based on the Regional Ocean Modeling System (ROMS): a free-surface, hydrostatic, primitive equation model discretized with a terrain following vertical coordinate system (Shchepetkin and McWilliams, 2005). Multiple subgridscale parameterizations of vertical mixing and several options for open boundary conditions have been included. Time-splitting of barotropic and baroclinic motions enables efficient integration. ROMS is coded in parallel for multi-threaded and multi-process architectures and has been widely applied in many applications from planetary scales down to estuary environments. In addition, ROMS offers a suite of state-of-the-art dynamical analysis tools, including an adjoint, tangent-linear, and linear models for advanced variational data assimilation (see Moore, et al. 2004 and Powell, et al, 2008) as well as a number of advanced biological models (e.g., Powell, et al., 2006, Fennel, et al., 2006, Fiechter, 2009).

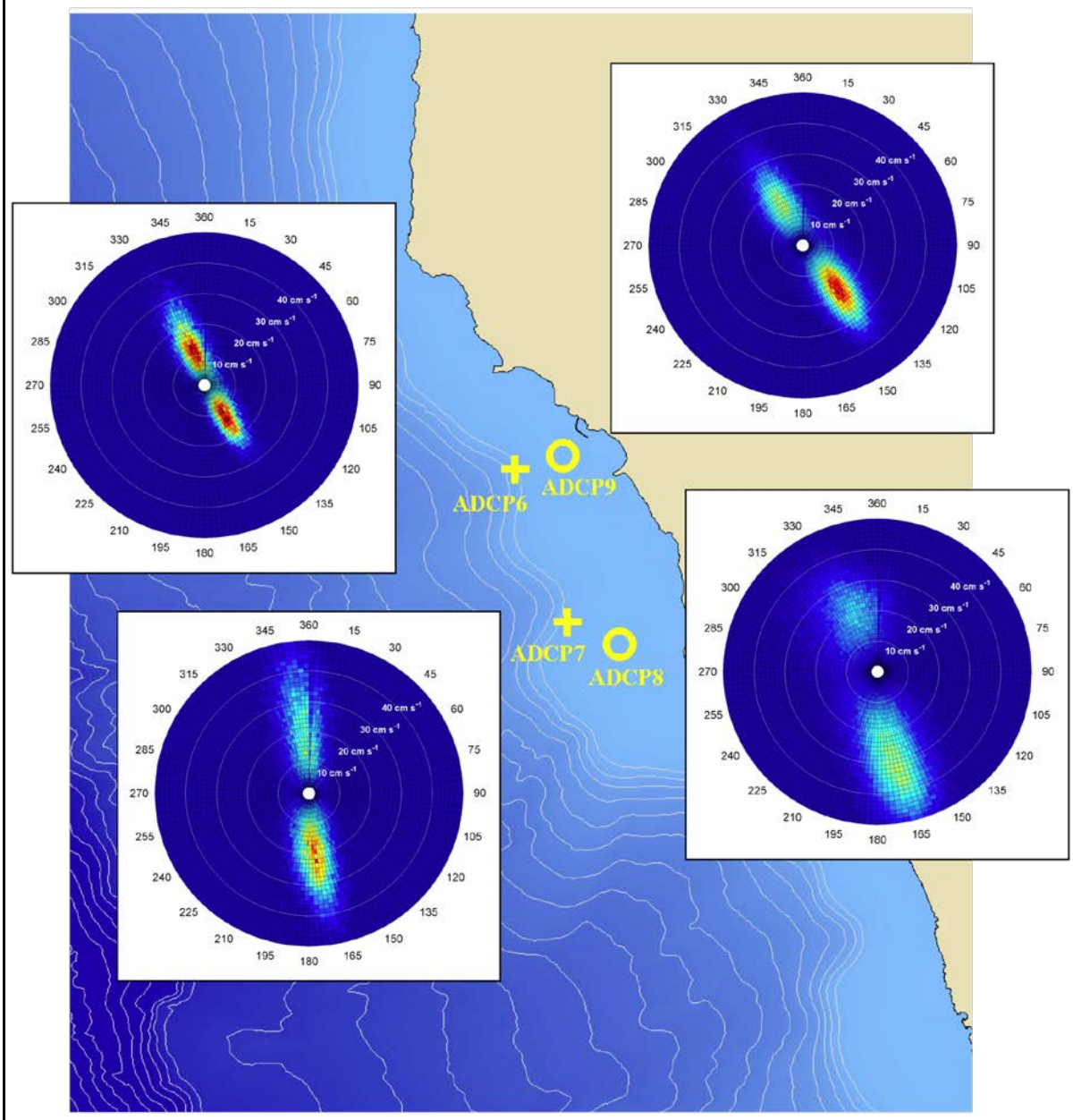

***Figure 3**: Histograms of current direction and magnitude at the four shallow water sites: ADCP6 (80 m depth; top left), ADCP7 (80 m depth; bottom left), ADCP8 (15 m depth; bottom right), ADCP9 (15 m depth; top right). Yellow and red regions within histogram plots represent current directions and magnitudes present over greater percentages of time than blue regions, indicating frequent alignment of currents in the along-shore direction. White depth contours in background are shown in 100 m intervals.*

Numerical model setup

For the Waiʻanae coast, it is necessary to use high resolution numerical model that is capable of representing key features of the region; however, we must step down from coarse global models by cascading down to the resolution of interest using nested model grids. In the case of Hawaiʻi, where internal wave dynamics has strong impact on the overall circulation (e.g., Carter et al, 2008), the nesting is critical. The outer model covers the Hawai'ian island chain (Figure 4) with a spatial resolution of 4 km. This model grid uses global model data from the Navy Couple Ocean Model (NCOM) at its boundaries. Embedded within this grid is a second grid covering the southern and western regions of the island of Oʻahu with variable resolution of ~2.5 km in deeper water and ~600 m along the coast. This grid is a significant improvement from the Hawaiʻian grid at resolving the steep bathymetry of the region and representing features such as Penguin Bank to the SE of the island. Embedded within the Oʻahu grid is the Waiʻanae grid (Figure 4) with variable resolution of 1 km along the deep, western boundary and 200 m along the coast. This is the model of interest created for this project. It uses 20 s-levels in the vertical. ROMS is a terrain-following coordinate model, using s-level transformation, which means that the depths of the levels vary in space and time. This is particularly advantageous for near-coastal regimes; however, one negative is regions of steep bathymetric changes (large vertical gradients over short horizontal distances). These steep gradients create pressure-gradient errors that must be reduced by "smoothing" the bathymetry. As a consequence (because the western coast of Oʻahu changes from 3km depth to 15m depth over a very short distance), the model bathymetry is a bit smoother than the actual. This is true for any model due to discretization, but the additional modifications mean that the ADCP depths and model grids do not match precisely. The consequence of this is discussed in the results.

The Hawaiʻian and Oʻahu grids were created for NOAA's PacIOOS effort, and the Waiʻanae grid for the purpose of evaluating the circulation along the western coast. Furthermore, each model was forced with the respective nested results from a locally produced Weather Research and Forecasting (WRF) atmospheric model as part of PacIOOS.

The modeling experiment encompasses two phases: i) ocean models forced by realistic atmosphere for three years (200—2010), and ii) models forced by realistic atmosphere and assimilating all available data (including ADCPs above) from August, 2009 through July, 2010.

The non-assimilated runs (i) were used for characterizing statistical conditions for the transport modeling, and the results from (ii) are used for the investigation at present. All following results are from experiment (ii).

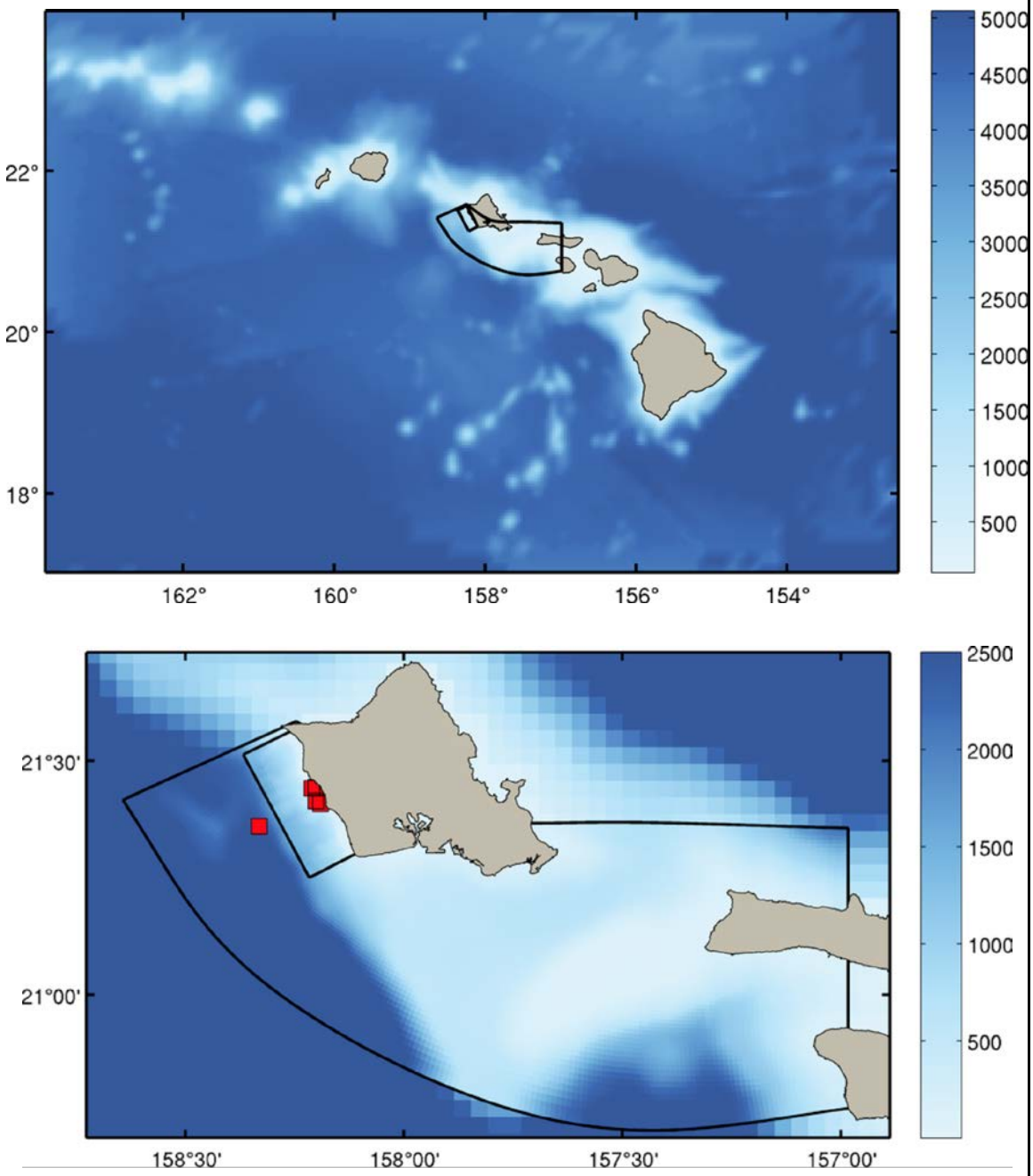

***Figure 4**: (top) Spatial extent and bathymetry of Hawaiian islands grid with both Oahu and Waianae grids outlined. (bottom) Same for the Oahu grid with Waianae Grid shown. Red boxes mark the locations of the ADCP's described in the previous section.*

The goal of any data assimilation scheme is to combine observations and a numerical model in a dynamically consistent way such that the result is a better estimate of the ocean circulation than either alone. The observations provide constraints in space and time while models provide context to the observational information.

Although there are a number of assimilation techniques (nudging, optimal interpolation, variational, and Markov-based), only those that consider the dynamical equations of the model (as described by the Navier-Stokes equations) achieve the goal described above. For this project, we used four-dimensional variational (4D-Var) assimilation. In 4D-Var, the model physics are used to propagate information both forward and backward in time, such that through a minimization effort, the resulting circulation is dynamically consistent and represents the data through time. The advantage is that it allows temporal windows, allowing more observations to constrain the model. Optimal interpolation and 3D-Var techniques hold time constant, and is capable only of resolving slowly evolving flows governed by simple balance relationships. 3D-Var is ill-suited for highly intermittent flows with irregularly sampled observations (not synoptic snapshots). 4D-Var is ideal for such scenarios because the physics of the model are used to constrain the model with the observations.

Using the observations, we generate a continual and full estimate of the ocean over the observation window, which for this project was 4 days for each grid. This is ideal for both accuracy and timeliness of current state estimates and future predictions, as a continuous field evolves by the nonlinear primitive equations. For the experiment described here, we used all available data found during the period, including: project ADCPs (both deep and shallow), autonomous glider data, HF-radar data, satellite sea surface temperature and height, fixed moorings available around Hawaiʻi, Argo floats, CTD casts from the Hawaiʻian Ocean Time-series, and other data of opportunity.

Model results

The general circulation around Hawai'i is well described in literature as per the introductory review; however, coastal processes with highly variable dynamics are less known. Circulation along the Western coast of O'ahu is dominantly driven by tidal forces exhibiting strong

alongshore circulation pattern (McManus et al, 2008). This regular, oscillatory motion is further modified by both the flow along bathymetric features and by event driven mesoscale dynamics. These processes were captured by the ADCPs as described in the previous section.

Before examining the modeled results, we aim to ensure consistency with the ADCP observations. The model provides context to the ADCP data; therefore, the ADCP data are valuable in model comparison. Barotropic tides are deterministic and are available from sources, such as the global TPXO 7.2 dataset. Because of this, the modeled tides are forced by the global tidal information; however, as discussed earlier, the model bathymetry cannot precisely match the ocean. This creates subtle differences between the modeled tidal flow and true ocean. To reconcile these differences, observations must have the tides removed before adding the modeled tides back into the observational data. In addition, the spatial and temporal resolution of the observations is greater than the model. For these reasons, the observations are binned together into the model grid cells in space and that are separated by less than 60s at the same location. This procedure changes the observations as it acts as a low-pass filter (both in smoother tides and binning together observations).

The modified observed speed and direction histograms for the ADCP data are shown in Figure 5 (as compared to the raw, unfiltered data in Fig. 3). The final modeled values are shown in Figure 6, and show a very high correlation to the filtered ADCP data. The correlation of the along-shore model currents to the ADCP data averages a correlation skill of 0.91 over the year. The power spectral density of the modeled currents at the ADCP locations in Figure 7 clearly show the majority of energy in the semidiurnal (10-15 hours) and diurnal (20-25 hours) band with more than order of magnitude stronger for along-shore currents compared to the cross-shore. Because the signal-to-noise ratio of the cross-shore currents is rather low, the correlation between the modeled cross-shore currents and the ADCPs is much lower at 0.65. The strong correlation of the dominant energies of the observed and modeled currents provides high confidence in the modeled results. Also shown in Figure 5 and 6 — as compared to Figure 3 — are the bathymetric lines from the model. You will notice that these lines have less variation along-shore as the true bathymetry.

Examining the mean, upper 5m surface currents from August 2009 – July 2010 (Figure 8), we note that the flow is directed from the South-West toward the coast region where it bifurcates near the ADCPs locations with one branch flowing along the coast toward the north and the second to the southern coast. This mean surface current is strongly polarized alongshore in the narrow strip close to the coast with weak flow close to the ADCP stations where it splits into the two branches.

Seasonality of the coastal current system during the 2009-2010 year (Figure 9) is more pronounced in surface layers where atmospheric forcing through atmosphere-ocean boundary layer dynamics has more effect. In the wintertime, surface flow is the strongest and directed to NW inside the whole domain (Figure 9, March 2010), as a direct consequence of strong Southerly winds dominated a weakened Trade Wind system. Even in the monthly mean transport currents, these winds drive water masses along the Western Oʻahu coast toward the North. During the summer/autumn, the western coast region is in the island-blocked wind shadow resulting in weak currents of the opposite direction.

Based on the averaged current fields at different depths we can point two distinct regions: (i) the shallow near coastal part characterized with stronger mean currents directed alongshore having similar vertical velocity structure and (ii) deeper part having vertically sheared flow with small vertically averaged mean currents. Dominant flow in the region is due to the tidal dynamics (both baroclinic and barotropic) in both the diurnal and semidiurnal spectrum. Tidal ellipses for phase locked M_2 tidal constituents are highly polarized with values for major semi-axes approximately 12 cm/s in the surface layers (Figure 10a). Barotropic M_2 tidal ellipses are even more influenced by bottom topography (Figure 10b). Variability of the along-shore currents is over one order of magnitude stronger than the across-shore (Figure 7) in the coastal region, and the ratio nears two orders of magnitude near the ADCP stations.

Temperature field shows vertically stable profiles with mean yearly values at the surface near $26^{\circ}C$ and a thermocline depth of ~200 m (Figure 11). Mean variability in temperature field (Figure 12) for Aug. 2009 - July 2010 period has maximal values up to $1.7^{\circ}C^2$ found at the thermocline depth due to heaving of the thermocline by internal tides (or other mesoscale features).

Summary

The western coast of Oʻahu sits in a dynamically active region with strong mean currents from the HLCC, dominating baroclinic tides generated at Kaʻena Ridge, and mesoscale activity that impinges upon the reef. From the observed and modeled data, the primary circulation is along-shore due to the dominance of the semi-diurnal and diurnal tides. Particles in this system are moved north and south along the coast with weak on- and off-shore motion as the tides change from ebb to flood. During periods of mesoscale activity, the flow is primarily along-shore (anticyclonic eddies impinging on the shore will push particles along-shore to the South).

The near-shore ADCPs captured this along- and cross-shore variance; however, the model revealed that ADCP 8 and 9 experience a different dynamical regime than the outer ADCPs. ADCP 8 is in the headland wake of the nearby point at the southern tip of Waiʻanae Bay. It was in the region that a bifurcation of the on-shore flow occurs.

What remains unexplored is the action of the waves. During the wintertime, strong Southern Pacific Ocean storms create storm swells that travel and impact the island of Oʻahu from the south-west. These waves impart friction along the bottom as well as a barotropic transport near the coast.

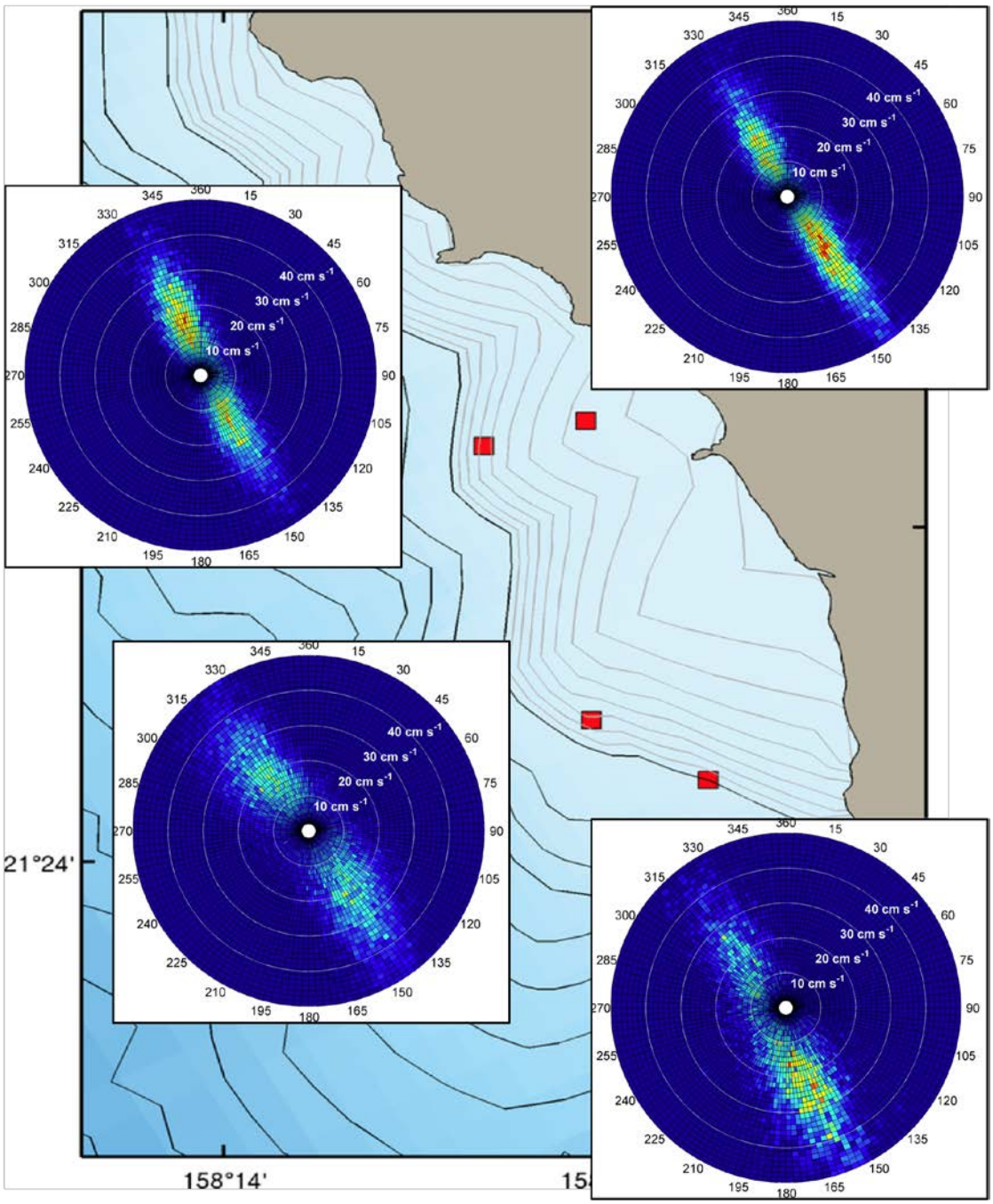

***Figure 5**: Histograms of filtered ADCPs 6,7,8, and 9. These data were binned, detided, and filtered for assimilation into the model.*

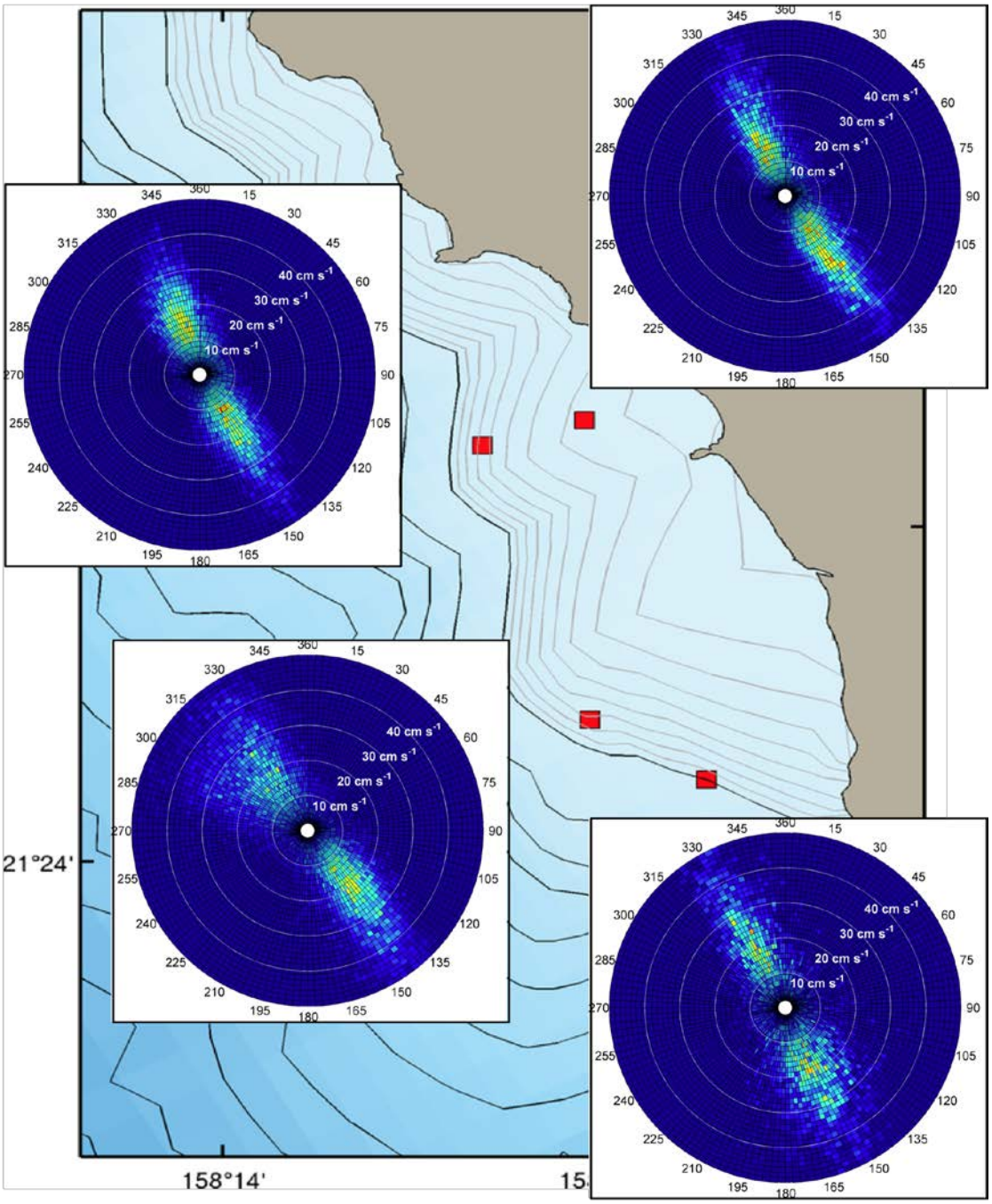

Figure 6*: Histograms of modeled currents at the locations ADCPs 6,7,8, and 9. The model shows very high correlation (0.9) with the observations shown in Figure 5.*

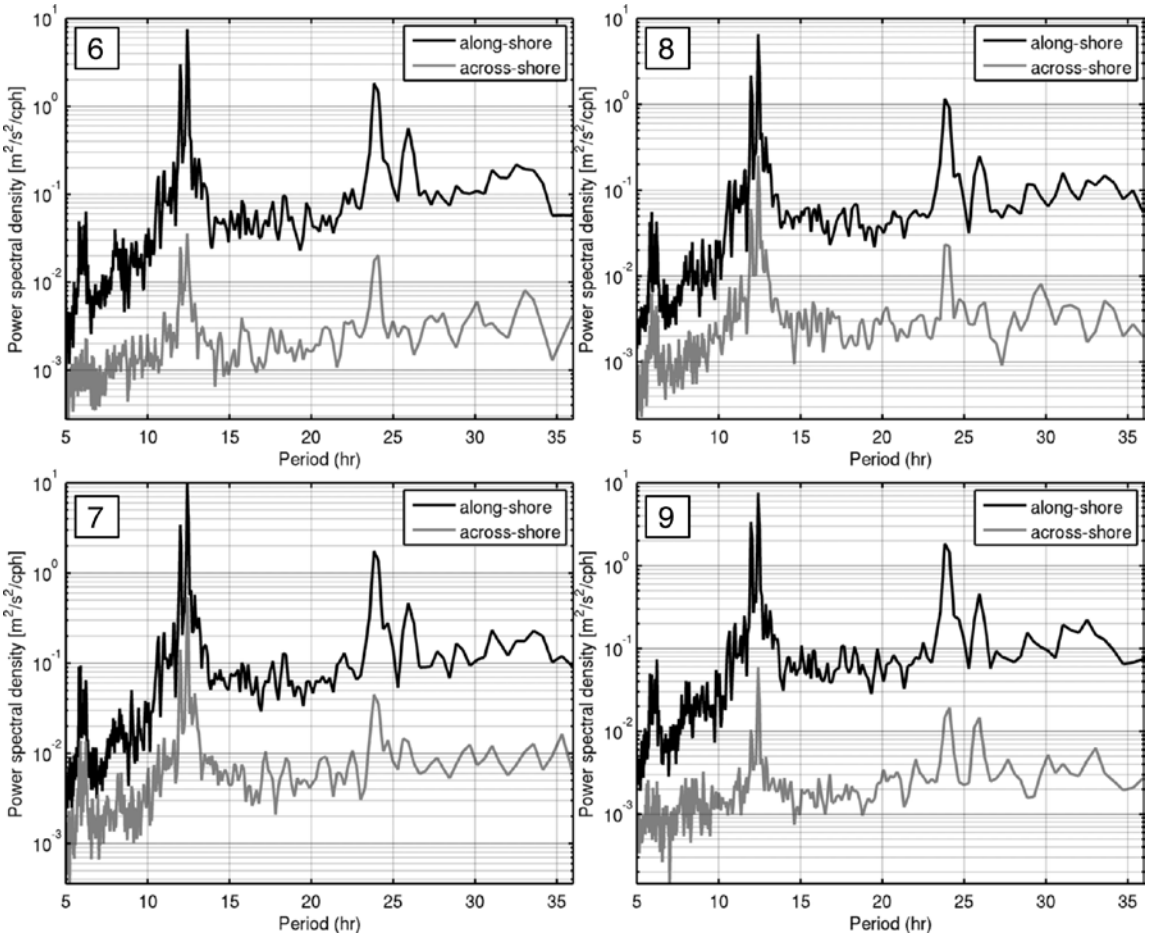

***Figure 7**: Power Spectral Density of modeled currents at the ADCP locations. The along-shore flow is nearly two orders of magnitude larger than the cross-shore with spectral peaks at the diurnal and semi-diurnal tidal frequencies.*

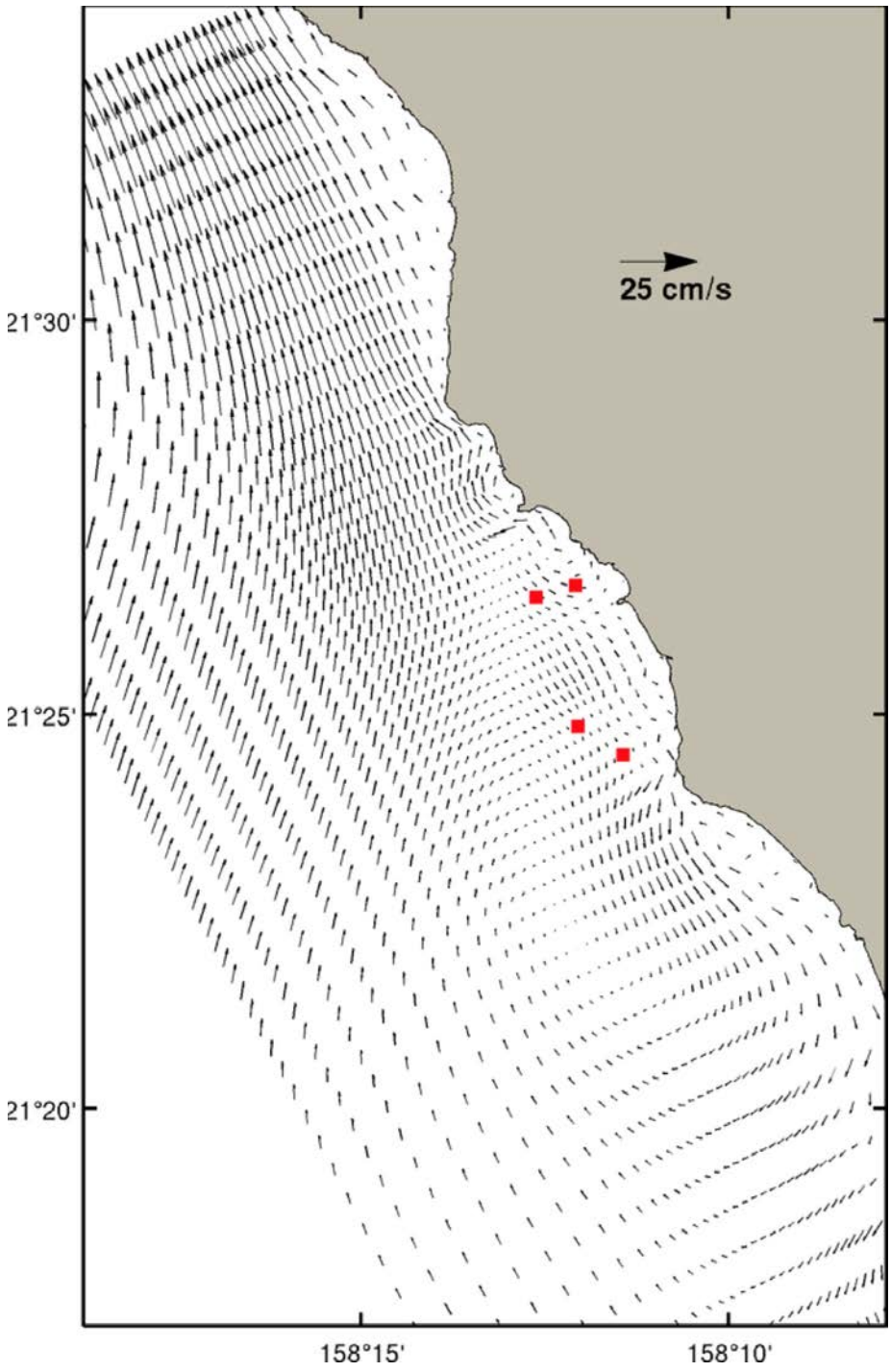

***Figure 8**: Model mean upper 5m currents from Aug., 2009 through July, 2010. ADCP locations are marked in red.*

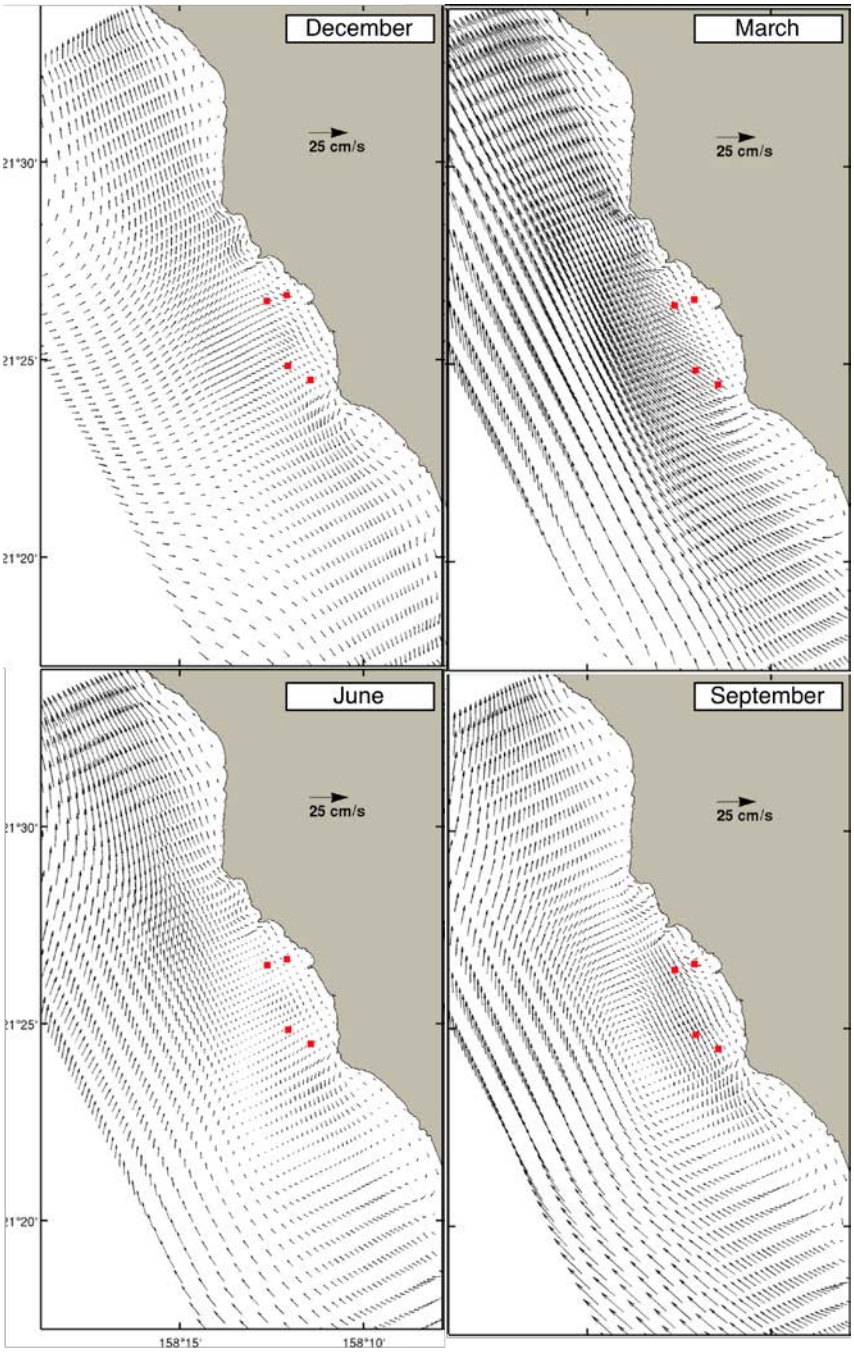

Figure 9*:Model mean upper 5m currents for (a) December (b) March (c) June, and (d) September, 2010.*

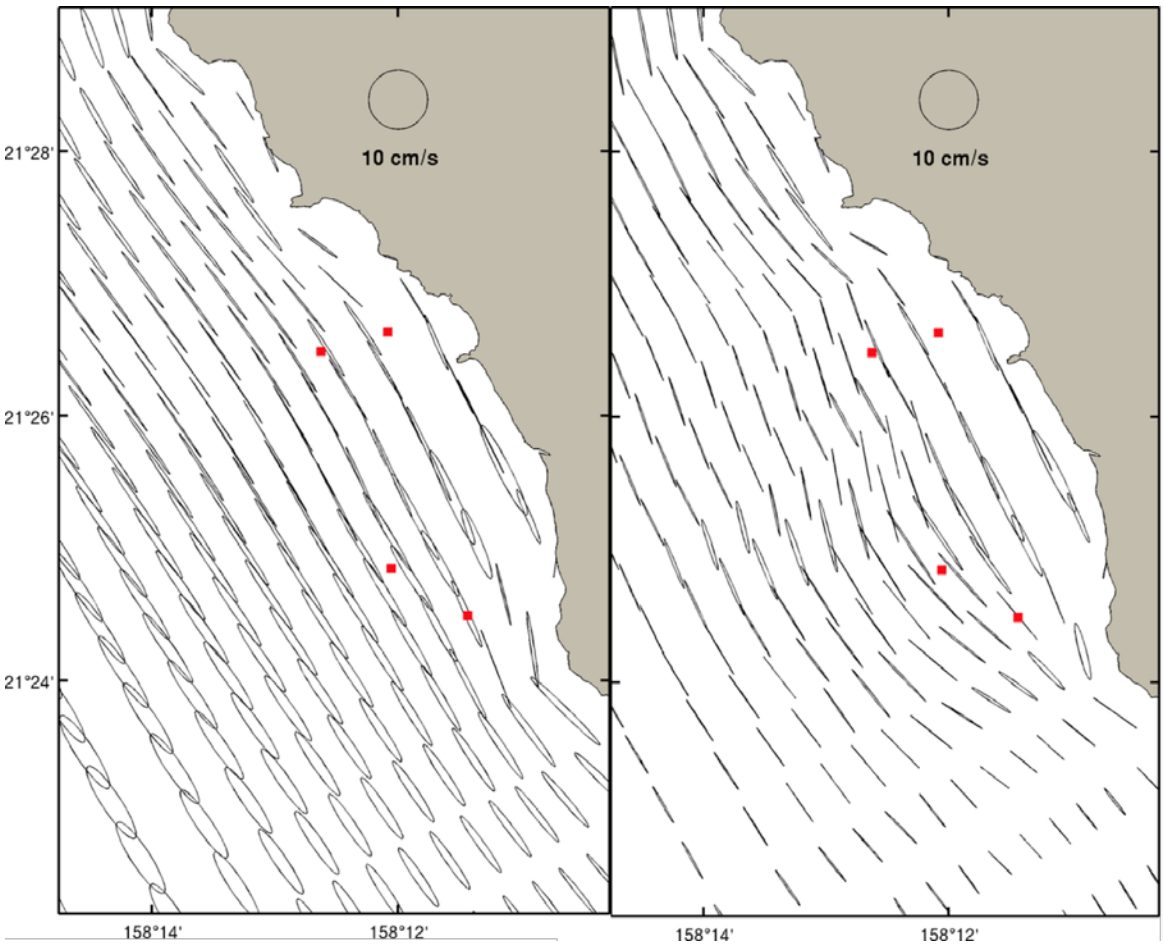

***Figure 10**: Modeled M_2 tidal variance for (a) surface and (b) barotropic.*

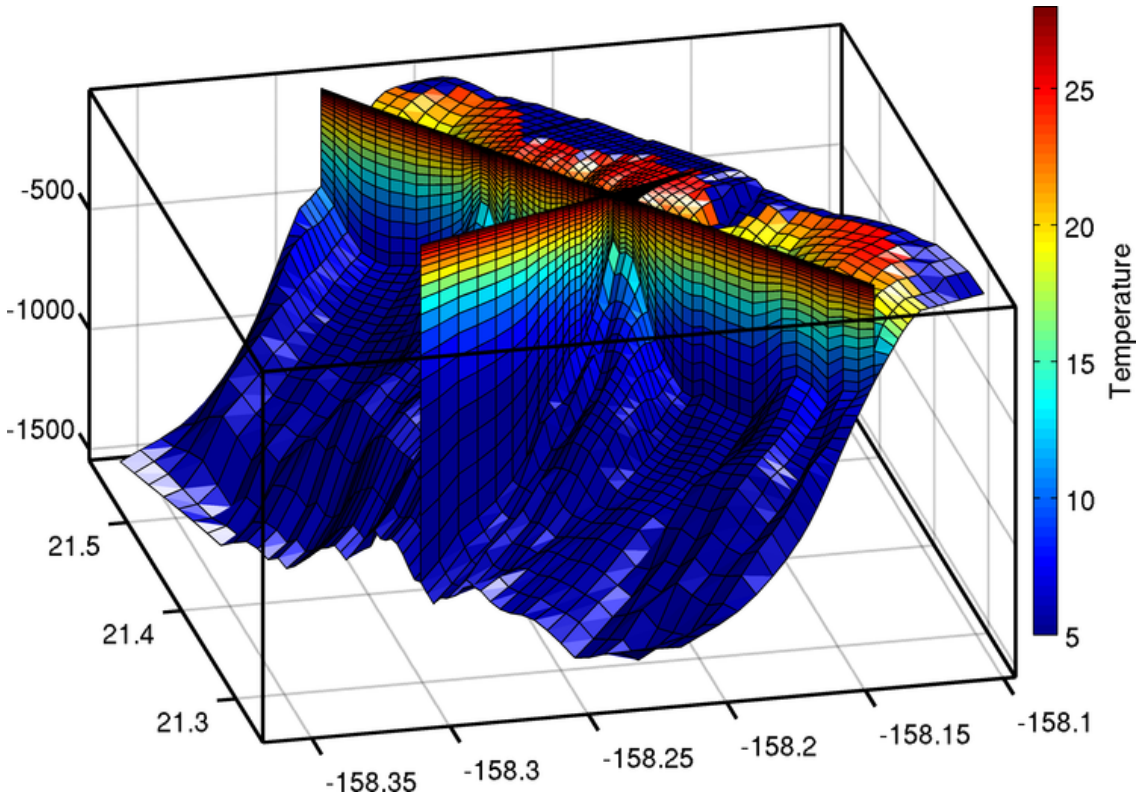

Figure 11*:Model mean potential temperature (°C) for the year of interest. The thermocline mean depth is near 200m with a sharp decrease in temperature under the thermocline. Along the coast, the temperatures vary as a function of the atmospheric forcing.*

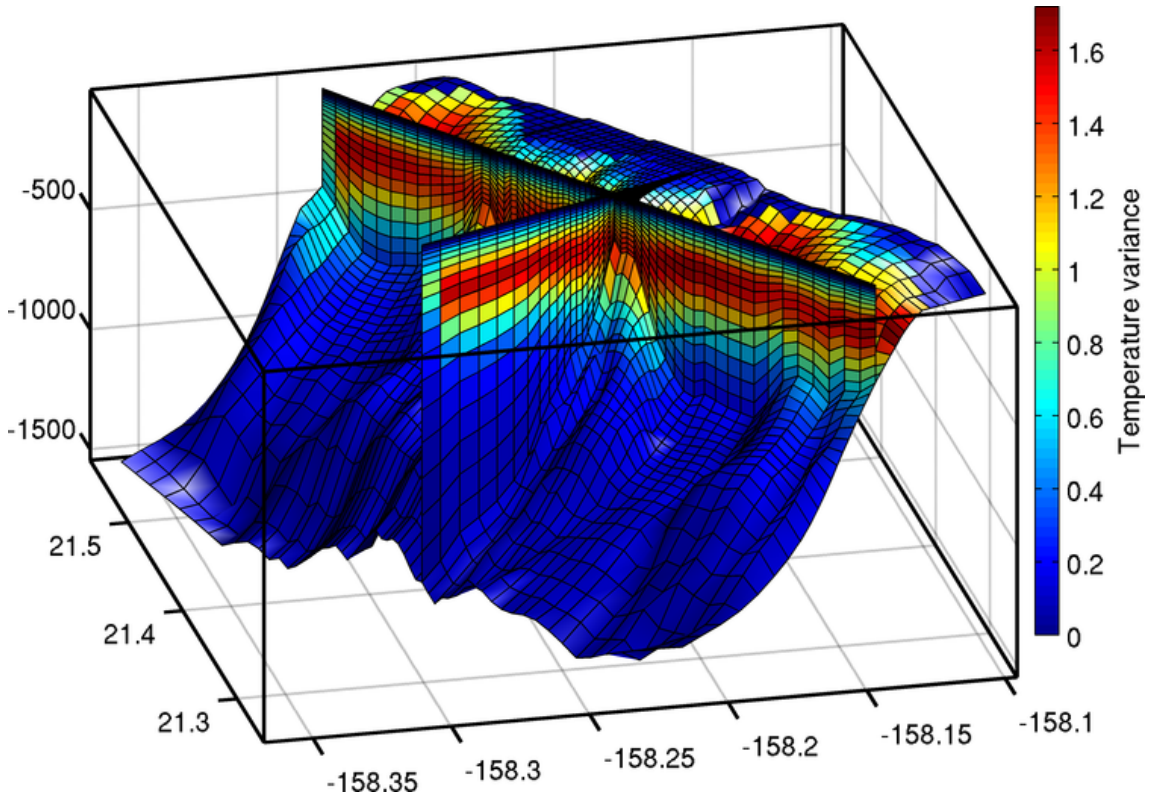

***Figure 12**:Model potential temperature variance (°C^2). The strongest variance shows the significant heaving of the thermocline that occurs due primarily to the propagating, tidally-induced internal waves that are generated at Ka ʻena ridge to the NW of the domain.*

References

Carter, G. S., M. A. Merrifield, J. M. Becker, K. Katsumata, M. C. Gregg, D. S. Luther, M. D. Levine, T. J. Boyd, and Y. L. Firing, 2008: Energetics of M2 barotropic-tobaroclinic tidal conversion at the Hawaiʻian Islands. J. Phys. Oceanogr., 38(10), 2205–2223.

Fiechter, J, A. M. Moore, C. A. Edwards, K. W. Bruland, E. Di Lorenzo, C.V.W. Lewis, T. M. Powell, E. N. Curchitser, and K. Hedstrom, 2009. A simple approach to model iron limitation on primary production in the coastal Gulf of Alaska, Deep Sea Res. II, doi: 10.1016/j.dsr2.2009.02.010.

Fennel, K., J. Wilkin, J. Levin, J. Moisan, J. O'Reilly, and D. Haidvogel, 2006. Nitrogen cycling in the Middle Atlantic Bight: Results from a three-dimensional model and implications for the North Atlantic nitrogen budget. Global Biogeochem Cy., 20, doi: 10/1029/2005GB002456.

Lumpkin, C., Eddies and currents of the Hawaiʻian Islands, Ph.D. dissertation, 1998. School of Ocean and Earth Sciences and Technology, University of Hawaiʻi at Manoa, Manoa, Hawaiʻi.

McManus, M. A., K. J. Benoit-Bird, C. B. Woodson, 2008. Behavior exceeds physical forcing in the diel horizontal migration of the midwater sound-scattering layer in Hawaiʻian waters. Mar Evol Prog Ser, 365, 91–101.

Moore, A. M., H. Arango, E. Di Lorenzo, B. Cornuelle, A. Miller, and D. J. Neilson, 2004. A comprehensive ocean prediction and analysis system based on the tangent linear and adjoint of a regional ocean model. Ocean Model., 7, 227-258.

Natarov, A. and B. S. Powell, A numerical study of the effects of wind and upstream conditions on the Hawaiʻian circulation, Dyn. Atmos. Oceans, in review, 2011.

Powell, B. S., H. Arango, A. Moore, E. Di Lorenzo, R. Milliff, and D. Foley, 2008. 4DVAR Data Assimilation in the Intra-Americas Sea with the Regional Ocean Modeling System (ROMS). Ocean Model., 25, 173-188.

Powell, B. S., A. Moore, H. Arango, E. Di Lorenzo, R. Milliff, and R. Leben, 2009. Real-Time Assimilation and Prediction in the Intra-Americas Sea with the Regional Ocean Modeling System (ROMS). Dyn. Atmos. and Oceans, 48:46-68.

Powell, T.M., C.V.W. Lewis, E. N. Curchitser, D. Haidvogel, A. J. Hermann and E. L. Dobbins, 2006. Results from a three-dimensional, nested biological-physical model of the California Current System and comparisons with statistics from satellite imagery, Jour. Geophys. Res., 111, doi:10/1029/2004JC002506.

Shchepetkin, A. F., and J. C. McWilliams, 2005. The Regional Oceanic Modeling System: A split-explicit, free-surface, topography-following-coordinate ocean model. Ocean Model., 9, 347-404.

Xie, S-P, W. Liu, Q. Liu, and M. Nonaka. Far-Reaching Effects of the Hawaiʻian Islands on the Pacific Ocean-Atmosphere System. Science, 292(5524):2057–2060, 2001.

NOAA Ordnance Transport
12-month ADCP data summary

1. Instrument deployment locations (Fig. 1)

Note: All times are HST.

1.1. Deep ADCP string (Fig. 2)

The deep ADCP string consisted of five ADCPs (ADCP1, ADCP2, ADCP3, ADCP4, and ADCP5). It was deployed on 24-July 2009 at 2200 at [-158.331, 21.360], at a water depth of 2528 m. It was recovered on 23-August 2010 at 0558.

1.2. Near-shore 300 kHz ADCPs

1.2.1. ADCP6 (North, offshore site)

ADCP6 was initially deployed on 24-July 2009 at 1348 at [-158.2100, 21.4415]. It was briefly recovered, and re-deployed due to being flipped on the original deployment. It was re-deployed on 9-September 2009 at 1517 at [-158.2104, 21.4414]. This location is 75 m from the original planned site at a heading of 251°. The average water depth was 104 m; the planned depth for this site was 90 m. This ADCP was recovered on 25-August 2010 at 0935.

1.2.2. ADCP7 (South, offshore site)

ADCP7 was deployed on 24-July 2009 at 1300 at a recorded location of [-158.2009, 21.4141], but was recovered at [-158.2006, 21.4123]. This recovery location is 199 m from the planned site at a heading of 165°. The average water depth was 72 m; the planned depth for this site was 90 m. The ADCP was recovered on 25-August 2010 at 1022.

Both near-shore 300 kHz ADCPs were briefly recovered and re-deployed on 17-Feb 2010 for data download.

1.3. Near-shore 1200 kHz ADCPs

1.3.1. ADCP8 (South, inshore site)

ADCP8 was deployed on 25-July 2009 at 1021 at [-158.1906, 21.4081]. This is 658 m from the planned site at a heading of 179°. The average water depth was 13.2 m; the planned depth for this site was 13.6 m. The ADCP was recovered on 25-August 2010 at 0853.

1.3.2. ADCP9 (North, inshore site)

ADCP9 was deployed on 25-July 2009 at 1106 at [-158.2014, 21.4439]. This is 47 m from the planned site at a heading of 336°. The average water depth was 16.9 m; the planned depth for this site was 16.9 m. The ADCP was recovered on 25-August 2010 at 0738.

Both near-shore 1200 kHz ADCPs were also briefly recovered and re-deployed on 17-Feb 2010 for data download.

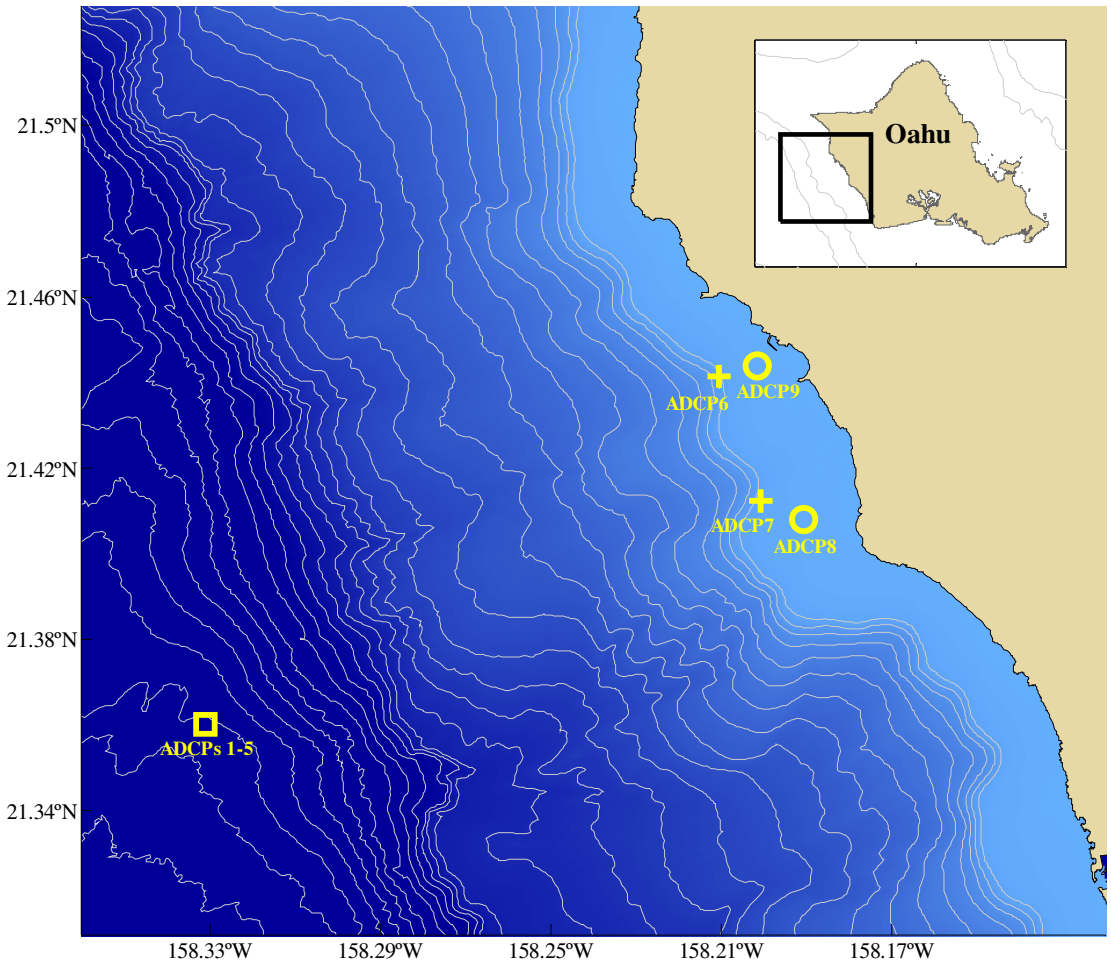

Figure 1. Map of the island of Oahu (1000 m and 2000 m depth contours shown) (inset) and deployment locations for the nine ADCPs. Solid white lines represent 100 m to 2700 m isobaths in 100 m intervals.

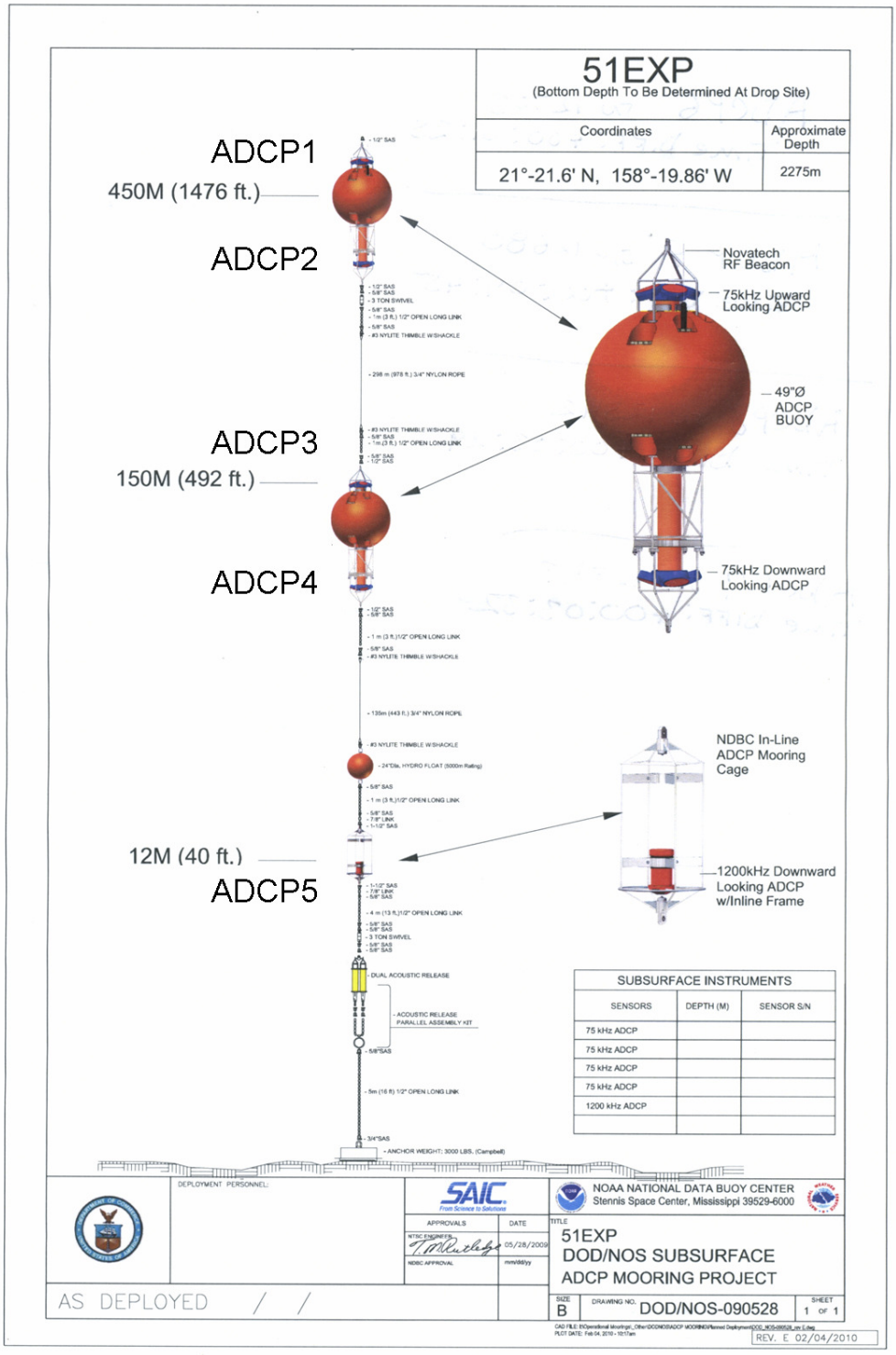

Figure 2. Deep ADCP string configuration, with the height above seafloor of each sensor given.

2. Data Availability (Table 1; Fig. 3)

Instrument	Start date	6-month recovery	6-month re-deployment	End date
ADCPs 1-5	24-Jul-2009 2200	N/A	N/A	23-Aug-2010 0558
ADCP6	09-Sep-2009 1517	17-Feb-2010 1118	17-Feb-2010 1515	25-Aug-2010 0935
ADCP7	24-Jul-2009 1300	17-Feb-2010 1238	17-Feb-2010 1634	25-Aug-2010 1022
ADCP8	25-Jul-2009 1021	17-Feb-2010 0940	17-Feb-2010 1754	25-Aug-2010 0853
ADCP9	25-Jul-2009 1106	17-Feb-2010 1013	17-Feb-2010 1534	25-Aug-2010 0738

Table 1. Start and end dates for ADCP deployment (HST). Dates refer to ensembles when ADCPs were upright and fully deployed.

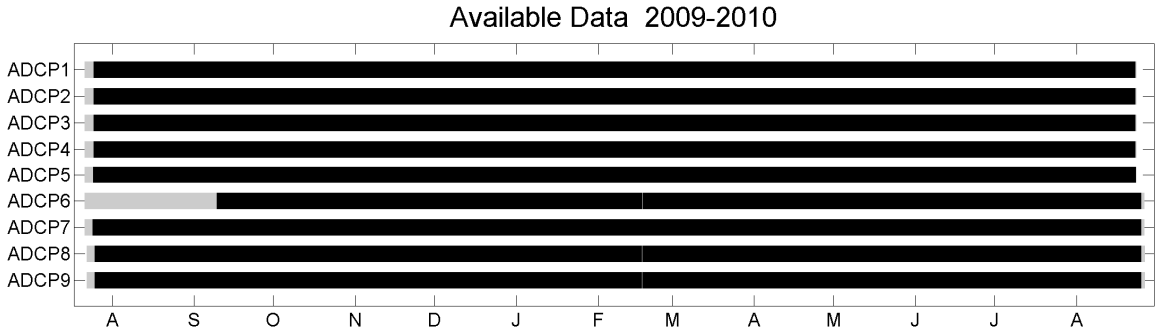

Figure 3. Start and end dates for ADCP deployment, as in Table 1. Black bars represent ensemble times when ADCPs were upright and fully deployed.

3. Data Collection parameters

3.1. Deep ADCP string

3.1.1. 75 kHz ADCPs

The four 75 kHz ADCPs at the deep string (ADCP1, ADCP2, ADCP3, and ADCP4) were programmed to collect 2 hr ensembles consisting of 40 pings per ensemble. The error in this configuration is 0.97 cm s^{-1}. A total of 8 depth bins of width 20 m each were recorded.

3.1.2. 1200 kHz ADCP

The downward-looking 1200 kHz ADCP at the bottom of the deep string (ADCP5) was programmed to collect 15 min ensembles consisting of 60 pings per ensemble. The error in this configuration is 0.90 cm s^{-1}. A total of 25 depth bins of width 50 cm each were recorded.

3.2. Near-shore 300 kHz ADCPs

The two near-shore 300 kHz ADCPs (ADCP6 and ADCP7) were programmed to collect 10 min ensembles consisting of 12 pings per ensemble. The error in this configuration is 0.50 cm s^{-1}. A total of 10 depth bins of width 8 m each were recorded.

3.3. Near-shore 1200 kHz ADCPs

The two near-shore 1200 kHz ADCPs (ADCP8 and ADCP9) were programmed to collect 3 min ensembles consisting of 12 pings per ensemble. The error in this configuration is 2.01 cm s^{-1}. A total of 24 depth bins of width 0.5 m each were recorded.

4. Summary of Data Processing

4.1 Compass calibration

The compass of each ADCP was calibrated prior to deployment to within 2° accuracy. The compass readings were internally corrected for the Earth's magnetic declination at the study area of +9.9°.

4.2. Internal data quality checks

Each ADCP was programmed to internally screen each ensemble for data quality. It is not possible to recover data values for these flagged data. The criteria for internal data quality processing for all ADCPs was set to the manufacturer recommended (default) settings. These settings, and a description of each criterion are detailed below.

4.2.1. Low Correlation Threshold = 64

The ADCP uses a low correlation threshold to screen water-track data for the minimum acceptable correlation requirements. The nominal (maximum) correlation depends on system frequency and depth cell size. The default threshold for all frequencies is 64 counts. A solid target would have a correlation of 255 counts.[1]

4.2.2. Error Velocity Maximum = 200 cm s^{-1}

The error velocity is the difference between two simultaneous estimates of vertical velocity. Error velocity depends on the data redundancy: only three beams are required to compute three-dimensional velocity. The fourth ADCP beam is redundant, but not wasted. Error velocity allows you to evaluate whether the assumption of horizontal homogeneity is reasonable.[2]

4.2.3. False Target Threshold Maximum = 50

The false target threshold maximum screens water-track data for false targets (usually fish). The threshold value chosen sets the maximum difference between echo intensity readings among the four profiling beams. If the threshold value is exceeded, the ADCP rejects velocity data on a cell-by-cell basis for either the

affected beam (fish detected in only one beam) or for the affected cell in all four beams (fish detected in more than one beam). This usually occurs when fish pass through one or more beams.[1] All depth cells were subjected to this test.

Typically, the vast majority of bad-flagged data points are located at bins of shallow depth (for upward-looking ADCPs), and bins close to the seafloor (for downward-looking ADCPs). This is due to interaction of the side-lobes of the acoustic signal with the sea surface or seafloor.[2] For the shallow water, upward-looking ADCPs used in this study, the 20° beam angle caused the upper 6% of the water column to be corrupted by side-lobe interference. For the downward-looking ADCP on the deep string, the bottom 1 m of the water column was corrupted by side-lobe interference. Other sources of error include data collected before and after deployment (i.e., see Fig. 3, gray bars).

The results of the internal data quality checks are listed in Table 2.

4.3. Post-processing

Raw binary ADCP data was converted to ASCII format using RD Instruments 'BBConv' software, before importing into Matlab for further processing.

4.3.1. Internal clock drift

The internal clocks of each ADCP were set before deployment. Upon recovery, the ADCP time stamp was compared to the time from the same clock source that was used to initially set the ADCP internal clock. The differences in these two times were used to correct the outputted time stamp by assuming a linear drift over the length of the deployment.

4.3.2. Calculation of sea surface height

Sea surface height was calculated from the ADCP pressure data using a UNESCO conversion formula. The altitude for each sensor was inferred from a NOAA engineering drawing (Fig. 2).

4.3.3. Correction of raw echo intensity (RSSI) data

Raw RSSI data were corrected for the effects of beam spreading and chemical absorption of sound with distance, using the equation:

$$EA = RSSI + 20 \log_{10} r + 2 \alpha r \qquad (1)$$

Where EA is the corrected echo amplitude, r is the slant-range to the portion of each bin where echo intensities are sampled[3], and α is the sound absorption coefficient[4]. RD Instruments ADCPs are not factory-calibrated to measure true acoustic scattering strength; EA is a relative measure that varies by instrument. To allow a first-order comparison of acoustic scattering strength over the nine ADCPs, EA calculated using Equation 1 was then normalized by the median value of EA for each instrument over the entire deployment.

4.3.4. Rotation of current velocity components to along- and cross-shore

The east and north components of current velocity were rotated to along- and cross-shore components using the 324° heading of the coastline within a 6 km distance of the near-shore sensor array.

4.3.5. Further data quality screening

Sea surface height and corrected echo amplitude were evaluated for depth bins that were corrupted by side-lobe interference with the sea surface or seafloor, but were not flagged by the internal screening process (as in Section 4.2). The entire time series of echo amplitude was inspected for each ADCP. Velocity data from the first bin that showed visual signs of corruption from the sea surface or seafloor was removed.

Additionally, visual inspection of current velocity outliers suggested further screening of all velocity data with corresponding error velocities of magnitude > 3 cm s^{-1} for each ADCP on the deep string, as well as all velocity data from the deepest bin of ADCP1.

All data were then truncated to the same beginning and end indices of 26-July 2009 0000 and 23-August 2010 0000 (with the exception of ADCP6 which had a beginning index of 09-September 2009 1517).

Table 2 shows the total number of velocity cells collected by each ADCP, as well as the number of cells rejected in internal processing (Section 4.2), the number of additional cells that were rejected in post-processing (Section 4.3), and the percentage of the total number of cells that were rejected either internally or in post-processing.

	Total number of velocity cells recorded	**Number of cells rejected internally**	**Number of additional cells rejected in post-processing**	**Final percentage of total cells rejected**
ADCP1	38,200	256	4,987	13.7%
ADCP2	38,200	256	721	2.6%
ADCP3	38,200	261	379	1.7%
ADCP4	38,200	259	9,872	26.5%
ADCP5	955,175	433,504	95,558	55.4%
ADCP6	576,710	71,063	6,236	13.4%
ADCP7	577,000	5,994	175,205	31.4%
ADCP8	4,610,136	33,626	1,183,963	26.4%
ADCP9	4,609,968	72,195	53,558	2.7%

Table 2. Results of internal data quality checks and post-processing screening.

5. Preliminary results

5.1. ADCP1

Currents at ADCP1 were generally <12 cm s^{-1}, and of varying directionality, although there was a slight bias towards the along-shore axis (NNW to SSE) (Fig 4).

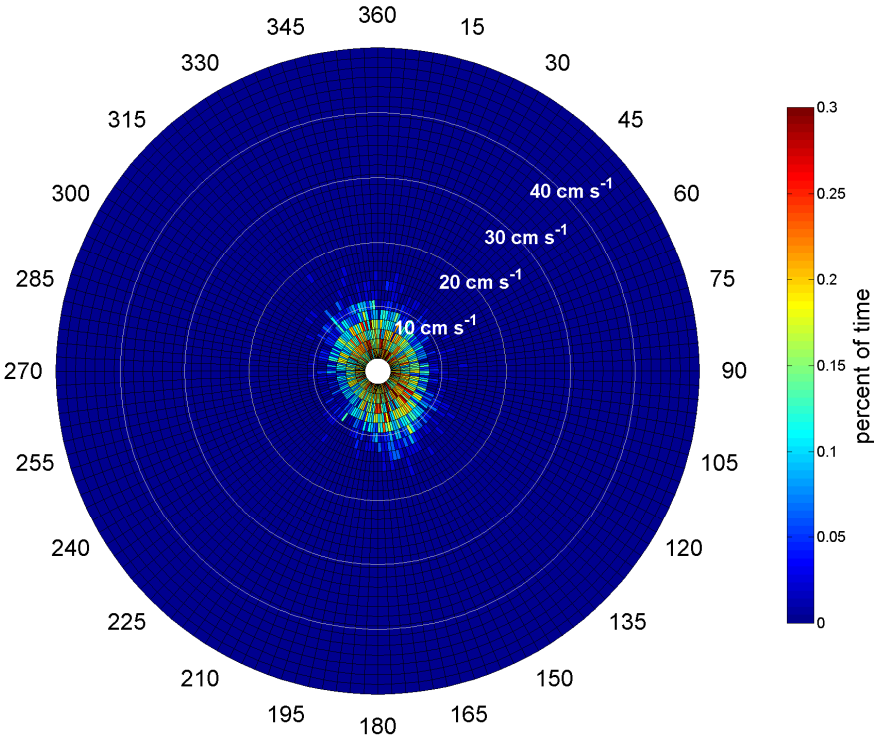

Figure 4. Histogram of current direction and magnitude for ADCP1.

Time series of data collected at ADCP1 are shown in Fig. 5.

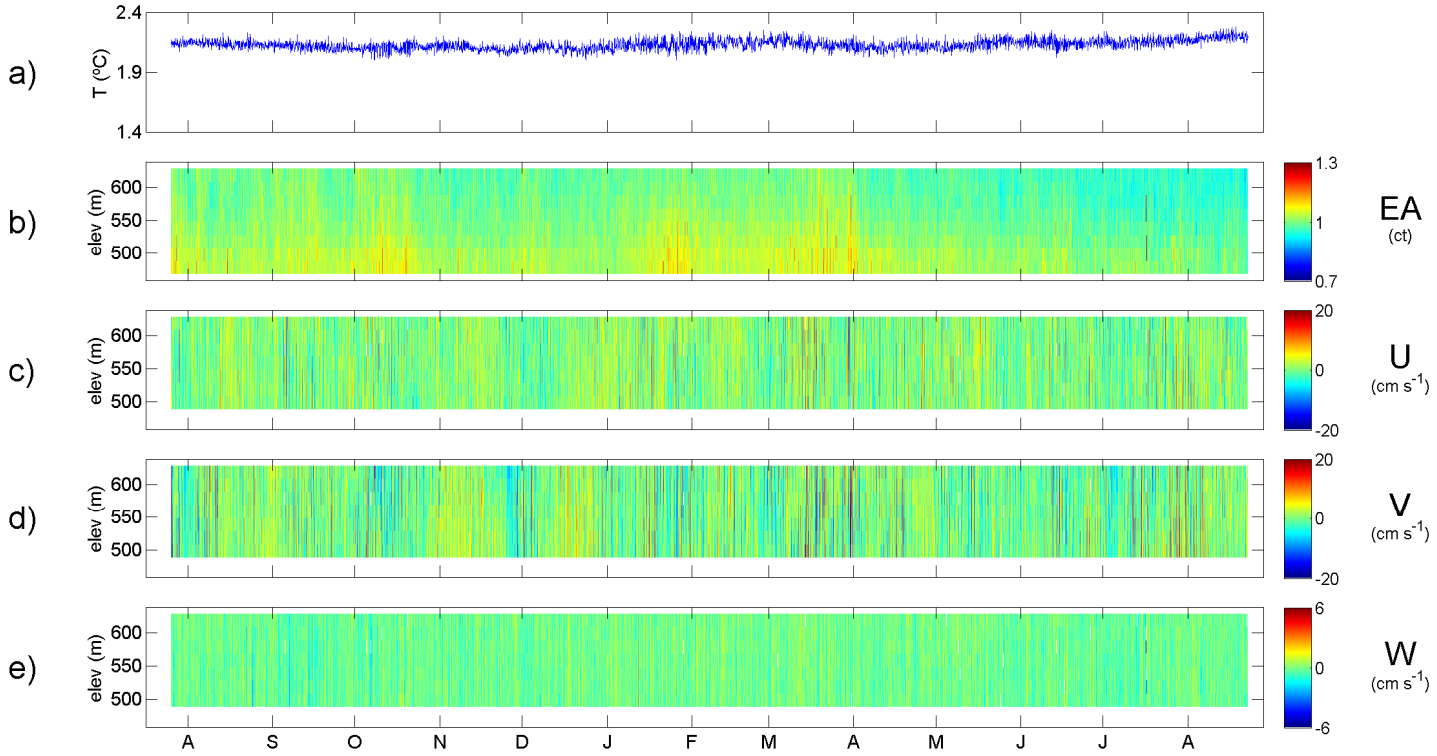

Figure 5. Time series of data collected at ADCP1, from August 2009 through August 2010. Panels (b) – (e) are rendered with elevation (m above seafloor) on the y-axis. (a) Temperature (°C); (b) corrected echo amplitude (counts); (c) cross-shore (NE[+] to SW[-]) current velocity (cm s^{-1}); (d) along-shore (NW[+] to SE[-]) current velocity (cm s^{-1}); (e) vertical (up[+] to down [-]) current velocity (cm s^{-1}).

5.2. ADCP2

Currents at ADCP2 were also generally <12 cm s^{-1}. Currents were most often oriented along the along-shore axis (NNW to SSE) (Fig 6).

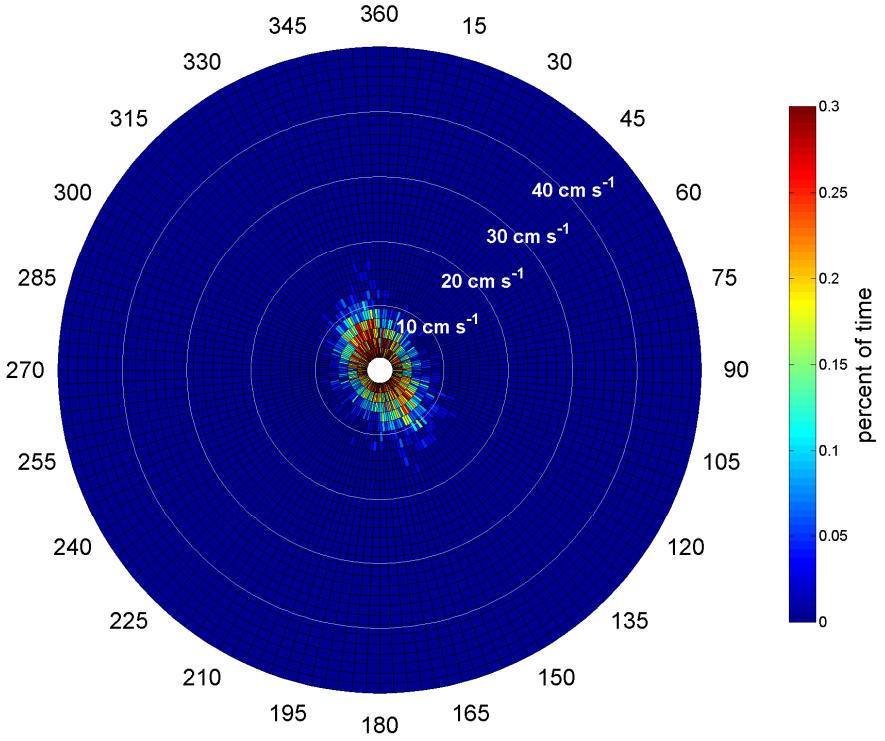

Figure 6. Histogram of current direction and magnitude for ADCP2.

Time series of data collected at ADCP2 are shown in Fig. 7.

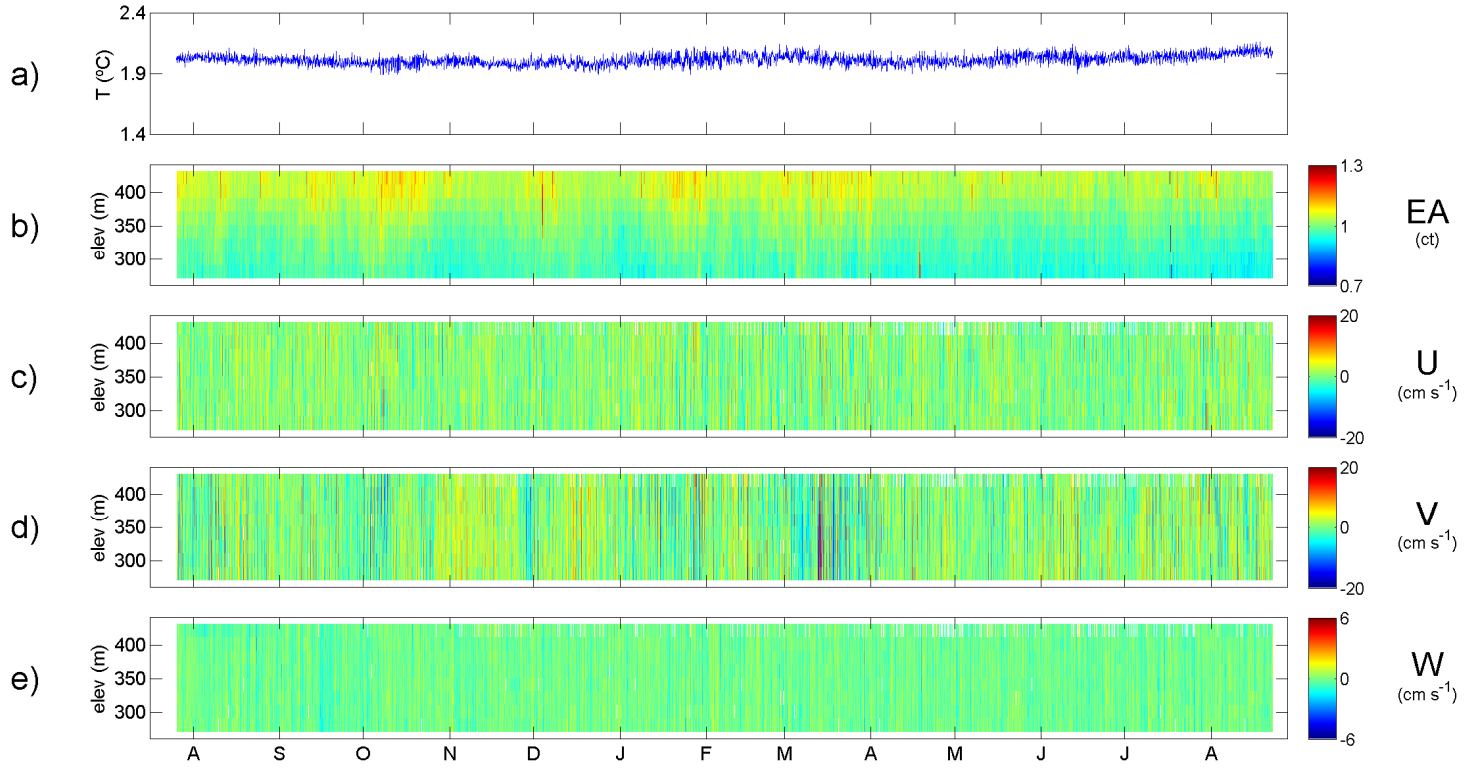

Figure 7. Time series of data collected at ADCP2.

5.3. ADCP3

Currents at ADCP3 were similar to that of ADCP2. Velocities were generally <10 cm s^{-1}, and oriented along the along-shore axis (NNW to SSE) (Fig 8).

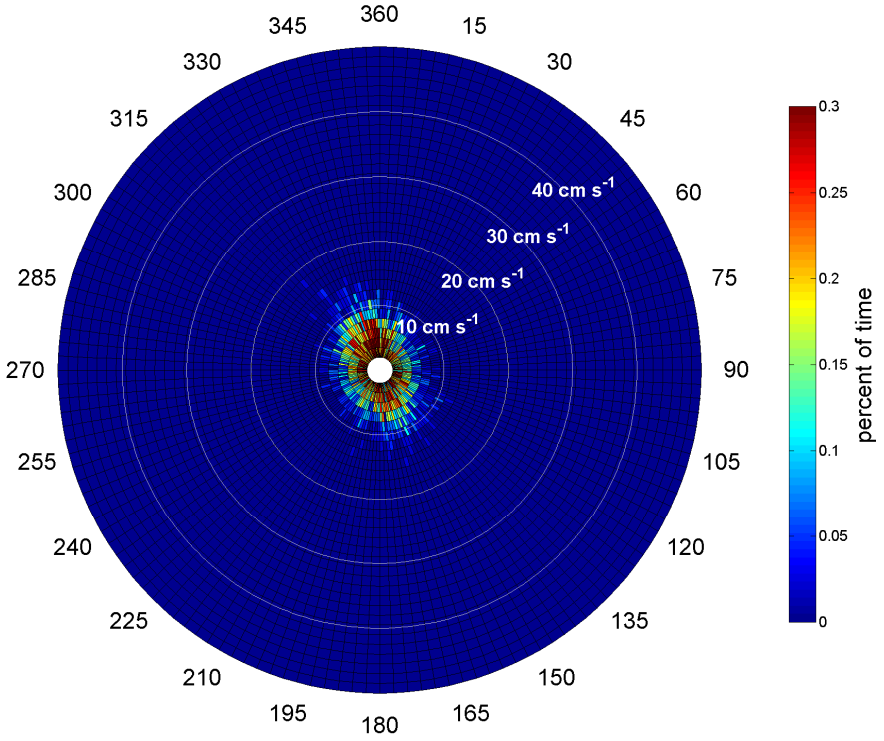

Figure 8. Histogram of current direction and magnitude for ADCP3.

Time series of data collected at ADCP3 are shown in Fig. 9.

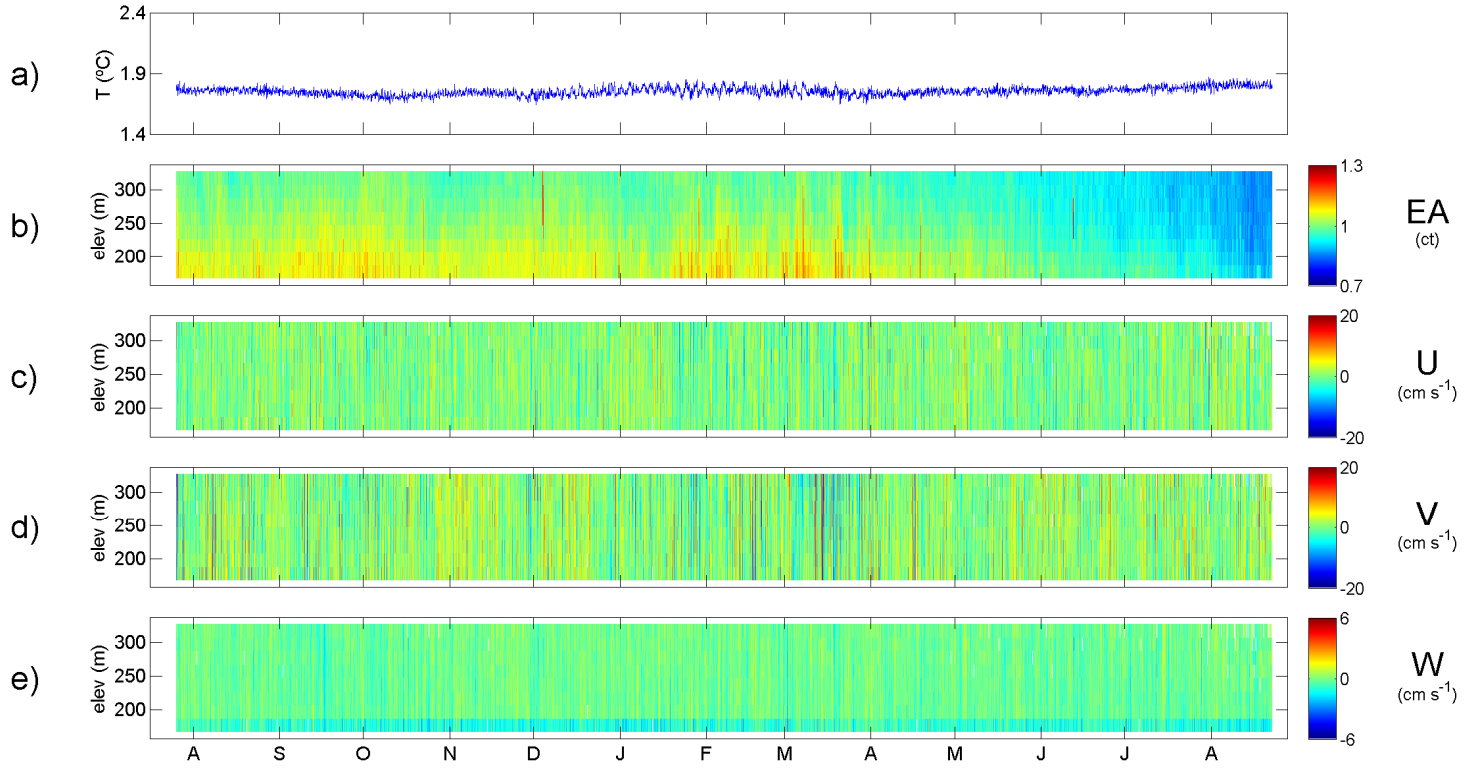

Figure 9. Time series of data collected at ADCP3.

5.4 ADCP4

Currents at ADCP4 were generally <10 cm s^{-1}, and of varying directionality, although there was a slight bias towards the along-shore axis (NNW to SSE) (Fig 10).

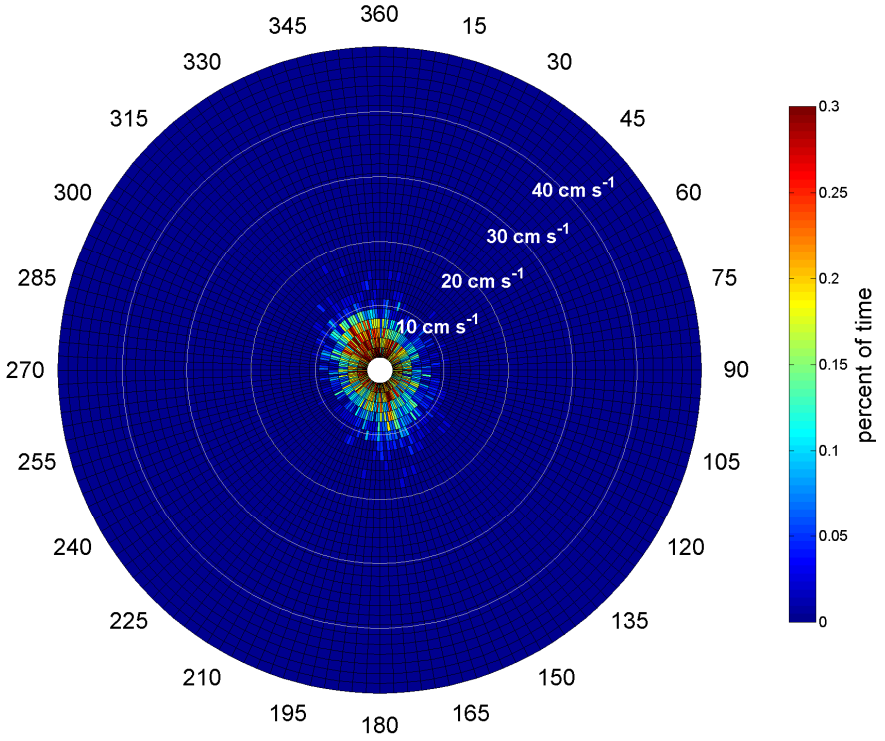

Figure 10. Histogram of current direction and magnitude for ADCP4.

Time series of data collected at ADCP4 are shown in Fig. 11.

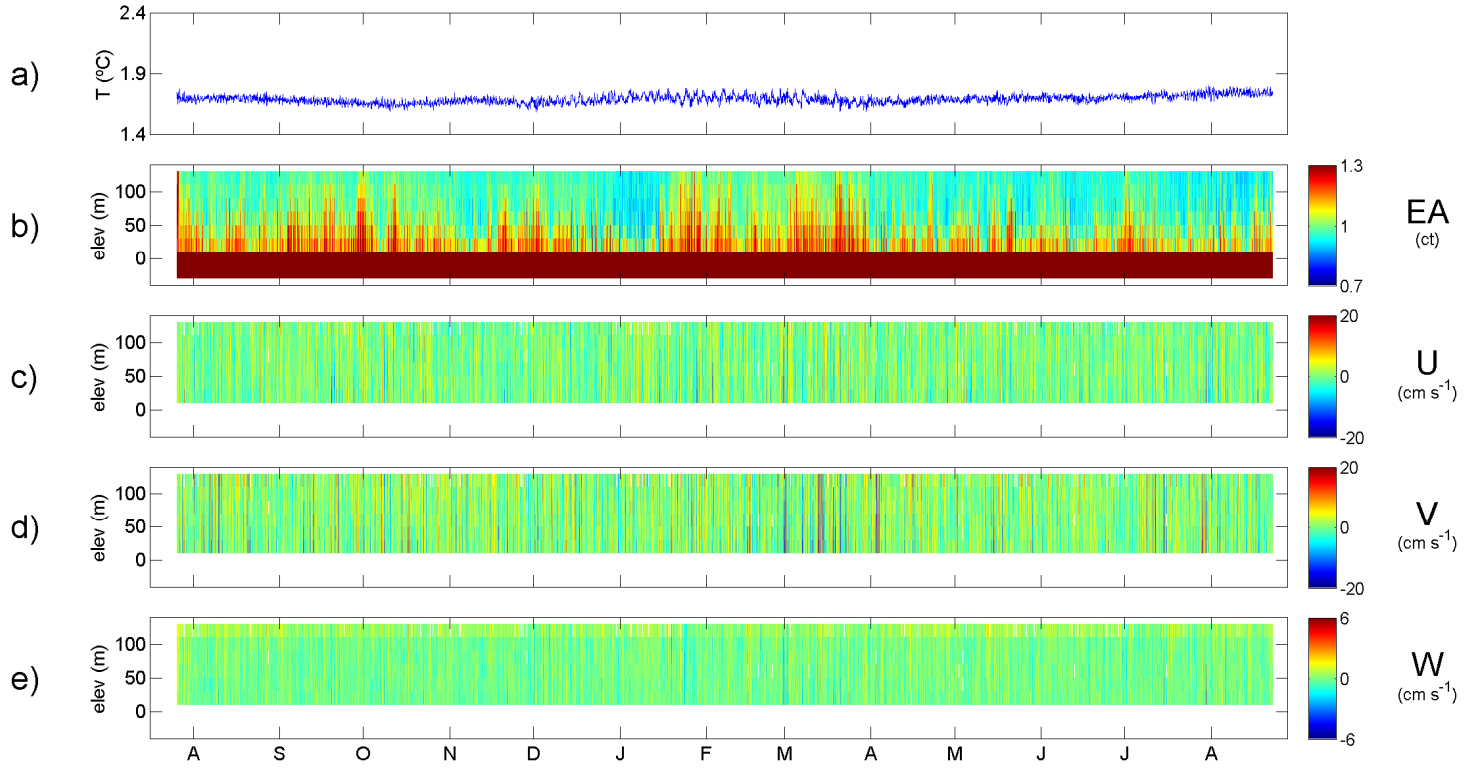

Figure 11. Time series of data collected at ADCP4.

5.5. ADCP5

Currents at ADCP5 were generally <15 cm s^{-1}, and of varying directionality, although there was a slight bias in the N to S direction (Fig 12).

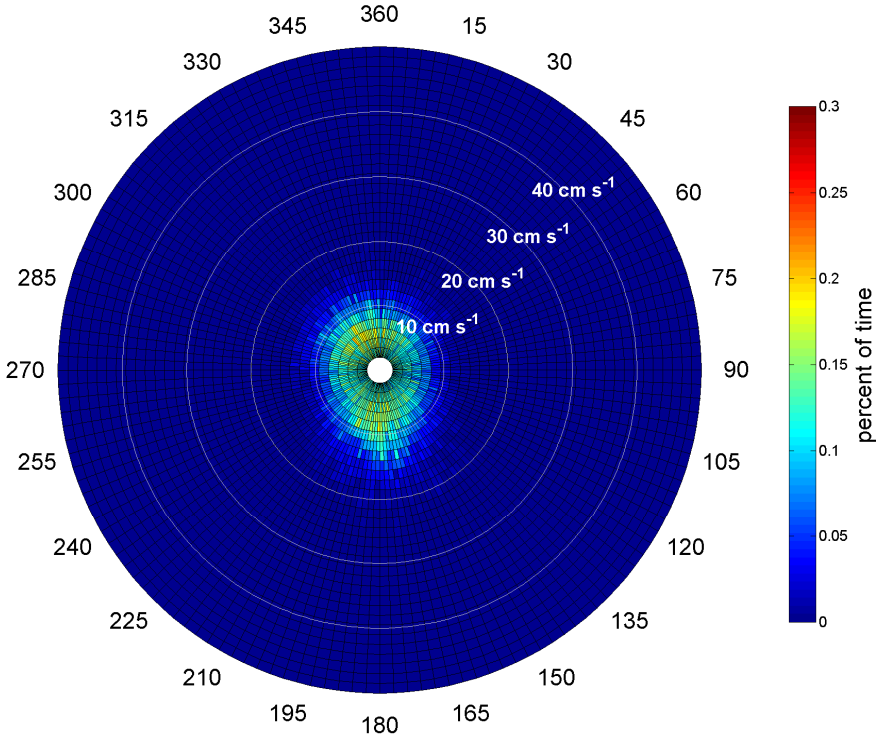

Figure 12. Histogram of current direction and magnitude for ADCP5.

Time series of data collected at ADCP5 are shown in Fig. 13.

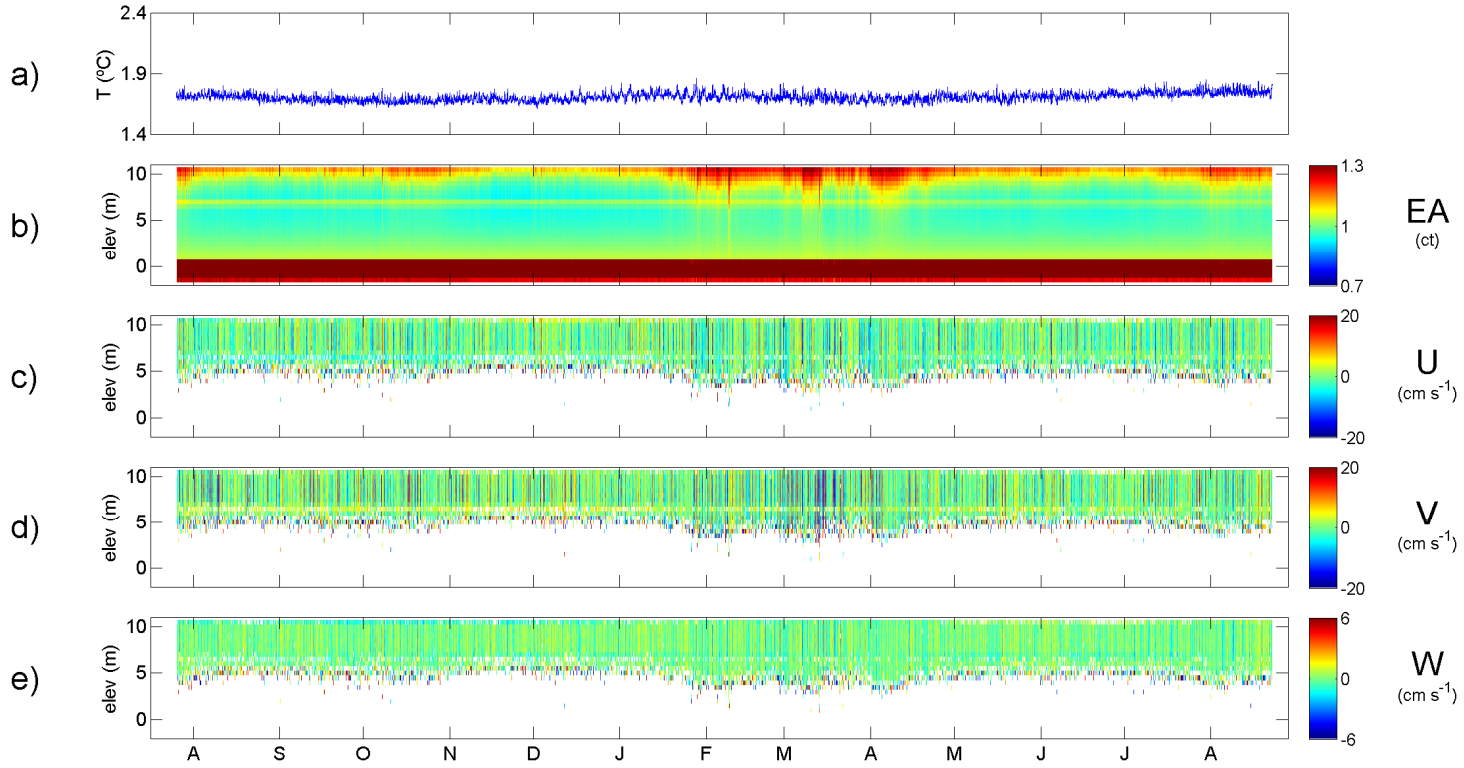

Figure 13. Time series of data collected at ADCP5.

5.6. ADCP6

Currents at ADCP6 were directed roughly equally to the NNW (between 320° and 350°) and to the SSE (between 135° and 160°). Current magnitudes at ADCP6 were the slowest of the four near-shore sensors, and were most often between 5 and 25 cm s^{-1} (Fig 14).

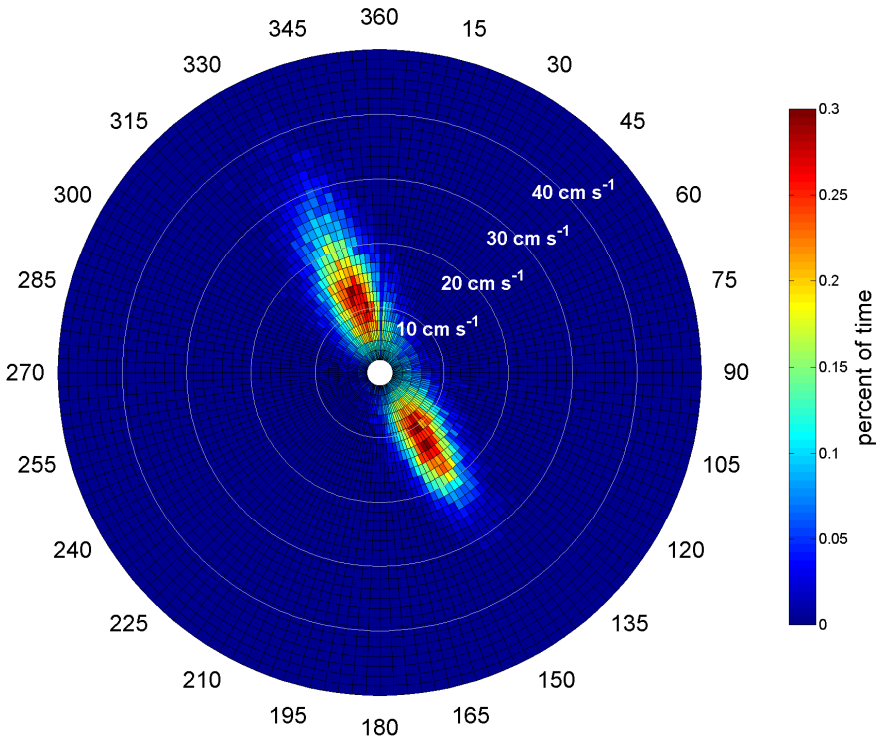

Figure 14. Histogram of current direction and magnitude for ADCP6.

Time series of data collected at ADCP6 are shown in Fig. 15.

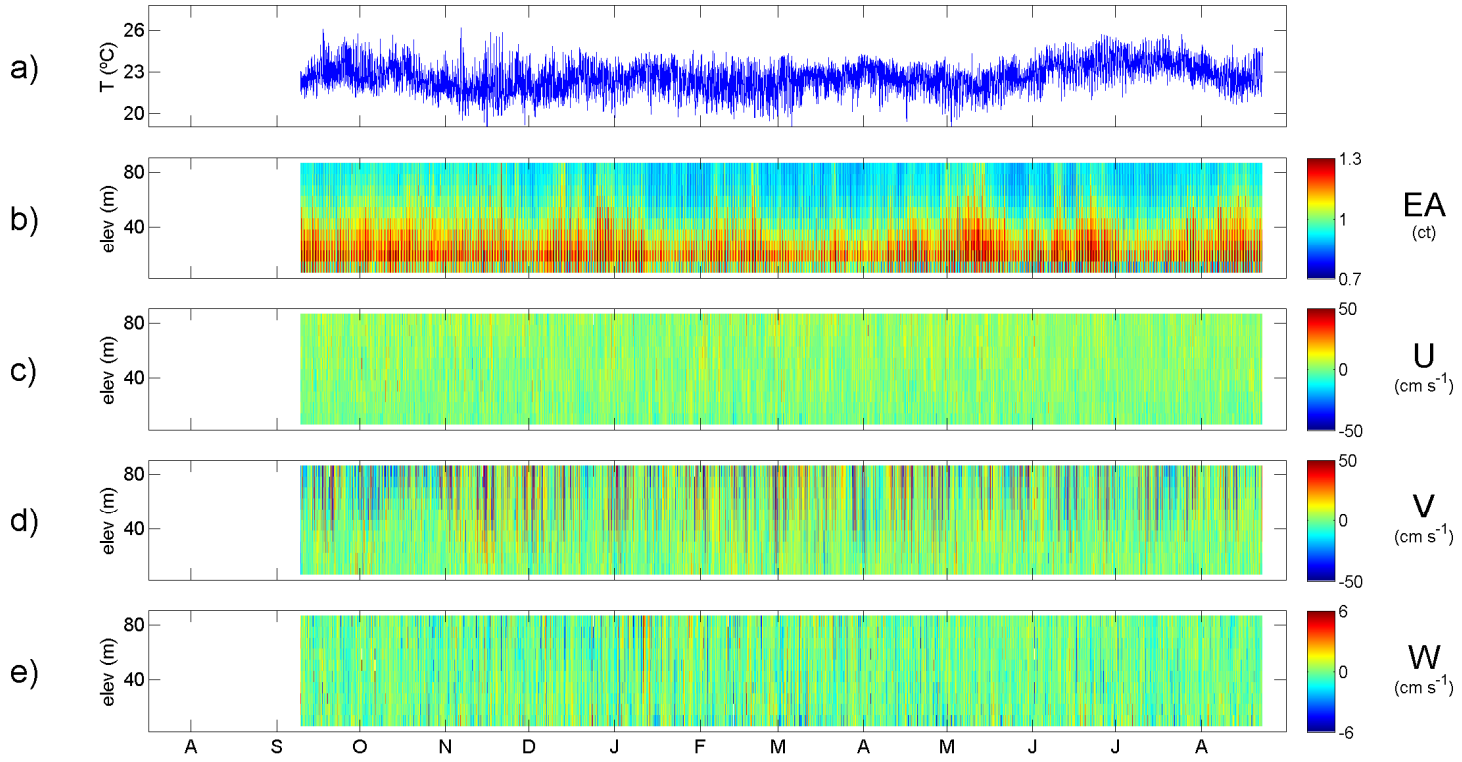

Figure 15. Time series of data collected at ADCP6.

5.7. ADCP7

Currents at ADCP7 were most often directed to the SSE (160° to 185°) but were occasionally directed to the NNW (345° to 5°). Current magnitudes were most often between 10 and 35 cm s^{-1} (Fig 16).

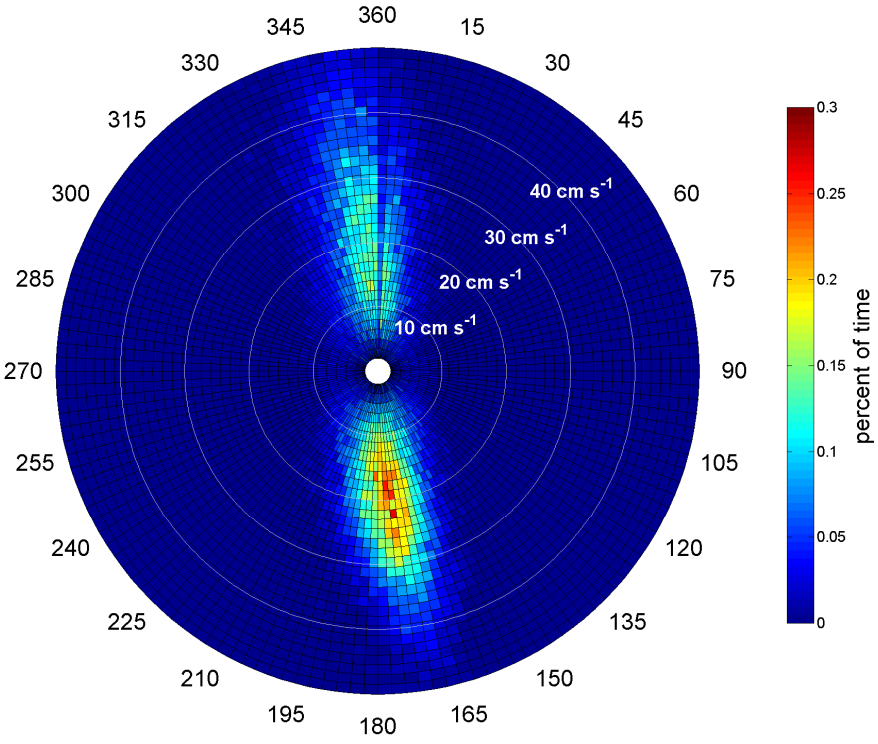

Figure 16. Histogram of current direction and magnitude for ADCP7.

Time series of data collected at ADCP7 are shown in Fig. 17.

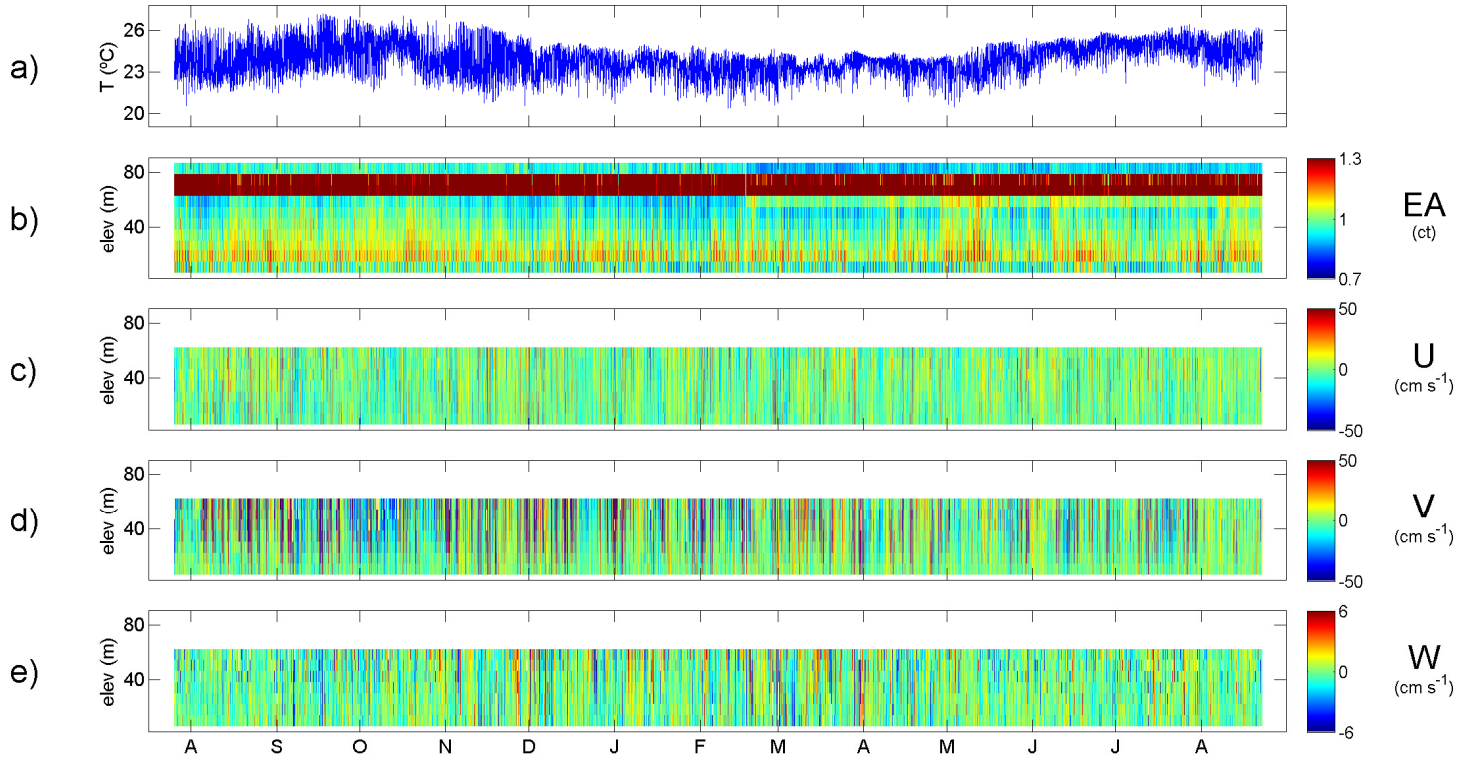

Figure 17. Time series of data collected at ADCP7.

5.8. ADCP8

The vast majority of currents at ADCP8 were directed to the SSE (150° to 180°). Current magnitudes were the fastest of the four near-shore ADCPs, and were most frequently between 15 and 50 cm s^{-1} (Fig 18).

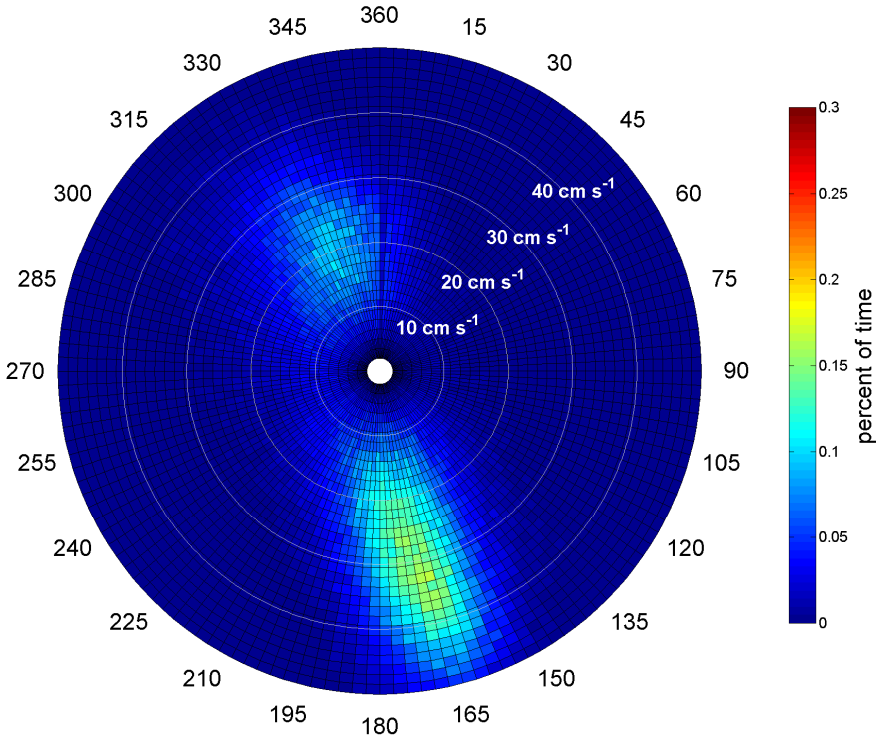

Figure 18. Histogram of current direction and magnitude for ADCP8.

Time series of data collected at ADCP8 are shown in Fig. 19.

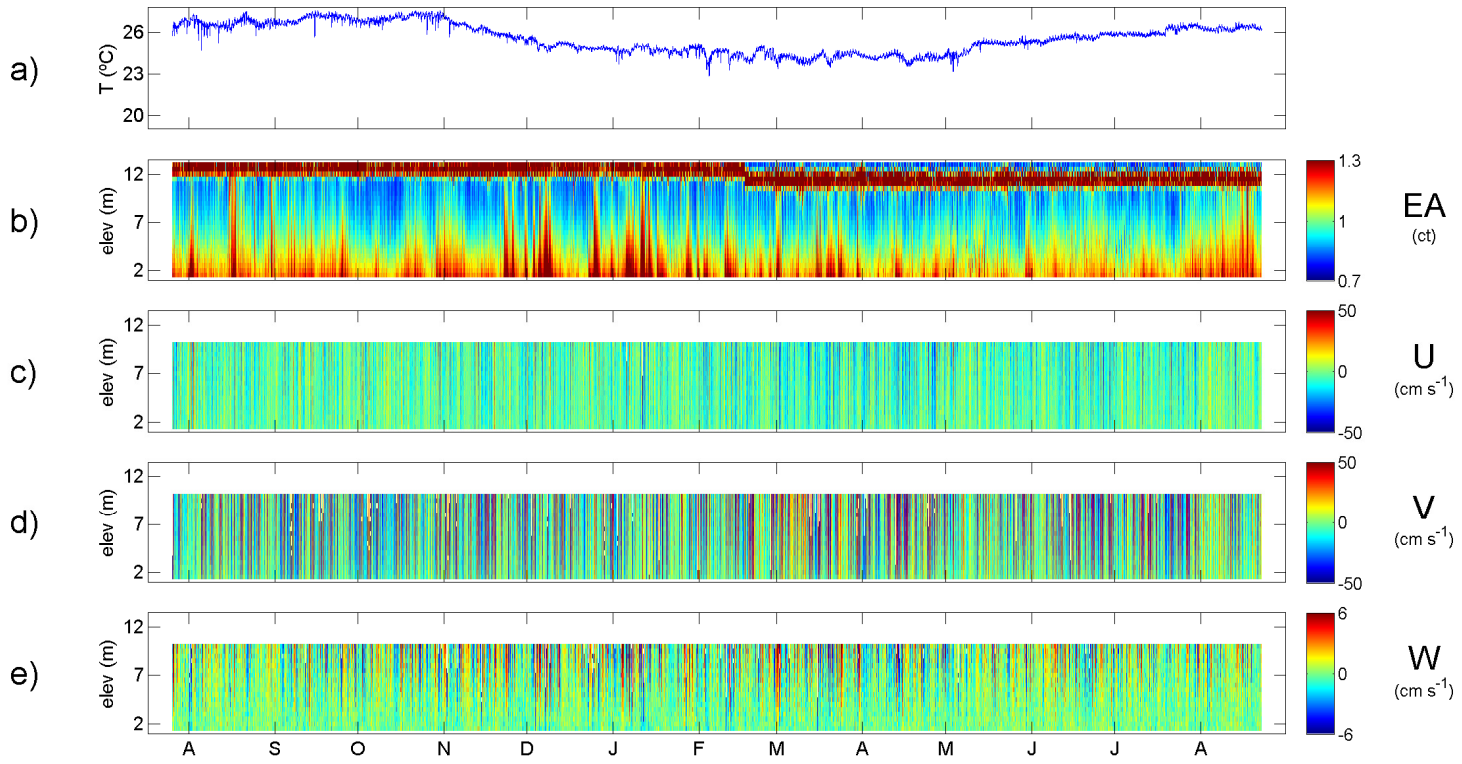

Figure 19. Time series of data collected at ADCP8.

5.9. ADCP9

Currents at ADCP9 were most often directed to the SSE (125° to 160°) but were occasionally directed to the NNW (320° to 345°). Current magnitudes were most often between 10 and 30 cm s^{-1} (Fig 20).

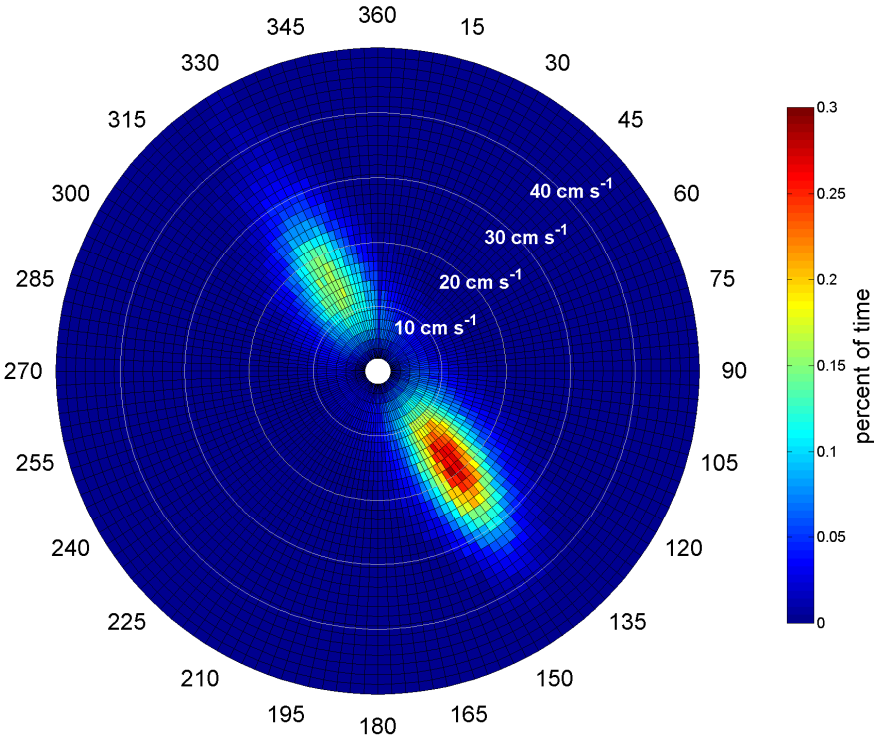

Figure 20. Histogram of current direction and magnitude for ADCP9.

Time series of data collected at ADCP9 are shown in Fig. 21.

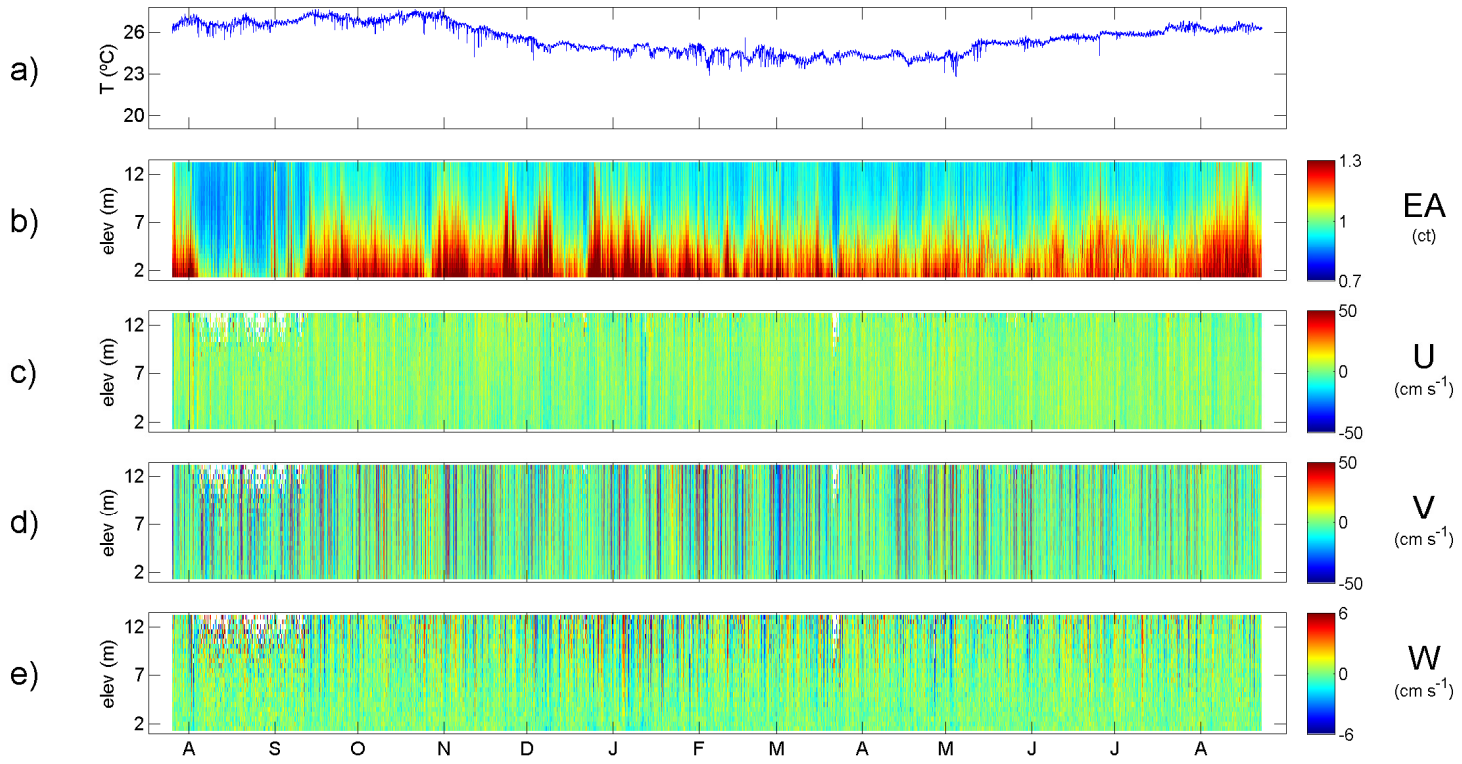

Figure 21. Time series of data collected at ADCP9.

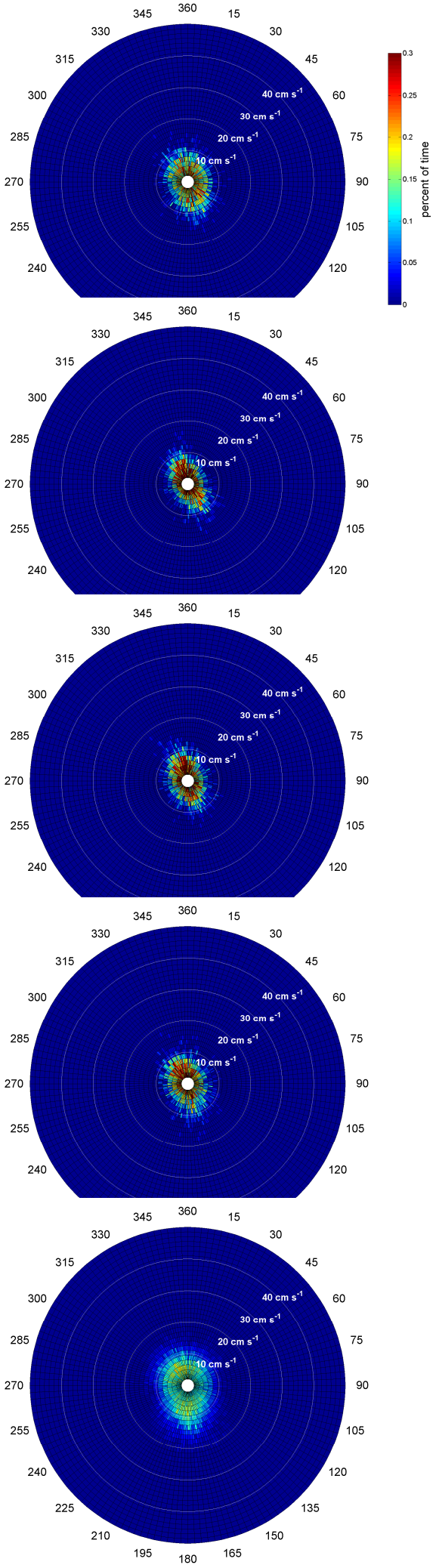

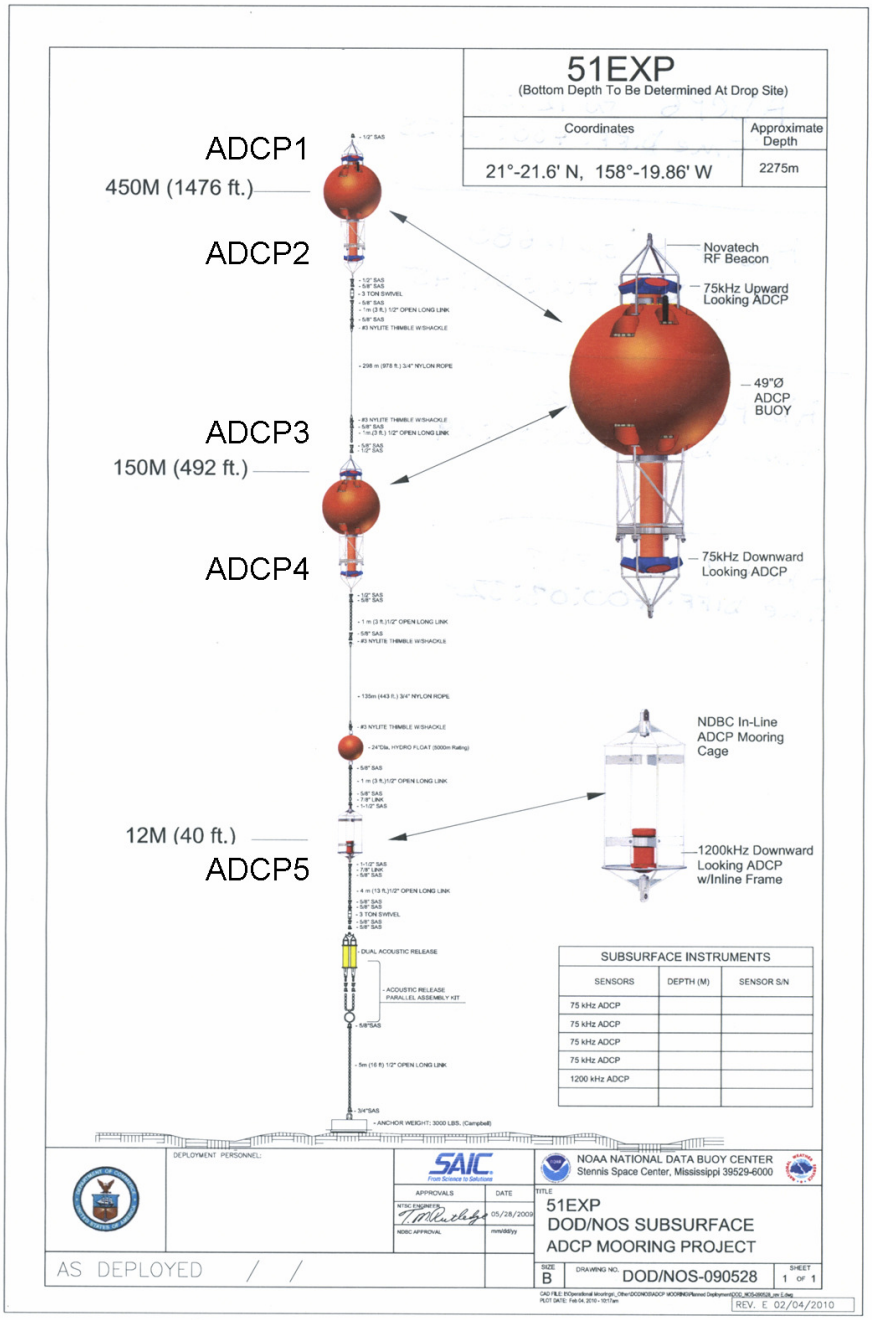

Figure 22. Summary of current directions and magnitudes for the five ADCPs on the deep string (ADCP1 [top] to ADCP5 [bottom]). Currents were most often between 2 - 8 cm s^{-1}. Directionality was varied, but exhibited a slight bias towards the along-shore axis (NNW to SSE).

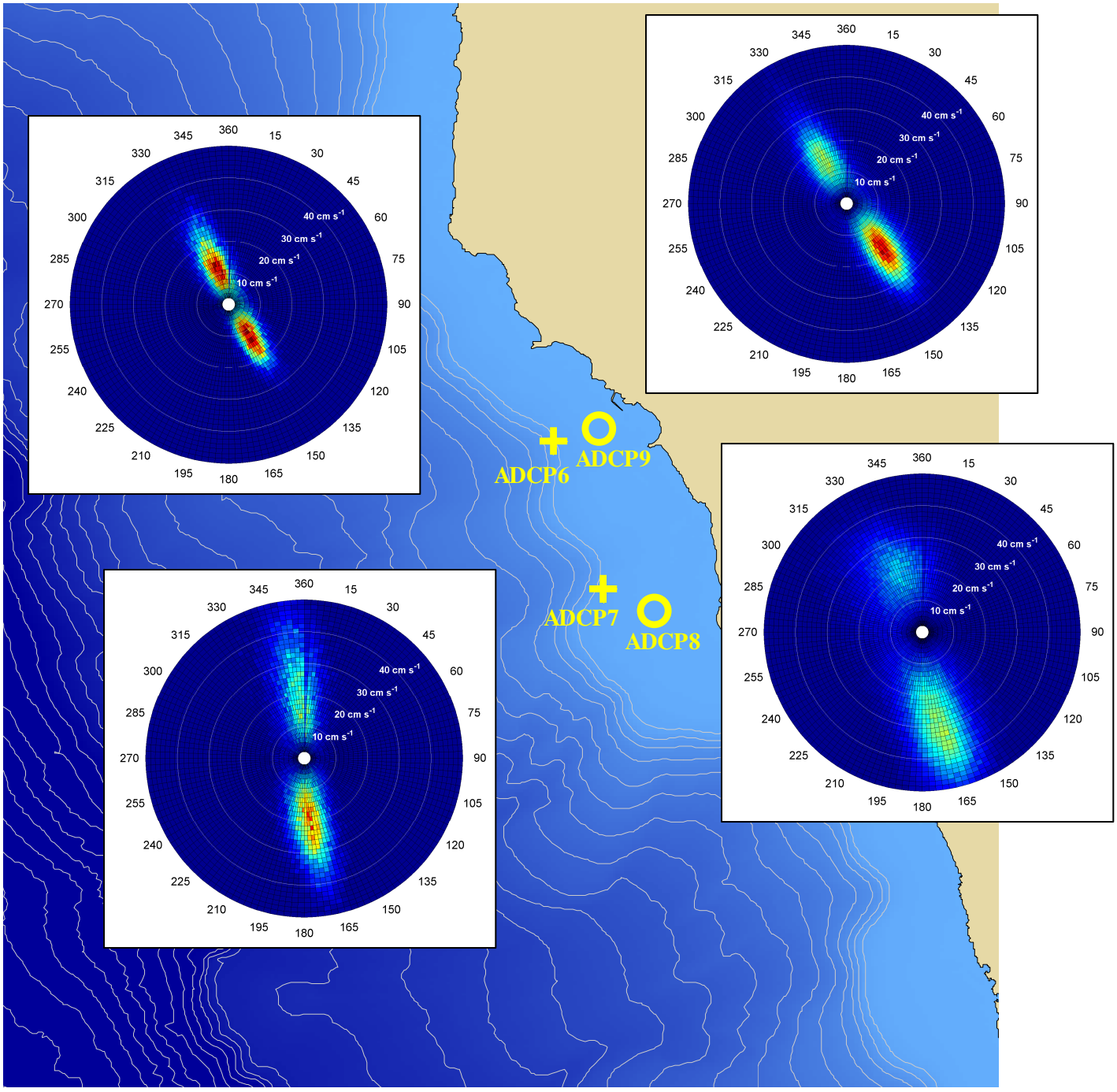

Figure 23. Summary of current directions and magnitudes for the four near-shore ADCPs. Currents were most often directed along isobaths.

6. References

1. Teledyne RD Instruments (2007) Workhorse Commands and Output Data Format. P/N 957-6156-00.

2. Teledyne RD Instruments (2006) Acoustic Doppler Current Profiler Principles of Operation: A Practical Primer. P/N 951-6069-00.

3. Deines KL (1999) Backscatter estimation using Broadband acoustic Doppler current profilers. Proceedings of the IEEE Sixth Working Conference on Current Measurement. San Diego, California.

4. Francois RE, Garrison GR (1982) Sound absorption based on ocean measurements: Part II: Boric acid contribution and equation for total absorption. J Acoust Soc Am 72(6)1879-1890.

Physicochemical Properties for Explosives at the Shallow Water Site Hawaii 6 (HI-06), O'ahu, Hawaii

June 2011

Prepared for:

National Oceanic and Atmospheric Administration

Contract GS10F0189T

noblis

3150 Fairview Park Drive South
Falls Church, Virginia 22042-4519

Executive Summary

This report provides physicochemical parameters that enable the determination of environmental fate of munitions constituents at the shallow disposal site Hawaii 6 (HI-06, known locally as Ordnance Reef) off the west coast of O'ahu near Wai'anae, Hawaii. The chemistry of these munitions constituents in a marine environment is presented within this report. The energetics addressed by this assessment include 2,4,6-trinitrotoluene (TNT), hexahydro-1,3,5-trinitro-1,3,5-triazine (RDX), octahydro-1,3,5,7-tetranitro-1,3,5,7-tetrazocine (HMX), ammonium picrate (Explosive D), and 2,4-dinitrotoluene (2,4-DNT). Although HMX has not been identified as an explosive at the site, it is included in the assessment due to its presence as an impurity in RDX.

The environmental fate of each munitions constituent is determined by a set of physical properties of the energetics as well as the physical properties of the marine environment. For the energetics, those properties include solubility, density, melting point, vapor pressure, Henry's Law constant, and partitioning coefficients. For the marine environment, physical parameters that determine the chemical fate of the energetics include temperature, pH, salinity, dissolved oxygen, and the ionic strength of seawater. All of these factors in combination determine whether the energetics will be found in the environment as a gas, liquid, or solid and to what extent each compound will react in the environment.

With the exception of Explosive D, all of these compounds are sparingly soluble in water and dissolve slowly into the marine environment. TNT, RDX, HMX, and 2,4-DNT are dense solids. Explosive D is a soluble salt and will readily dissolve into the water column.

Possible chemical reactions in a marine environment include hydrolysis, photolysis, thermolysis, and oxidation. With the exception of Explosive D, photolysis is the main mechanism for degradation of the dissolved energetic compounds. Photolysis reactions create a plethora of nitrogenous organic compounds for TNT and 2,4-DNT, both soluble and insoluble. The photolysis rate of reaction is enhanced for both of these compounds in the seawater (versus pure water) environment. RDX and HMX have very nearly identical photolysis products and full degradation leads to formaldehyde, nitrate, nitrite, and nitrous oxide.

Explosive D is a soluble salt also known as ammonium picrate. The salt dissolves and exists as ammonium and picrate ions. Picrate is the conjugate base of picric acid and will reside in the water column as such. Picric acid is not susceptible to hydrolysis or photolysis, but can be biotransformed to picramic acid. Both picric and picramic acid are toxic.

Explosive D will also react with the metal casing of the munitions to form metal picrates. Metal picrates do not possess the explosive force of ammonium picrate or picric acid. All metal picrates are shock sensitive and sensitivity increases with the size of the metal ion. Hydration desensitizes the compounds to explosion. Drying out metal picrates during the removal of munitions could increase their shock sensitivity creating an explosion hazard. If dried, they could potentially act as a primary ignition source for all the explosive remaining in a munition. Such an event would depend on many factors, including the composition of the munition hardware.

Several data gaps exist in the literature. For example, the larger polymerization photolysis products for TNT and 2,4-DNT have yet to be identified. An increase in the rate of photolysis of TNT and 2,4-DNT in seawater over a pure/fresh water environment has been reported, but reasons for this increase are speculative. There is also a large gap in the literature for RDX and HMX studies in seawater. Much work has been done in fresh/groundwater environments due to wastewater effluent from munition production plants, but there is little to no data in the literature regarding the effects of saltwater on solubility or dissolution and photolysis rates, which is also true for Explosive D studies in seawater. Most data presented in this paper for ammonium picrate were obtained from studies in a freshwater or laboratory environment.

Table of Contents

List of Figures

List of Tables

noblis

List of Acronyms

µg	microgram(s)
2,4-DNT	2,4-dinitrotoluene
2,6-DNT	2,6-dinitrotoluene
ADCP	Acoustic Doppler Current Profiler
atm	atmosphere
CDOM	chromophoric dissolved organic matter
cm	centimeter(s)
cm^2	square centimeter(s)
D	density
g	gram(s)
GC/MS	gas chromatograph/mass spectrometer
HMX	octahydro-1,3,5,7-tetranitro-1,3,5,7-tetrazocine
hr	hour(s)
I	ionic strength
k	rate constant
K_a	acid dissociation constant
K_H	Henry's Law constant
K_{oc}	organic carbon partition coefficient
K_{ow}	octanol water partition coefficient
K_s'	salting-out parameter
L	liter(s)
m	meter(s)
m^3	cubic meter(s)
mg	milligram(s)
mol	mole
nm	nanometer(s)
NOAA	National Oceanic and Atmospheric Administration
P	vapor pressure
ppt	precipitate
RDX	hexahydro-1,3,5-trinitro-1,3,5-triazine
S	solubility
S_s	solubility in salt solution
S_w	solubility in water solution
SSR	simulated solar radiation
TNT	2,4,6-trinitrotoluene
TOC	total organic carbon
UV	ultraviolet
WWTP	Wastewater Treatment Plant

1 Introduction

This report documents Noblis' effort to provide environmental fate information regarding the munitions constituents likely to exist in World War II munitions at the shallow disposal site Hawaii 6 (HI-06 known locally as Ordnance Reef) off the west coast of O'ahu near Wai'anae, Hawaii. The energetic munitions constituents identified as important by National Oceanic and Atmospheric Administration (NOAA) include 2,4,6-trinitrotoluene (TNT), hexahydro-1,3,5-trinitro-1,3,5-triazine (RDX), octahydro-1,3,5,7-tetranitro-1,3,5,7-tetrazocine (HMX), ammonium picrate (Explosive D), and 2,4-dinitrotoluene (2,4-DNT). Although HMX was not identified as an explosive at the site, it is included in the assessment due to its presence as an impurity in RDX.

1.1 Background

The Office of Response and Restoration and the Office of National Marine Sanctuaries of the NOAA are conducting an assessment of conditions relevant to the fate and transport of energetic munitions constituents in Hawaiian waters.[1] This assessment addresses several energetic munitions constituents from conventional munitions that were disposed in a shallow water site west of the community of Wai'anae on the Hawaiian island O'ahu. In support of this assessment, Noblis was contracted to survey the existing data on the fate and transport of a subset of munitions constituents likely to be present at the site.

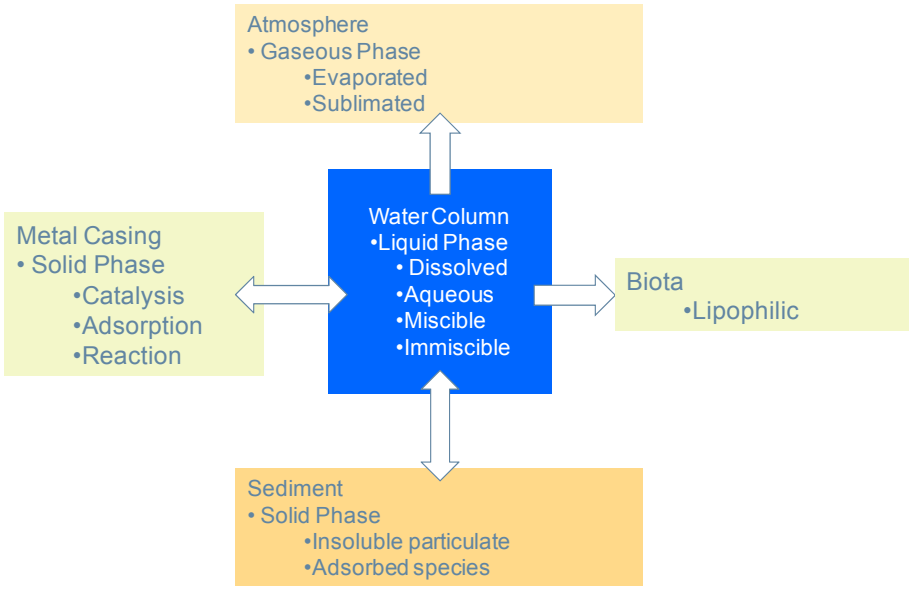

Figure 1-1. Possible Residences of Munitions Constituents in a Marine Environment

1.2 Environmental Residence

The possible residences of the munitions constituents in a marine environment are represented in Figure 1-1 and are first determined by the phase of the munitions constituent; i.e., whether it is solid, liquid, or gas. Liquid phase will be found in the water column as a dissolved constituent in the aqueous phase or as a miscible or immiscible liquid. Solid munitions constituents could be found as insoluble particulate on the ocean floor, adsorbed species in sediment or particulate in the water column, or still within metal casing that may provide a surface for reaction with the encased metal. If a chemical has the ability to reach the surface, i.e., if it has a density less than water, it may evaporate or sublimate depending on its vapor pressure at atmospheric pressure and temperature. Finally, a chemical in a marine environment may also be found to accumulate in biota, depending on the solubility of the substance in a fatty tissue.

To determine in which environmental compartment shown in **Figure 1-1** that each compound resides, chemical parameters of both the marine environment and the energetics themselves must be considered. For the marine environment, water temperature, salinity, pH, dissolved oxygen, and ionic strength are all factors that determine chemical fate. For the energetic compounds, solubility (S), density (D), vapor pressure (P), Henry's Law constant (K_H), the partition coefficient between total organic carbon (TOC) and water (K_{oc}), and the partition coefficient between octanol and water (K_{ow}) are all used to determine where a compound will reside. Once this is determined, the chemistry in that environment can be ascertained.

NOAA collected site-specific data from July 2009 to August 2010 from four sites that bound the Ordnance Reef using Acoustic Doppler Current Profilers (ADCPs). The ADCPs were equipped to measure current velocity, temperature, depth, and salinity. Two of the sites were 15 meters (m) deep and two were 88 m deep. The temperature of the four sites at depth varied from 23–26°C over the course of the data collection. The practical salinity value will be used to estimate the ionic strength of ions in solution. The practical salinity value measured at the four sites had a range of 34.8–35.1. From measurements made in 2006, the pH was consistent throughout the water column at a value of 8.12. The only exception was for measurements made at Station WO, which was measured throughout the column at 8.18. These differences were explained in the March 2007 report[1] as due to two possibilities: (1) an influence of the Wai'anae Wastewater Treatment Plant (WWTP) outflow or (2) an artifact of the accuracy of the pH probes used for measurement. Although TOC in the sediment is likely very low, measurements would give an indication of explosives in sediment.

Several physical and chemical parameters are necessary to determine the fate and transport of the energetics in a marine environment such as Wai'anae. Boiling and melting points determine the initial physical state of a chemical while density determines whether undissolved compounds will rise or sink in the water column. Vapor pressure, solubility, Henry's Law constant, and partition coefficients are important parameters for determining the phases and matrices in which the chemical resides and is transported. K_{ow} is also used to determine whether an agent bioaccumulates in the food chain. Acid dissociation constants (K_a) determine the form that agents with acidic or basic character exist in a marine environment. Rate constants (k) for dissolution and reactions such as hydrolysis, photolysis, oxidation, and thermolysis determine the

lifetime of an agent and its degradation products and therefore are key in the full determination of the fate of each compound under consideration.

2 Chemistry of Explosives in Seawater

The main chemical reactions that occur in a marine environment that must be considered in the degradation of compounds include hydrolysis, oxidation, thermolysis, and photolysis. For hydrolysis, the solubility and rate of dissolution of a compound determines how fast a molecule can undergo this reaction. If the compound is insoluble or sparingly soluble, a hydrolysis reaction may be minimal due to the fact that it will not go into the liquid phase fast enough to ever have significant concentration to undergo hydrolysis. Oxidation and thermolysis reactions for most of the explosives considered here are unlikely. For oxidation reactions, the alkaline environment favors hydrolysis. As for thermolysis, these compounds are thermally stable at ocean temperatures. Photolysis reactions are the main chemical mechanism for degradation of several nitrogen-based explosives. The factors affecting the rate and extent of these reactions will be the wavelengths that cause this chemistry and the photon density at the depth of the munition.

2.1 TNT

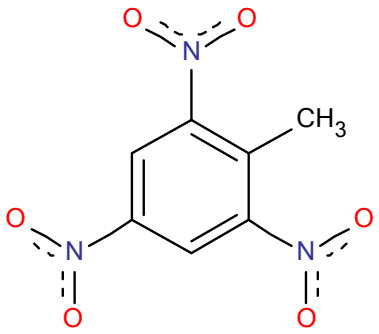

Figure 2-1. 2,4,6-Trinitrotoluene (TNT)

The molecular formula for 2,4,6-trinitrotoluene (TNT) is $C_7H_5N_3O_6$ with a corresponding molecular weight of 227.1 grams (g)/mole (mol). **Figure 2-1** shows the molecular structure. At room temperature, TNT is a yellow solid that is slightly soluble in water. The melting point and boiling point are 80.7 °C and 210 °C, respectively.[2] **Table 2.1** lists some of the physical properties that can be used to determine the environmental fate of TNT in a marine environment.[2-11]

Table 2-1. Physical Properties of TNT[2-11]

Physical Properties of TNT		Reference
Solubility at 25 °C in Sea Water	94.4 mg/L	Hoffsommer [3]
Density	1.654 g/ml	Yinon [2], Meyer[5]
Henry's Law Constant, K_H, 20 °C	4.57×10^{-7} atm m^3/mol	Brannon [4], Lyman [6]
Vapor Pressure, 25 C	5.8×10^{-6} torr	Yinon [2], Dionne [7]
Log K_{oc}	2.48 – 3.2	Brannon [4], Spanggord [8]
Log K_{ow}	1.6 - 1.99	Hansch [9], Leggett [10] Claussen [11]

The solubility of TNT in seawater at 25 °C is 94.4 milligrams per liter (mg/L), which is less that the its solubility in fresh water.[3] The equilibrium solubility of TNT in seawater has also been

determined as a function of ionic strength (I) and temperature (T).[12] The equilibrium solubility as a function of temperature in pure water is:

$$C[TNT] = 50.3e^{0.0403T}$$ **Equation 2.1**[12]

where C is the concentration of TNT in mg/L and

T is the temperature in °C.

The solubility of TNT is lower in seawater due to the salt, and can be described by the equation:

$$\log\frac{Sw}{S} = Ks'I$$ **Equation 2.2**[12]

where S_w is the solubility in pure water,

S is the solubility in a salt solution,

K_s' is the salting-out parameter, and

I is the ionic strength.

The salting-out parameter for TNT was determined to be 0.12 ± 0.02 L/mol. This parameter does not vary greatly with temperature. Finally, the equation for 100% seawater as a function of temperature is:

$$C[TNT] = 45.9\ e^{0.0352T}$$ **Equation 2.3**[12]

However, for HI-06, the temperature measured at the ocean floor during data collection varied between 23–26 °C, so the solubility reported for 25 °C should be an appropriate value for use in the NOAA model.

Because the density of TNT is greater than water, the solid will sink in the water column and reside on the ocean floor. The vapor pressure and K_H for TNT are very low, so gas-phase TNT will be negligible to non-existent. The log K_{oc} and K_{ow} are calculated estimates, but are numbers that indicate moderate partitioning into organic carbon and octanol. However, TOC in Wai'anae sediment is very low.[1] The dissolution rate has been measured to be r = 4.6 mg per square centimeter per hour (mg/cm^2/hr),[13] a release rate dependent on the surface area of TNT exposed to the water column for further breakdown by hydrolysis in a seawater environment. Those hydrolysis products are shown in **Figure 2.2** and include dinitrocresols and dinitrophenols that will precipitate (ppt) as salts, and picric acid, which is soluble.

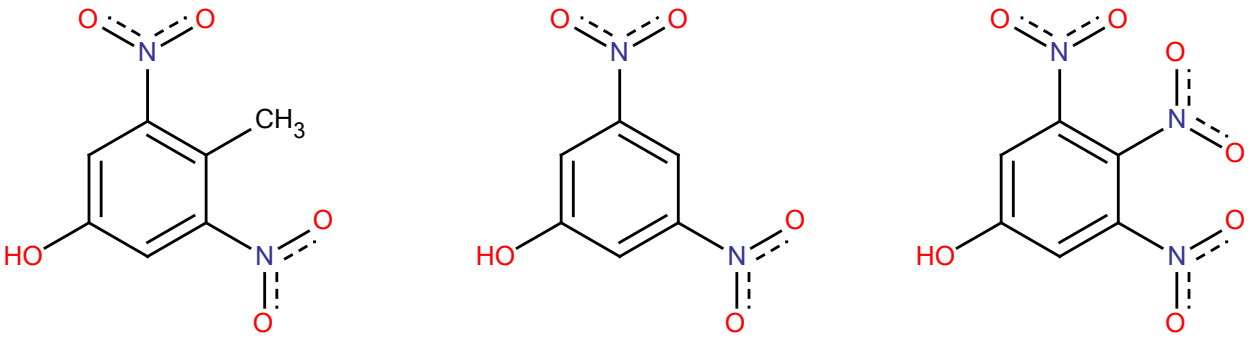

Figure 2-2. Hydrolysis Products of TNT

The picric acid has an acid-base dissociation constant $K_a = 0.38$, meaning it is present almost exclusively as the anionic form at a pH of ~8.1. The dinitrocresols and dinitrophenols have a density greater than water and will sink in the water column. It is of note, however, that hydrolysis rates have not been measured at a pH similar to seawater. This is due to the fact that TNT does not hydrolyze to any great extent at this pH. Alkaline hydrolysis is reported at pH ≥ 10.[14]

Photolysis of TNT in natural sunlight causes a color change to red or pink in an aqueous environment. Photodecomposition mechanisms have been shown to be more rapid at the higher pH of river water than in distilled water. However, the rate has been suggested to be more dependent on the natural substances in the water than the pH.[15] Phototransformation products that have been identified from irradiation of TNT in an aqueous environment in a laboratory are listed in **Table 2.2**.[4,16-18] The photodecomposition products identified in these laboratory experiments were both aqueous and precipitate, 45–50% of which were recovered in solution. The precipitate is postulated to be oligmers of azo and azoxy compounds.[15]

Table 2-2. Photodecomposition Products of TNT[4,16-18]

Phototransformation Products of TNT
1,3,5-trinitrobenzene
2,4,6-trinitrobenzaldehyde
2,4,6-trinitrobenzonitrile
2,2',6,6'-tetranitro-4,4'-azoxytoluene
4,4',6,6'-tetranitro-2,2'-azoxytoluene
2',4-dimethyl-3,3'5,5'-tetranitro-ONN-azoxybenzene
2,4'-dimethyl-3,3'5,5'-tetranitro-ONN-azoxybenzene
2,4-dinitroisoanthranil
2,2'-dicarboxy-3,3',5,5'-tetranitroazobenzene
2-dicarboxy-3,3',5,5'-tetranitro-NNO-azoxybenzene
2-amino-4,6-dinitrobenzoic acid
Syn-2.4.6-trinitrobenzaldoxime
2,4,6-trinitrobenzyl alcohol
3,5-dinitrophenol
2,2'-dicarboxy-3,3',5,5'-tetranitroazoxybenzene
2,4,6-trinitrobenzoic acid
N-(2-carboxy-3,5-dinitrophenyl)-2,4,6-trinitrobenzamide
4,6-dinitro-1,2-benzisoxazole
4,6-dinitro-2,1-benzisoxazole

The rate of photolysis in the environment is dependent on atmospheric conditions such as seasonal variation in solar radiation and concentrations of chromophoric dissolved organic matter (CDOM). Marine ecosystems at subtropical latitudes have low amounts of CDOM. Sunlight attenuation has been measured off the coast of O'ahu and the effective photic zone depth extends up to 40 m, which was the limit of detection of the radiometer used for the measurement. In laboratory experiments where simulated solar radiation (SSR) at approximately 2.5–3 times the intensity of clear sky conditions at noon at 39°N was used, the loss of TNT fit first order kinetics with r^2 >0.9. In seawater, the half-life of TNT under these conditions was 69 minutes, whereas for pure water the half-life was measured to be 770 minutes.[19]

The rate of photolysis of TNT has been measured in laboratories in pure, fresh, estuarine, and seawater.[19] The rate decreased in the following order: seawater > estuarine > fresh > pure. The direct photolysis of TNT in a dilute aqueous solution can be described by the following equation:

$$\frac{-d[TNT]}{dt} = k_{obs}[TNT] = 2.303\varphi_{\lambda} I_{o\lambda} \epsilon_{\lambda} l[\text{TNT}] \qquad \textbf{Equation 2.4}$$

where φ_{λ} is the quantum yield,

$I_{o\lambda}$ is the incident light intensity,

ϵ_{λ} is the molar absorptivity, and

l is the path length.

Nitroaromatic compounds absorb electromagnetic radiation in the ultraviolet (UV) range from 200–400 nanometers (nm), but the environmentally relevant wavelength range is 290–400 nm. The molar absorptivity of TNT is dependent on the solvent/solution in which it is dissolved. In pure water, the molar absorptivity was measured to be 1450 ± 30 $M^{-1}cm^{-1}$ at 300 nm. As the ionic strength is increased from pure water to seawater, the molar absorptivity decreases for TNT. At a salinity of 34 and an ionic strength of 0.68 (an ionic strength value consistent with the complex mixture of salts in seawater), the molar absorptivity has been measured in laboratory experiments at a value of 1,290 $M^{-1}cm^{-1}$ at 300 nm.[19] However, the photolysis rate of TNT increases from pure water to seawater and this increase is not accounted for by the decrease in molar absorptivity. Studies have shown that the presence of oxidizing agents and catalysts can increase degradation of TNT with sunlight through secondary photochemical processes.[20-25] Species such as hydrogen peroxide, nitrate, and dissolved organic matter are all contained in seawater and have the ability to produce hydroxyl radicals to provide an oxidation pathway with UV photolysis.[26]

2.2 RDX

The molecular formula for hexahydro-1,3,5-trinitro-1,3,5-triazine (RDX) is $C_3N_6O_6H_6$ and has a molecular weight of 222.15 g/mol. See **Figure 2-3** for the molecular structure of RDX. At room temperature, RDX is a colorless solid that is very sparingly soluble in water. The melting point and boiling point of RDX is 205.5°C and 234°C, respectively. **Table 2.3** lists some of the physical properties that can be used to determine the environmental fate of RDX in a marine environment.

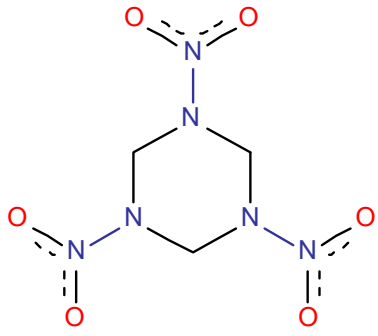

Figure 2-3. Hexahydro-1,3,5-trinitro-1,3,5-triazine (RDX)

The equilibrium solubility of RDX in seawater at 25 °C has been measured to be 55.6 mg/L,[3] almost half of that of TNT by mass. The density of RDX is 1.82 g/ml, nearly twice that of water. The vapor pressure for RDX is 4.1×10^{-9} torr, which is three orders of magnitude lower than that of TNT. The K_H for

Table 2-3. Physical Properties of RDX[2-4,27]

Physical Properties of RDX		References
Solubility at 25 °C in Seawater	55.6 mg/L	Hoffsommer [3]
Density	1.82 g/ml	Yinon [2]
Henry's Law Constant, K_H, 25 °C	1.96×10^{-11} atm m^3/mol	Brannon [4]
Vapor Pressure	4.1×10^{-9} torr	Yinon [2]
Log K_{oc}	2.00	Rosenblatt [27]
Log K_{ow}	0.87	Rosenblatt [27]

RDX is also extremely low, four orders of magnitude less than that of TNT, so gas-phase RDX will be negligible. The log K_{oc} is 2.00 and indicates that moderate partitioning into organic carbon will occur. However, the log K_{ow} value is very low such that almost no partitioning into a non-polar substance will occur. With all physical factors of RDX taken into account, it is a compound that will reside on the sea floor as a solid with dissolution into the water column over time.

The dissolution rate of RDX into an aqueous solution has been measured to be r = 361 micrograms (µg)/cm^2/hr,[13] which is a rate dependent on the particle size, or more specifically the surface area of RDX that comes into contact with the water column. Once dissolved into the water column, hydrolysis or photolysis can occur.

There are conflicting reports on the hydrolysis of RDX in seawater. One laboratory study reported an 11% decrease in RDX after 112 days in seawater.[3] However, no products were identified. Other studies have reported hydrolysis half-lives of 170 days to several years in seawater, indicating that it is not a significant fate mechanism.[8,29]

RDX undergoes photolysis as the main transformation process. The resulting transformation products have been reported to include azoxy compounds, ammonia, formaldehyde, nitrate, nitrite, nitrous oxide, and N-nitroso-methylenediamine.[30] The rate of photolytic degradation of RDX has been measured in Holston River water in depths ranging from 0–300 cm,[28] and could be described by the first-order rate equation:

Table 2-4. Photolytic Degradation Rates for RDX in Summer in Holston River Water [28]

Depth, cm	Rate constant, k (day^{-1})
0	0.94
50	0.32
100	0.18
150	0.12
200	0.089
250	0.072
300	0.060

$$\ln C = \ln C_0 - kt \qquad \textbf{Equation 2.5}$$

Where C_0 (mg/L) is the initial concentration,

k (time^{-1}) is the degradation constant,

t is time, and

C (mg/L) is the concentration at time t.

The degradation rate constants were measured as a function of season and depth and the results for summer are shown in **Table 2.4**,[28] as they are most likely representative of the temperatures and light intensity of the climate of Wai'anae. There are no data in the literature on the effect of ionic strength or salinity on the rate of photolysis for RDX.

2.3 HMX

Octahydro-1,3,5,7-tetranitro-1,3,5,7-tetrazocine (HMX) is a colorless polycrystalline solid with a molecular formula of $C_4H_8N_8O_8$ and a molecular weight of 296.20 g/mol. See **Figure 2-4** for the molecular structure of HMX. HMX has a melting point range of 276–286°C, depending on the purity. HMX exists in four polymorphic forms: α, β, γ, and δ. The β form of HMX is the least sensitive to impact, and the most preferred for use as a high explosive.

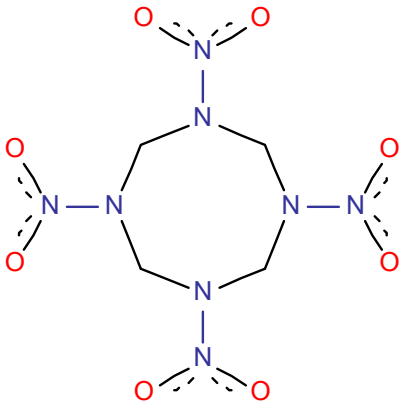

Figure 2-4. Octahydro-1,3,5,7-tetranitro-1,3,5,7-tetrazocine (HMX)

Some common physical properties of HMX are listed in **Table 2.5**. The equilibrium solubility of HMX is 3.3 mg/L, even less soluble than RDX and TNT by an order of magnitude. HMX is the densest of all the explosives discussed with a value of 1.96 g/ml, so the solid will sink in the water

Table 2-5. Physical Properties of HMX[2,4,27]

Physical Properties of HMX		References
Solubility at 25 °C	3.3 mg/L	Brannon [4]
Density	1.96 g/ml	Yinon [2]
Henry's Law Constant, K_H, 20 °C	2.6×10^{-15} atm m^3/mol	Brannon [4]
Vapor Pressure	3.3×10^{-14} torr	Yinon [2]
Log K_{oc}	0.54	Rosenblatt [27]
Log K_{ow}	0.19	Rosenblatt [27]

column. The vapor pressure and K_H are on the order of 10^{-14} and 10^{-15} at 20 °C, respectively, so gas-phase explosive is not a consideration in this environment.

The dissolution rate for HMX is reported for an aqueous solution to be r = 702 µg/cm^2/hr.[13] Again, the rate is dependent on the surface area of explosive that is exposed to the seawater, and therefore the particle size of the explosive as well as the size of the aperture in a damaged or corroded munition.

Although HMX is much less soluble than RDX, their chemistries in seawater are very similar. HMX does not hydrolyze to any extent at pH 8, and its main chemical transformation mechanism is photolysis. The rate and products for this mechanism has only been reported for Holston River water, with similar results to those of RDX in identical experiments. The photolysis rate can be described by **Equation 2.5.** The rate constants determined for HMX in river water in summer are shown in **Table 2.6**.[28] The resulting transformation products are identical to those from RDX: azoxy compounds, ammonia, formaldehyde, nitrate, nitrite, nitrous oxide, and N-nitroso-methylenediamine. In comparing the rate constants for the identical experiment with RDX, the constants for HMX are much smaller. The literature suggests this is due to a larger molar absorptivity for RDX; however, there were no absorptivity values determined for either compound.[31] It must also be noted that no similar studies for seawater were found in existing literature.

Table 2-6. Photolytic Degradation Rates for HMX in Summer in Holston River Water [28]

Depth, cm	Rate constant, k (day^{-1})
0	0.40
50	0.12
100	0.063
150	0.042
200	0.032
250	0.025
300	0.021

2.4 Ammonium Picrate

Ammonium picrate, or Explosive D, is a salt formed from picric acid and ammonium cation. **Figure 2-5** shows the molecular structure for Explosive D. The molecular formula is $C_6N_4O_7H_7$ with a corresponding molecular weight of 246.13 g/mol and it decomposes at ~265 °C. Some pertinent physical parameters for Explosive D are in **Table 2.7**. The K_H and vapor pressure of ammonium picrate are 2.94×10^{-22} atmosphere (atm) cubic meter (m^3)/mol and 3.37×10^{-11} torr, respectively. Each value is so low that gaseous agent in the atmosphere is of no concern. At the temperature of the waters off O'ahu at HI-06, the equilibrium solubility in water is ~10 g/L. In this environment, if a munition is breached with a large enough aperture, the infinite supply of water will allow the ammonium picrate to dissolve into the water column. There is disagreement in the literature for both partition coefficients for ammonium picrate. The log K_{oc} has reported values ranging from -1.37 to 2.03.[27,32,33] The log K_{ow} value is reported over the range of -1.4 to 2.0.[27,32,33]Although the range for both of these partition coefficients is quite large, the high solubility of ammonium picrate gives a low probability of partitioning to either the sediment or a nonpolar compound.[32] Because ammonium picrate is a salt, it dissolves

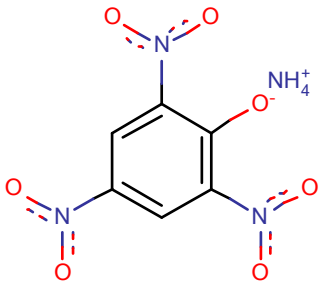

Figure 2-5. Ammonium Picrate (Explosive D)

as ammonium and picrate ions. Picrate is the conjugate base of picric acid, which has a pK_a of 0.38 or 0.42,[34,35] (there is a discrepancy in the literature) so the conjugate base is most prevalent. No data were found on the dissolution rate of ammonium picrate in water or seawater in the literature.

Table 2-7. Physical Properties of Explosive D[33,37-42]

Physical Properties of Explosive D		References
Solubility at 20 °C	10.2 g/L	Akhaven [33] Greenwald [36]
Density	1.72 g/ml	Keshavarz [34]
Henry's Law Constant, K_H, 20 °C	2.94×10^{-22} atm m^3/mol	Meylan [38]
Vapor Pressure	3.37×10^{-11} torr	Neely [39]
Log K_{oc}	-1.37 – 2.3	Rosenblatt [27] Pascoe [32] Lundblad [33]
Log K_{ow}	-1.4 – 2.0	Rosenblatt [27] Pascoe [32] Lundblad [33]
pK_a	0.38	Perez [34] Hornback [35]

Transformation mechanisms of the picric acid conjugate base are limited chemically. It does not undergo hydrolysis or photolysis to any great extent. One study of picric acid in seawater under SSR showed no significant photolysis in up to 47 days.[36] This same study looked at picric acid breakdown in marine sediment using sandy and a fine-grained sediment, with 0.25% and 1.1% TOC, respectively. Several breakdown products of picric acid were identified by gas chromatograph/mass spectrometry (GC/MS), including 2,4-dinitrophenol, amino dinitrophenols (e.g., picramic acid), 3,4-diamino phenol, amino nitrophenol, and nitro diaminophenol. Several studies have identified picramic acid as the major product of biotransformation of picric acid.[43,44] See **Figure 2-6** for the molecular structures of picric and picramic acid.

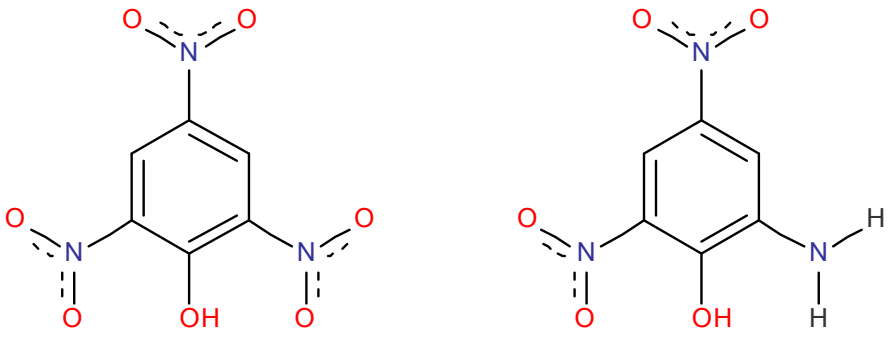

Figure 2-6. (a) Picric acid (b) Picramic acid

Picric and picramic acid are both toxic. One study tested the possible impacts of picric and picramic acid to two species: rainbow trout (*Salmo gairdneri)* and American oysters (*Crassostrea virginica)*.[45] Picramic acid was more toxic than picric acid to both species tested. The rate at which picramic acid is formed in the environment in Wai'anae is dependent on the biota in sediment.

Reaction of the ammonium picrate with the metal casing of munitions is of concern, particularly during the retrieval of munitions from the shallow site. Picric acid is known to react with metals to form unstable metallic picrates by the addition of the metal to the 2,4,6-trinitrophenol at the hydroxide position. Because the metallic picrates are more shock sensitive than both the ammonium picrate and picric acid, they have been known to cause explosive accidents.[46] Their explosive strength is 48–70% lower than that of picric acid depending on the salt. However, the sensitivity is much greater, and increases with increasing metal ion size. Wetting metal picrates diminishes their explosive sensitivity.

2.5 2,4-DNT

In the 2006 sampling of sediment, 2,4-dinitrotoluene (2,4-DNT) and 2,6-dinitrotoluene (2,6-DNT) were detected in four of the 90+ aliquots taken over the mapped area of the shallow water site. Although neither compound is a large constituent of the munitions at HI-06, these compounds are used as stabilizers and ballistic modifiers in propellant and may be present as an impurity of the TNT in the munitions from manufacture. Each compound is also produced from biotransformation mechanisms of TNT. Of the two isomers, 2,4-DNT has the longest lifetime in the environment and has a toxicity level that 2,6-DNT does not. Due to the shorter lifetime and reduced toxicity of 2,6-DNT, 2,4-DNT is the only isomer included in this report. **Figure 2-7** shows the molecular structure for 2,4-DNT.

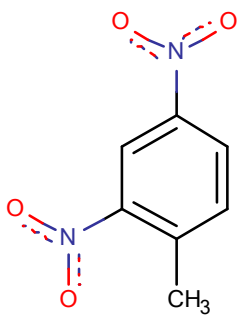

Figure 2-7. 2,4-Dinitrotoluene (DNT)

The physical properties of 2,4-DNT are listed in **Table 2.8**. 2,4-DNT is a yellow crystalline solid with a melting point of 70 °C.[5] It has a molecular formula of $C_7H_6N_2O_4$ with a molecular weight of 182.1 g/mol. 2,4-DNT has a density of 1.52 g/ml, consequently solid

Table 2-8. Physical Properties of 2,4-DNT[5,12,47,48]

Physical Properties of 2,4-DNT		References
Solubility at 20 °C in seawater	127 mg/L	Luning-Prak [12]
Density	1.52 g/ml	Meyer [5]
Henry's Law Constant, K_H, 20 °C	9.26×10^{-8} atm m^3/mol	Rosenblatt [27]
Vapor Pressure, 20 °C	5.10×10^{-3} torr	Meyer [5]
Log K_{oc}	2.82	Rosenblatt [27]
Log K_{ow}	2.01	Mabey [48]

2,4-DNT will reside at the bottom of the water column. The K_H of 9.26×10^{-8} atm m^3/mol ensures the gaseous compound above water will be negligible. The vapor pressure is high enough that if solid 2,4-DNT comes into contact with the atmosphere, the compound will vaporize over long periods of time. However, unless munitions wash ashore or the compound is exposed during low tide, which is not likely, gas-phase 2,4-DNT will not vaporize into the atmosphere.

The equilibrium solubility of 2,4-DNT in seawater has been measured to be 127 mg/L at 20 °C, but has also been determined as a function of ionic strength and temperature.[12] The equilibrium solubility as a function of temperature in pure water is:

$$C[DNT] = 74.8\, e^{0.0408t} \qquad \textbf{Equation 2.6}$$

Where C is the concentration of 2,4-DNT in mg/L and

t is the temperature in °C.

The solubility of 2,4-DNT is lower in seawater due to the salt, and can be described by the equation:

$$\log \frac{Sw}{Ss} = Ks'I \qquad \textbf{Equation 2.7}$$

Where S_w is the solubility in pure water,

S_s is the solubility in a salt solution,

K_s' is the salting-out parameter, and

I is the ionic strength.

The salting-out parameter for 2,4-DNT was determined to be 0.11 ± 0.01 L/mol. This parameter does not vary greatly with temperature. Finally, the equation for 100% seawater as a function of temperature is:

$$C[DNT] = 63.2\, e^{0.0391t} \qquad \textbf{Equation 2.8}$$

Like all nitroaromatics, hydrolysis reactions for 2,4-DNT are reported for pH > 10,[49] but no literature results on hydrolysis reactions at pH < 10 were found.

Photolysis is the most significant chemical removal process for 2,4-DNT in water. The photolytic half-lives for 2,4-DNT in river, bay, and pond waters have been measured to be 2.7, 9.6, and 3.7 hrs, respectively.[8] These rates are dependent on the amount of CDOM material present in the water. Mihas et. al. found that 2,4-DNT was transformed faster in seawater than in pure water when exposed to UV light.[50] O'Sullivan et. al. measured the rate of photolysis of 2,4-DNT in seawater and modeled the reaction to first-order rate processes using **Equation 2.5**. The

rate was measured for 2,4-DNT in filtered seawater with the SSR filter cut off at 295, 305, and 320 nm and gave rate constants of 0.052, 0.054, and 0.044 hr^{-1}, respectively. Mihas et. al. studies gave a half-life of 2,4-DNT exposed to UVA in seawater of 1 hr, whereas O'Sullivan et. al. studies for direct photolysis of 2,4-DNT gives a much longer half-life of 14 hrs. While the half-lives of the studies vary greatly, there are relative consistencies in each study. Most notable are the increase in photolysis rate in seawater over pure water and the rate of photolysis for 2,6-DNT is 6–10 times greater than the rates measured for 2,4-DNT. The observed differences in half-lives are likely due to differences in the intensity and spectra of the sources used for each study.

Photolysis products identified by GC/MS included 4-nitrotoluene, 2,4-dinitrobenzaldehyde, and 2,4-dinitrobenzoic acid. The dinitrobenzaldehyde was a short-lived product with an early increase in concentration followed by further photolysis reaction. The dinitrobenzoic acid was present in trace levels. Three other compounds were isolated by GC/MS and two were tentatively identified as methyl 4-cyanobenzoate and either 4-nitro-1,2-benzisoxazole or 4-nitrile-2-nitrotoluene.[26] It is of note that a dinitro-benzisoxazole was an identified photolysis product of TNT.[15] Other compounds isolated by GC/MS had molar masses in excess of the parent 2,4-DNT and still required separation and identification; however, they are likely the formation of azo and azoxy polymerization products.[26]

This page intentionally blank.

3 Conclusion

The physical properties of TNT, RDX, HMX, Explosive D, and 2,4-DNT that determine the environmental fate in a marine environment such as solubility, Henry's Law constant, vapor pressure and partition coefficients are presented. These properties in conjunction with the conditions of Wai'anae such as ionic strength, pH, and temperature are considered to ascertain the chemistry of each compound in seawater.

Although TNT and 2,4-DNT are slightly soluble in seawater, photolysis reactions dominate over hydrolysis as the main chemical degradation mechanisms once they are in solution. The ionic strength of seawater decreases both the solubility and molar absorptivity of the compounds; however, the rate of photolysis is increased in all experimental data in the literature. This effect is postulated to be due to enhanced secondary photochemical processes from natural agents residing in the water column. While the theory is based on proven catalytic enhancements to photodegradation of TNT with compounds such as titanium dioxide (TiO_2), the supposed catalytic agents in the seawater environment have not been identified, but likely produce hydroxyl radicals.

Both RDX and HMX are the least soluble of all the compounds reviewed for HI-06. For the dissolved compounds, each undergoes photolysis degradation that yields very similar if not identical degradation products. Although there were data on these compounds for fresh water and groundwater, the effects on solubility and photolysis of RDX and HMX in a marine environment are not reported in the literature.

Ammonium picrate is soluble in water and will reside in the water column as picric acid. Picric acid is not susceptible to hydrolysis or photolysis. The main transformation mechanism for picric acid is biotransformation into picramic acid, both picric and picramic acids are toxic. Removal of munitions containing ammonium picrate from a hydrated environment to a dry environment may permit metal picrates developed from reaction with the shell casing to become sensitized. Metal picrates are unstable in a dry environment; water desensitizes the compounds to shock induced explosion.

Several data gaps exist in the literature. For example, the larger polymerization photolysis products for TNT and 2,4-DNT have yet to be identified. The increase in the rate of photolysis of TNT and 2,4-DNT in seawater over a pure water environment has been observed, but reasons for this increase are speculative. There is also a large gap in the literature for RDX and HMX studies in seawater. Much work has been done in fresh/groundwater environments due to wastewater effluent from munition production plants, but there are little to no data in the literature regarding the effects of saltwater on solubility or dissolution and photolysis rates, which is also true for Explosive D studies in seawater. Most data presented in this paper for ammonium picrate were obtained from studies in a freshwater or laboratory environment.

This page intentionally blank.

4 References

1 Cox, E., Decarlo, E. H. & Overfield, M. *Marine Sanctuaries Conservation Series* (ed National Oceanic and Atmospheric Administration U. S. Department of Commerce, National Marine Sanctuary Program) 112 pp (Silver Spring, MD, 2007).

2 Yinon, J. *Forensic and environmental detection of explosives*. (John Wiley & Sons Ltd., 1999).

3 Hoffsommer, J. C. & Rosen, J. M. Hydrolysis of Explosives in Sea Water. *Bulletin of Environmental Contamination &Toxicology*, 78-79 (1973).

4 Brannon, J. M. & Pennington, J. C. (ed U. S. Army Corps of Engineers) (Vicksburg, MS, 2002).

5 Meyer, R., Kohler, J. & Homburg, A. *Explosives*. 5 edn, (Wiley-VCH, 2002).

6 Lyman, W. J., Reehl, W. F. & Rosenblatt, D. H. *Handbook of chemical property estimation methods; Environmental behavior of organic compounds*. (McGraw-Hill, 1982).

7 Dionne, B. C., Rohmbehler, D. P., Achter, E. K., Hobbs, J. R. & Fine, D. H. Vapor Pressure of Explosives. *Journal of Energetic Materials* **4**, 447 - 472 (1986).

8 Spanggord, R. J. (ed U. S. NTIS) (1980).

9 Hansch, C. & Leo, A. in *Issue 28* (Claremont College, Pomona, CA, 1987).

10 Leggett, D. C., Miyares, P. H. & Jenkins, T. F. Apparent donor-acceptor between nitroaromatics and acetonitrile. *Journal of Solution Chemistry* **21**, 105 - 108 (1992).

11 Claussen, J. L., Bennett, E. & Linkov, I. (ed Cold Regions Research and Engineering Laboratory U. S. Army Corps of Engineers) (Hanover, NH, 2009).

12 Luning-Prak, D. J. & O'Sullivan, D. W. Solubility of 2,4-Dinitrotoluene and 2,4,6-Trinitrotoluene in Seawater. *Journal of Chemical & Engineering Data* **51**, 448-450 (2006).

13 Jenkins, T. F. & Miyares, P. H. *Unpublished data* (Cold Regions Research and Engineering Laboratory, U. S. Army Engineer Research and Development Center, Hanover, NH, 1997).

14 Mills, A., Seth, A. & Peters, G. Alkaline hydrolysis of trinitrotoluene, TNT. *Physical Chemistry and Chemical Physics* **5**, 3921 - 3927 (2003).

15 Burlinson, N. E., Sitzmann, M. E., Glover, D. J. & Kaplan, L. A. (ed Naval Surface Weapons Center) (Silver Spring, MD, 1979).

16 Kaplan, L. A., Burlinson, N. E. & Sitzmann, M. E. (ed Naval Surface Weapons Center) (Silver Spring, MD, 1975).

17 Epstein, J., Sommer, H. Z. & Hackley, B. E. (ed Chemical Systems Laboratory) (Aberdeen Proving Ground, MD, 1978).

18 Burlinson, N. E., Kaplan, L. A. & Adams, C. E. (ed Naval Ordnance Laboratory) (Silver Spring, MD, 1973).

19 O'Sullivan, D. W., Denzel, J. R. & Luning-Prak, D. J. Photolysis of 2,4,6-Trinitrotoluene in Seawater: Effect of salinity and nitrate concentration. *Manuscript in progress* (2010).

20 Schmelling, D. C., Gray, K. A. & Kamat, P. V. Role of reduction in the photocatalytic degradation of TNT. *Environmental Science and Technology* **30**, 2547-2555 (1996).

21 Son, H. S., Lee, S. J., Cho, I. H. & Zoh, K. D. Kinetics and mechanism of TNT degradation in TiO_2 photocatalysis. *Chemosphere* **57**, 309-317 (2004).

22 Rodgers, J. D. & Bunce, N. J. Review Paper: Treatment Methods for the Remediation of Nitroaromatic Explosives. *Water Resources* **35**, 2101 - 2111 (2001).

23 Ho, P. C. Photooxidation of 2,4-dinitrotoluene in aqueous solution in the presence of hydrogen peroxide. *Environmental Science and Technology* **20**, 260 - 267 (1986).

24 Larson, R. A., L., M. P. & Crowley, T. O. Borohydride photoreduction of nitroaromatic compounds related to military ordnance constituents. *Environmental Science and Technology* **30**, 1192 - 1197 (1996).

25 Liou, M.-J., Lu, M.-C. & Chen, J.-N. Oxidation of TNT by photo-Fenton process. *Chemosphere* **57**, 1107 - 1114 (2004).

26 O'Sullivan, D. W., Denzel, J. R. & Luning-Prak, D. J. Photolysis of 2,4-Dinitrotoluene and 2,6-Dinitrotoluene in Seawater. *Aquatic Geochemistry* **16**, 491 - 505 (2010).

27 Rosenblatt, D. H., Burrows, E. P., Mitchell, W. R. & Parmer, D. L. in *The Handbook of Environmental Chemistry* Vol. 3 Part G (ed O. Hutzinger) 195 - 232 (Springer-Verlag, 1991).

28 Spanggord, R. J. *et al.* (ed U. S. Army Medical Research and Development Command) (Fort Detrick, MD, 1983).

29 Sikka, H. C., Banjeree, S., Pack, E. J. & Appelton, H. T. (ed U. S. Army Medical Research and Development Command) (Fort Detrick, MD, 1981).

30 Glover, D. J. & Hoffsommer, J. C. (1979).

31 Card, R. E. & Autenrieth, R. (ed Amarillo National Resource Center for Plutonium) (Amarillo, TX, 1998).

32 Pascoe, G. A., Kroeger, K., Leisle, D. & Feldspausch, R. J. Munition constituents: Preliminary sediment screening criteria for the protection of marine benthic invertebrates. *Chemosphere* **81**, 807 - 816 (2010).

33 Lundblad, R. L. in *Biochemistry and Molecular Biology Compendium* (ed CRC Press) Ch. 4, 327 - 300 (2007).

34 Perez, G. V. & Perez, A. L. Organic Acids without a Carboxylic Acid Functional Group. *Journal of Chemical Education* **77**, 910 - 915 (2000).

35 Hornback, J. M. *Organic Chemistry*. 2 edn, 124 (Thomson Brooks/Cole, 2006).

36 Nipper, M., Y., Q., S., C. R. & K., M. Degragation of picric acid and 2,6-DNT in marine sediments and waters: the role of microbial acrivitry and ultra-violet exposure. *Chemosphere* **56**, 519-530 (2004).

37 Akhaven, J. in *Encyclopedia of Chemical Technology* Vol. 10 (ed Kirk-Othmer) 719 - 744 (John Wiley & Sons, 1993).

38 Keshavarz, M. H. New Method for Calculating Densities of Nitroaromatic Explosive Compounds. *Journal of Hazardous Materials*, 263 - 269 (2007).

39 Medicine, U. S. N. L. o. <http://chem.sis.nlm.nih.gov/chemidplus/>

40 Greenwald, I. On the Solubility of some Picrates and the Determination of Guanidines in Urine. *Biochemical Journal* **20**, 665 -667 (1926).

41 Meylan, W. M. & Howard, P. H. Bond Contribution Method for Estimating Henry's Law constants. *Environmental Toxicology and Chemistry* **10**, 1283 - 1293 (1991).

42 Neely, W. B. & Blau, G. E. in *Environmental Exposure from Chemicals* (eds W. B. Neely & G. E. Blau) 1 - 11 (CRC Press, 1985).

43 Nipper, M. Fate and effects of picric acid and 2,6-DNT in marine environments: Toxicity of degradation products. *Marine Pollution Bulletin* **50**, 1205 - 1217 (2005).

44 Lotufo, G., Nipper, M., Carr, R. S. & Conder, J. M. *Ecotoxicology of Explosives*. (CRC Press, 2009).

45 Goodfellow, W. L., Burton, D. T., Graves, W. C., Hall, L. W. & Cooper, K. R. Acute toxicity of picric and picramic acid to Rainbow Trout, Salmo Gairdneri, and American

Oyster, Crassostrea Virginica. *Journal of the American Water Resources Association* **19**, 641-648 (1983).

46 Matsukawa, M., Matsunaga, T., Yoshida, M. & Fujiwara, S. Synthesis of alkaline-earth metal picrates. *Science and Technology of Energetic Materials* **64**, 227 - 235 (2003).

47 (ed Public Health Service Agency for Toxic Substances and Disease Registry (ATSDR), U. S> Department of Health and Human Services) (Atlanta, GA, 1998).

48 Mabey, W. R., Smith, J. H. & Podoll, R. T. (ed Environmental Protection Agency) (Washington, DC, 1982).

49 Emmrich, M. Kinetics of the Alkaline Hydrolysis of Important Nitroaromatic Co-contaminants of 2,4,6-Trinitrotoluene in Highly Contaminated Soils. *Environmental Science and Technology* **35**, 874 - 877 (2001).

50 Mihas, O., Kalogerakis, N. & Psillakis, E. Photolysis of 2,4-dinitrotoluene in various water solutions: effect of dissolved species. *Journal of Hazardous Materials* **146**, 535 - 539 (2007).

Physicochemical Properties for Chemical Warfare Agents at the Deep Water Site Hawaii 1 (HI-01), O'ahu, Hawaii

June 2011

Prepared for:

National Oceanic and Atmospheric Administration

Contract GS10F0189T

noblis

3150 Fairview Park Drive South
Falls Church, Virginia 22042-4519

noblis

Executive Summary

This report provides physicochemical parameters for chemical warfare agents that enable the determination of environmental fate. The parameters discussed in this report can be used to model the fate for hypothetical release scenarios for the agents identified by the National Oceanic and Atmospheric Administration (NOAA) in the deep site (HI-01) west of Ordnance Reef (HI-06) off the west coast of O'ahu near Wai'anae, Hawaii. The parameters necessary to examine the fate of the chemical agents sulfur mustard (HD), lewisite (L), cyanogen chloride (CK), and hydrogen cyanide (AC) in a marine environment are presented in this report.[1]

While site-specific data were collected for the nearby shallow site HI-06 (locally known as Ordnance Reef), there are no data sets for the deep site. Therefore, several of the parameters that control environmental fate were estimated based on reported site conditions (approximately 8,000 ft deep). For the marine environment, water temperature, salinity, pH, dissolved oxygen, and the ionic strength are all factors that determine chemical fate. For the chemical agents, solubility, density, vapor pressure, Henry's Law constant, the partition coefficient between total organic carbon and water, and the partition coefficient between octanol and water determine chemical fate. Together, these site and chemical parameters may be used to predict environmental fate.

Sulfur Mustard (HD) – The main chemical reaction for HD in a marine environment is hydrolysis. The presence of the chloride ion in seawater does inhibit the hydrolysis reaction rate. If the hydrolysis reaction reaches completion, the product is thiodiglycol, which is a benign compound. However, the hydrolysis reaction produces several intermediate sulfonium cations that become stable salts in seawater. These salts become a "film" on HD droplets and shield the agent from further degradation. Droplets or lumps of HD with a sulfonium salt boundary layer are reported to exist in seawater for decades.

Lewisite (L) – Lewisite undergoes rapid hydrolysis to a pair of compounds that exist in equilibrium: 2-chlorovinylarsonous acid and lewisite oxide. This pair of compounds is no less toxic than the parent lewisite compound. Further hydrolysis yields arsorous acid and finally inorganic arsenic.

Cyanogen chloride (CK) – Cyanogen chloride hydrolyses first to cyanic acid and hydrochloric acid. These compounds exist as chloride and cyanate in seawater pH. Secondary hydrolysis of cyanic acid produces ammonia and carbon dioxide.

Hydrogen Cyanide (AC) – Volatilization and biotransformation are the major chemical reactions for AC in a marine environment. However, volatilization in the deep site will be decreased significantly such that it may be considered negligible. Biodegradation of AC yields products of ammonia and carbon dioxide, but the extent of this reaction will be determined by the nutrient and microbial populations in the deep site.

For both CK and AC, spontaneous and violently explosive polymerization can occur after long periods of containment.

---

[1] The abbreviations for each agent are their respective military designators.

This Page Intentionally Left Blank.

noblis

Table of Contents

List of Figures

List of Tables

List of Acronyms

AC	hydrogen cyanide
atm	atmosphere
CClN	cyanogen chloride
CK	cyanogen chloride
CVAA	2-chlorovinylarsonous acid
D	density
g	gram(s)
HCN	hydrogen cyanide
HD	sulfur mustard
hr	hour(s)
I	Ionic strength
Ka	acid dissociation constant
KH	Henry's Law constant
kJ	kilojoules(s)
K_{oc}	organic carbon partition coefficient
K_{ow}	octanol water partition coefficient
L	lewisite
L	liter(s)
L1	2-chlorovinylarsonous dichloride
L2	bis(2-chlorovinyl)arsinous chloride
L3	tris(2-chlorovinyl)arsine
m3	cubic meter(s)
ml	milliliter(s)
mol	mole
NOAA	National Oceanic and Atmospheric Administration
P	vapor pressure
pKa	acid dissociation constant at logarithmic scale
S	solubility
TDG	thiodiglycol

This Page Intentionally Left Blank.

1 Introduction

This report provides physicochemical data for chemical warfare agents in order for the National Oceanic and Atmospheric Administration (NOAA) to produce a dispersion model descriptive of a hypothetical release of the chemical warfare agents suspected to exist in the deep site water, Site Hawaii 1 (HI-01) off the west coast of O'ahu near Wai'anae, Hawaii. The parameters necessary to examine the fate chemical warfare agents sulfur mustard (HD), lewisite (L), cyanogen chloride (CK), and hydrogen cyanide (AC) in a marine environment is presented in this report.[1]

1.1 Background

The Office of Response and Restoration and the Office of National Marine Sanctuaries of the NOAA are conducting an assessment of conditions relevant to fate and transport of munitions constituents in Hawaiian waters. This assessment includes constituents of chemical munitions that were disposed in HI-01 approximately 10 nautical miles west of the community of Wai'anae on O'ahu, Hawaii. In support of this assessment, Noblis gathered existing data on the parameters controlling the fate and transport of chemical in support of a predictive ocean dispersion model.

While site-specific data were collected for the shallow site HI-06 locally known as Ordnance Reef, there is no similar corresponding data for HI-01 (a deep site), though several parameters can be estimated. The water temperature at a depth of about 8,000 feet (ft) is estimated to be 0 °C. Since most of the compounds undergo hydrolysis, the concentration of hydroxide anion is important and, therefore, so is the pH of the seawater. The pH of the sea water at depth is estimated to be 8.1. At the depth of this site, a value of 34 for salinity is estimated. An average value for the ionic strength (I) in seawater is 0.70 M (moles/liter).

1.2 Environmental Residence

The possible residences of the munitions constituents in a marine environment are represented in Figure 1-1 and are first determined by the phase of the munition constituent, i.e., whether it is a solid, liquid, or gas. Liquid phase agent will be found in the water column as a dissolved constituent in the aqueous phase or as a miscible or immiscible liquid. Solid munitions constituents could be found as insoluble particulate on the ocean floor, adsorbed species in sediment or particulate in the water column, or still within metal casing that may provide a surface for reaction with the encased metal. If a chemical has the ability to reach the surface, i.e., if it has a density less than that of water, it may evaporate or sublimate depending on its vapor pressure at atmospheric pressure and temperature. Finally, a chemical in a marine environment may also be found to accumulate in biota, depending on the solubility of the substance in a fatty tissue.

To determine in which environmental compartment shown in Figure 1-1 that each compound resides, chemical parameters of both the marine environment and the chemical agents themselves must be considered. For the marine environment, water temperature, salinity, pH, dissolved oxygen, and the ionic strength (I) are all factors that determine chemical fate. For the chemical

[1] The abbreviations for each agent are their respective military designators.

agents, solubility (S), density (D), vapor pressure (P), Henry's Law constant (K_H), the partition coefficient between total organic carbon and water (K_{oc}), and the partition coefficient between octanol and water (K_{ow}) are all used to determine where a compound will reside. Once this is determined, the chemistry in that environment can be ascertained.

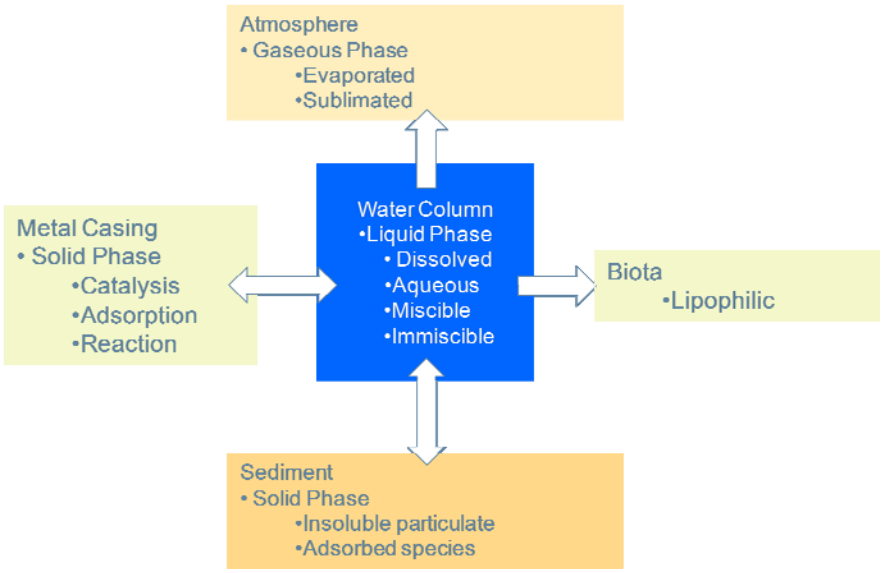

Figure 1-1. Possible Residences of Chemical Agents in a Marine Environment

The main chemical reactions that occur in a marine environment that must be considered in the degradation of compounds include hydrolysis, oxidation, thermolysis, and photolysis. For HD, L, and CK, hydrolysis is the major chemical reaction these compounds undergo in a marine environment. The most important processes for AC are volatilization or biotransformation.

2 Physical and Chemical Parameters

Several physical and chemical parameters for the compounds are necessary to determine the fate and transport of the chemical agents in marine environments. Boiling and melting points determine the initial physical state of an agent while density *(D)* determines whether undissolved agent will rise or sink in the water column. Vapor pressure *(P)*, solubility *(S)*, Henry's Law constant *(K_H)*, and partition coefficients *(K_{ow}* and *K_{oc})* are important parameters for determining the phases and matrices in which the agent resides and is transported. Partition coefficients are also used in risk assessment to determine whether an agent bioaccumulates in the food chain. Acid dissociation constants (K_a) determine the form that agents with acidic or basic character exist in a marine environment. Finally, rate constants (k) for reactions, such as dissolution or hydrolysis, for an agent and their products are important in the full determination of the fate of each agent under consideration. The main chemical reactions that occur in a marine environment that must be considered in the degradation of compounds include hydrolysis, oxidation, thermolysis, and photolysis. For hydrolysis, the solubility and rate of dissolution of an agent determines how fast a molecule can undergo this reaction. If the compound is insoluble or sparingly soluble, a hydrolysis reaction may be minimal due to the fact that it will not go into the liquid phase fast enough to ever have significant concentration to undergo hydrolysis. Oxidation and thermolysis reactions for most of the agents under the conditions at HI-01 are unlikely. For oxidation reactions, the alkaline environment favors hydrolysis. As for thermolysis, these compounds are thermally stable at ocean temperatures.

2.1 Sulfur Mustard (HD)

Sulfur mustard is a strong vesicant, which is a colorless and odorless liquid in pure form. However, military- or agent-grade material, which is not pure, is yellow to dark brown in color with an odor of horseradish. The principle active component in sulfur mustard is 1,1´-thiobis(2-chloroethane), which has a molecular formula of $C_4H_8Cl_2S$ and a molecular weight of 159.08 grams (g)/mole (mol). The boiling and melting points have been measured in several studies and their mean values respectively are 216.9 ± 0.2 °C[15-19] and 14.46 ± 0.04 °C.[7,20-23] Lower values have been reported presumably from less pure material. The molecular structure of HD is shown in Figure 2-1.

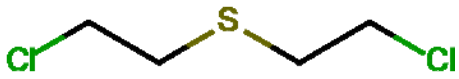

Figure 2-1. Sulfur Mustard, 1,1´-thiobis[2-chloroethane]

The physical properties of HD relevant to environmental fate are listed in Table 2-1.[3-7] The density at 20 °C has been reported as 1.27 g/milliliter (ml). However, it has also been reported as a function of temperature in several studies.[7,23-26] Combining the data from all studies shows good agreement and yields Equation 2.1.1, which describes the density of 1,1´-thiobis[2-chloroethane] over a temperature range of 15–90 °C:

$$D\ (g/ml) = 1.295(\pm 0.001) - 0.00112(\pm 0.00002)T(°C) \quad \textbf{(2.1.1)}$$

Table 2-1. Physical Properties of Sulfur Mustard (HD)[3-9]

Physical Properties of Sulfur Mustard		References
Solubility at 20 °C in Seawater	0.8 g/L	Franke [4]
Solubility at 10 °C in Seawater	0.7 g/L	Hopkins [3]
Solubility at 5 °C in Seawater	0.3 g/L	Franke [4]
Density	1.27 g/mL	Franke [4]
Henry's Law Constant, K_H, 20 °C	2.60×10^{-5} atm m^3/mol	Redemann [7]
Vapor Pressure, 20 °C	0.11 torr	Munro [7]
Log K_{oc}	2.12	Lyman [5]
Log K_{ow}	1.37, 2.41	Lyman [5], Meylan [8]

The vapor pressure (P) has also been measured as a function of temperature by several workers.[7,18,19,27-30] Using the data from all the studies, the vapor pressure is found to obey Equation 2.1.2[31] over the temperature range of 14–217 °C:

$$Log\ P(Torr) = 9.1(\pm 0.1) - \frac{2990(\pm 40)}{T(K)} \quad \textbf{(2.1.2)}$$

A recent study provided Equation 2.1.3 for the vapor pressure of solid HD over the temperature range of -25–13 °C[32,33]:

$$Log\ P(Torr) = 13.33(\pm 0.09) - \frac{4230(\pm 20)}{T(K)} \quad \textbf{(2.1.3)}$$

Because the temperature of HI-01 is in the range of 0–4 °C, Equation 2.1.3 produces the vapor pressure of HD under the conditions at the site. Note that this equation differs from the equation for liquid HD because the slope is related to the heat of sublimation (79 kilojoules [kJ]/mol) rather than the heat of fusion (55 kJ/mol). While the vapor pressure and K_H are relatively high (in comparison to explosives, for example), the HD is under the pressure of about 10,000 ft of seawater, or approximately 300 atm. Much like corked sparkling wine or a soda can, any vapor from HD will stay dissolved.

HD is only sparingly soluble in water.[34] However, the saturation water solubility is less important to the fate of HD released into marine environments than the rate of dissolution. Brookfield et al. measured the dissolution rate as a function of temperature and found that Equation 2.1.4 described this behavior:[35]

$$k(\mathrm{g/cm^2 s}) = 233.7\ e^{-[(12350/1987T(\mathrm{K})]} \quad \textbf{(2.1.4)}$$

Demek et al. measured the rate of HD dissolution as 3.4×10^{-7}g/cm^{2}s at 4 °C in a 0.15 knot current.[36] However, lumps or droplets of HD have persisted in the ocean for decades,[37,38] suggesting that these values overestimate the dissolution rate. Formation of a sulfonium salt-rich layer at the mustard water interface slows the dissolution of HD and produces the droplets.[39] This layer of sulfonium salts or "skin" protects the active HD from dissolution into the marine environment. In Figure 2-2, the salts that produce the thick boundary layer between HD and water are shown and include [H-TDG], [H-2DG], and [CH-TDG].

The primary reaction of HD in seawater is hydrolysis, primarily to thiodiglycol (TDG) and hydrogen chloride. Hydrolysis mechanisms are shown in Figure 2-2; the degree to which the reaction proceeds through the sulfonium chloride intermediates [H-TDG], [H-2TDG], and [CH-TDG] depends on the concentration of mustard in the aqueous solution.[40-42] The initial formation of H-TDG in the aqueous phase requires accumulation of the TDG reaction product and appears less significant in a marine environment where currents can remove the hydrolysis product.

The rate constants for the hydrolysis reaction of HD have been measured and calculated by many

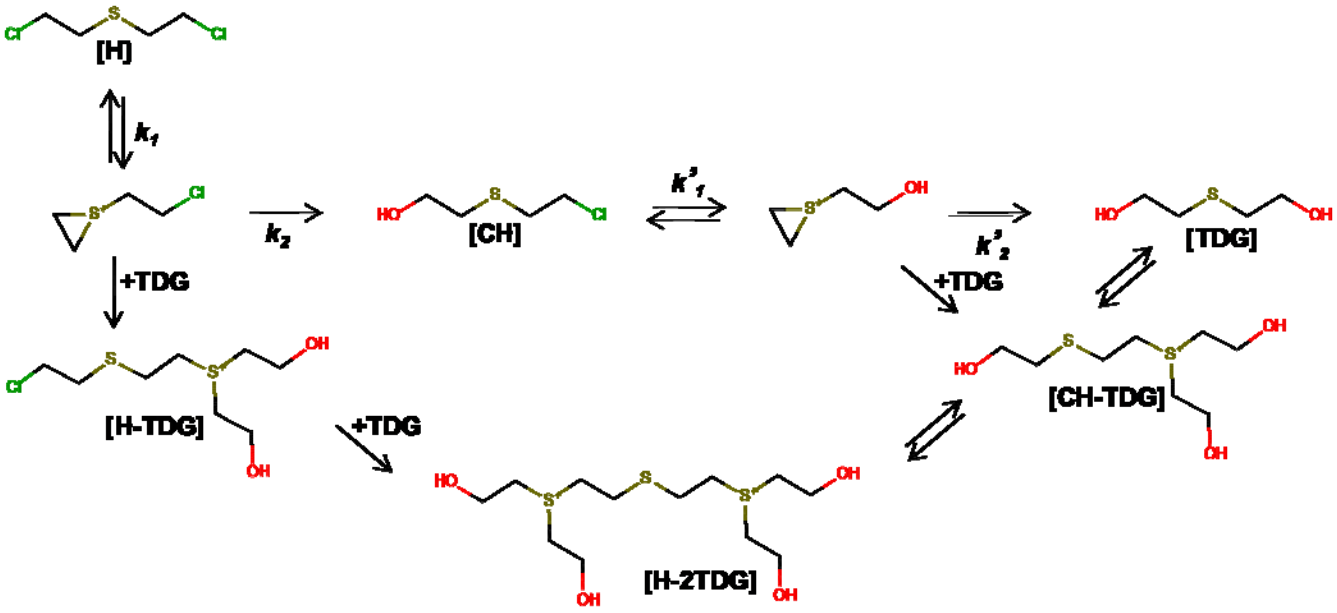

Figure 2-2. Hydrolysis Mechanism for 1,1´-thiobis[2-chloroethane], Principle Active Component of HD

Table 2-2. Half-Lives of HD in Seawater

Temperature, °C	Seawater, $t_{1/2}$ (min.)	k_1, calc'd (min^{-1})
5	175	0.0040
15	49	0.0141
25	15	0.046

groups. At 25 °C, k_1 has been measured to be 0.174 min^{-1} and 0.155 min^{-1}, and k'_1 was reported as 0.223 min^{-1} and 0.260 min^{-1}. Epstein, et al. measured the half-life of HD in seawater at several temperatures (see Table 2-2**).**[1] The rates are slower than those measured in pure water due to the aqueous chloride ion displacing the equilibrium towards the reactants by a factor equal to:

$$\frac{k_{Cl^-}}{k_{H2O}} = \frac{1}{1+ [Cl^-]F^I_{Cl^-}} \quad \textbf{(2.1.5)}$$

where F varies with the ionic strength (I) according to the Brønsted-Bjerrum Equation with a limiting value of F^0_{Cl-} = 32.2 L/mol at I:[43]

$$\log_{10} F^I_{Cl^-} = \log_{10} F^0_{Cl^-} + 2\, AZ_{R_3S^+}Z_{Cl^-}I^{\frac{1}{2}} \quad \textbf{(2.1.6)}$$

which uses the constant from the Debye-Hückel equation:[44]

$$A = \left[\frac{\sqrt{2\pi N_0}}{2.303}\right]\left[\frac{e^2}{10\varepsilon kT}\right]^{\frac{3}{2}} \quad \textbf{(2.1.7)}$$

The value of the Debye-Hückel *A* term is calculated as 0.55. The charges $Z_{R_3S^+}$ and Z_{Cl^-} are +1 and -1, and the ionic strength of seawater (I = 0.70) gives a value of F^I_{Cl-} = 3.8 for seawater at 0 °C. If the hydrolysis rate constant in freshwater is 0.0068 min^{-1} at 0 °C, this gives a hydrolysis rate constant k = 0.0022 min^{-1} in seawater. It is of note that the ionic strength of seawater is above the level that the Debye-Huckel equations were derived. Therefore, the rate constant may be higher due to deviation from the law.

Two different numbers are reported for the log of partition coefficient K_{ow}, each of which is an estimate based on fragment constants. The values are 1.37 and 2.41, neither of which was at a specified temperature. The values predict low to moderate partitioning into a non-polar substance. The reported log K_{oc} value of 2.12 also predicts low to moderate partitioning into organic carbon in sediment.

Photolysis reactions of HD and the hydrolysis products does not occur to any significant extent due to the lack of sunlight at the depth of HI-01.

Sulfur mustard will undergo oxidation in air; however, oxidation reactions are unlikely to compete with hydrolysis in seawater.

Mustard "heel" is a solid material that forms in munitions after prolonged storage. It is composed of occluded liquid mustard in a mixture of iron salts and S-(2-chloroethyl)-1,4-dithianium chloride. No kinetic data on the formation of mustard heel formation at the temperature of HI-01 were located, so the extent of its presence is unknown. However, mustard heel is water soluble, so if it has formed within a munition, it will dissolve if the munition is breached. No quantitative data on fate of mustard heel were located.

2.2 Lewisite (L)

The chemical agent lewisite is a mixture of *cis*- and *trans*-2-chlorovinylarsonous dichloride (L1), isomers of bis(2-chlorovinyl)arsinous chloride (L2), and isomers of tris(2-chlorovinyl)arsine (L3). The vesicant and main component in most lewisite is L1. Although commercial-grade lewisite is known for a strong geranium odor, the vesicant L1 is odorless. L1 has a molecular weight of 207.32 and a molecular formula of $C_2H_4AsCl_3$. A range of boiling and melting points have been reported, most likely due to the different amounts of mixtures of L1, L2, and L3 isomers in each mixture tested.[15,45-47] The boiling point at ambient pressure has been reported in the range of

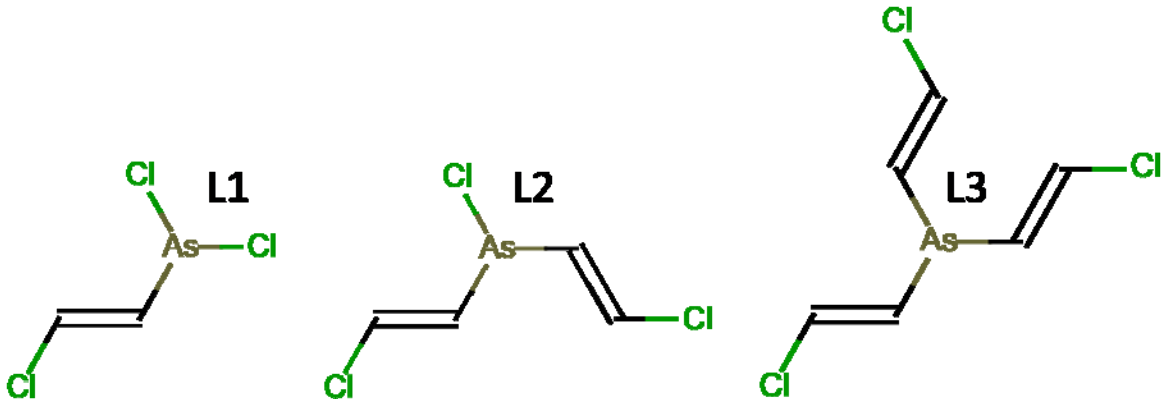

Figure 2-3. 2-chlorovinylarsonous dichloride (L1), bis(2-chlorovinyl)arsinous chloride (L2), tris(2-chlorovinyl)arsine (L3)

190–203 °C, and the melting point has been reported from -44.7 to -0.1 °C. No explicit data for melting and boiling points could be found on only L1, L2, or L3. Weapons-grade lewisite is expected to remain liquid at substantially lower temperatures due to the presence of L2 and L3. The molecular structures of the three compounds are shown in Figure 2-3.

Physical parameters relevant to the environmental fate of lewisite are listed in Table 2-3. The density of 2-chlorovinylarsonous chloride is reported in the literature at 20 and 25 °C, which

Table 2-3. Physical Properties of Lewisite (L)

Physical Properties of Lewisite		References
Solubility at 25 °C in Sea Water	0.5 g/L	Franke [4]
Density at 25 °C	1.88 g/ml	Whiting [45] Lewis [49]
Henry's Law Constant, K_H, 20 °C	3.2×10^{-4} atm m^3/mol	Redemann [48]
Vapor Pressure	0.35 torr	Franke [4]
Log K_{oc}	No data	
Log K_{ow} (estimated)	2.56	Meylan [8]
Log K_d for Arsenic	2.3	Baes [9]

were measured 1.888 g/ml at 20 °C and 1.8799 and 1.8793 g/ml at 25 °C.[45,48,49] Although there is no density value for lewisite at 0 °C in the literature, these values indicate that the density is significantly greater than water regardless of the temperature of the seawater in the deep site.

The vapor pressure *(P)* of lewisite has been reported at 20 °C as 0.35 torr.[4] An equation for vapor pressure over the range of 0–60 °C was determined and obeys Equation 2.2.1:[48]

$$Log\ P(Torr) = 9.1 - \frac{2786.6}{T(K)} \quad \textbf{(2.2.1)}$$

The largest component of lewisite—L1—also is the most volatile and, therefore, has the highest vapor pressure individually.

Table 2-4. Properties of Lewisite Hydrolysis Products[1,2]

Compound	Molecular Weight	Solubility, g/L	Estimated log K_{ow}
CVAA	170.43	~20	1.4 to 2.4
Lewisite oxide	152.41	~20	-1.4 to -0.4

Because the hydrolysis of lewisite (L1) happens so quickly after dissolution, these values for both K_H and log K_{ow} are questionable. Since the fate of L1 in water is primarily hydrolysis, accurate values of these numbers are not critical to assessing environmental impact since the actual agent exists in water mere minutes. Solubility and estimated partition coefficients for the hydrolysis products would be more important and are found in Table 2-4. The log Kow values are estimated using Syracuse Research Corporation software LOGKOW version 1.5.

After dissolution, hydrolysis is the main reaction mechanism to investigate for a marine envi-

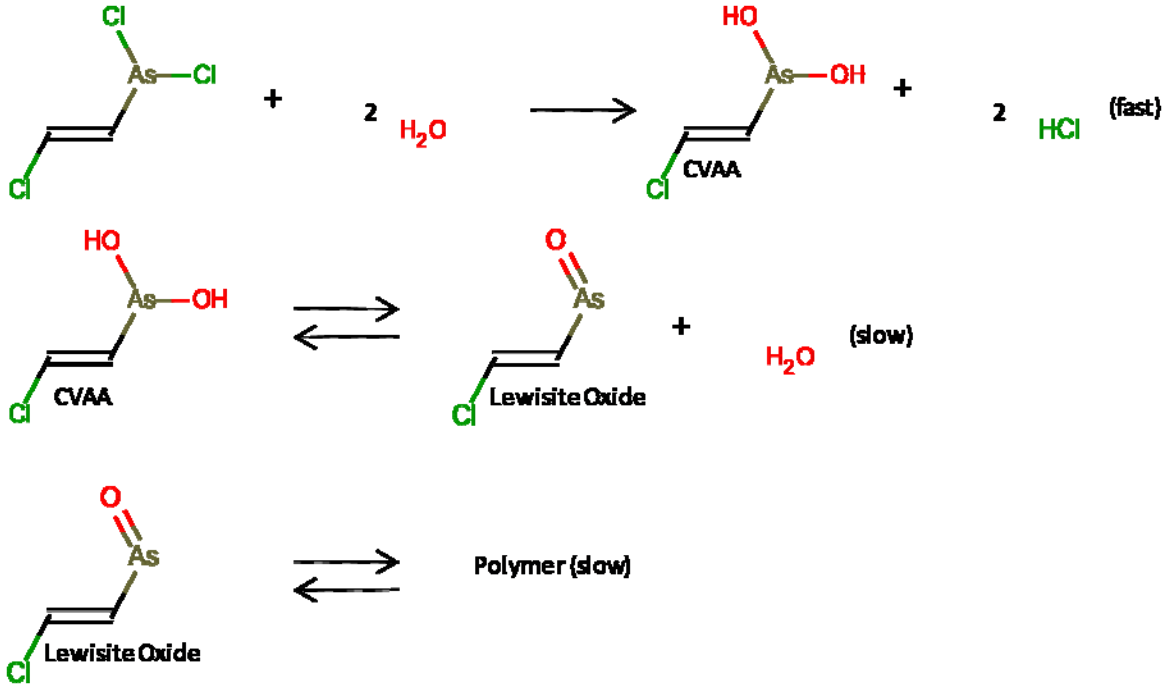

Figure 2-4. Hydrolysis Mechanism for L1

ronment since lewisite does not oxidize significantly, photolyze in sunlight, thermolyze below 49 °C, or undergo acid-base dissociation.

Figure 2-4 shows the hydrolysis mechanism for L1. L1 undergoes hydrolysis to form 2-chlorovinylarsonous acid (CVAA)/lewisite oxide equilibrium quickly.[50] The rate at which the hydrolysis and subsequent equilibrium between CVAA/lewisite oxide is established has not been accurately measured due to the rapidity of the reaction. However, it can be estimated that the hydrolysis rate constant at 20 °C is on the order of 1 min^{-1}.[51] Both of the resulting hydrolysis equi-

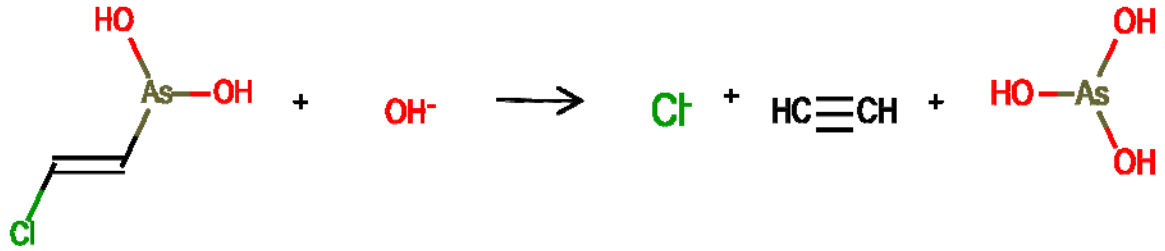

Figure 2-5. 2-Chlorovinylarsonous Acid (CVAA) Alkaline Hydrolysis

librium products are vesicants with no appreciable difference in toxicity from the parent mixture. The vesicant properties of the mixture are reported to remain unchanged after ten weeks in seawater.[1]

There is evidence that cold alkali decomposes CVAA into arsorous acid, acetylene, and chloride as seen in Figure 2-5. However, at pH of 8.5 and 17 °C, there were no detectable acetylene product after 24 hours (hrs), but substantial amounts of decomposition product could be detected after 2 hrs at pH 10.5.[50] An approximate extrapolation to 0 °C and pH 8.1 indicates that the reaction should occur on a time-scale of months in seawater. The product of arsorous acid will undergo inorganic arsenic transformation in the environment.

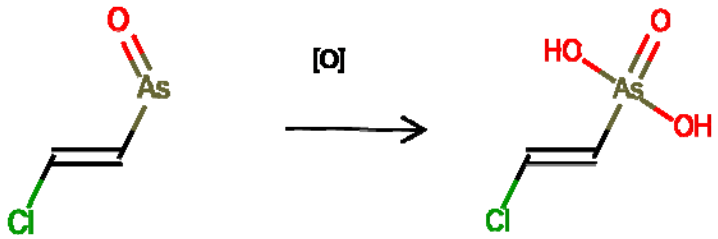

Figure 2-6. Lewisite Oxide to 2-chlorovinylarsonic acid Oxidation Mechanism

Finally, although L1 does not undergo oxidation due to the rapidity of the hydrolysis mechanism, the lewisite oxide from the equilibrium pair does oxidize to 2-chlorovinylarsonic acid as shown in Figure 2-6.

2.3 Cyanogen Chloride (CK)

Figure 2-7. Cyanogen Chloride (CK)

Cyanogen chloride is a blood agent that has a molecular formula of CClN and molecular weight of 61.47 g/mol. The boiling point and melting point are 13 and -6.6 °C, respectively.[31] Pure CK is a clear, colorless liquid that has irritating effects on mucous membranes, that will often prevent one from noticing its pungent, biting odor.[52] The molecular structure of CK is shown in Figure 2-7. Physical parameters pertinent to the environmental fate of CK are shown in Table 2-5. For density values at other temperatures, Equation 2.3.1 has been developed to describe the density over the range of -5.8–14 °C[31] from a combination of studies. [11,53-56]

Table 2-5. Physical Properties of Cyanogen Chloride (CK)[10-12]

Physical Properties of Cyanogen Chloride		References
Solubility at 25 °C in Water	69 g/L	Romano [10]
Density at 0 °C	1.2 g/ml	Cook [11]
Henry's Law Constant, K_H, 20 °C	Not in available literature	
Vapor Pressure, 25 °C	1230 torr	Douglas [2]
Log K_{oc}	Not in available literature	
Log K_{ow}	Not in available literature	

$$D\left(\frac{g}{ml}\right) = 1.2228(\pm 0.0007) - 0.00208T(\pm 0.00008, °C) \quad \textbf{(2.3.1)}$$

Many values for the vapor pressure *(P)* have been reported for CK at room temperature. For temperatures in the range of HI-01, vapor pressure in the range of -12–17.82 °C is described by Equation 2.3.2 and comes from three studies.[2,11,57]

$$Log\ P(Torr) = 10.562 - \frac{4068}{T(K)} \quad \textbf{(2.3.2)}$$

The equilibrium solubility of CK in aqueous sodium chloride solution has been measured at 30 °C and may be estimated using Equation 2.3.3:[58]

$$[ClCN](M) = 0.91(\pm 0.05) - 0.16(\pm 0.03)[NaCl](M) \quad \textbf{(2.3.3)}$$

No literature values of log K_{ow}, log K_{oc}, or K_H were located in the available literature. However, the log of the partition between water and olive oil has been reported as 1.6.[59] The value for log K_{ow} would also be similarly low.

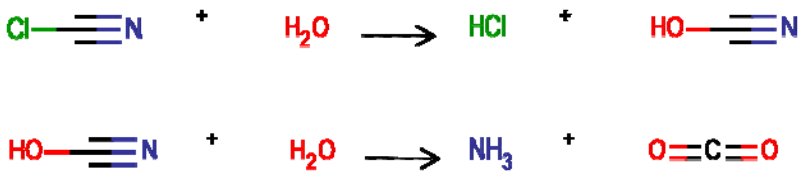

Figure 2-8. Hydrolysis Mechanism for Cyanogen Chloride (CK)

The primary fate of CK in water is hydrolysis to chloride and cyanate species, and subsequent hydrolysis of cyanic acid to ammonia and carbon dioxide, as shown in Figure 2-8. Rate constants have been reported for the hydrolysis reaction.[2,55,60] Analysis of these studies shows that the data fits a first-order rate constant over a temperature range of 5–45 °C and is expressed in Equation 2.3.4.

$$k_{obs}(s^{-1}) = 99.97 \times 108\ e^{-87180/8.134T(K)} + 2.06 \times 1011\ e^{-60980/8.134T(K)}\ [OH^-](mol/L) \quad \textbf{(2.3.4)}$$

At seawater pH, this expression yields that CK has a half-life of about 3 days at 25 °C, and 19 days at 5 °C. This expression only takes basicity into account. The chloride ion content in sea-water, however, will inhibit the hydrolysis slightly. On the basis of the relatively short half-life of CK, hydrolysis will dominate the fate of CK in the deep ocean should a munition be breached.

Cyanogen chloride is known to polymerize after long periods of containment.[61] The primary polymerization is to the trimer, cyanuric chloride. The reaction is violent and cylinders containing cyanogen chloride have been reported to explode.[62]

2.4 Hydrogen Cyanide (AC)

Hydrogen cyanide is a clear, colorless liquid with an odor of bitter almonds.[63] Hydrogen cyanide has a molecular formula HCN and a molecular weight of 27.026 g/mol. The molecular structure of AC is shown in Figure 2-9. There are many publications that reference both boiling and melting points. A review of these papers gives the average of these values as 25.9 and -13.3 °C, respectively.[31] Hydrogen cyanide is completely miscible with water at temperatures greater than -23.3 °C.[64] Relevant physical properties are listed in Table 2-6.

Figure 2-9. Hydrogen Cyanide (AC)

The density of HCN has been measured as a function of temperature many times. Bizzigotti et al. combined the data from these studies and fit Equation 2.4.1 for a temperature range of -13.3 to 25.7 °C:[31]

Table 2-6. Physical Properties of Hydrogen Cyanide (AC)[13,14]

Physical Properties of Hydrogen Cyanide		References
Solubility at 25 °C in Sea Water	miscible	Franke [4]
Density	0.68 g/ml	Franke [4]
Henry's Law Constant, K_H, 20 °C	1.22×10^{-4} atm m^3/mol	Yoo [12]
Vapor Pressure, 20 °C	630 torr	Perry [65]
Log K_{oc}	No Data	
Log K_{ow}	-0.25	Hansch [14]
pK_a, 25 °C	9.21	Beck [13]

$$D\left(\frac{g}{ml}\right) = 0.7161(\pm 0.0002) - 0.00142T(\pm 0.00001, °C) \quad \textbf{2.4.1}$$

The vapor pressure *(P)* of hydrogen cyanide has been also studied by several groups as a function of temperature.[65-67] Combining the studies yields Equation 2.4.2, which describes the vapor pressure *(P)* over the range of -8–46 °C.[31]

$$Log\ P(Torr) = 7.746(\pm 0.006) - \frac{1457(\pm 2)}{T(K)} \quad \textbf{(2.4.2)}$$

K_H has been measured as a function of temperature over the range 0–100 °C and fits Equation 2.4.3:

$$\ln K_H\ (kg - atm/mol) = 9.585 - 0.03147\ T\ (K) + \ln T - \frac{6302}{T(K)} \quad \textbf{(2.4.3)}$$

AC is a weak acid that has been measured as a function of temperature and obeys Equation 2.4.4:

$$\ln Ka = -12.1960 - 0.031482\ T\ (K) + 3.7658 \ln T - \frac{6340.7}{T(K)} \quad \textbf{(2.4.4)}$$

Several studies indicate that the pKa of AC decreases with the ionic strength of seawater, to a value of 8.95 at 25 °C.

AC hydrolyzes slowly at low pH to form ammonium ion and formic acid, but will not be a significant source of reaction under marine conditions. The major reactions of AC in surface water are volatilization and biotransformation. However, at HI-01, volatilization will be slowed dramatically. Therefore, biotransformation to ammonia and carbon dioxide is likely to be the major fate of AC in a deep water site, and is dependent on concentration, pH, temperature, availability of nutrients, and acclimation of microbes.[68-70] The U.S. Environmental Protection Agency has

found no data to indicate that AC bioconcentrates in aquatic organisms.[71] Information on nutrients and microbial populations in deep water is unlikely to be available. Therefore, estimating the lifetime of AC in deep waters from a breached munition is difficult.

Similar to CK, AC is also known to polymerize after long periods of containment.[61] The primary polymerization is to the trimer, *sym*-triazine. The reaction is violent and cylinders containing AC were reported to explode.[62] There was one study that worked to define the time sensitivity of the explosive nature of AC, and for a given system (container volume, temperature, amount of AC), equations were developed to estimate the time the AC would remain stable.[72] A similar set of experiments could be used to determine such equations for an AC-filled munition.

3 Conclusion

With the exception of AC, all of the agents undergo hydrolysis as the major chemical reaction in a marine environment. HD hydrolysis had two reaction pathways that lead to a benign thiodiglycol (TDG) compound. However, the sulfonium cation intermediates form stable salts with the ions in seawater, which allows droplets of HD with a "film" of sulfonium salt to exist for decades.

Lewisite undergoes rapid hydrolysis to a pair of compounds that exist in equilibrium: CVAA and lewisite oxide. This pair of compounds is no less toxic than the parent lewisite compound. In fact, the hydrolysis happens in water so rapidly, it has been proposed that these species are responsible *in vivo* for the effects of lewisite.[6] Further hydrolysis yields arsorous acid and finally inorganic arsenic.

CK hydrolyses first to cyanic acid and hydrochloric acid. These compounds exist as chloride and cyanate in seawater pH. Secondary hydrolysis of cyanic acid produces ammonia and carbon dioxide.

Volatilization and biotransformation are the major chemical reactions for AC in a marine environment. However, volatilization at HI-01 will be decreased significantly such that it may be considered negligible. Biodegradation of AC yields products of ammonia and carbon dioxide, but the extent of this reaction will be determined by the nutrient and microbial populations in the deep site.

For both CK and AC, spontaneous and violently explosive polymerization can occur after long periods of containment.

This Page Intentionally Left Blank.

noblis

4 References

1 Epstein, J., Rosenblatt, D. H., Gallacio, A. & McTeague, W. F. (ed Edgewood Arsenal) (Edgewood, MD, 1973).

2 Douglas, D. E. & Winkler, C. A. The preparation, purification, physical properties, and hydrolysis of cyanogen chloride. *Canadian Journal of Research* **25B**, 381 - 386 (1947).

3 Hopkins, E. F. On Dichloroehtylsulphide (Mustard Gas). III. Solubility and Hydrolysis of Dichloroethylsulphide with a New Method for Estimating Small Amounts of the Same. *Journal of Pharmacology* **12**, 393 - 403 (1919).

4 Franke, S. (ed Deutscher Militarverlag) (Translated from German by U. S. Department of Commerce, National Bureau of Standards, Institute for Applied Technology, Berlin, 1967).

5 Lyman, W. J., Reehl, W. F. & Rosenblatt, D. H. *Handbook of Chemical Property Estimation Methods*. (1981).

6 Munro, N. B. *et al.* The Sources, Fate, and Toxicity of Chemical Warfare Agent Degradation Products. *Environmental Health Perspectives* **107** (1999).

7 Redemann, C. E., Chaikin, S. W. & Fearing, R. B. The volatility and vapor pressure of eight 2-chloroethyl Alkyl (orcycloalkyl) sulfides. *Journal of the American Chemical Society* **70**, 631 - 633 (1948).

8 Meylan, W. M. & Howard, P. H. Atom/fragment contribution method for estimating octanol-water partition coefficient. *Journal of Pharmaceutical Science* **84**, 83 - 92 (1995).

9 Baes, C. F. (ed Oak Ridge National Laboratory) 58 (Oak Ridge, TN, 1984).

10 Romano, J. A., Lukey, B. J. & Salem, H. (CRC Press, Taylor & Francis Group, Boca Raton, FL, 2008).

11 Cook, R. P. & Robinson, P. L. Certain physical properties of cyanogen and its halides. *Journal of the Chemical Society*, 1001 (1935).

12 Yoo, K. P., Lee, S. Y. & Lee, W. H. Ionization and Henry's Law constants for volatile, weak electrolyte water pollutants. *Korean Journal of Chemical Engineering* **3**, 67 - 72 (1986).

13 Beck, M. T. Critical evaluation of stability constants of metal complexes in solution. Critical survey of stability constatns of cyano complexes. *Pure and Applied Chemistry* **59**, 1703 - 1720 (1987).

14 Hansch, C. & Leo, A. J. Medchem Project. *Claremont College* **Pomona College** (1985).

15 Herbst, H. Uber die Fluchtigkeit und Vernebelung einer Reihe Organischer Stoffe. *Kolloidchemische Beihefte* **23**, 313 (1926).

16 Meyer, V. Ueber Thiodiglykolverbindungen. *Chem. Ber.* **19**, 3259 - 3266 (1886).

17 Mohler, H. & Sorge, J. Chemische Kampfstoffe XV. Parachor von β, β′-Dichlor-diäthyl-sulfid, β-Chlordiäthyl-sulfid, Diäthyl-sulfid und Thio-diglykol. Einfache Apparatur zur Bestimmung der... *Helvetica Chimica Acta* **23**, 119 (1940).

18 Clarke, H. T. Synthersis of 4-alkyl-1,4-thiazans. *Journal of the Chemical Society, Transactions* **101**, 1583 (1912).

19 Davies, W. Synthetical experiments with β, β'-dichloroethyl sulphide. *Journal of the Chemical Society, Transactions* **117**, 297 (1920).

20 Felsing, W. A., Hunting, C. A. & Fell, S. D. The melting point of mustard gas. *Journal of the American Chemical Society* **70**, 1966 (1948).

21 Fuson, R. C., Lipscomb, R. D., McKusick, B. C. & Reed, L. J. Thermal conversion of mustard gas to 1,2-bis(2-chloroethylthio)ethane and bis[2-(2-chloroethylthio)ethyl] sulfide. *Journal of Organic Chemistry* **11**, 513 (1946).

22 du Vigneaud, V. & Stevens, C. M. Preparation of highly purified mustard gas and its action on yeast. *Journal of the American Chemical Society* **69**, 1808 (1947).

23 Mumford, S. A. & Phillips, J. W. C. Observations on the chlorination products of BB'-dichlorodiethyl sulphide. *Journal of the Chemical Society*, 155 (1928).

24 Gibson, C. S. & Pope, W. J. β, β'-Dichloroethyl Sulphide. *Journal of the Chemical Society* **117**, 271 (1920).

25 Wilkinson, J. A. & Wernlund, C. Density and coeffiecient of expansion of dechloroethyl sulfide. *Journal of the American Chemical Society* **42**, 1382 (1920).

26 Harkins, W. D., Clark, G. L. & Roberts, L. E. The orientation of molecules in surfaced, surface energy, adsorption, and surface catalysis. V. The adesional work between organic liquids and water *Journal of the American Chemical Society* **42**, 700 (1920).

27 Mumford, S. A., Phillips, J. W. C. & Ball, W. C. The vapour pressure of B Bə-dichlorodiethyl sulphide. *Journal of the Chemical Society*, 589 (1932).

28 Balson, E. W., Denbigh, K. G. & Asam, N. K. Studies in vapour pressure measurement. part I. - the vapour pressure of 2,2'-dichloroethylsulphide (mustard gas). *Transactions of the Faraday Society* **43**, 42 - 47 (1947).

29 Lamb, E. W., Carleton, P. W., Hughes, W. S. & Nichols, L. W. The copper flame test for halogens in air. *Journal of the American Chemical Society* **42**, 78 (1920).

30 Pecorella, S. S. & Macy, R. (ed U. S. Army Chemical Warfare Center) (Edgewood Arsenal, MD, 1943).

31 Bizzigotti, G. O., Castelly, H., Hafez, A. M., Smith, W. H. B. & Whitmire, M. T. Parameters for Evaluation of the Fate, Transport, and Environmental Impacts of Chemical Agents in Marine Environments. *Chemical Reviews* **109**, 236 (2009).

32 Buchanan, J. H., Buettner, L. C. & Tevault, D. E. (ed Development and Engineering Center Edgewood Research) (Aberdeen Proving Ground, MD, 2005).

33 Buchanan, J. H., Buettner, L. C. & Tevault, D. E. Vapor pressure of solid bis(2-chloroethyl) sulfide. *Journal of Chemical & Engineering Data* **51**, 1331 (2006).

34 Wilson, R. E., Fuller, E. W. & Schur, M. O. The solubility and specific rates of hydrolysis of mustard gas in water *Journal of the American Chemical Society* **44**, 2867 (1922).

35 Brookfield, K. J., Moelwyn-Hughes, E. A. & Phillips, J. W. C. (ed Military Intelligence Division) (Sutton Oak, UK, 1942).

36 Demek, M. M., Davis, G. T., Dennis, W. H. J., Hill, A. L. & Farrand, R. L. (ed Edgewood Arsenal) (Edgewood, MD, 1970).

37 Institute, S. I. P. R. (Taylor and Francis, London, 1980).

38 Jorgensen, B. S., Olesen, B. & Berntsen, O. Mustard gas accidents on Bornholm. *Ugeskr. Laefer* **147**, 2251-2254 (1985).

39 Small, M. J. (ed U. S. Army Medical Bioengineering Research and Development Laboratory) (Fort Detrick, MD, 1984).

40 Stein, W. H., Moore, W. & Bergmann, M. Chemical Reactions of Mustard Gas and Related Compounds. I. The Transformations of Mustard Gas in Water. Formation and Properties of Sulfonium Salts Derived from Mustard Gas. *Journal of Organic Chemistry* **11**, 664 (1946).

41 Yang, Y.-C., Szafraniec, L. L., Beaudry, W. T. & Ward, J. R. Direct NMR measurements of sulfonium chlorides produced from the hydrolyses of 2-chloroethyl sulfides. *Journal of Organic Chemistry* **52**, 1637 - 1638 (1987).

42 Yang, Y.-C., Szafraniec, L. L., Beaudry, W. T. & Ward, J. R. Kinetics and mechanism of the hydrolysis of 2-chloroethyl sulfides. *Journal of Organic Chemistry* **53**, 3293 - 3297 (1988).

43 Bartlett, P. D. & Swain, C. G. Kinetics of Hydrolysis and Displacement Reactions of β,β'-Dichlolrodiethyl Sulfide (Mustard Gas) and of β-Chloro-β-hydroxydiethyl Sulfide (Mustard Chlorohydrin). *Journal of the American Chemical Society* **71**, 1406-1415 (1949).

44 Castellan, G. W. *Physical Chemistry*. 2nd edn, (Addison-Wesley, 1971).

45 Whiting, J. H. Some physiochemical properites of cis-2-chlorovinyldichloroarsine. *Journal of the Chemical Society*, 1209 - 1210 (1948).

46 Gibson, C. S. & Johnson, J. D. A. A new complex hydrocarbon of the probable formula $C_{16}H_{14}$. *Journal of the Chemical Society*, 753 - 756 (1931).

47 Lebedev, B. V., Kulagina, T. G., Cheremukhina, A. A. & Karataev, E. N. Thermodynamic properties of (beta-chlorovinyl)dichloroarsine at 0 - 330 K and standard pressure. *Russian Journal of General Chemistry* **66**, 880 - 885 (1996).

48 Redemann, C. E., Chaikin, S. W., Fearing, R. B. & Benedict, D. The volatility and vapor pressure of nine organic arsines. *Journal of the American Chemical Society* **70**, 637 - 639 (1948).

49 Lewis, W. L. & Perkins, G. A. The beta-chlorovinyl chloroarsines. *Industrial Engineering and Chemical Research* **15**, 290 - 295 (1923).

50 Waters, W. A. & Williams, J. H. Hydrolyses and Derivatives of Some Vesicant Arsenicals. *Journal of the Chemical Society*, 18 - 22 (1950).

51 Rovida, G. Richerche sperimentali con la Lewisite. I. Storia e generality della Lewisite. Il comportamento delle clorovinilcloroarsine con l'aqua. *Sperimentale* **80**, 5 (1926).

52 Stewart, C. E. *Weapons of Mass Casualties and Terrorism Response Handbook*. (Jones and Bartlett Publishers International, 2006).

53 Mauguin, C. & Simon, L. J. Sur la preparation et quelques constantes physiques du chlorure de cyanogene. *J Ann. Chim.* **9**, 18 - 41 (1921).

54 Enklaar, C. J. Deterinations de structure en rapport avec la theorie des electrons. *Recueil des Travaux Chimiques des Pays-Bas* **42**, 1000 - 1016 (1923).

55 Price, T. S. & Green, S. J. The preparation of cyanogens chloride on a large laboratory scale. *Journal of the Society of Chemical Industry* **39**, 98T - 101T (1920).

56 Gordon, A. R. & Benson, G. C. Liquid-vapor equilibrium for the system hydrogen cyanide-cyanogen choride. *Canadian Journal of Research* **24B**, 285 - 291 (1946).

57 Klemenc, A. & Wagner, G. Bernerkungen uber das Cyanchlorid. *Zeitschrift fuer Anorfanische und Allgemeine Chemie* **235**, 427 - 430 (1938).

58 Lister, M. W. Some observations on the hydrolysis of cyanogen chloride. *Canadian Journal of Chemistry Pays-Bas* **35**, 736 - 739 (1957).

59 Macy, R. Partition coefficients of fifty compounds between olive oil and water at 20 degrees C. *Journal of Industrial Hygiene Toxicology* **30**, 140 - 143 (1948).

60 Pedersen, E. J. I. & Marinas, B. J. The hydroxide-assisted hydrolysis of cyanogen chloride in aqueous solution. *Water Research* **35**, 643 - 648 (2001).

61 Migridichian, V. *The Chemistry of Organic Cyanogen Compounds*. (Reinhold Publishing Company, 1947).

62 Aaron, H. S. *et al.* (ed U. S. Army Research Laboratory) (Aberdeen Proving Ground, MD, 1996).

63 Ruth, J. Odor thresholds and irritation levels of several chemical substances: a review. *Journal of American Industrial Hygiene Association* **47**, 299 - 302 (1986).

64 Coates, J. E. & Hartshorne, N. H. Studies on hydrogen cyanide: III. The freezing points of hydrogen cyanide-water mixtures. *Journal of the Chemical Society*, 657 - 665 (1931).

65 Perry, J. H. & Porter, F. The vapor pressures of solid and liquid hydrogen cyanide. *Journal of the American Chemical Society* **48**, 299 - 302 (1926).

66 Giauque, W. F. & Ruehrwein, R. A. The entropy of hydrogen cyanide, heat capacity, heat of vaporization and vapor pressure, hydrogen bond polymerization of the gas in chains of indefinite length. *Journal of the American Chemical Society* **61**, 2626 - 2633 (1939).

67 Hara, R. & Sinozaki, H. The vapor pressure of hydrocyanic acid. *Kogyu Kagaku Zasshi* **26**, 84 - 85 (1923).

68 Ebbs, S. Biological degradation of cyanide compounds. *Current Opinions in Biotechnology* **15**, 231 - 236 (2004).

69 Ludzack, F. J., Moore, W. A., Krieger, H. L. & Ruchhoft, C. C. Effect of cyanide on biochemical oxidation in sewage and polluted water. *Sewage Inustrial Wastes* **23**, 1298 - 1307 (1951).

70 Boening, D. W. & Chew, C. M. A Critical Review: General Toxicity and Environmental Fate of Three Aqueous Cyanide Ions And Associated Ligands. *Water Air Soil Pollution* **109**, 67 - 79 (1999).

71 Agency, U. S. E. P. Vol. 1 (ed Office of Water and Waste Mangement Office of Water Planning and Standards) (Washington, D. C., 1979).

72 Gause, E. H. & Montogmery, P. D. Hydrogen Cyanide Stability and Heat of Polymerization. *Journal of Chemical and Engineering Data* **5**, 351 - 354 (1960).

Modeling Chemical Transport at the Deep Ocean Disposed Munitions Site near O'ahu

Dr. Melissa Rice

24 May 2012

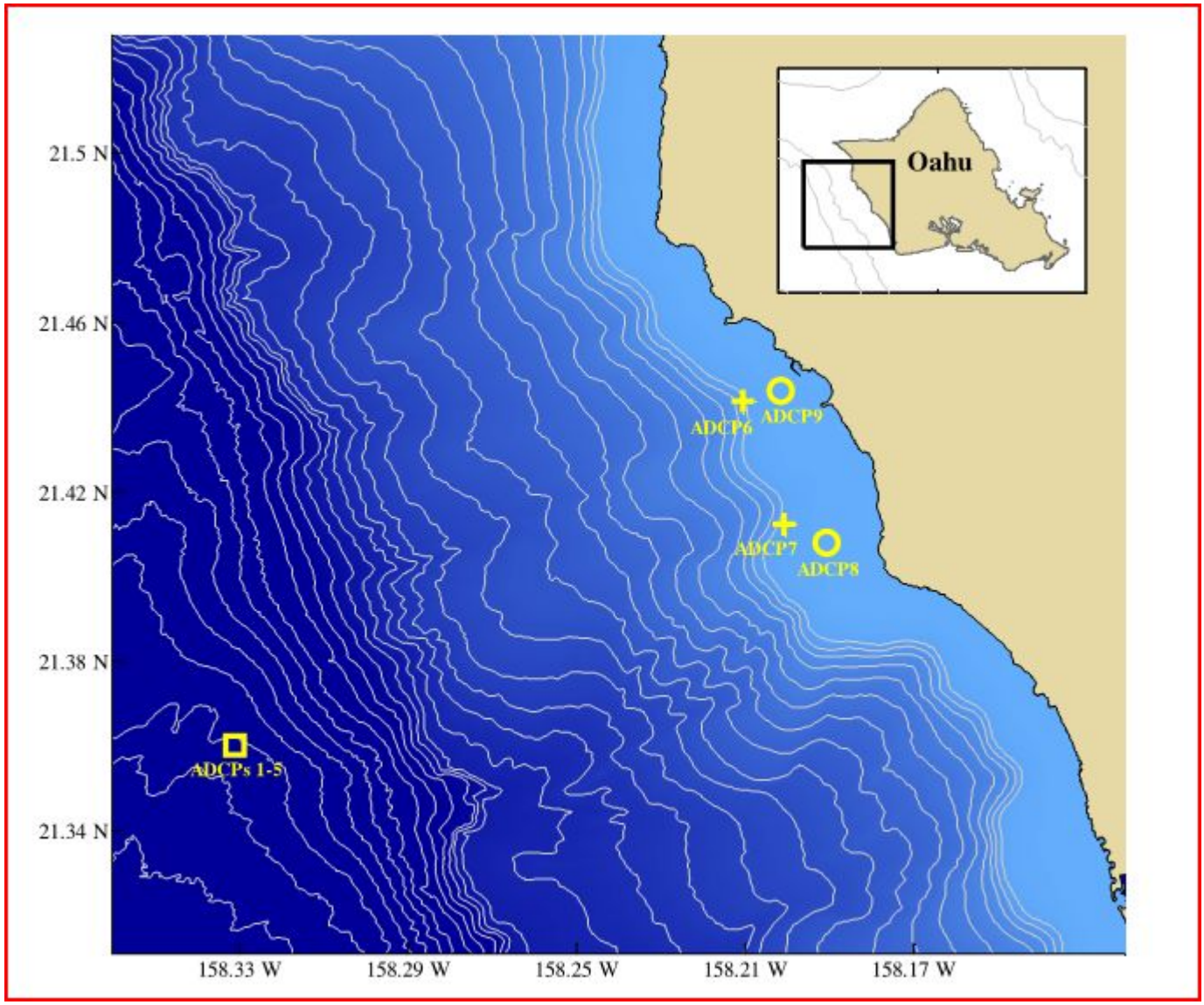

Contents

This report presents the results of modeling the ocean transport of disposed chemical warfare agents which might potentially be released from a deep ocean disposal site off the west coast of O'ahu in the Hawai'ian Islands chain. Disposal occurred during the 1940s in water about 2500 meters (over 1.5 miles) deep. The actual fate of these chemicals isnt known and would be difficult to ascertain given their depth. The purpose of this work is to estimate where these chemicals might be transported to, in what concentration, and for what exposure time, in the event that they are released.

The summary conclusion of this analysis is that concentrations in excess of 1 ppb are unlikely to be transported to areas which are more than about 300 meters above the bottom. Areas experiencing concentrations higher than 1 ppb in these very deep waters are limited to areas within roughly 5–16 km of the disposal site in the cross-shore direction and roughly 10–45 km in the along-shore direction (depending on model assumptions), suggesting that O'ahu would not be within the path of the plume in the event of a release.

1 Introduction

Until the 1970s it was standard practise to dispose of unwanted munitions, ordnance, and chemical warfare agents in the ocean. There are two sites off the west (leeward) coast of O'ahu where such disposal is known to have occurred during this period. At a shallow site, called Ordnance Reef, discarded military munitions were disposed in waters approximately 9–91 m (30–300 ft) deep. This site is the subject of other studies ([Ordnance Reef Hawaii, 2011]). The present study focuses on a deep-water site where chemical warfare agents were disposed.

Roughly 10 nautical miles off the west coast of O'ahu, at approximately 21.360 N latitude and 158.331 W longitude, in 2528 m (over 1.5 miles) of water, approximately 2,000 tons of chemical warfare agents (including mustard, cyanogen chloride, lewisite, and cyanide) were disposed during the 1940s. The disposed chemicals were packaged as munitions, ordnance, or in ton containers. These were further packaged in steel shipping containers prior to disposal.

Beginning in July 2009, about 13 months of current data was collected at the site and we use this data, together with a simple chemical transport model, to estimate how the chemicals might be dispersed in the event that they either were released in the past or might be released in the future.

Section 2 develops the physics of chemical transport, including a brief discussion of the chemicals concerned and their packaging in section 2.1, development of the governing equation for chemical transport (the advection-diffusion equation) in section 2.2, discussion of initial and boundary conditions in section 2.3, and a discussion of turbulent diffusivity and mixing in section 2.4.

The velocity data for the deep disposal site was collected at one x-y location over a 13 month period at various depths in the bottom 620 m (approximately 2000 ft) of the water column using a string of Acoustic Doppler Current Profilers (ADCPs). This data set is discussed in detail in section 3.

Considering the velocity field as known (based on the measured data), chemical transport is modeled by a linear partial differential equation for concentration, which is solved analytically under certain simplifying assumptions. These models are developed in section

4 and the results are presented in section 5. In particular, pathlines are computed which estimate the advection of the plume center based on various potential release times (section 5.1) and based on these pathlines, concentration, exposure time, and exposure footprints are computed (section 5.2) which estimate where the chemical will be transported to, in what concentration, and for what exposure time, in the event of a release of the disposed chemicals from their containers. In addition, footprints are computed for a smaller release under a variety of diffusivity assumptions (section 5.3). Finally, in section 6, conclusions are drawn based on these estimated potential transport scenarios.

2 The Physics of Chemical Transport

The physical transport processes at work include advection, molecular diffusion, shear mixing (in the boundary layer near the sea floor), and turbulent diffusion. These processes are assumed to act on neutrally-buoyant dissolved chemicals, so in section 2.1 we briefly discuss the disposed chemicals involved to establish that it is appropriate to model their transport in this way and to discuss the selection of release amounts for modeling.

Advection is movement due to ocean currents. Velocity data are available at one location in x,y and at a number of depths, sampled in time over the course of approximately 13 months. We assume that currents do not vary in x or y (horizontally) and are given by the measured velocities in the z-direction (vertically) and in time. Further discussion of the velocity data is found in section 3.

Turbulent diffusion is the name given to mixing by turbulent fluid motion which occurs at a scale below the resolution of our measurements of the velocity field (i.e., subgrid advection). Empirically, these motions have an effect which is modeled well as a diffusive process, with associated diffusivities much larger than for molecular diffusion. As a result, molecular diffusivity is considered to be subsumed into the larger turbulent diffusivity, which is empirically estimated. Selection of values for the turbulent diffusivities is discussed in section 2.4, as are other issues related to mixing.

The models used in this report are simplified models which admit analytical solutions. They do not directly model shear mixing and consequently may somewhat overstate concentrations. In this regard, the models are viewed as conservative. We also use bracketing scenarios of different values of turbulent diffusivity as a surrogate method of placing outer bounds on the effects of decreased or increased mixing.

The advection-diffusion equation with known velocity $(u(z,t), v(z,t), w(z,t))$ is developed and discussed in section 2.2. Although this is a linear partial differential equation, closed-form analytical solutions are not known in general for arbitrary velocity fields. There is also the matter of setting initial and boundary conditions, which influences both the ease with which the equation is solved as well as the character of the solutions. The selection of appropriate initial and boundary conditions is discussed in section 2.3.

2.1 Disposed Chemicals

The model developed in this report does not depend explicitly on specific physical properties of the released chemicals other than assuming that they are neutrally buoyant when dissolved in water. The model makes the idealization that a quantity, Q kg, of a chemical is instantaneously released from a point source and rapidly dissolves in water. Consequently, the discussion of the particular chemicals in this report will be limited to that information which is likely to suggest physically reasonable Q values and to establishing that the chemicals are neutrally buoyant when dissolved in water and do not float.

Since the modeled concentration is linear in Q the value selected for Q is not particularly critical in the sense that the model predictions for concentrations can be scaled linearly for different Q values. That is, doubling Q simply causes all predicted concentrations to double, while halving Q similarly causes all predicted concentrations to be halved. However, exposure and exposure times do not scale linearly.

The chemical warfare agents known to have been disposed at the deep water site under

study are sulfur mustard (HD), cyanogen chloride (CK), Lewisite (L), and hydrogen cyanide (AC). Table 1 shows disposed quantities and most prevalent packaging for each chemical. Roughly half of the chemicals were packaged as bombs, projectiles, or mortar shells. The other half of the chemicals were packaged in ton containers. Additional detail of the packaging of the chemicals is available in the table NOAA DMM Chemicals [2010]. All of these packaged chemicals were additionally placed in steel shipping containers prior to disposal. Structural analysis of the likely effects of pressure and corrosion from seawater on the packaging are detailed in the report Jackson et al. [2007].

Table 1: Chemicals Dumped at the Deep-Water DMM Site

Chemical Name (code)	Total Disposed (tons)	Most prevalent packaging
Mustard (HD)	1,525	ton containers (817kg each)
Cyanogen Chloride (CK)	204	large ordnance (159 kg each)
Lewisite (L)	181	ton containers (862 kg each)
Hydrogen Cyanide (AC)	2	large ordnance (91 kg each)
Total	1,912	

According to Noblis Chemical Munitions Report [2011] and the NOAA summary thereof [NOAA Chemical Warfare Agents Summary, 2011], of the four chemical warfare agents disposed at the deep water site, hydrogen cyanide (AC) is the one of most concern for possible transport because it is completely miscible in water at 0° C (hence would immediately dissolve, if released) and is likely to persist in toxic form in solution. Fortunately, there was relatively little hydrogen cyanide disposed at this site compared to the other chemicals. According to NOAA DMM Chemicals [2010], the disposed hydrogen cyanide was packaged as 20 large bombs, each containing about 91 kg (200 lbs) of hydrogen cyanide. Thus $Q = 91$ kg would be representative of one such munition being breached and the contents immediately dissolving.

Mustard (HD), which accounts for nearly 80% (by mass) of the disposed chemicals at this site, is denser than water, sparingly soluble, and hydrolyzes to benign compounds [Noblis Chemical Munitions Report, 2011]. A notable hazard of mustard is that it can form encrusted balls which persist for decades and have been accidentally brought up in fisherman's trawls [Danish Environmental Protection Agency, 1994, Beddington and Kinloch, 2005]. This should be less of a concern at this site due to its depth, as well as to the fact that it is already off limits to fishing due to the presence of communications cables on the sea floor. In any case, the present model is only concerned with modeling that amount of chemical which has dissolved and is therefore amenable to transport in the water column.

Lewisite is also denser than water and sparingly soluble. All of its breakdown products are toxic, and some are more soluble than Lewisite itself, but the rate at which they are produced is limited by the slow dissolution of the Lewisite [NOAA Chemical Warfare Agents Summary, 2011].

According to NOAA Chemical Warfare Agents Summary [2011]: "Since they dissolve very slowly, these compounds [Lewisite and mustard] reach a concentration close to their

human levels of concern only a matter of feet away from any possible source, and thus are expected to have no impact on human health under these conditions."

Cyanogen chloride is denser than water and significantly soluble in water but reacts with water to form compounds which are not dangerous [NOAA Chemical Warfare Agents Summary, 2011].

Both cyanogen chloride and hydrogen cyanide can explosively polymerize after long periods of containment [NOAA Chemical Warfare Agents Summary, 2011], hence larger Q values might be physically reasonable in the event of an explosion. We do not model an actual explosion, but merely consider that an explosion might release a larger amount of chemical.

It is clear that none of the disposed chemicals will float since all are denser than water except hydrogen cyanide, which is completely miscible and will therefore dissolve rather than float. Therefore, the transport of each of these chemicals in the water column can be modeled by the techniques developed here, to the extent that each dissolves in water. Any material which remains undissolved is assumed not to be transported from the disposal site. We do not model chemical interactions nor breakdown of chemicals.

Based on this information, an initial release amount of $Q = 182$ kg was selected because hydrogen cyanide is the chemical of most concern (the most likely to be transported in toxic form) and the disposed hydrogen cyanide at this site was packaged in 91 kg munitions. Thus, we model the reasonable scenario of the release of hydrogen cyanide from two munitions. However, for the comparative diffusivity study in section 5.3, an initial release amount of $Q = 91$ kg was used.

2.2 Governing Equation Development

We will model the advection and diffusion of a neutrally buoyant chemical species dissolved in water, assuming incompressible flow. Neither chemical interaction nor breakdown is modeled, and the model does not rely on any specific chemical properties beyond the assumption of neutral buoyancy. Consequently, the model will produce the same concentration estimates regardless of the particular chemical which is transported, and depending only on the mass of chemical released.

The velocity field is considered to be known since it is measured at discrete points in time and in the z-direction (vertically) and is assumed not to vary horizontally (in the x and y directions). The following notation is used:

t	time
$\vec{x} = (x, y, z)$	position in space
$\vec{u} = (u(z,t), v(z,t), w(z,t))$	measured velocity field
$c = c(\vec{x}, t) = c(x, y, z, t)$	concentration of the chemical species
$\vec{f} = \vec{f}(\vec{x}, t) = (f_1(x, y, z, t), f_2(x, y, z, t), f_3(x, y, z, t))$	flux of the chemical species
$\vec{K} = (K_H, K_H, K_V)$	turbulent diffusivities
Q	mass of released chemical

The governing principle for chemical transport in an incompressible flow is that changes in the chemical concentration $c(\vec{x}, t)$ in time are the result of advection (movement by currents) and diffusion (molecular and turbulent), where turbulent diffusion is understood as

an empirical method of modeling mixing due to turbulent advection occurring at scales below the resolution in time and space of the velocity measurements. We model the chemical release as an instantaneous point source in the initial conditions, which is discussed in the next section, and which explains why there is no source term in the differential equation.

Considering molecular diffusion only, for the moment, Fick's first law states that the flux of the chemical species ($\vec{f}(t,\vec{x})$) is proportional to the concentration gradient of the chemical species (∇c) with the diffusivity, K, as the constant of proportionality:

$$\vec{f}(t,\vec{x}) = -K\nabla c.$$

Fick's second law states that the time rate of change in concentration ($\partial c/\partial t$) is the result of diffusion (i.e., changes in the flux: $-\nabla\cdot\vec{f}$), which is to say:

$$\begin{aligned}\frac{\partial c}{\partial t} &= -\nabla\cdot\vec{f}\\ &= -\nabla\cdot(-K\nabla c)\\ &= K\nabla^2 c.\end{aligned}$$

Thus, with constant diffusivity, in the absence of advection, the fate of chemical pollutants in the water is governed by the same equation as for heat diffusion, a classic parabolic, linear partial differential equation.

Considering advection (chemical transport due to currents and tides) as well as molecular diffusion, the flux becomes

$$\vec{f}(t,\vec{x}) = -K\nabla c + \vec{u}c.$$

If we had perfect knowledge of the velocity field at all points of time and space this flux model would be accurate. However, there are subgrid turbulent motions (below the temporal and spatial resolution of our measurements of the velocity field) which result in a greater rate of mixing than this flux model would predict based on our imperfect knowledge of the velocity field. Empirically, these turbulent mixing processes are found to be well-modeled as diffusive processes, but the associated proportionality constants (which we will call turbulent diffusivities) are much larger than molecular diffusivities. As a result, we consider the turbulent diffusivities to subsume the molecular diffusivities. Henceforth, K will represent turbulent diffusivity.

There are two further complications in properly modeling the turbulent diffusivity, the first of which is that density stratification severely restricts vertical motions in the ocean in comparison to horizontal motions and, consequently, the vertical turbulent diffusivity, K_V, is generally observed to be at least several orders of magnitude smaller than the horizontal turbulent diffusivity, K_H. The second complication is that turbulent diffusivities are sometimes modeled as depending either on time or space variables, depending on a variety of factors. The details of these issues are discussed more thoroughly in section 2.4, but for now let it suffice to say that we will consider both K_H and K_V to be constant but with different values.

It is notationally convenient to write K as a vector with $\vec{K} = (K_H, K_H, K_V)$. For notational compactness we will write $\vec{K}.\nabla c$ to signify the component-wise product of $\vec{K}$ with ∇c, so that $\vec{K}.\nabla c$ is the vector

$$\vec{K}.\nabla c = \left(K_H\frac{\partial c}{\partial x}, K_H\frac{\partial c}{\partial y}, K_V\frac{\partial c}{\partial z},\right).$$

Considering both advection and turbulent diffusivity, the flux becomes

$$\vec{f}(t,\vec{x}) = -\vec{K}.\nabla c + \vec{u}c$$

and applying Fick's second law to this flux, together with the assumption of incompressible flow ($\nabla \cdot \vec{u} = 0$) we have:

$$\begin{aligned}
\frac{\partial c}{\partial t} &= -\nabla \cdot \vec{f} \\
&= -\nabla \cdot (-\vec{K}.\nabla c + \vec{u}c) \\
&= \nabla \cdot (\vec{K}.\nabla c) - \vec{u} \cdot \nabla c - c\nabla \cdot \vec{u} \\
&= \nabla \cdot (\vec{K}.\nabla c) - \vec{u} \cdot \nabla c
\end{aligned}$$

which, in fully expanded notation, is the advection-diffusion equation governing the transport of chemicals which are approximately neutrally buoyant:

$$\frac{\partial c}{\partial t} = K_H \frac{\partial^2 c}{\partial x^2} + K_H \frac{\partial^2 c}{\partial y^2} + K_V \frac{\partial^2 c}{\partial z^2} - u\frac{\partial c}{\partial x} - v\frac{\partial c}{\partial y} - w\frac{\partial c}{\partial z}. \tag{1}$$

A similar development of the governing equations may be found in Nihoul [1975, equation 3.21 on page 78] or Fischer et al. [1979, equation 2.59 on page 51]. Recall that the scalar concentration field, $c = c(\vec{x}, t)$, is the only unknown and that the velocities u, v, and w are considered known quantities varying only in z and t for the purposes of this model because we have empirical data for the velocity field. Consequently (1) is a homogeneous, second order, linear, parabolic partial differential equation with variable coefficients. Adding a source term would render the equation non-homogeneous. For the present analysis we leave the source in the initial condition, as will be elaborated below.

2.3 Initial and Boundary Conditions

Because (1) is an evolution equation in time and space, it should have both initial and boundary conditions in order to be well-defined (that is, for questions of the existence of a unique solution to make sense). The initial and boundary conditions we choose depend on the solution method as well as the physics. For the simplified models which have analytical solution, we use a point source initial condition and unbounded domain in all of the spatial dimensions. This is physically unrealistic in the z-direction but leads to a very simple and useful analytical solution. These initial and boundary conditions are developed in section 2.3.2.

A more physically reasonable formulation would be a spatial domain bounded in z with zero-flux conditions at the seafloor and air-sea boundaries. This is developed in section 2.3.1. In both of these cases the mathematically simple formulation of point source release is used.

As a general rule of thumb, the solution of an initial-boundary value problem is most heavily influenced in its early evolution by the initial conditions; in its intermediate evolution by the governing equation(s); and in its long-time evolution by the boundary conditions. With this in mind, we note that the use of an instantaneous point source release model might result in a very early evolution of the concentration field which is faster than would be expected in reality. A more complex but more realistic approach would be to treat the

source as a steady release of chemical over time modeled as a non-homogeneous term in the governing equation. This adds complexity and is worth pursuing, but is not investigated in the current report due to time constraints.

Another approach to introducing the chemical would be to use initial conditions which involve a constant concentration of chemical confined to a rectilinear region as an initial condition. This has a simple mathematical solution involving the error function (erf) which is considerably more time consuming to compute than a Gaussian function, since erf is an indefinite integral of a Gaussian function. In section 4.2 we compare these two solutions and see that they are essentially identical after a few seconds of evolution.

2.3.1 Unbounded x, y domain and bounded z domain with point source release

From a physical point of view, particularly since we assume no velocity variation in the x- and y-directions, it seems reasonable to model the ocean as infinite horizontally and to assume that both concentration and concentration gradients go to zero as $x, y \longrightarrow \pm\infty$. Physically, we expect the chemical to become more and more diluted as the plume spreads over, and mixes with, a larger and larger volume of ocean.

On the other hand, selecting horizontal boundaries for the ocean would force the selection of boundary conditions at those locations, which are bound to be somewhat arbitrary or unphysical. That is, at a particular finite horizontal location, we don't know what the concentration or concentration gradient is, but hope for the model to predict this. If we set this as a boundary condition the model will predict what we specified, which is unhelpful. So an unbounded x, y domain seems most desirable from a physical standpoint.

As an initial condition, we take

$$c(\vec{x}, 0) = Q\delta_a(x, y, z) \tag{2}$$

where $\delta_a(x, y, z)$ is the Dirac delta centered at $(x, y, z) = (0, 0, a)$ and Q expresses the mass of the initial release. To be clear, the Dirac delta is an impulse function and is therefore defined not by its pointwise values, but by its behavior when integrated against a smooth function f:

$$f(0, 0, a) = \int\int\int \delta_a(x, y, z) f(x, y, z)\, dx\, dy\, dz.$$

We can think of this initial condition as representing a mass, Q, of chemical being instantly released at time $t = 0$ at the location $(x, y, z) = (0, 0, a)$ where a represents the height of the container or some other relevant height, and the location $(x, y) = (0, 0)$ represents the horizontal center of the disposal area. Expressing the chemical release in this way is both mathematically convenient and likely to be conservative in the sense of not underestimating the impact of a release. Releasing the chemical slowly over time would be expected to result in better dispersal since the currents vary in direction over time and since smaller releases will quickly disperse below the level of concern under the action of diffusion.

The boundary conditions in the z-direction should express the physical reality that there is no chemical flux through the ocean floor boundary ($z = 0$), nor through the air-sea boundary ($z = h$), which we can express as

$$\frac{\partial c}{\partial z}(z, t) = 0 \qquad \text{for } z = 0, h \tag{3}$$

for constant K_V.

In the x and y directions it seems most natural to consider the ocean to be infinite with concentration and concentration gradients going to zero as x and y go to infinity. That is:

$$c(\vec{x},t) \longrightarrow 0 \qquad \text{as } x,y \longrightarrow \pm\infty \tag{4}$$

$$\frac{\partial c}{\partial x}(\vec{x},t) \longrightarrow 0 \qquad \text{as } x,y \longrightarrow \pm\infty \tag{5}$$

$$\frac{\partial c}{\partial y}(\vec{x},t) \longrightarrow 0 \qquad \text{as } x,y \longrightarrow \pm\infty. \tag{6}$$

To summarize, a reasonable initial-boundary value problem to model chemical transport would be:

$$\frac{\partial c}{\partial t} = K_H\frac{\partial^2 c}{\partial x^2} + K_H\frac{\partial^2 c}{\partial y^2} + K_V\frac{\partial^2 c}{\partial z^2} - u\frac{\partial c}{\partial x} - v\frac{\partial c}{\partial y} - w\frac{\partial c}{\partial z} \tag{7}$$

$$c(\vec{x},0) = Q\delta_a(x,y,z) \tag{8}$$

$$\frac{\partial c}{\partial z}(z,t) = 0 \qquad \text{for } z = 0,h \tag{9}$$

$$c(\vec{x},t) \longrightarrow 0 \qquad \text{as } x,y \longrightarrow \pm\infty \qquad \text{for } t > 0 \tag{10}$$

$$\frac{\partial c}{\partial x}(\vec{x},t) \longrightarrow 0 \qquad \text{as } x,y \longrightarrow \pm\infty \qquad \text{for } t > 0 \tag{11}$$

$$\frac{\partial c}{\partial y}(\vec{x},t) \longrightarrow 0 \qquad \text{as } x,y \longrightarrow \pm\infty \qquad \text{for } t > 0 \tag{12}$$

where K_H and K_V are constant and Q represents the mass of the initial release of chemical.

The solutions to this initial-boundary value problem involve Gaussian diffusion in the x and y directions and a Sturm-Liouville problem in the z direction resulting in an eigenfunction expansion in the z-direction in cosine functions. This formulation is ideal for a semi-analytical approach to the solution of the full problem where the velocity field varies arbitrarily in z and t. The time available for the work did not permit the completion of this approach, but it is recommended as a good direction for follow-up work, along the lines of what was done in Alves et al. [2001]. The next section develops a formulation which is mathematically simpler but does not model shear mixing.

2.3.2 Unbounded x, y, z domain with point source release

Although it is somewhat unphysical to consider the ocean unbounded in the z-direction, it is very convenient mathematically, and leads to an extremely simple Gaussian analytical solution where the source term is modeled, as above, as a Dirac delta in the initial conditions and where velocities do not depend on z. In this case, assuming constant turbulent diffusivities K_H and K_V and an initial mass Q of chemical released instantaneously at $t = 0$, we have the following initial boundary value problem for concentration.

$$\frac{\partial c}{\partial t} = K_H \frac{\partial^2 c}{\partial x^2} + K_H \frac{\partial^2 c}{\partial y^2} + K_V \frac{\partial^2 c}{\partial z^2} - u\frac{\partial c}{\partial x} - v\frac{\partial c}{\partial y} - w\frac{\partial c}{\partial z} \tag{13}$$

$$c(\vec{x}, 0) = Q\delta_a(x, y, z) \tag{14}$$

$$c(\vec{x}, t) \longrightarrow 0 \quad \text{as } x, y, z \longrightarrow \pm\infty \quad \text{for } t > 0 \tag{15}$$

$$\frac{\partial c}{\partial x}(\vec{x}, t) \longrightarrow 0 \quad \text{as } x, y, z \longrightarrow \pm\infty \quad \text{for } t > 0 \tag{16}$$

$$\frac{\partial c}{\partial y}(\vec{x}, t) \longrightarrow 0 \quad \text{as } x, y, z \longrightarrow \pm\infty \quad \text{for } t > 0 \tag{17}$$

$$\frac{\partial c}{\partial z}(\vec{x}, t) \longrightarrow 0 \quad \text{as } x, y, z \longrightarrow \pm\infty \quad \text{for } t > 0. \tag{18}$$

We use this formulation in the present work in order to achieve useful and reasonable predictions for chemical transport within the time frame available for the work. One caveat regarding this formulation is that it does not prevent transport of chemical in the negative z domain (below the seafloor). This will be discussed in more detail when the solution is developed.

2.4 Turbulent Diffusivities and Mixing

Physical processes which promote mixing are important in determining the transport and fate of chemical releases in the ocean, but models have limitations in the degree to which these mixing processes can be accurately modeled. We discuss the nature and implications of the some of the modeling decisions made here which affect mixing, as well as some general background related to mixing scales in the deep ocean.

Any numerical model which relies on an Eulerian framework or spatial-temporal grid has limited resolution and processes occurring below this resolution cannot be represented in the same way by the model as were the larger scale processes. Advection on the scale of the velocity measurement grid is directly modeled since the velocity field is treated as a known quantity on this scale, but advection below this scale must necessarily be modeled in some empirical way since we don't have measurements at finer resolution. In the present work, turbulent diffusivity is used in this way. Rather than attempt to reproduce fine scale advective processes which were not measured, we treat them as diffusive in nature. Diffusive processes are like smoothing operators which blur out gradients and hence have a different character than complex turbulent motions which stretch, strain, and fold the fluid, producing complex streaky structures. Yet, it is hoped that diffusive processes can roughly model the dispersive nature of these more complex turbulent processes and mimic their tendency to eventually dissipate chemicals through mixing.

In fact, it has been shown [Thiffeault et al., 2004] that the mixing efficiency of a particular flow field can be characterized by bounds in such a way that similar mixing effects can be achieved by diffusive processes by choosing appropriate effective diffusivity values. This suggests that we can bound the mixing behavior of any unmodeled processes by suitably bracketing with different effective diffusivity values.

As will be seen below, the most difficult aspect of solving the advection-diffusion equation is the z dependence of the velocity field. We approach this difficulty by considering advection along a pathline where the pathline we choose is the one starting at the location and time

of the chemical release. This results in advection of the diffusing chemical plume along the path taken by an imaginary particle traveling in the flow field at the center of the plume. This approach skirts the difficulty of explicit dependence of velocity on z by making the z-dependence implicit, based on the time-parameterized path of the plume center. This lets us take some advantage of the z-dependence of velocity without having it explicitly in the equation, however it does not produce the same complex solutions as explicit and general dependence of the velocity on z. The character of the resulting solutions is very simple: Gaussian diffusion about a moving center. This solution will not reproduce shear mixing or the streakiness, stretching, straining, and folding of a real flow field. However, we hope that by exploring a range of values for effective diffusivity, we can bound the mixing behavior in a simpler way using diffusive processes. Henceforth, we will refer to these effective diffusivities as turbulent diffusivities.

Another complication is that turbulent diffusion in the context of chemical transport is generally modeled as being scale-dependent [Garrett, 2006]. That is, a small chemical plume will experience mixing as a result of motions on scales which are smaller than the plume. Motions on scales much larger than the plume will tend to advect the entire plume without mixing it. Thus, as the plume grows in size, over time, due to diffusion and mixing, the scales of turbulence which tend to cause mixing in the plume will change and hence the turbulent diffusivity will change. Our present model does not use time-dependent diffusivity, though it would be interesting to explore this. For the present study, we take the position that bracketing the expected range of mixing behaviors by use of different fixed values of the turbulent diffusivities is expected to be adequate to estimate the transport of chemical plumes for the purpose of assessing the potential for risk to humans or the environment in the event of a chemical release.

Values for turbulent diffusivity in abyssal environments have been inferred in a variety of ways [Garrett, 2006] and an interesting new study describes a method for estimating turbulent diffusivity in an Eulerian framework from ADCP current readings [Holtappels and Lorke, 2011]. This has not been applied to the velocity data in this project as yet, though it would be interesting to pursue. For present, we use a range of widely accepted values for turbulent diffusivities in the horizontal (K_H) and vertical (K_V) directions.

Based on a study of diapycnal mixing completed on the opposite side of the Hawai'ian ridge from the deep water disposal site [Finnigan et al., 2002], values of K_V as high as $O\left(10^{-3}m^2/s\right)$ were observed at a station at 2500 m depth, thought to be related to enhanced mixing due to interaction of the topography with tidally-driven internal waves. More typical estimates of abyssal K_V are $O\left(10^{-4}m^2/s\right)$ or $O\left(10^{-5}m^2/s\right)$ [Decloedt and Luther, 2010]. We take $K_V = 10^{-4}m^2/s$ or $(1cm^2/s)$ as a nominal value, and consider $K_V = 10^{-3}m^2/s$ and $K_V = 10^{-5}m^2/s$ as reasonable bracketing values [Glover et al., 2011]. For horizontal turbulent diffusivity, we take $K_H = 1m^2/s$ as a nominal value, with bracketing values of $K_H = 0.1m^2/s$ and $K_H = 10m^2/s$. Based on the results predicted for the higher of these diffusivity values, it will be clear that it is not necessary to model higher diffusivities than these, since these values disperse the plume very rapidly.

The vertical transport of water in much of the deep ocean is minimal due to stable stratification. This is evidenced by tritium tracer studies [Fine et al., 1981, for instance], low dissolved oxygen in the deep ocean [Thurman, 1981], and diapycnal mixing studies [Finnigan et al., 2002] for example. According to Decloedt and Luther [2010] diapycnal mixing in the abyssal ocean occurs on scales ranging from a 1 mm to about 10 m. However, in areas

with significant bottom topography (such as the Hawai'ian ridge), enhanced mixing may be observed [Finnigan et al., 2002]. This information will be relevant in assessing the plausibility of vertical motion of estimated pathlines in section 5.1.

3 Velocity Data

A single string of five Acoustic Doppler Current Profilers (ADCPs) collected current and other data at a single location at the deep ocean disposed munitions site. Data was collected at 57 different heights above bottom during a 13 month period with a sampling period of 15 minutes for ADCP5 (bottom-most measurement heights) and a sampling period of 2 hours for the other instruments. Measurement heights were spaced 0.5 m apart for ADCP5 and generally 20 m apart for the other instruments. The data were post-processed and collected into five Matlab data files, with each file corresponding to one of the five ADCPs. This original data set is the starting point for the present work and will be described in more detail below in subsection 3.1. The preparation of the data for use in modeling chemical transport is described in section 3.2. Finally, for insight into the current patterns at this location in time and depth, the velocity data is visualized in several ways in section 3.3.

3.1 The Original Data

A string of 5 ADCPs was deployed at the deep ocean disposed munitions site (at approximately 21.360 N latitude and 158.331 W longitude) on 24 July 2009 at 2200 HST and recovered on 23 August 2010 at 0558 HST. During post-processing, the data was truncated to the time period 26 July 2009 at 0000 HST through 23 August 2010 at 0000 HST. The collected and post-processed data was stored in five Matlab data files: ADCP1000.mat, ADCP2000.mat, ADCP6000.mat, ADCP4000.mat, and ADCP5000.mat. Each data file represents the data from one ADCP instrument (referred to as ADCP1 – ADCP5). ADCP5 was the bottom-most instrument and ADCP1 was the instrument closest to the sea surface. The data file ADCP6000.mat corresponds to ADCP3, though the reason for the naming anomaly is not known.

The uppermost four instruments (ADCP1 – ADCP4) were 75kHz instruments recording at 8 depths per instrument (every 20 m vertically) with a sampling period of 2 hours and estimated error of 0.97 cm/s. The bottom-most instrument (ADCP5) was a 1200kHz instrument recording at 25 depths (every 0.5 m) with a sampling period of 15 minutes and estimated error of 0.90 cm/s. For more detailed information on the original data collection and analysis, see NOAA ADCP Report [2010].

Each data set consists of a Matlab *.mat file with a set of saved variables as illustrated in Table 2 below. The data files may be loaded with a command of the form load('filename.mat') from the Matlab command prompt or from a matlab script.

The fields which interest us for the present analysis are time, mab, cross, along, and up. These are discussed in more detail below. For additional information on the other fields, see NOAA ADCP Report [2010]. The data sets are available from NOAA ADCP Data [2010].

3.1.1 mab Field

The mab field records the height at which a measurement was taken, in meters above bottom. A mab data value was recorded for each measurement (in time and depth) because the instrument height can vary with time as the instrument moves in the water. However, the present data are in deep water and do not show any variation in mab with time, so for our purposes, mab is treated as a one-dimensional array.

Table 2: Original ADCP Data Fields

Field name	Meaning	Array size	
		(ADCP1–4)	(ADCP5)
press	pressure	1x4775	1x38207
time	date and time (HST) as Matlab datestr	1x4775	1x38207
ssh	sea surface height	1x4775	1x38207
mab	meters above bottom (height of measurement)	8x4775	25x38207
EA	echo amplitude	8x4775	25x38207
east	component of velocity (cm/s) toward the east	8x4775	25x38207
north	component of velocity (cm/s) toward the north	8x4775	25x38207
up	upward component of velocity (cm/s)	8x4775	25x38207
error	error	8x4775	25x38207
cross	cross-shore component of velocity (cm/s)	8x4775	25x38207
along	along-shore component of velocity (cm/s)	8x4775	25x38207
temp	temperature	1x4775	1x38207

When combining the data sets from the different instruments there are some further observations about the measurement heights which bear mentioning. First, the measurement heights increase with array index in some data sets and decrease in others. Second, the distance between measurement heights of adjacent instruments is not uniform, so samples are not all 20 m apart when these data sets are combined. The measurement heights for ADCP2 and ADCP3 are interleaved. Finally, some measurement heights have no valid data and so do not contribute to the final prepared data set, which has a total of 51 measurement heights.

3.1.2 Time Field

The time field records the time at which the measurement was taken in local time (HST) and is stored as a Matlab datenum value. Differences of datenum values are in units of days. To display the time field in the desired format, use the Matlab command datestr, as in the following examples for displaying the first element of the time field:

command	output
datestr(time(1))	21-Jul-2009 16:00:00
datestr(time(1),'dd mmmm yy HH:MM:SS')	21 July 09 16:00:00

As mentioned earlier, ADCP1-4 use a sample period of two hours and ADCP5 uses a sample period of 15 minutes. However, there is some drift in the sample times which accumulates to several minutes by the end of the study period. That is, although adjacent samples may appear to be precisely 2 hours apart, we may note that at the start of the study period, a sample is taken at 22-Jul-2009 04:00:00, whereas by the end of the study period, a sample is taken at 23-Aug-2010 04:02:44, not 23-Aug-2010 04:00:00. It is also the case that the different instruments do not sample at the same times.

3.1.3 Velocity Fields

All velocities are recorded in cm/s. The rows of the velocity arrays represent measurements taken in time at a fixed depth. The columns represent measurements taken at different depths at a fixed time. The up field is the vertical or w component of velocity (where up is positive and down is negative).

The horizontal velocity components are supplied in two different coordinate systems: one uses north-south and east-west components and the other uses cross-shore and along-shore velocity components. Each coordinate system is orthogonal. In the present work we use the cross-shore/along-shore system with the x-coordinate corresponding to the cross-shore direction and the y-coordinate to the along-shore direction.

The cross field represents the cross-shore velocity component, u, with positive values corresponding to velocity along a heading of 54 degrees (roughly toward NNE) and negative values to a heading of 234 degrees (roughly SSW). The along field represents the along-shore velocity component, v, with positive values corresponding to velocity along the heading of 324 degrees (roughly toward the WNW) and negative values to a heading of 144 degrees (roughly toward ESE). In this coordinate system, traveling from the disposal site in the positive x (cross-shore) direction takes one roughly in the direction of O'ahu, which is approximately 18.5 km (10 nautical miles) from the disposal site.

The north field represents the north-south component of velocity (velocity toward the north is positive and velocity toward the south is negative). The east field represents the east-west component of velocity (velocity toward the east is positive and velocity toward the west is negative). We do not use these fields in the present work.

3.1.4 Rejected Data

Some data values were rejected during post-processing, in which case the velocity array records a value of NaN (IEEE Standard notation for Not a Number). In some data sets as much as half of the data were rejected. This is particularly evident in the ADCP5 data (from the deepest instrument). Rows 21–25 in the velocity array for ADCP5 represent depths ranging from 0.5 m above bottom down to -1.5 m above bottom and these rows contain no valid data (all data values are NaN). Rows 16–20, representing 3.0 m above bottom to 1.0 m above bottom contain only tens to hundreds of data values per row. The 12th data row (representing 5.0 m above bottom) is the first row in which more than half the measurements are valid. In the remaining rows of the ADCP5 velocity arrays somewhere between 1% and 33% of the data were rejected. All velocities were rejected for the first approximately 400 sample times. The data for ADCP1-4 are similarly missing values, particularly at certain heights and in the first approximately 400 sample times.

Figures 1 through 5 allow some sense of the scope and distribution of missing data. In each case black indicates missing data and white indicates valid data and the element (1,1) of the velocity array is in the upper left corner of the figure. The z indices are labeled with their height in meters above bottom and the time indices are labeled with the first letter of the month at the first sample index for that month. Not all missing data can be seen due to limited resolution of the figures; instances where only a single data value is missing might or might not be seen. This will be especially true for ADCP5 which has higher resolution sampling both in time and height. The figures give an overall sense of where data is missing though.

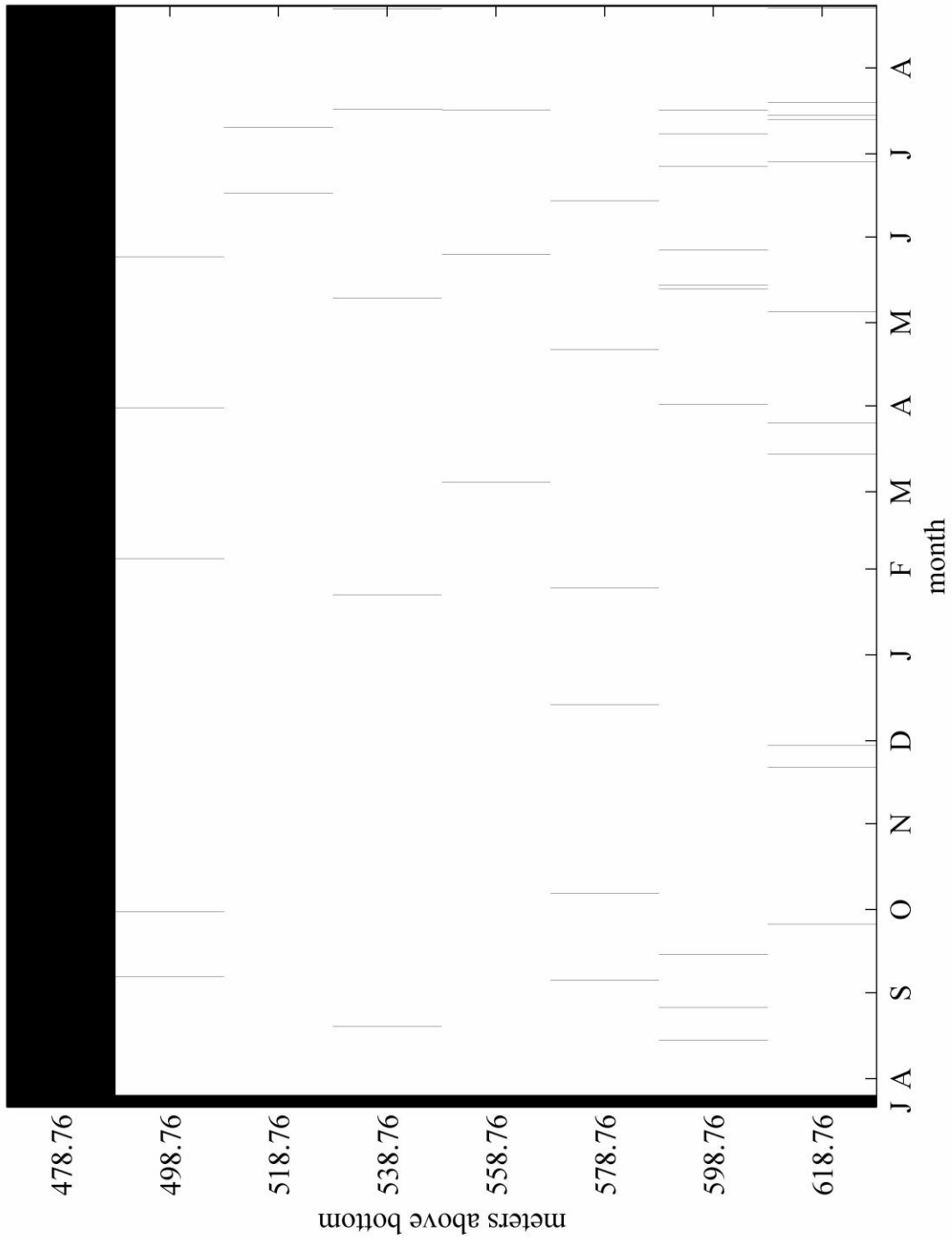

Figure 1: Missing ADCP1 velocity data in black

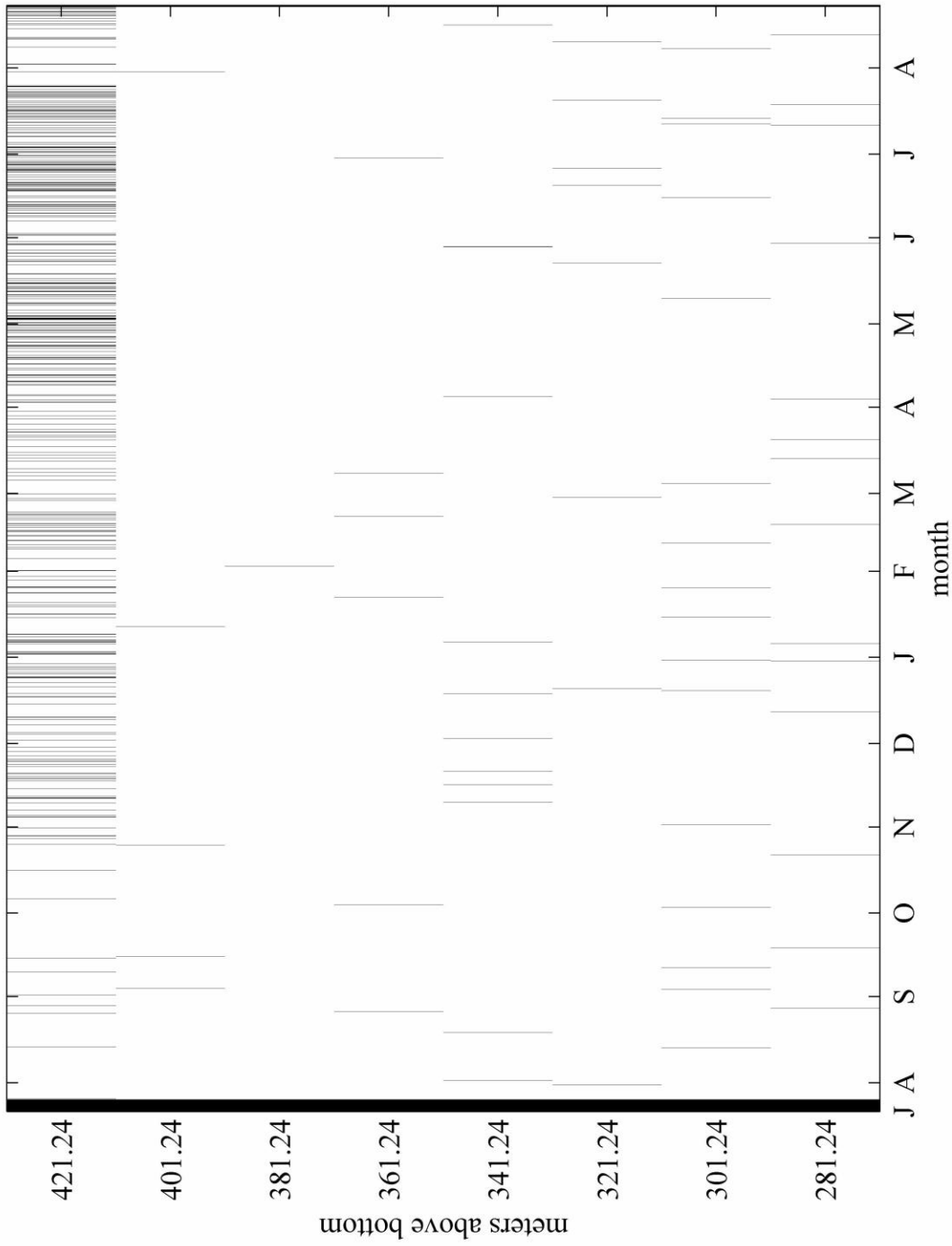

Figure 2: Missing ADCP2 velocity data in black

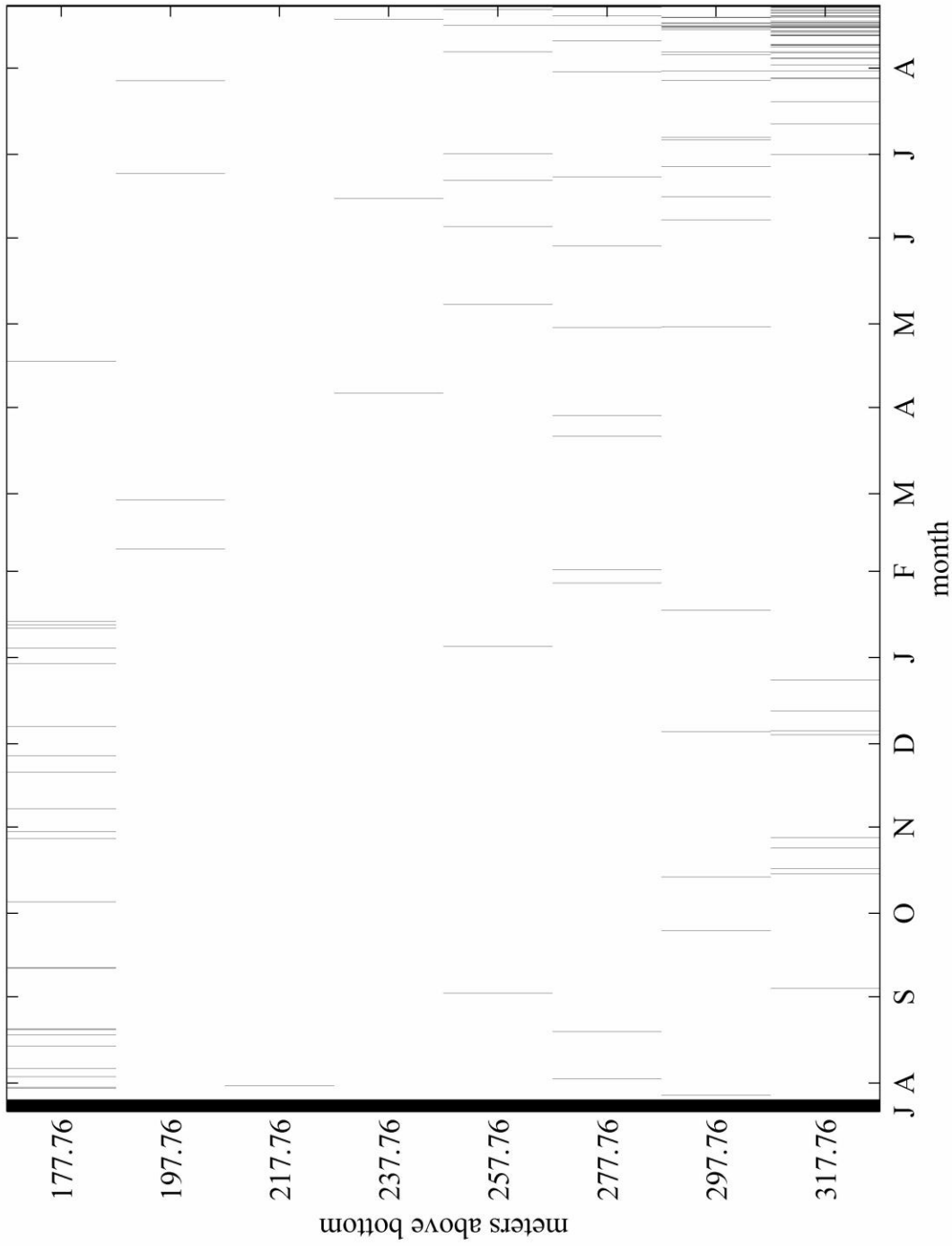

Figure 3: Missing ADCP3 velocity data in black

Figure 4: Missing ADCP4 velocity data in black

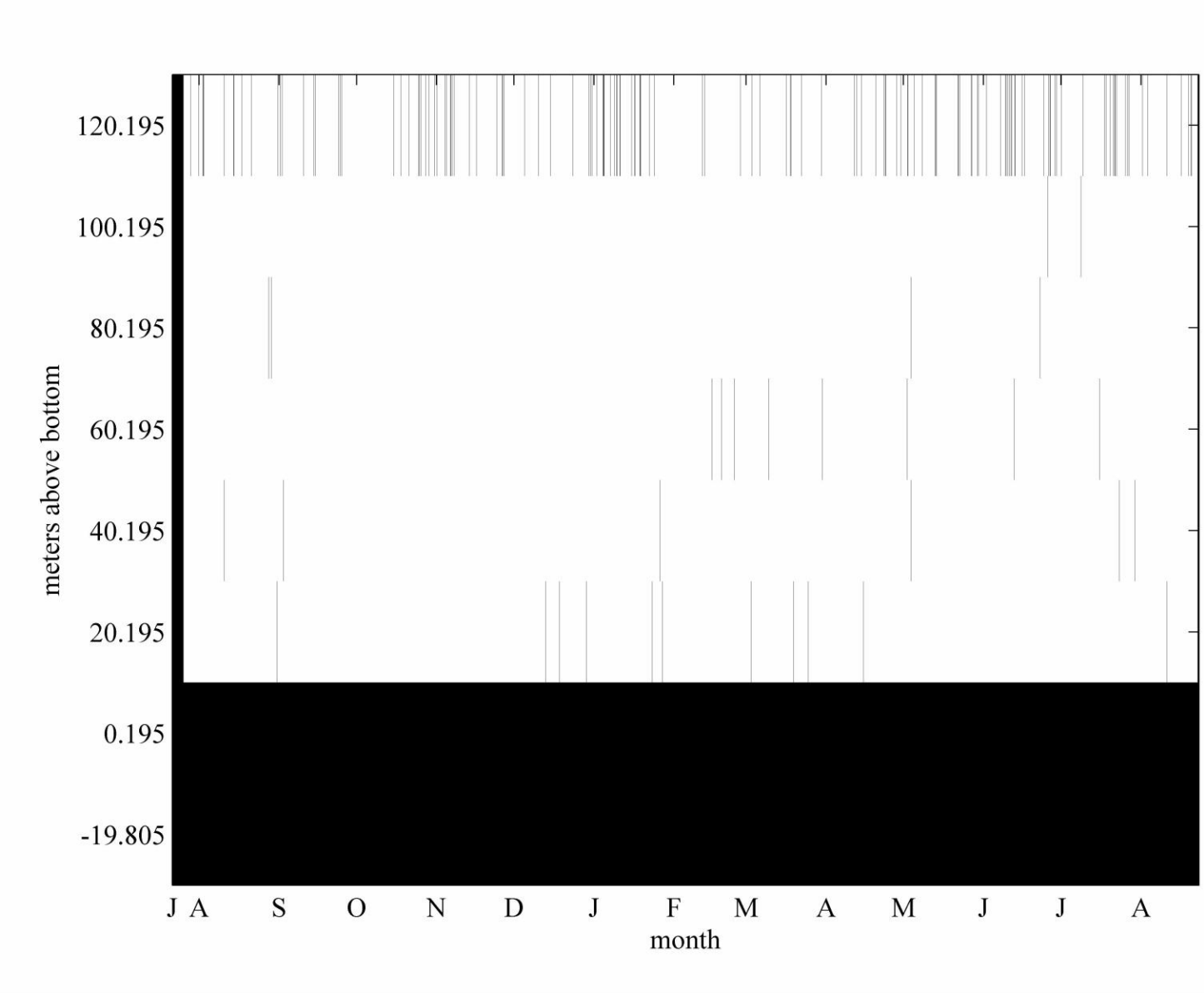

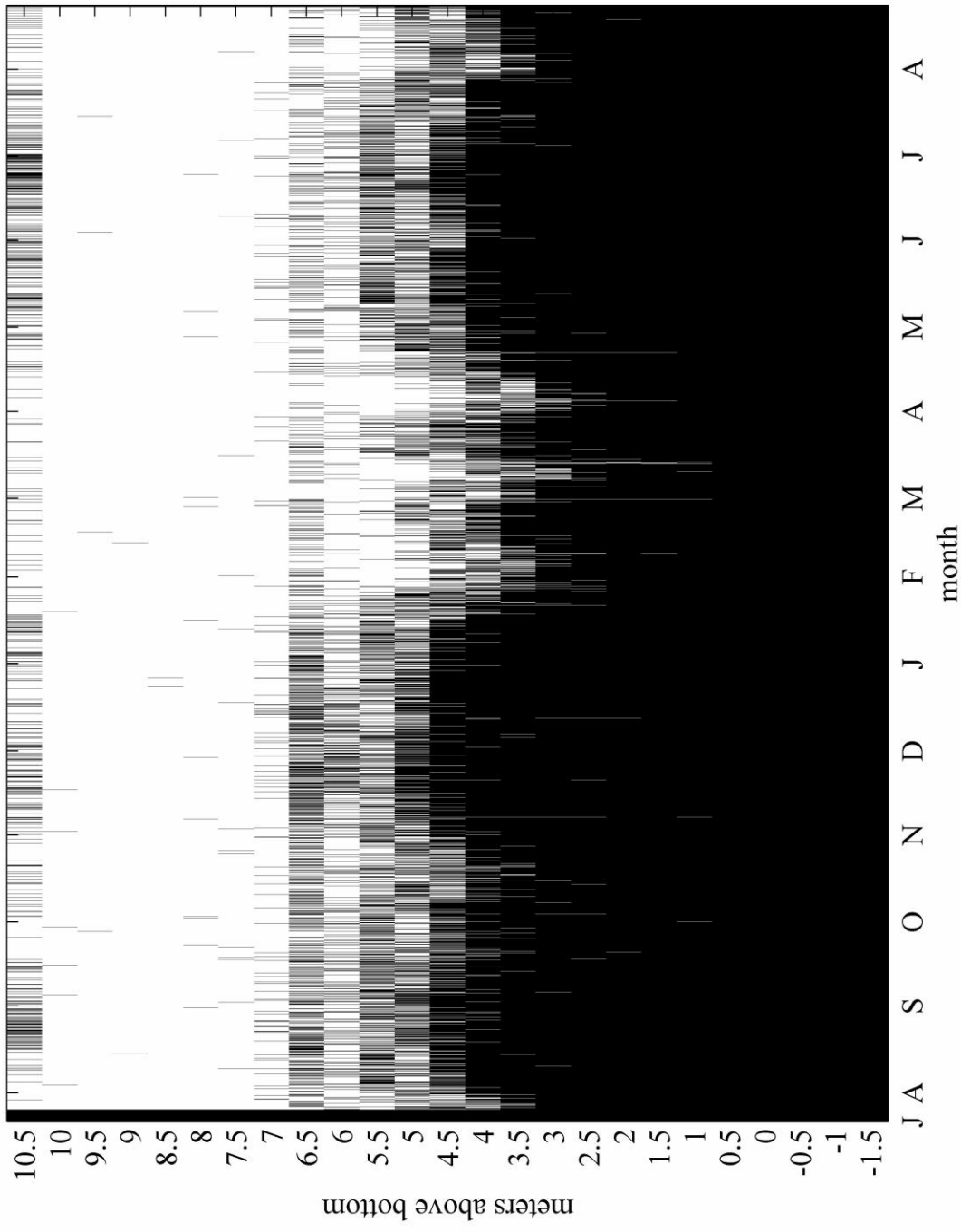

Figure 5: Missing ADCP5 velocity data in black

3.2 The Prepared Data

For the present work, a velocity data set was required covering roughly the bottom 600m of the water column with no NaN values, and sampled consistently on a regular time grid. To achieve this, the following steps were taken:

1. Each data set (ADCP1-ADCP5) was trimmed of any rows or columns which had no valid data.

   The resulting data set has a sampling period of 2 hours starting at 26-Jul-2009 06:00:02 (HST) and ending at 22-Aug-2010 16:00:02 (HST). Samples are irregularly spaced in the z-direction at the following heights in meters above bottom: 0, 0.5, 1.0, 1.5, 2.0, 2.5, 3.0, 3.5, 4.0, 4.5, 5.0, 5.5, 6.0, 6.5, 7.0, 7.5, 8.0, 8.5, 9.0, 9.5, 10.0, 10.5, 20.195, 40.195, 60.195, 80.195, 100.195, 120.195, 177.76, 197.76, 217.76, 237.76, 257.76, 277.76, 281.24, 297.76, 301.24, 317.76, 321.24, 341.24, 361.24, 381.24, 401.24, 421.24, 498.76, 518.76, 538.76, 558.76, 578.76, 598.76, and 618.76. The ADCP2 and ADCP3 data sets interleave between 277.76 and 321.24 mab, as can be identified by noting the least significant digits of their z-values.

   A data set sampled at 15 minute intervals was also constructed (by interpolating ADCP1-4 data; ADCP5 is already sampled at this frequency). This data set was not used in the present analysis because the computation-time was prohibitively long.

2. Each data set was linearly interpolated in time (using Matlab interp1) to correct (most) invalid data values. No extrapolation was performed, so this does not correct the data in the first or last time sample if that data is not valid. However, such data points are corrected later by interpolating in the z-direction.

3. Each data set was resampled (using linear interpolation) so that all velocity data was represented on a consistent and regular time grid.

   As was mentioned earlier, there were two reasons for resampling. First, the original data sets were sampled at different times. Second, there was a minor issue of sample time drift over the course of the 13 months of sampling. The sample drift alone would probably not have been worth correcting for by itself, as the jitter error introduced by not correcting would probably not have been more than the interpolation error from correcting it. However, since the data needed to be resampled anyway to have the entire data set on the same time grid, the second problem was corrected in the course of correcting the first.

4. Each data set was re-ordered so that the z values increase with array index, for consistency. The original indexing is apparent in figures 1 through 5.

5. Data sets were combined in the z-direction, interleaving values from ADCP2 and ADCP3 so that z values increase with array index in the combined data set. The final data set has 51 z values where velocity measurements are available. As can be seen from figures 1 through 5, some of the original measurement heights had no valid data.

6. The combined data set was linearly interpolated in the z-direction to correct any remaining NaN values.

7. The bottom-most measurements of the ADCP5 data were replaced by a linear boundary layer because the measured data appeared to spurious. Specifically, measured velocity values below 6.5 mab were discarded and replaced by the result of linearly interpolating from the measured velocity value at $z = 6.5$ mab to zero velocity at $z = 0$ mab.

   The accuracy of the bottom-most data was questioned because the values were erratic and much larger than the values immediately above them, whereas one would expect velocities to be reduced within a few meters of the bottom. This is visualized in figures 9–11 in the next section.

The corrected data set is stored in a matlab struct with fields as shown in Table 3 below.

Table 3: Prepared Velocity Data Fields

Field name	Meaning	Array size
S.u	u (cross-shore) velocity in cm/s	51x4710
S.v	v (along-shore) velocity in cm/s	51x4710
S.w	w (upward) velocity in cm/s	51x4710
S.mab	z (height of measurement) in meters above bottom	51x1
S.time	sample date and time (HST) as Matlab datenum	1x4710
S.uDescription	string description of u	string
S.vDescription	string description of v	string
S.wDescription	string description of w	string
S.timeDescription	string description of time	string
S.linearBoundaryLayerDescription	string description of imposed boundary layer	string
S.statsRaw	statistics for raw data (before preparation)	string
S.statsProcessed	statistics for prepared data (printable string)	string
S.description	short string description of this data set	string

Selected statistics for the prepared data with a 2 hour sampling period are presented in Table 4 below.

Table 4: Velocity Statistics

z (mab)	$z = 10$	$z = 20.195$	$z = 120.195$	$z = 237.76$	$z = 361.24$	$z = 618.76$
u mean	-0.41	-0.18	-0.12	0.14	0.27	0.20
u quartile 1	-3.29	-2.31	-2.14	-1.87	-1.66	-2.34
u median	-0.39	-0.16	-0.13	0.17	0.25	0.20
u quartile 3	2.43	1.98	1.91	2.16	2.19	2.64
v mean	-0.20	0.10	0.82	0.61	0.20	-0.41
u quartile 1	-3.71	-2.60	-1.96	-2.10	-2.48	-3.45
u median	0.02	0.31	0.86	0.62	0.31	-0.44
u quartile 3	3.41	2.88	3.58	3.30	3.08	2.57
w mean	-0.04	-0.13	0.33	-0.23	-0.16	-0.16
u quartile 1	-0.52	-0.50	0.00	-0.58	-0.49	-0.50
u median	0.00	-0.10	0.30	-0.20	-0.11	-0.14
u quartile 3	0.49	0.29	0.70	0.11	0.19	0.20

3.3 Visualizations of the Velocity Field

Because the velocity field is a 3-dimensional vector quantity defined (potentially) on a 4-dimensional space (x, y, z, t), it can be challenging to visualize. In our case, we have velocity data at only one (x, y) location, so we make the assumption that the velocity field does not vary in x or y. This still leaves a 2-dimensional space (z, t) on which to visualize a 3-dimensional velocity field. We take several approaches to this.

The first set of approaches involves viewing the components of velocity separately. Figure 6 shows the u velocity component (velocity in the x or cross-shore direction) plotted as a collection of vertical profiles with one line for each z-profile. That is, each colored line represents a z-profile of the u velocity for a different point in time. This gives some feeling for the typical shape of the variation in z and for the variability of this over time. We see, for example, that the bulk of the u-velocity values are clustered between -10 and 10 cm/s. We can note that there is no persistent pattern of currents flowing in one direction at a certain depth and another direction at a different depth. Instead, we see essentially the full range of current values taken on at all depths measured.

There are several other features or artifacts worth noting in figure 6. At about 450 mab (meters above bottom) we note what appears to be a reduction in velocities, however this is probably an artifact. The lower-most measurement height in the ADCP1 data set is 498.76 mab and the upper-most measurement height in the ADCP2 data set is 421.24 mab so there is not any measured data at 450 mab where the neck appears in the plot. Instead this probably represents a change in current magnitude and/or direction between the neighboring measurement points with the appearance of a neck being created as these lines cross.

In the vicinity of 300 mab, there appear to be some very rapid changes in velocity in a very short vertical space which are likely artifacts. The measurement depths of ADCP2 and ADCP3 overlap here and the data from these two instruments is interleaved. Specifically, measurements at 281.24, 301.24, and 321.24 mab are from ADCP2, while measurements at 257.76, 277.76, 297.76, and 317.76 mab are from ADCP3. Therefore, we have measurements just a few meters apart vertically but coming from two different instruments. Large differences in velocities could potentially be caused by a number of factors, including calibration differences between instruments, velocity measurement error, depth measurement error, or interpolation error (since the instruments sample at different times and the data had to be resampled to a common time grid).

Finally, there appears to be an increase in velocity near the top of the ADCP5 data set (10.5 mab) which might be an artifact. It is difficult to resolve the ADCP5 data at this scale since the z-resolution is very fine compared to the scale of this plot. The lower-most data is examined in more detail in figures 9–11.

Figure 7 shows the v velocity component (velocity in the y or along-shore direction) plotted as a collection of vertical profiles with one line for each z-profile in time. The same observations apply as in figure 6.

Figure 8 shows the w velocity component (velocity in the z or upward direction) plotted as a collection of vertical profiles with one line for each z-profile in time. The white dotted lines through the data represent a quantization artifact. The w velocities are nearly an order of magnitude smaller than the u and v velocities and they are therefore effectively recorded with coarser quantization (larger gaps between possible values) due to the limited accuracy of the instrument. The white gaps represent numeric values which are not recorded by the

Figure 6: Profiles in z of the u (cross-shore) velocity at each time for prepared data.

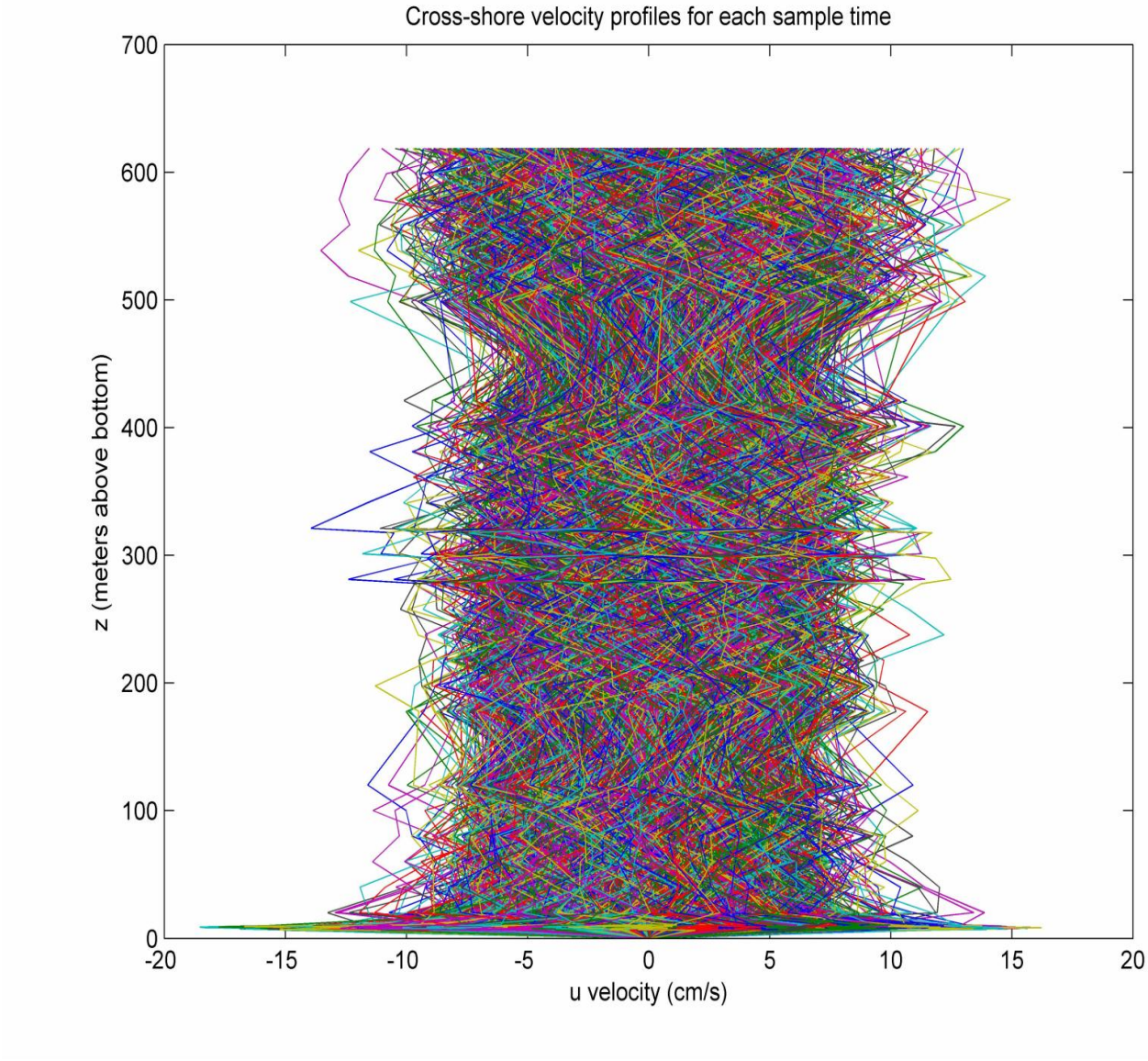

Figure 7: Profiles in z of the v (along-shore) velocity at each time for prepared data.

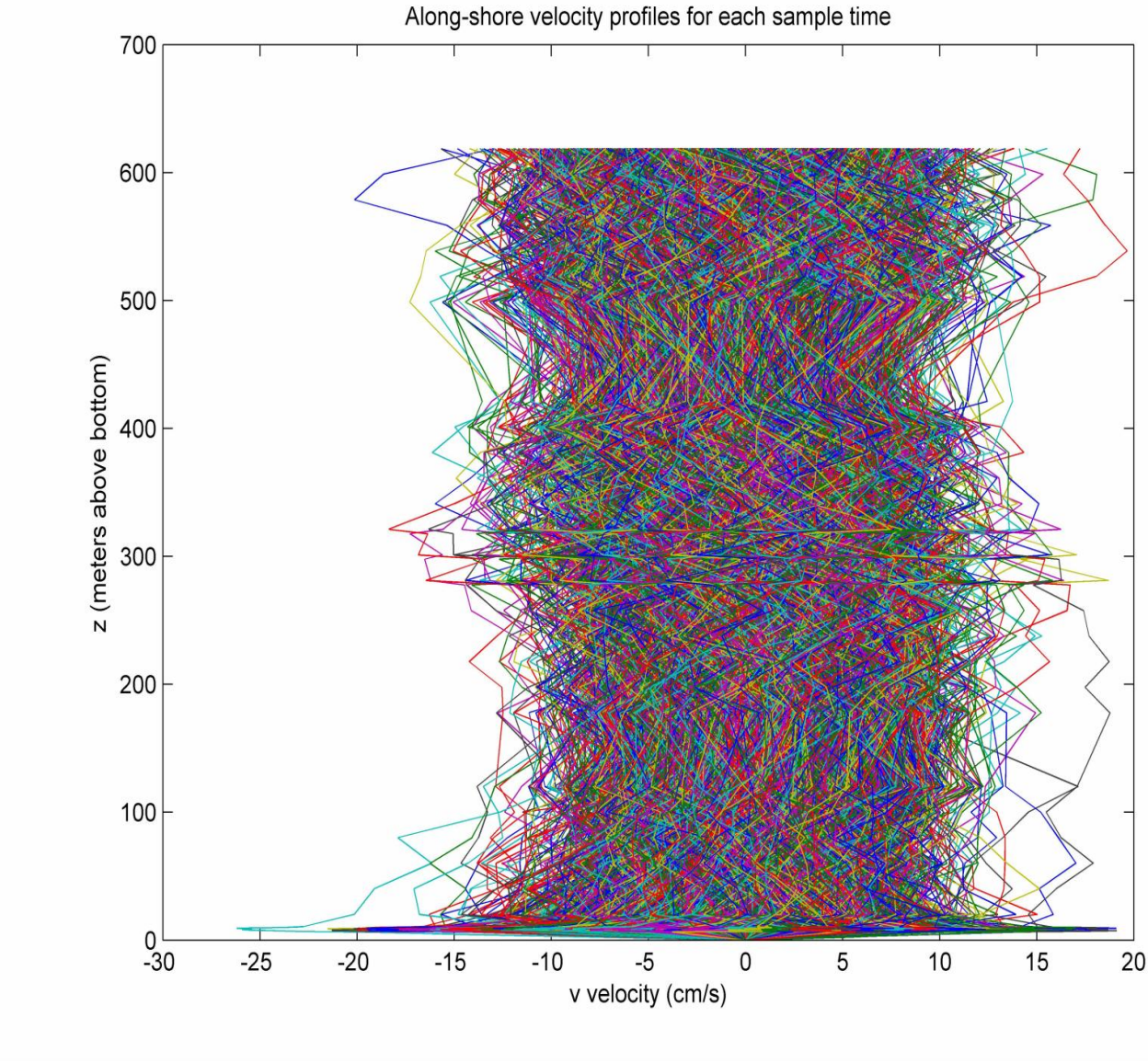

instrument due to limited precision.

The lowest measurement height of ADCP3 is 177.76 mab and the highest measurement height of ADCP4 is 120.195 mab. There are large excursions in the w velocities at these heights. It is unclear whether these represent some kind of real feature in the velocity field or instrument error but the magnitude and consistency across time of these features compared to the rest of the data suggest that they may be spurious.

Figure 8: Profiles in z of the w (upward) velocity at each time for prepared data.

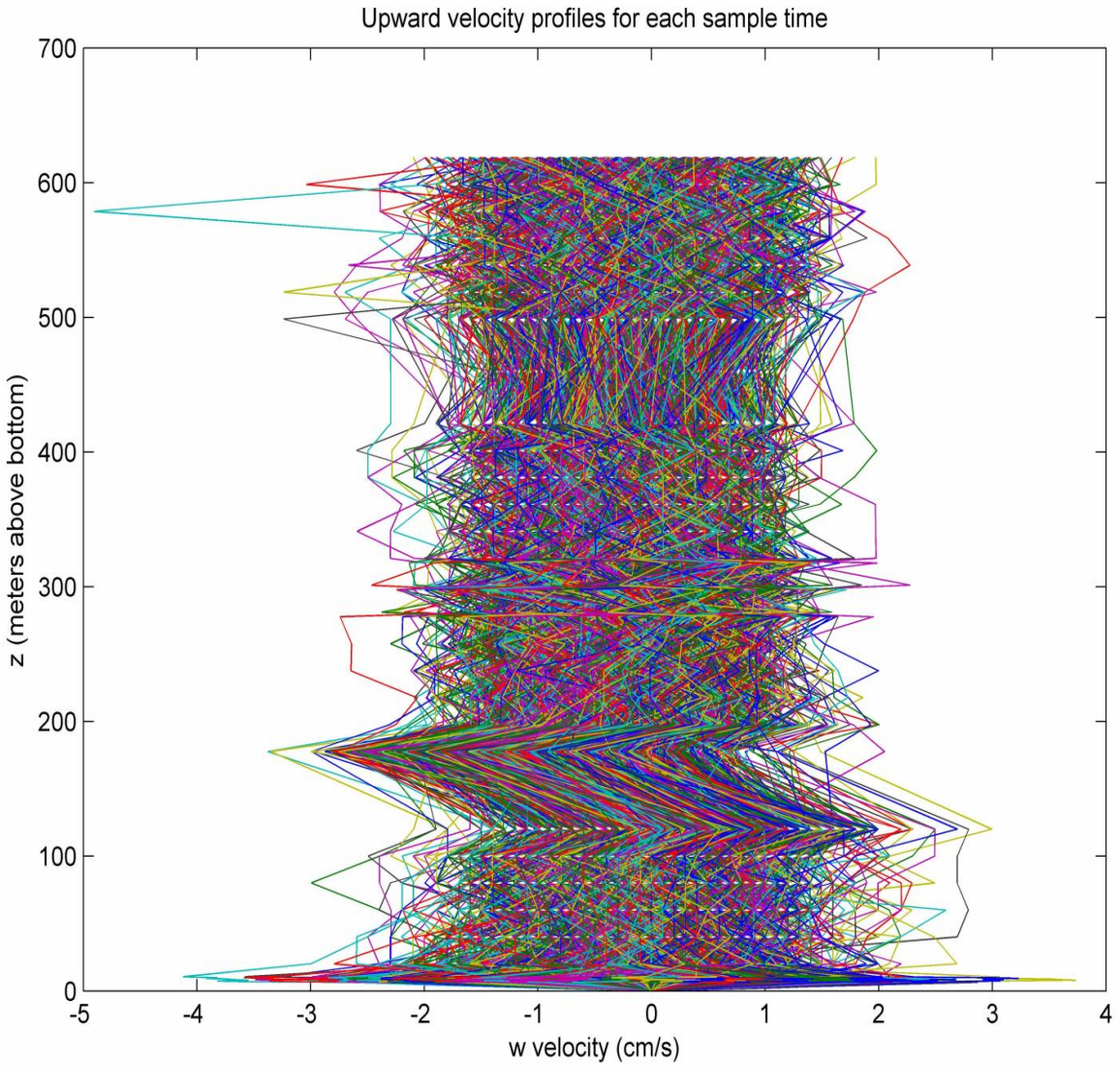

Figure 9 shows the z profiles of the u velocity component near the bottom (ADCP5 data only), and compares the original data to the prepared data. In the plots of the original data, NaN values do not plot, so valid data which are interspersed with NaN values will plot as isolated points or segments. The prepared data has no NaN values as they have been replaced by values interpolated from the surrounding valid data.

It is clear that the character of the original data changes markedly below about 6.5 mab. The greatly increased magnitude and erraticness of the velocity data below 6.5 m does not correspond to expected boundary layer behavior, so we assume this represents instrument error of some sort. Consequently, we have chosen to replace the data below 6.5 mab with a linear boundary layer that is obtained by interpolating linearly from the velocity value at 6.5 mab down to zero velocity at 0 mab. This is shown in the right hand side of the figure, entitled "Prepared Data". Similar plots are shown for the other velocity components in figures 10 and 11. Note that the same scale is retained in all three figures which makes it visually more clear that the w velocities are much smaller than u and v.

Figure 9: Profiles in z of the u (cross-shore) velocity near the bottom at each time for the original and prepared data.

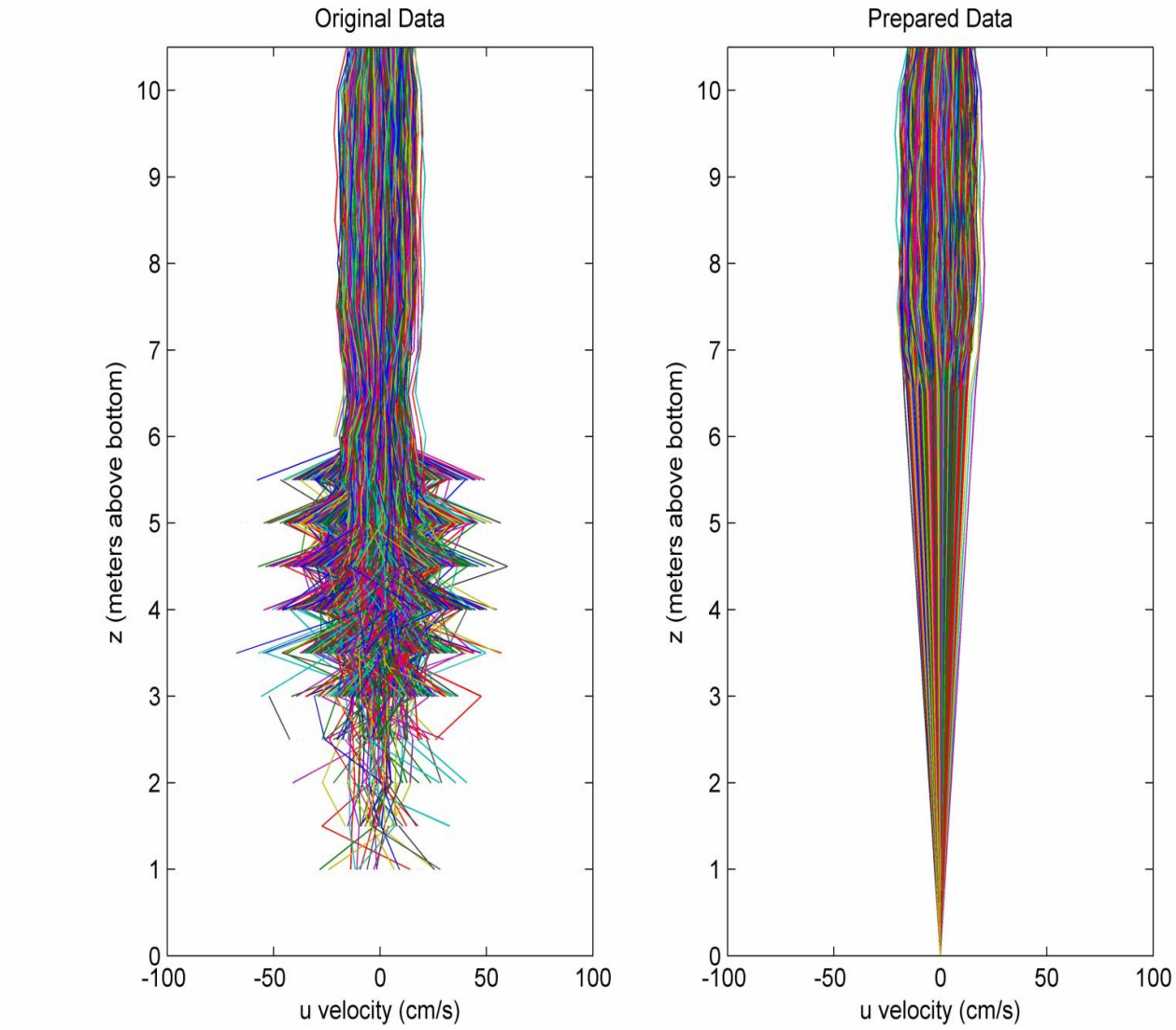

Figure 10: Profiles in z of the v (along-shore) velocity near the bottom at each time for the original and prepared data.

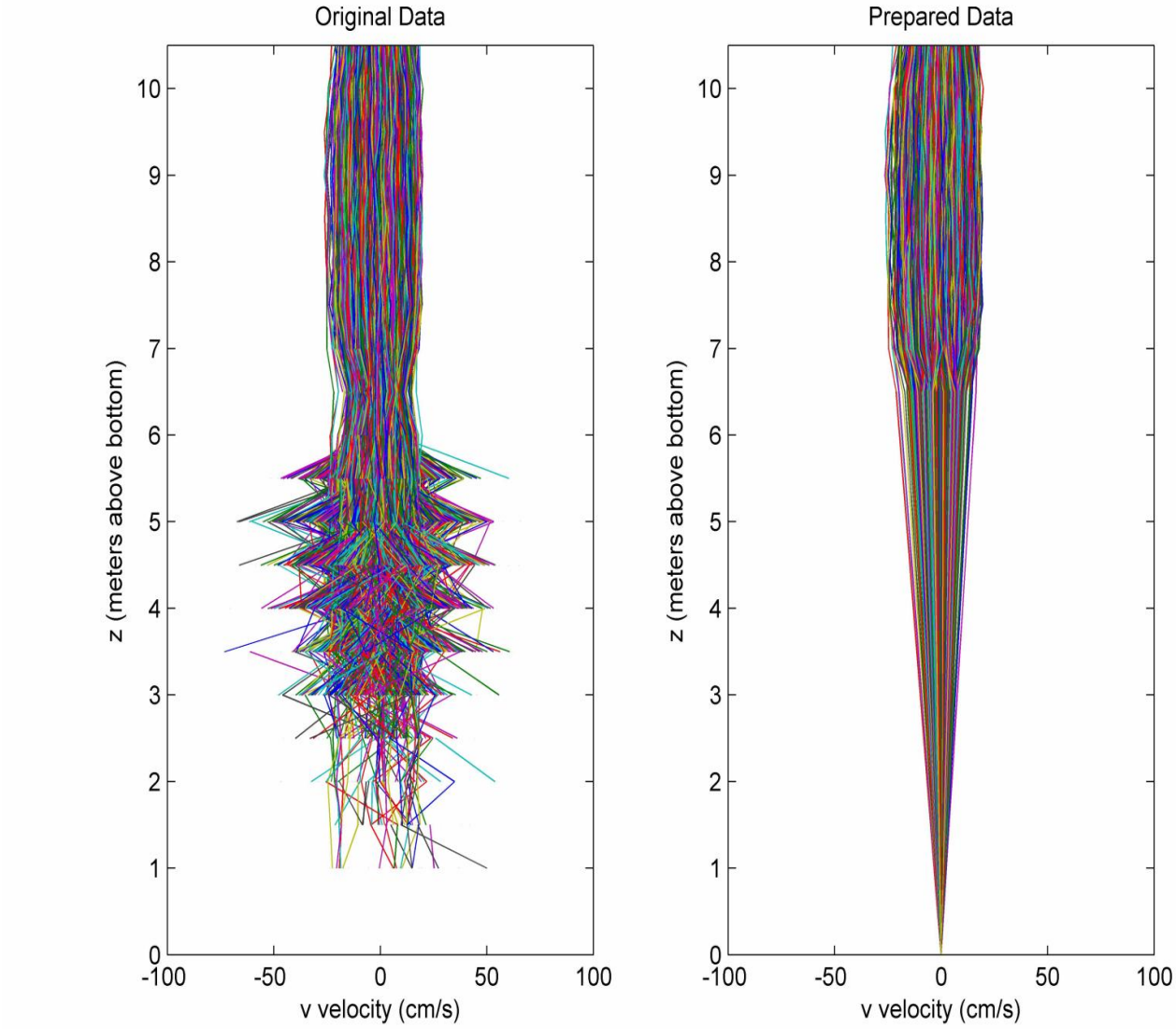

Figure 11: Profiles in z of the w (upward) velocity near the bottom at each time for the original and prepared data.

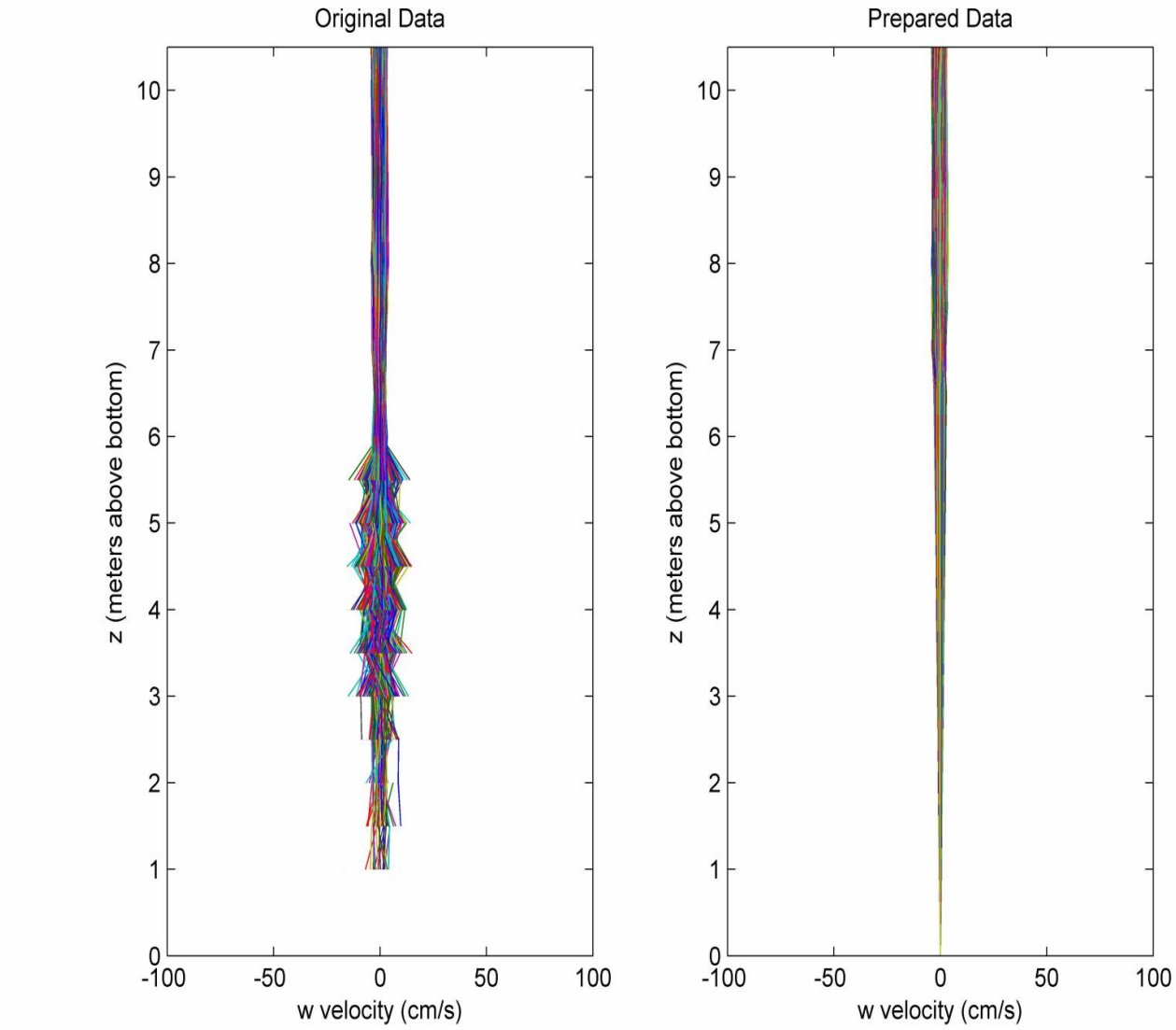

In order to view the temporal and spatial structure of the velocity field we can plot individual components of the velocity in red, green, and blue, corresponding to u, v, and w, and then combine these into an RGB image of the vector velocity field. This has been done in figures 12–15. In figure 12 the u velocity is mapped as a function of z and t, where the largest positive velocity in the x (cross-shore) direction (roughly NNE) corresponds to bright red and the most negative values of u correspond to black, representing velocities roughly toward the SSW. This colormap is a reasonable choice for the purpose of making a false-color image of the full vector velocity field, but other color maps are probably better suited to examination of individual components of the velocity. In particular, this color map does not help us clearly distinguish zero velocity from modest positive or negative velocities, which all look medium red.

Figure 13 provides a visualization of the v velocity field in a green color map, with bright green corresponding to the largest positive velocities in the along-shore direction (roughly toward the WNW) and black corresponding to the most negative along-shore velocities (roughly toward the ESE). Figure 14 visualizes the upward velocity in bright blue and downward velocity in black. Finally, combining these three plots into a single RGB image results in figure 15, which is a false color visualization of the vector velocity field.

We can make the following observations based on these figures. The velocity field plotted here is the prepared velocity with a linear boundary layer imposed below 6.5 mab. The fact that velocity goes to zero near the bottom is evident by the bottom of figure 15 being uniform medium gray.

We can also observe a number of discontinuities in the data, some of which seem to be related to the transition from one instrument to another, which may suggest calibration differences between the instruments. Table 5 shows the heights (mab) where some transitions occur related to instrument changes or interleaving of data from different instruments. For convenience in analyzing the figures, the vertical scale of the figures is also marked with ticks at some of these heights. Note that there are a total of 51 different measurement heights, which are not evenly spaced. Most of them do not appear in the table or as marked ticks on the graphs. Although some irregularities are clearly visible, the only data which was discarded is that in the bottom 6 meters of the water column, where much of the data was NaN and that which was finite was much larger than reasonable and very erratic.

Table 5: Measurement heights and correspondence to measuring instrument.

Height (mab)	Instrument	Comment
618.76	ADCP1	top-most measurement for ADCP1
498.76	ADCP1	bottom-most usable measurements for ADCP1
478.76	ADCP1	no usable data
421.24	ADCP2	top-most measurement for ADCP2
321.24	ADCP2	very near top-most ADCP3 measurement
317.76	ADCP3	top-most measurement for ADCP3
301.24	ADCP2	interleaved with ADCP3 data
297.76	ADCP3	interleaved with ADCP2 data
281.24	ADCP2	bottom-most measurement for ADCP2
277.76	ADCP3	very near bottom-most ADCP2 measurement
177.76	ADCP3	bottom-most measurement for ADCP3
120.195	ADCP4	top-most measurement for ADCP4
20.195	ADCP4	bottom-most usable measurements for ADCP4
10.5	ADCP5	top-most measurement for ADCP5
6.5	ADCP5	linear boundary layer imposed below this point
0	ADCP5	no usable data: zero velocities assumed

Figure 12: Color map of cross-shore velocity u = u(z,t)

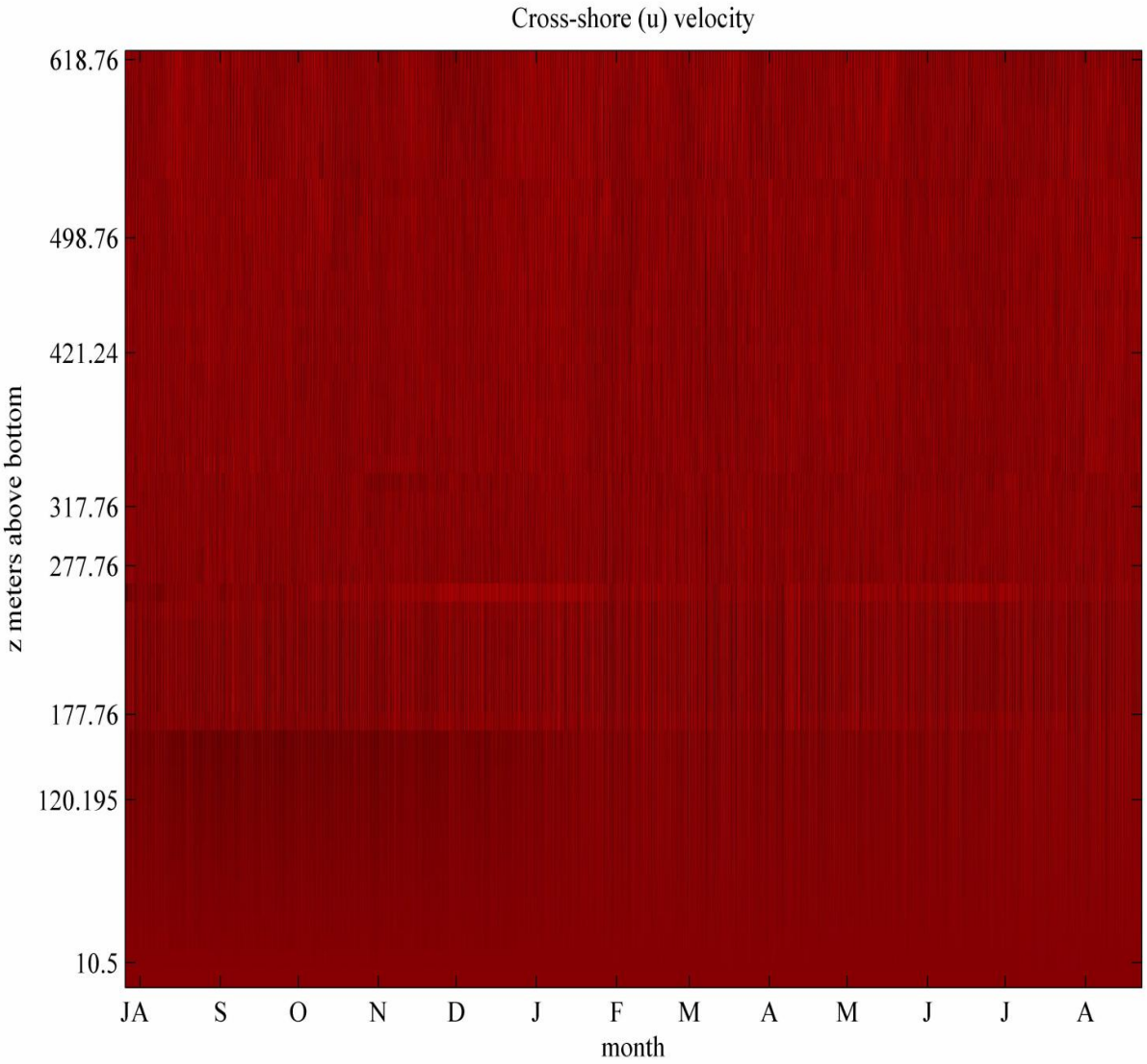

Figure 13: Color map of along-shore velocity v = v(z,t)

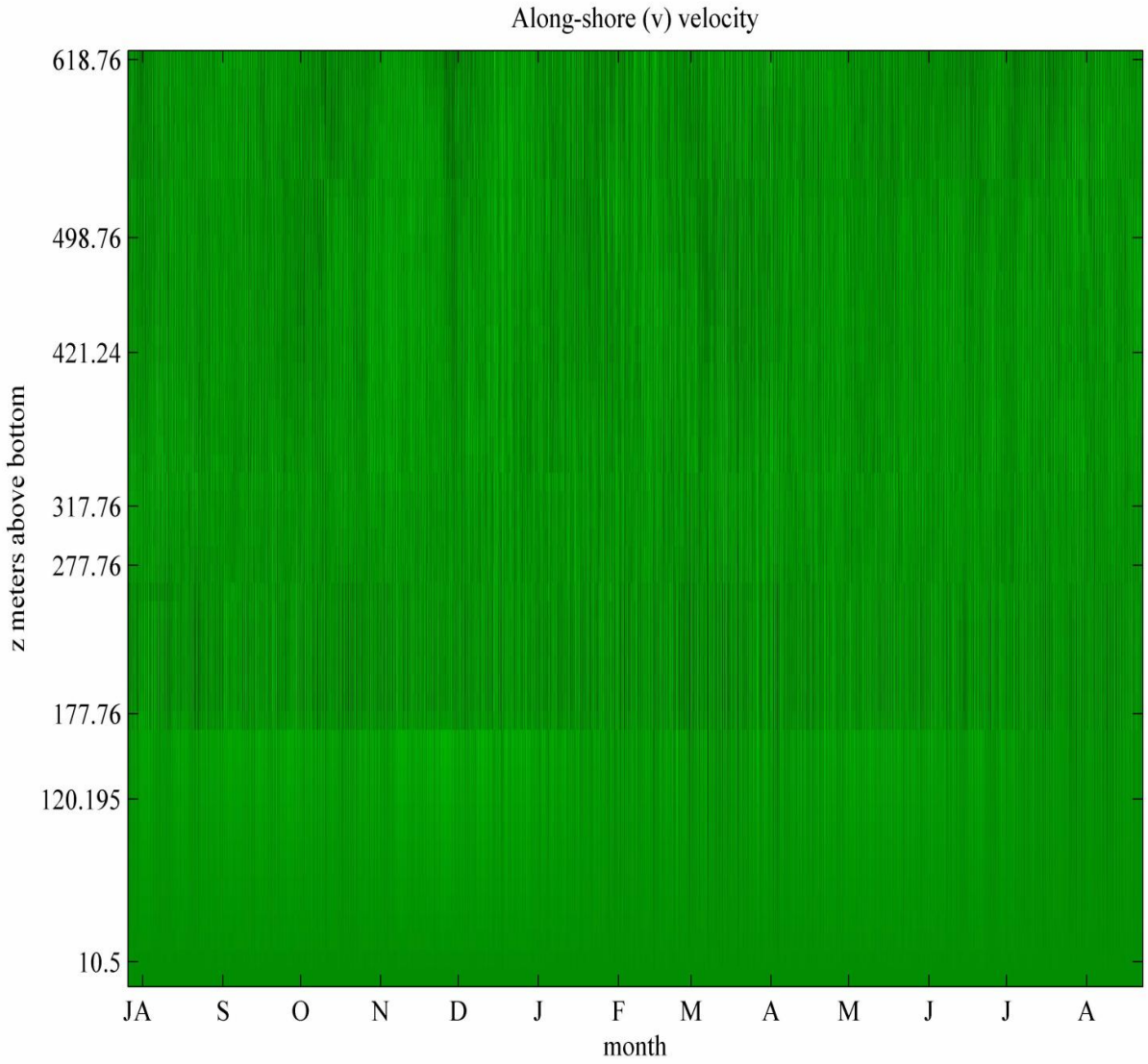

Figure 14: Color map of cross-shore velocity w = w(z,t)

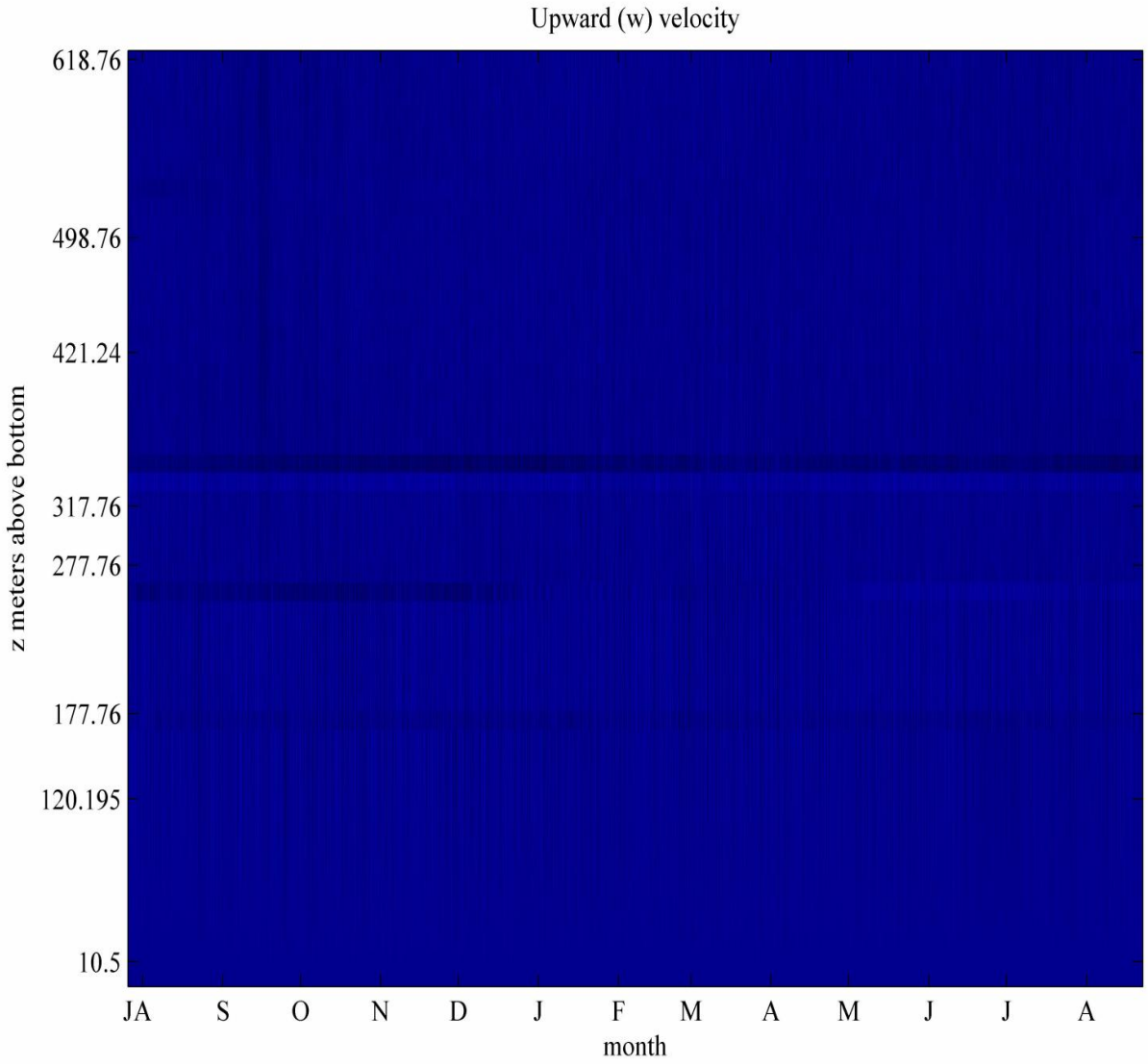

Figure 15: Color map of vector velocity as a function of z and t.

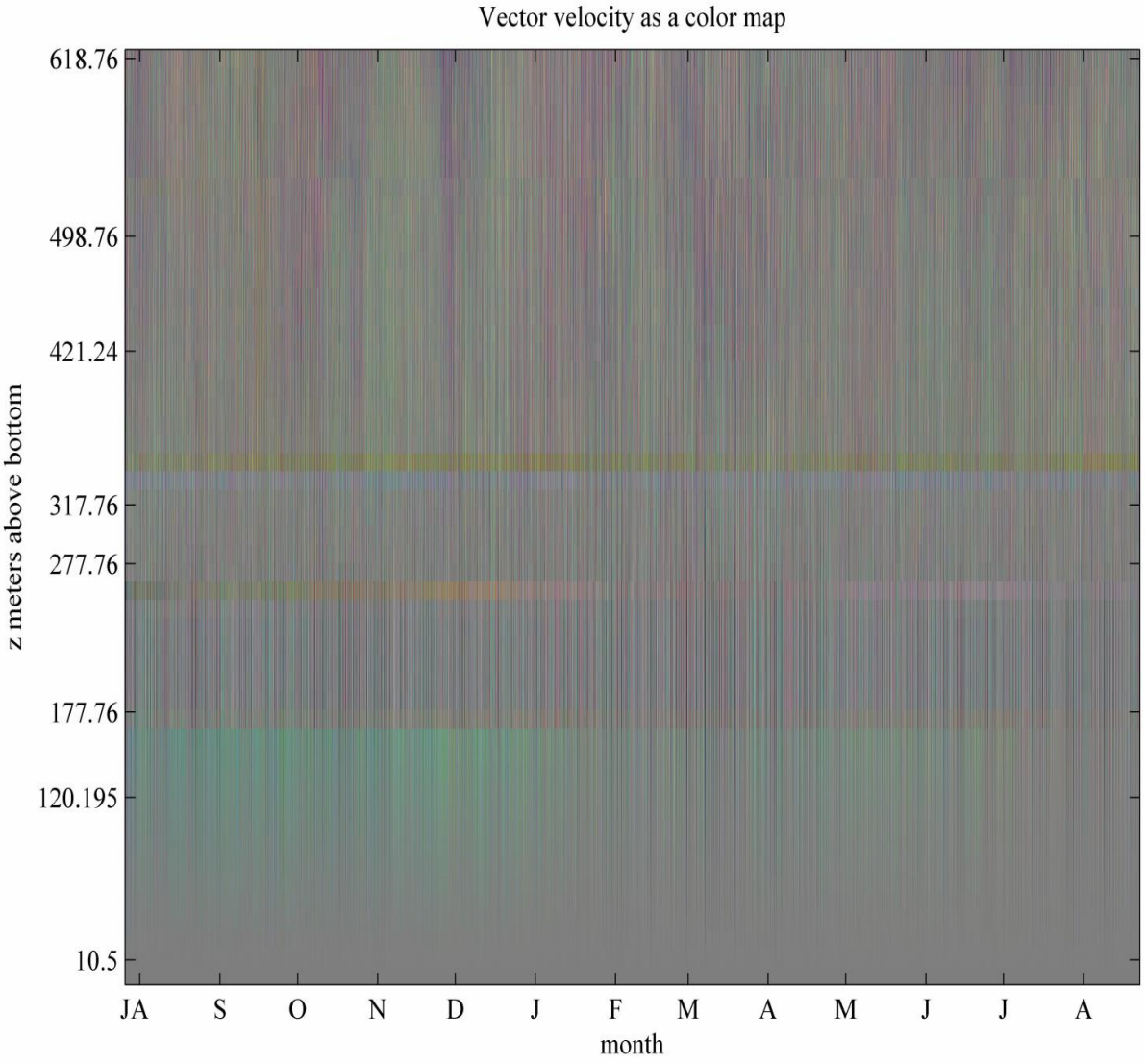

Another way to view multiple components of velocity in one plot is to view two velocity components together in a phase space plot with the third component visualized in color. Figure 16 is a phase space plot of the horizontal velocity in the u-v plane with the vertical velocity visualized in color (see the colorbar on the right for w in cm/s). The yellow traces represent the u and v velocities plotted as a time series in the u-v plane for the entire 13 months of data. On top of that, in blue-magenta, is plotted roughly the first half of the same data set (about 6 months) in the same time-parameterization in u-v phase space. However, in this portion of the plot the vertical velocity value is mapped to a color on the blue-magenta scale as indicated by the colorbar on the right.

One observation based on this visualization is that when the horizontal current is headed roughly northward (the upper right in the plot), the w velocity tends to be magenta, hence positive (upward), and when the horizontal current is headed roughly southward (the lower left in the plot), the w velocity tends to be blue, hence negative (downward). Another observation is that there does not seem to be a significant difference in character to the phase space coverage between the first half of the year (blue-magenta) and the last half of the year (visible portion of the yellow). The visible yellow seems to represent just some increased variability, which is expected from having more data, but does not appear to occupy a different area of phase space than the data in blue-magenta.

Figure 16: Velocity visualization at 10.5 mab in u-v phase space with colormapped w.

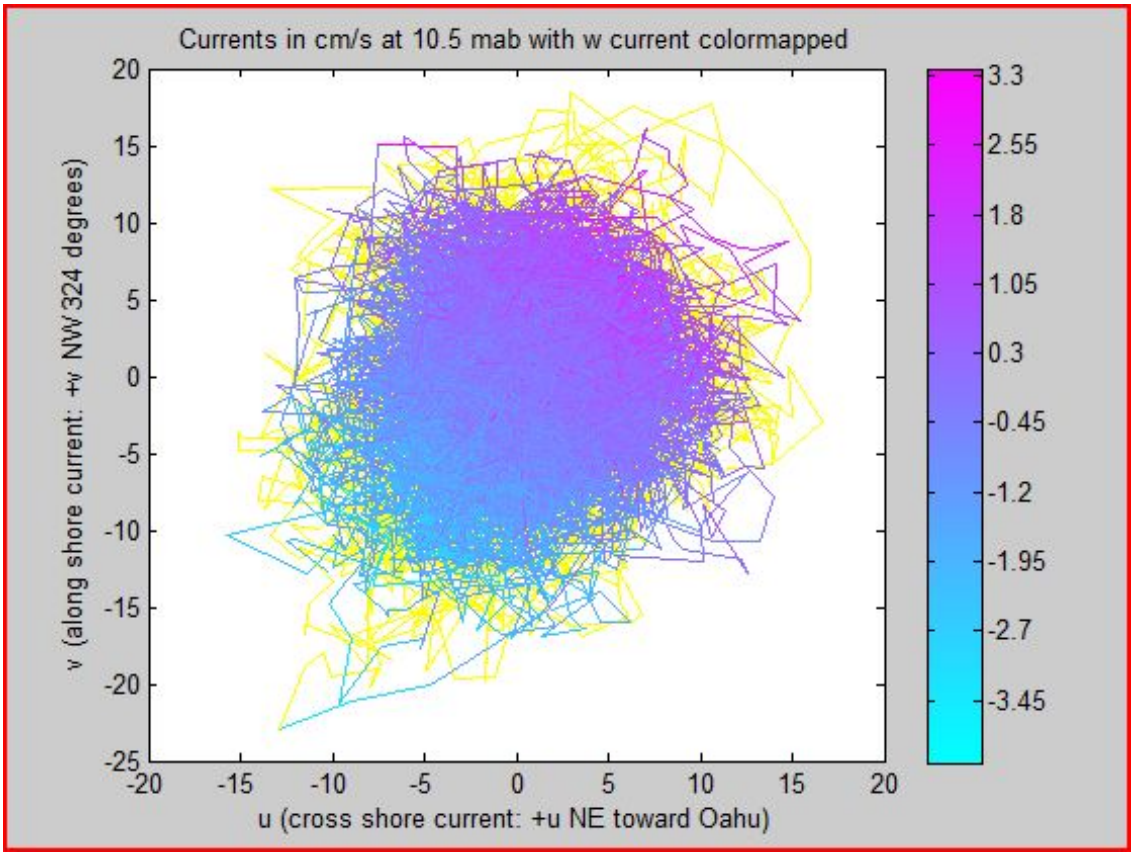

Finally, figures 17–19 show the spectrograms (short-time Fourier transforms) of the velocity field in time at a particular height (10 mab). Each vertical strip in these figures represents a Fourier transform of a short time segment of the velocity data. Moving from left to right in the figure, the time window of the signal moves left to right. Thus, we see the temporal evolution of the spectrum of the velocity. Moving from bottom to top the frequency increases. Color represents the amount of power in each frequency, based on the scale on the color bar with the top of the color bar representing the most energetic.

From these figures we can see that the bulk of the energy is in tidal frequencies (primarily twice daily and, to a lesser extent, once daily and harmonics thereof). The along-shore velocity has a stronger once daily frequency component than the cross-shore velocity and this frequency is energetic at certain times in the vertical velocity as well. Note that the power scale is different for the spectra of the vertical and horizontal velocity components since the vertical velocity component is less energetic than the horizontal velocity components. Both along-shore velocity and vertical velocity show energy in the "dc" at certain times. That is, both of these velocity components exhibit a non-zero average during part of the year.

These spectrograms were prepared using a Blackman window ($\alpha = 0.16$) with width 2048 and step 32 and no extra padding.

Figure 17: Spectrogram of the u velocity at $z = 10$ mab

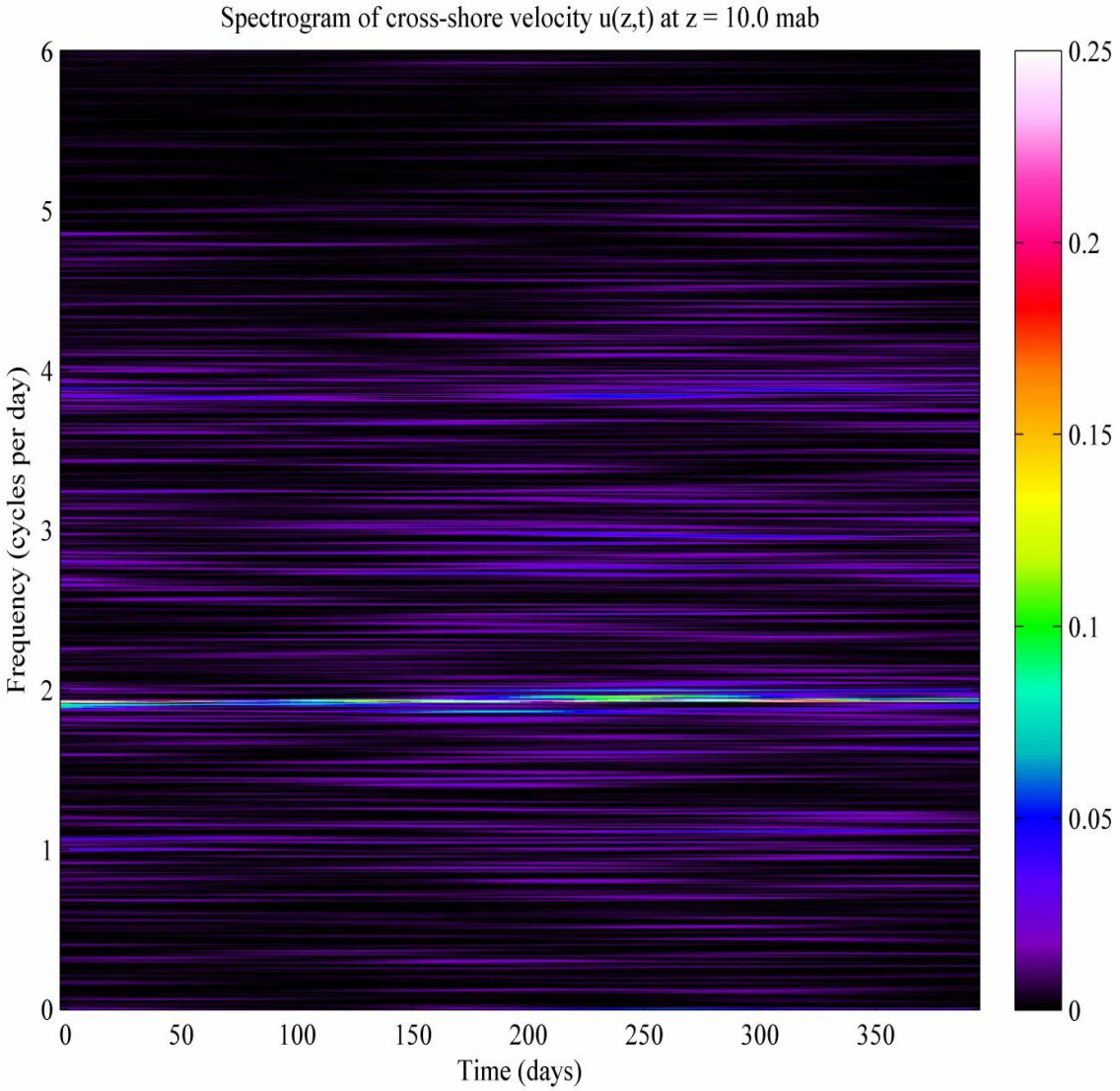

Figure 18: Spectrogram of the v velocity at $z = 10$ mab

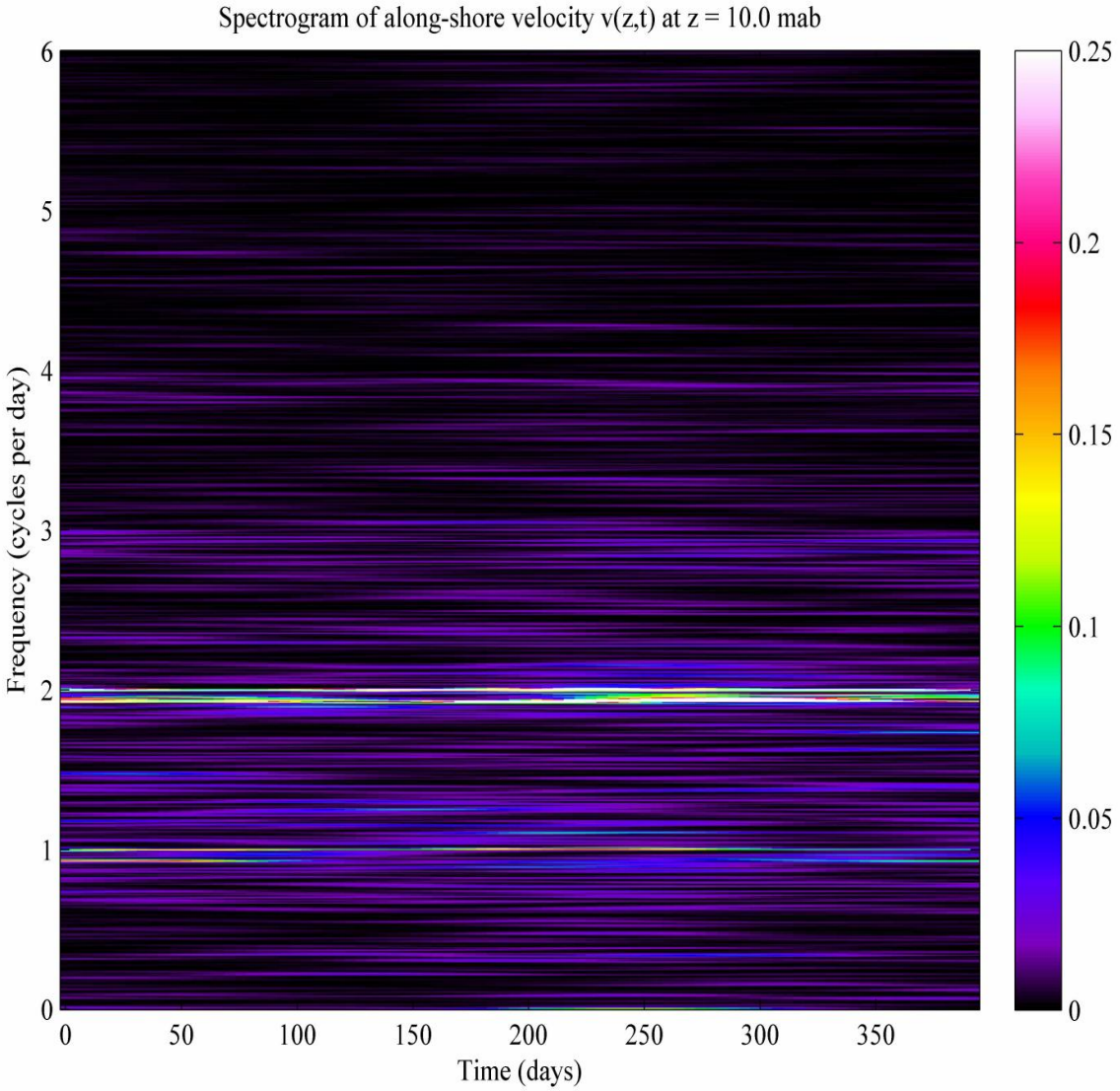

Figure 19: Spectrogram of the w velocity at $z = 10$ mab

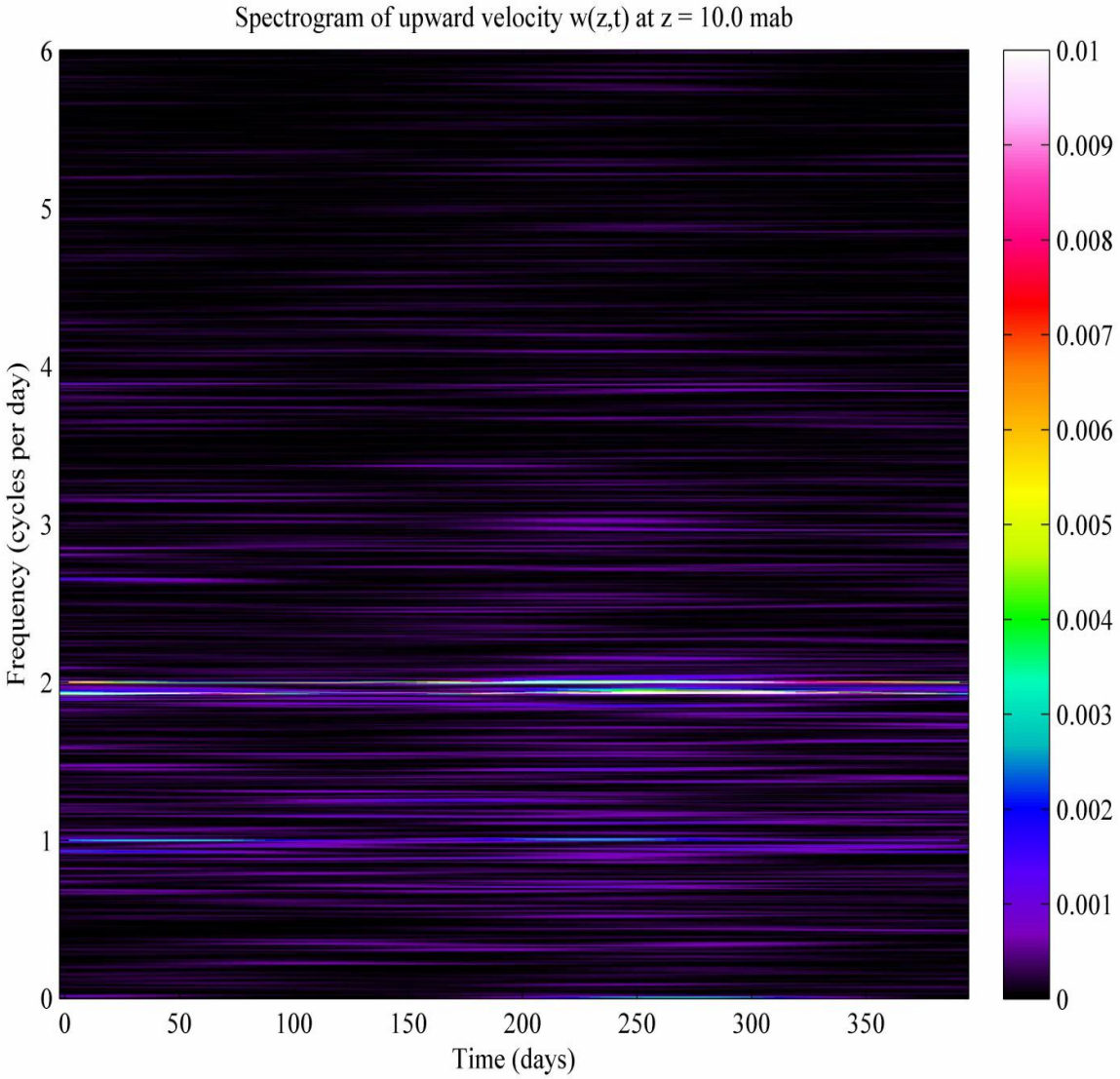

4 Simple Models with Analytical Solutions

The governing equation for chemical transport in this case is a second order, linear partial differential equation with coefficients varying in z and t. The z-variation of the velocities in the advective terms is the most difficult aspect of this equation, mathematically, in that it blocks the analytical solution of the transport equation by Fourier transform methods and couples the spatial dimensions.

General analytical solutions for the transport equation with velocities varying in the z-direction are not currently known. To handle this more difficult case we recommend a semi-analytical approach which reduces the original partial differential equation (pde) to a coupled system of ordinary differential equations (odes) in time, which could be solved with a combination of symbolic and numerical techniques in Matlab's Symbolic Math Toolbox. A method of this type is exemplified in Alves et al. [2001]. This work was not undertaken under the present project.

If we ignore the z-dependence of the velocities it is possible to analytically solve the transport equation using a point source instantaneous release of pollutant at the disposal site as the initial condition. A set of simplified models are presented which use this approach. One drawback of these models is that due to the lack of direct z-dependence of the velocities, these simple models cannot reproduce shear mixing directly, however additional mixing can be roughly modeled by increasing the turbulent diffusivity, if desired.

There are numerous benefits to having analytical solutions to the model equations. The development of these solutions is much faster than setting up and validating a numerical model. We can be confident that the solutions model diffusion and advection accurately within the limitations imposed by our assumptions since the solutions proceed directly from modeling the physics of the transport processes. Closed-form solutions can be manipulated algebraically to provide answers to many kinds of questions without the need to run time-consuming simulations. To the extent that numerical methods are avoided, we avoid the artifacts and errors inherent to these methods.

The development of these analytical models is contained in section 4 and subsequent analysis of chemical transport using these models is contained in section 5. We proceed in several steps. First, we consider the simple case of diffusion without advection. Next, we consider diffusion with constant advection and then diffusion with time-dependent advection. The first two are clearly just special cases of the last, but it is convenient to proceed in these three steps to make the solution process clear. Finally, by considering a pathline $(\tilde{x}(t), \tilde{y}(t), \tilde{z}(t))$ taken by a particle in the flow field, we can use the velocities $(\tilde{u}(t), \tilde{v}(t), \tilde{w}(t))$ experienced along the pathline as an expression of a time-dependent velocity field. This allows us to incorporate z-dependence into the solution in a limited, implicit way. Effectively, this allows the plume center to advect along this pathline while diffusing. This is not equivalent to solving the original problem with z-dependent velocities but is much more realistic than a constant velocity solution.

In all cases we assume that the turbulent diffusivities K_H and K_V are constant (though unequal) and that the pollutant is released as an instantaneous point source. In the case of no advection, we see Gaussian diffusion away from the chemical source. In the case of constant advection, we see the same Gaussian diffusion away from the source, but with the center of the plume moving with the constantly advecting water. In the case of time-dependent advection, where the time dependence of velocity is defined as the velocity experienced as

the plume center is advected through the velocity field which depends on z and t, we again have the same Gaussian diffusion pattern but here the center of the advected plume moves along a pathline which is obtained as the integral of the velocity field. The complex folding, stretching, straining, and streaking noted in real fluid flows (such as when stirring cream into coffee) will not be reproduced by the present models, but we expect that equivalent mixing behavior can be modeled with the right choice of diffusivities.

Each of these models is posed on an unbounded 3-dimensional spatial domain, which makes them mathematically very simple. However, this means that we are ignoring the existence of the seafloor (the chemical plume can theoretically diffusive through the seafloor boundary in this model). In such cases it is common to make a correction for this by "reflecting" the chemical concentration from negative z to positive z. We do not make this correction, for three reasons. First, the correction has no effect once the plume has moved sufficiently far from the bottom. Second, a factor of two difference in concentration near the bottom likely has little consequence since the bottom is expected to have limited marine life and no likelihood of human interaction at these depths. Third, the model's accuracy depends on the correct choice of turbulent diffusivity, which will have a larger effect on the actual results than a possible factor of two correction which is needed only near the seafloor.

Variations in the model predications due to choice of turbulent diffusivities are handled by bracketing with a range of turbulent diffusivities.

Finally, in section 4.2, we also briefly explore the impact of using instantaneous point source initial conditions by comparing the solution achieved in this way to that where the chemical is initially present as a cube of constant concentration. There is no significant difference in these solutions after about 5 seconds or so.

4.1 Diffusion Only in an Unbounded Domain with Instantaneous Point Source

This first preliminary model considers turbulent diffusion as the only transport process. This will help us understand the time and length scales of the diffusive processes. With zero advection and constant diffusivities, taking $a = 0$ so that $\delta_a(x, y, z) = \delta_0(x, y, z) = \delta(x, y, z)$, the initial-boundary value problem from section 2.3.2 is

$$\frac{\partial c}{\partial t} = K_H \frac{\partial^2 c}{\partial x^2} + K_H \frac{\partial^2 c}{\partial y^2} + K_V \frac{\partial^2 c}{\partial z^2} \tag{19}$$

$$c(\vec{x}, 0) = Q\delta(x, y, z) \tag{20}$$

$$c(\vec{x}, t) \longrightarrow 0 \quad \text{as } x, y \longrightarrow \pm\infty \quad \text{for } t > 0 \tag{21}$$

$$\frac{\partial c}{\partial x}(\vec{x}, t) \longrightarrow 0 \quad \text{as } x, y \longrightarrow \pm\infty \quad \text{for } t > 0 \tag{22}$$

$$\frac{\partial c}{\partial y}(\vec{x}, t) \longrightarrow 0 \quad \text{as } x, y \longrightarrow \pm\infty \quad \text{for } t > 0 \tag{23}$$

$$\frac{\partial c}{\partial z}(\vec{x}, t) \longrightarrow 0 \quad \text{as } x, y, z \longrightarrow \pm\infty \quad \text{for } t > 0 \tag{24}$$

which can be analytically solved by Fourier transform methods. Let us define the Fourier

transform of a function f and the inverse Fourier transform of $\hat{f}$ as follows:

$$\begin{aligned}\mathcal{F}\left(f(x)\right) &= \hat{f}(\xi) = \int_{-\infty}^{\infty} f(x)e^{-2\pi i x\xi}\,dx \\ \mathcal{F}^{-1}\left(f(\xi)\right) &= f(x) = \int_{-\infty}^{\infty} f(\xi)e^{2\pi i x\xi}\,d\xi\end{aligned}$$

We begin by taking Fourier transforms in the x, y, and z directions of the partial differential equation (19). We will proceed formally, which is to say, we will freely exchange the order of integration and differentiation and take other such liberties without any justification because at the end we will directly verify that the derived solution does, in fact, satisfy the original initial-boundary value problem (19)–(24). Let $\hat{c}(\xi,\theta,\zeta,t)$ denote the Fourier transform of the concentration field in the three spatial directions and let $\mathcal{F}$ denote the 3-d Fourier transform operator. Then we proceed to transform (19) term by term. The time derivative term becomes

$$\mathcal{F}\left(\frac{\partial c}{\partial t}(x,y,z,t)\right) = \frac{\partial \hat{c}}{\partial t}(\xi,\theta,\zeta,t).$$

Using integration by parts in the x-integral, together with the boundary conditions (21) and (22), the x-diffusion term becomes

$$\begin{aligned}&\mathcal{F}\left(K_H\frac{\partial^2 c}{\partial x^2}(x,y,z,t)\right) \\ =\;& K_H\int_{-\infty}^{\infty}\int_{-\infty}^{\infty}\int_{-\infty}^{\infty}\frac{\partial^2 c}{\partial x^2}(x,y,z,t)e^{-2\pi i(x\xi+y\theta+z\zeta)}\,dx\,dy\,dz \\ =\;& K_H\int_{-\infty}^{\infty}\int_{-\infty}^{\infty}\left(\int_{-\infty}^{\infty}\frac{\partial^2 c}{\partial x^2}(x,y,z,t)e^{-2\pi i x\xi}\,dx\right)e^{-2\pi i(y\theta+z\zeta)}\,dy\,dz \\ =\;& K_H\int_{-\infty}^{\infty}\int_{-\infty}^{\infty}\left(\left[\frac{\partial c}{\partial x}(x,y,z,t)e^{-2\pi i x\xi}\right]_{x=-\infty}^{x=\infty} - \int_{-\infty}^{\infty}\frac{\partial c}{\partial x}(x,y,z,t)\left(-2\pi i\xi\right)e^{-2\pi i x\xi}\,dx\right)e^{-2\pi i(y\theta+z\zeta)}\,dy\,dz \\ =\;& K_H\int_{-\infty}^{\infty}\int_{-\infty}^{\infty}\left(2\pi i\xi\int_{-\infty}^{\infty}\frac{\partial c}{\partial x}(x,y,z,t)e^{-2\pi i x\xi}\,dx\right)e^{-2\pi i(y\theta+z\zeta)}\,dy\,dz \\ =\;& K_H\int_{-\infty}^{\infty}\int_{-\infty}^{\infty}\left(\left[c(x,y,z,t)e^{-2\pi i x\xi}\right]_{x=-\infty}^{x=\infty} - 2\pi i\xi\int_{-\infty}^{\infty}c(x,y,z,t)\left(-2\pi i\xi\right)e^{-2\pi i x\xi}\,dx\right)e^{-2\pi i(y\theta+z\zeta)}\,dy\,dz \\ =\;& K_H\int_{-\infty}^{\infty}\int_{-\infty}^{\infty}\left(-\left(2\pi\xi\right)^2\int_{-\infty}^{\infty}c(x,y,z,t)e^{-2\pi i x\xi}\,dx\right)e^{-2\pi i(y\theta+z\zeta)}\,dy\,dz \\ =\;& -4\pi^2 K_H\xi^2\hat{c}(\xi,\theta,\zeta,t)\end{aligned}$$

Proceeding similarly with the other diffusive terms and using the boundary conditions (21), (23) and (24), we see that the Fourier transform of (19) is

$$\frac{\partial \hat{c}}{\partial t}(\xi,\theta,\zeta,t) = -4\pi^2(K_H\xi^2 + K_H\theta^2 + K_V\zeta^2)\hat{c}(\xi,\theta,\zeta,t)$$

which has solution

$$\hat{c}(\xi,\theta,\zeta,t) = b(\xi,\theta,\zeta)e^{-4\pi^2(K_H\xi^2+K_H\theta^2+K_V\zeta^2)t}$$

for some constant $b(\xi,\theta,\zeta)$ with respect to the t-integration. To solve for b, we take the Fourier transform of the initial condition (20) to get a new initial condition in the Fourier domain.

$$\mathcal{F}\left(c(x,y,z,0)\right) = \int_{-\infty}^{\infty}\int_{-\infty}^{\infty}\int_{-\infty}^{\infty} Q\delta_a(x,y,z)e^{-2\pi i(x\xi+y\theta+z\zeta)}\,dx\,dy\,dz = Q$$

and so

$$\hat{c}(\xi,\theta,\zeta,0) = b(\xi,\theta,\zeta) = Q$$

and the solution of (19) in the Fourier domain is

$$\hat{c}(\xi,\theta,\zeta,t) = Qe^{-4\pi^2(K_H\xi^2+K_H\theta^2+K_V\zeta^2)t}. \tag{25}$$

Applying the inverse Fourier transform $\mathcal{F}^{-1}$ to (25) yields

$$\begin{aligned}
c(x,y,z,t) &= \mathcal{F}^{-1}\left(\hat{c}(\xi,\theta,\zeta,t)\right) = \int_{-\infty}^{\infty}\int_{-\infty}^{\infty}\int_{-\infty}^{\infty}\hat{c}(\xi,\theta,\zeta,t)e^{2\pi i(x\xi+y\theta+z\zeta)}\,d\xi\,d\theta\,d\zeta\\
&= \int_{-\infty}^{\infty}\int_{-\infty}^{\infty}\int_{-\infty}^{\infty} Qe^{-4\pi^2(K_H\xi^2+K_H\theta^2+K_V\zeta^2)t}e^{2\pi i(x\xi+y\theta+z\zeta)}\,d\xi\,d\theta\,d\zeta\\
&= Q\int_{-\infty}^{\infty}\int_{-\infty}^{\infty}\int_{-\infty}^{\infty} e^{-4\pi^2K_Ht\xi^2}e^{2\pi ix\xi}\,d\xi\,e^{-4\pi^2K_Ht\theta^2}e^{2\pi iy\theta}\,d\theta\,e^{-4\pi^2K_Vt\zeta^2}e^{2\pi iz\zeta}\,d\zeta\\
&= \frac{Q}{4\pi K_Ht\sqrt{4\pi K_Vt}}e^{-(x^2+y^2)/4K_Ht-z^2/4K_Vt}.
\end{aligned}$$

4.2 Diffusion Only in an Unbounded Domain with Box Source

If we define the initial chemical release in the initial conditions but as a constant concentration spread over a cube, then we can derive a solution in terms of the error function, erf. This is computationally much more costly than evaluating a Gaussian but it is instructive to compare this to the point source diffusion-only model to see what difference these two different forms of initial condition make to the early diffusion behavior to understand if we are introducing artificially fast diffusion in the early evolution by the choice of point source initial chemical release. For simplicity we make this comparison in the one-dimensional diffusion-only problem.

Setting the initial conditions for a box-car style release as

$$c(x,0) = QB_a(x) \tag{26}$$

where

$$B_a(x) = \begin{cases} 1 \text{ if } x\in[-a,a] \\ 0 \text{ otherwise} \end{cases}, \tag{27}$$

and solving the initial-boundary value problem from the previous section in just the x dimension with this initial condition yields

$$c(x,t) = \frac{Q}{2}\left[\text{erf}\left(\frac{x+a}{\sqrt{4K_Ht}}\right) - \text{erf}\left(\frac{x-a}{\sqrt{4K_Ht}}\right)\right]. \tag{28}$$

Figure 20 shows the effect on the solution of these two different initial conditions types. The red line indicates the box-car style initial condition where initially there is a cube of

chemical at a constant concentration corresponding to dissolving $Q = 182$ kg of chemical in the cube of side $a = 0.5$ m. The blue line corresponds to the point source release solution, developed in the previous section, also with a release amount of $Q = 182$ kg. It is clear that these two solutions are noticeably different for only a few seconds. This should allay any fears about the unphysicality of a point source release, since the solution relaxes so quickly to a physically reasonable Gaussian and in much the same way the box car type of release does so.

Figure 20: Effect of initial conditions of release on solution.

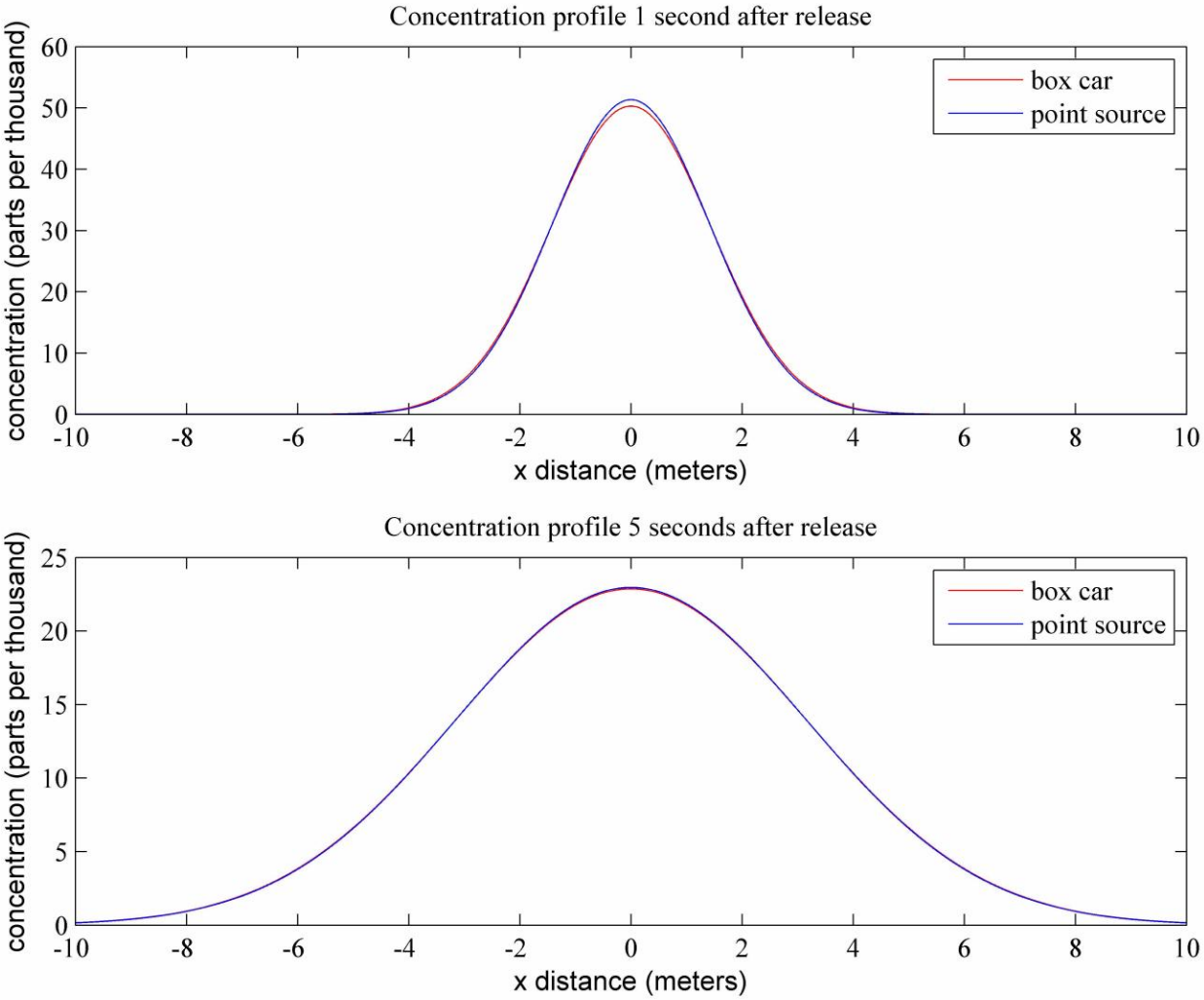

4.3 Diffusion with Constant Advection

The second preliminary model considers diffusion and constant advection. Assuming constant advection and constant diffusivities, taking $a = 0$ so that $\delta_a(x, y, z) = \delta_0(x, y, z) = \delta(x, y, z)$, the initial-boundary value problem is

$$\frac{\partial c}{\partial t} = K_H \frac{\partial^2 c}{\partial x^2} + K_H \frac{\partial^2 c}{\partial y^2} + K_V \frac{\partial^2 c}{\partial z^2} - u\frac{\partial c}{\partial x} - v\frac{\partial c}{\partial y} - w\frac{\partial c}{\partial z} \tag{29}$$

$$c(\vec{x}, 0) = Q\delta(x, y, z) \tag{30}$$

$$c(\vec{x}, t) \longrightarrow 0 \quad \text{as } x, y \longrightarrow \infty \quad \text{for } t > 0 \tag{31}$$

$$\frac{\partial c}{\partial x}(\vec{x}, t) \longrightarrow 0 \quad \text{as } x, y \longrightarrow \infty \quad \text{for } t > 0 \tag{32}$$

$$\frac{\partial c}{\partial y}(\vec{x}, t) \longrightarrow 0 \quad \text{as } x, y \longrightarrow \infty \quad \text{for } t > 0 \tag{33}$$

$$\frac{\partial c}{\partial z}(\vec{x}, t) \longrightarrow 0 \quad \text{as } x, y \longrightarrow \infty \quad \text{for } t > 0 \tag{34}$$

which can also be solved analytically by Fourier transform methods.

As before, we begin by formally taking Fourier transforms in the x, y, and z directions of the partial differential equation (29). Let $\hat{c}(\xi, \theta, \zeta, t)$ denote the Fourier transform of the concentration field in the three spatial directions and let $\mathcal{F}$ denote the 3-d Fourier transform operator. Then we proceed to transform (29) term by term. The time derivative term becomes

$$\mathcal{F}\left(\frac{\partial c}{\partial t}(x, y, z, t)\right) = \frac{\partial \hat{c}}{\partial t}(\xi, \theta, \zeta, t).$$

Using integration by parts in the x-integral, together with the boundary conditions (31) and (32), as before, the x-diffusion term becomes

$$\mathcal{F}\left(K_H \frac{\partial^2 c}{\partial x^2}(x, y, z, t)\right) = -4\pi^2 K_H \xi^2 \hat{c}(\xi, \theta, \zeta, t)$$

The Fourier transform of the advective term in the x-direction with u constant is accomplished similarly to that of the diffusive term, using integration by parts in x once and applying the boundary condition (31).

$$\begin{aligned}
&\mathcal{F}\left(u\frac{\partial c}{\partial x}(x, y, z, t)\right) \\
&= u\int_{-\infty}^{\infty}\int_{-\infty}^{\infty}\int_{-\infty}^{\infty} \frac{\partial c}{\partial x}(x, y, z, t) e^{-2\pi i(x\xi + y\theta + z\zeta)}\, dx\, dy\, dz \\
&= u\int_{-\infty}^{\infty}\int_{-\infty}^{\infty}\left(\int_{-\infty}^{\infty} \frac{\partial c}{\partial x}(x, y, z, t) e^{-2\pi i x\xi}\, dx\right) e^{-2\pi i(y\theta + z\zeta)}\, dy\, dz \\
&= u\int_{-\infty}^{\infty}\int_{-\infty}^{\infty}\left(\left[c(x, y, z, t)e^{-2\pi i x\xi}\right]_{x=-\infty}^{x=\infty} - (-2\pi i\xi)\int_{-\infty}^{\infty} c(x, y, z, t) e^{-2\pi i x\xi}\, dx\right) e^{-2\pi i(y\theta + z\zeta)}\, dy\, dz \\
&= 2\pi i\xi u\int_{-\infty}^{\infty}\int_{-\infty}^{\infty}\int_{-\infty}^{\infty} c(x, y, z, t) e^{-2\pi i(x\xi + y\theta + z\zeta)}\, dx\, dy\, dz \\
&= 2\pi i u\xi \hat{c}(\xi, \theta, \zeta, t)
\end{aligned}$$

Proceeding similarly with the other diffusive and advective terms, we see that the Fourier transform of (29) is

$$\frac{\partial \hat{c}}{\partial t}(\xi,\theta,\zeta,t) = \left[-4\pi^2(K_H\xi^2 + K_H\theta^2 + K_V\zeta^2) - 2\pi i(u\xi + v\theta + w\zeta)\right]\hat{c}(\xi,\theta,\zeta,t)$$

which has solution

$$\hat{c}(\xi,\theta,\zeta,t) = b(\xi,\theta,\zeta)e^{\left[-4\pi^2(K_H\xi^2+K_H\theta^2+K_V\zeta^2)-2\pi i(u\xi+v\theta+w\zeta)\right]t}$$

for some constant $b(\xi,\theta,\zeta)$ with respect to the t-integration. To solve for b, we take the Fourier transform of the initial condition (20) to get a new initial condition in the Fourier domain.

$$\mathcal{F}\left(c(x,y,z,0)\right) = \int_{-\infty}^{\infty}\int_{-\infty}^{\infty}\int_{-\infty}^{\infty} Q\delta(x,y,z)e^{-2\pi i(x\xi+y\theta+z\zeta)}\,dx\,dy\,dz = Q$$

and so

$$\hat{c}(\xi,\theta,\zeta,0) = b(\xi,\theta,\zeta) = Q$$

and the solution of (29) in the Fourier domain is

$$\hat{c}(\xi,\theta,\zeta,t) = Qe^{\left[-4\pi^2(K_H\xi^2+K_H\theta^2+K_V\zeta^2)-2\pi i(u\xi+v\theta+w\zeta)\right]t}. \tag{35}$$

Applying the inverse Fourier transform $\mathcal{F}^{-1}$ to (35) yields

$$\begin{aligned}
&c(x,y,z,t)\\
&= \mathcal{F}^{-1}\left(\hat{c}(\xi,\theta,\zeta,t)\right)\\
&= \int_{-\infty}^{\infty}\int_{-\infty}^{\infty}\int_{-\infty}^{\infty} \hat{c}(\xi,\theta,\zeta,t)e^{2\pi i(x\xi+y\theta+z\zeta)}\,d\xi\,d\theta\,d\zeta\\
&= \int_{-\infty}^{\infty}\int_{-\infty}^{\infty}\int_{-\infty}^{\infty} Qe^{\left[-4\pi^2(K_H\xi^2+K_H\theta^2+K_V\zeta^2)-2\pi i(u\xi+v\theta+w\zeta)\right]t}e^{2\pi i(x\xi+y\theta+z\zeta)}\,d\xi\,d\theta\,d\zeta\\
&= Q\int_{-\infty}^{\infty}\int_{-\infty}^{\infty}\int_{-\infty}^{\infty} e^{-4\pi^2K_Ht\xi^2-2\pi iu\xi t}e^{2\pi ix\xi}\,d\xi\,e^{-4\pi^2K_Ht\theta^2-2\pi iv\theta t}e^{2\pi iy\theta}\,d\theta\,e^{-4\pi^2K_Vt\zeta^2-2\pi iw\zeta t}e^{2\pi iz\zeta}\,d\zeta\\
&= Q\int_{-\infty}^{\infty}\int_{-\infty}^{\infty}\int_{-\infty}^{\infty} e^{-4\pi^2K_Ht\xi^2}e^{2\pi i(x-ut)\xi}\,d\xi\,e^{-4\pi^2K_Ht\theta^2}e^{2\pi i(y-vt)\theta}\,d\theta\,e^{-4\pi^2K_Vt\zeta^2}e^{2\pi i(z-wt)\zeta}\,d\zeta\\
&= \frac{Q}{4\pi K_Ht\sqrt{4\pi K_Vt}}e^{-((x-ut)^2+(y-vt)^2)/4K_Ht-(z-wt)^2/4K_Vt}.
\end{aligned} \tag{36}$$

4.4 Diffusion with Pathline Advection

The solution developed in the previous section assumes that advection is constant in time and space, however the same solution method works, with a minor variation, for the case of time-dependent advection. If we define

$$\tilde{x}(t) = \int_0^t u(s)\,ds \tag{37}$$

$$\tilde{y}(t) = \int_0^t v(s)\,ds \tag{38}$$

$$\tilde{z}(t) = \int_0^t w(s)\,ds. \tag{39}$$

where the velocity field is assumed to depend on time in some arbitrary (but integrable) way, then it is straightforward to show that the solution of the advection-diffusion equation with time-dependent velocity is

$$c(x,y,z,t) = \frac{Q}{4\pi K_H t\sqrt{4\pi K_V t}} e^{-((x-\tilde{x}(t))^2+(y-\tilde{y}(t))^2)/4K_H t-(z-\tilde{z}(t))^2/4K_V t}. \tag{40}$$

We would prefer to solve the advection-diffusion equation for the case where velocities depend on z and t, however the solution method above does not extend to this case, and, in fact, there are no known closed-form solutions for this general case. In order to continue with the development of analytical models, we consider an intermediate approach.

A pathline is the path or trajectory that an idealized particle would take if released in the velocity field at a particular location and time. We can estimate the pathline for a particle released at time $t = t_0$ at the location of the chemical release by integrating over the velocity experienced by the particle in time. Since we are assuming that velocities depend on z and t, we have the following type of expression for this pathline:

$$\tilde{x}(t) = \int_{t_0}^{t} u(\tilde{z}(s), s)\, ds \tag{41}$$

$$\tilde{y}(t) = \int_{t_0}^{t} v(\tilde{z}(s), s)\, ds \tag{42}$$

$$\tilde{z}(t) = \int_{t_0}^{t} w(\tilde{z}(s), s)\, ds \tag{43}$$

where the pathline is given by $(\tilde{x}(t), \tilde{y}(t), \tilde{z}(t))$. It is straightforward to numerically estimate $\tilde{x}(t)$ and $\tilde{y}(t)$, once we know $\tilde{z}(t)$. However, $\tilde{z}(t)$ appears on both sides of the integral equation (43) so we must either solve the integral equation or solve the equivalent differential equation

$$\frac{d}{dt}\tilde{z}(t) = w(\tilde{z}(t), t). \tag{44}$$

We choose to solve equation (44) numerically as this is expected to be more stable [Press et al., 2007]. This is discussed in more detail in section 5.2.2.

Once we have the pathline $(\tilde{x}(t), \tilde{y}(t), \tilde{z}(t))$ it is clear that the solution, given by equation (40), represents Gaussian diffusion centered on the plume center, which moves with the pathline under the influence of the velocity field. The degree of spread of the Gaussian depends on time and on the turbulent diffusion constants.

5 Results based on Analytical Models

The primary question these models are designed to answer is: if chemicals are released from their containers at the deep water disposal site, where are they likely to end up, in what concentration, and for how long? To understand where currents are likely to transport a chemical plume, we compute a pathline representing the estimated path of a particle situated at the disposal site at the time of release. This will represent the path of the plume center. Since currents change over time, we compute pathlines corresponding to various different release times. Pathlines are discussed further in section 5.1.

Based on a pathline, we can estimate the diffusion of the chemical as the plume center travels along the pathline in time and from this we can estimate concentration, exposure time, and exposure at each location in a three-dimensional spatial grid. In this context *exposure time* means the amount of time the concentration exceeds some threshold at a point and *exposure* is (approximately) the integral of concentration over the exposure time. In section 5.2 we present a variety of *footprint* plots showing where a chemical release is likely to be transported, in what concentration, and for how long, as predicted by the model.

Section 5.3 demonstrates the effect of the choice of turbulent diffusivity values on the predictions of the model.

5.1 Pathlines

The pathline model which is used to predict the transport of the chemical plume represents Gaussian diffusion occurring around a moving center point, where the center moves along a pathline of the velocity field. Sometimes we think of this as following an imaginary particle in time as it flows with the velocity field. The particle we have in mind is the one starting at the release location at the time of release. The path of this imaginary particle is the same as the path of the center of the plume.

The pathline is estimated by numerically solving

$$\frac{dz}{dt} = w(z,t) \tag{45}$$

for $z = z(t)$, the z component of the pathline, where $w(z,t)$ is the vertical component of the known velocity field, and the starting location is the point of release of the chemical. This equation is solved with a standard ODE solver in Matlab (ode45). Since $u(z,t)$ and $v(z,t)$, the horizontal components of the velocity field, are also known and depend only on z and t (according to our assumption), once we know the z component of the pathline in time, we can readily estimate the x and y components of the pathline in time. Since the velocities are assumed not to vary in x or y then the differential equation above is not coupled to the u and v components of velocity.

Unfortunately, a conflict is introduced by assuming that u, v, and w do not depend on x or y. Recall that we made this assumption because we only have current data at one x, y location. The assumption is probably not terribly unreasonable for u and v. However for w it is likely to be problematic. The assumption implies that if there is a positive (upward) velocity at (x, y, z, t) then across the entire ocean at this time t and height z, there is also upward velocity, so an entire layer of the ocean is moving upward at once. This is clearly unphysical. Instead, we expect vertical motion to be more wavelike, with both spatial and

temporal variations. That is, we expect that the water sloshes up and down a bit, rather than flowing like a vertical river. To say this more mathematically, once we assume that there is no velocity gradient in x or y, then the continuity equation tells us immediately that vertical velocity is everywhere zero. Consequently, since we choose to use the vertical velocity field as measured (rather than assume it is zero) we should not be surprised to see some anomalous behavior in the vertical direction. It would be interesting to add some random noise to the velocity field which has the effect of restoring zero divergence (continuity), however this has not yet been pursued.

Another difficulty in computing the z-component of a pathline is that it cannot be allowed to be negative (to move below the seafloor). In addition, if z were allowed to be zero then because velocities are assumed to be zero at the seafloor, the pathline would then stay on the seafloor for all time thereafter. Hence, we restrict z by enforcing a minimum z value, which is a settable parameter. In the figures shown here it was set to 0.5 mab.

All pathlines begin at $(x, y, z) = (0\text{m}, 0\text{m}, 0.5\text{m})$ and continue in time until the last time sample where velocity data is available in the prepared velocity data set. The first set of figures shown illustrate the pathline starting at the first time index of the prepared velocity data set. Later figures will show data for ensembles of pathlines where each pathline starts at a randomly selected time index.

Figure 21 shows the estimated x (cross-shore) coordinate of the pathline for a particle starting at the release site at the first time sample of the prepared velocity data set. The blue line is the x-component of the pathline in time.

The green line represents the path which would be taken if the particle traveled for the same amount of time but at the constant u velocity given by the average u velocity along the pathline (0.18 cm/s). We expect these to end at the same point if the pathline is valid.

The red lines in the following figures are of less interest and were initially included as a crude double check. They are referred to in the figures as field averages and are computed as the path taken by a particle traveling at the field average velocity where the field average velocity is computed by taking the average of all measurements of the relevant velocity component over all times in the pathline and over the entire range of depths visited by the pathline. The pathline shown in the next several figures visits depths from 0 mab to about 280 mab and therefore the field average velocity is the average over all velocity measurements taken at or below 278 mab for all times in the prepared velocity data set. Because the velocity measurements are not evenly spaced in the z direction, but are more closely spaced in the bottom 10.5 m, this has the effect of weighting the average toward the velocities near the bottom. For this reason, the red lines are probably indicative of how the plume center would travel if it stayed closer to the bottom. For reference, the field average of the u velocity for this pathline was (-0.48 cm/s).

Figure 22 shows the estimated y (along-shore) coordinate of the pathline for a particle starting at the release site at the first time sample of the prepared velocity data set. The blue line is the y-component of the pathline in time. We observe that the particle travels much farther in the y direction than it did in the x direction along this particular pathline.

The green line represents the path which would be taken if the particle traveled for the same amount of time but at the constant v velocity given by the average v velocity along the pathline (0.82 cm/s). As in the last figure, we expect these to end at the same point if the pathline is valid. The field averaged v velocity was 0.54 cm/s (see the previous remarks about what this means).

Figure 21: Example pathline x coordinate in time with averages.

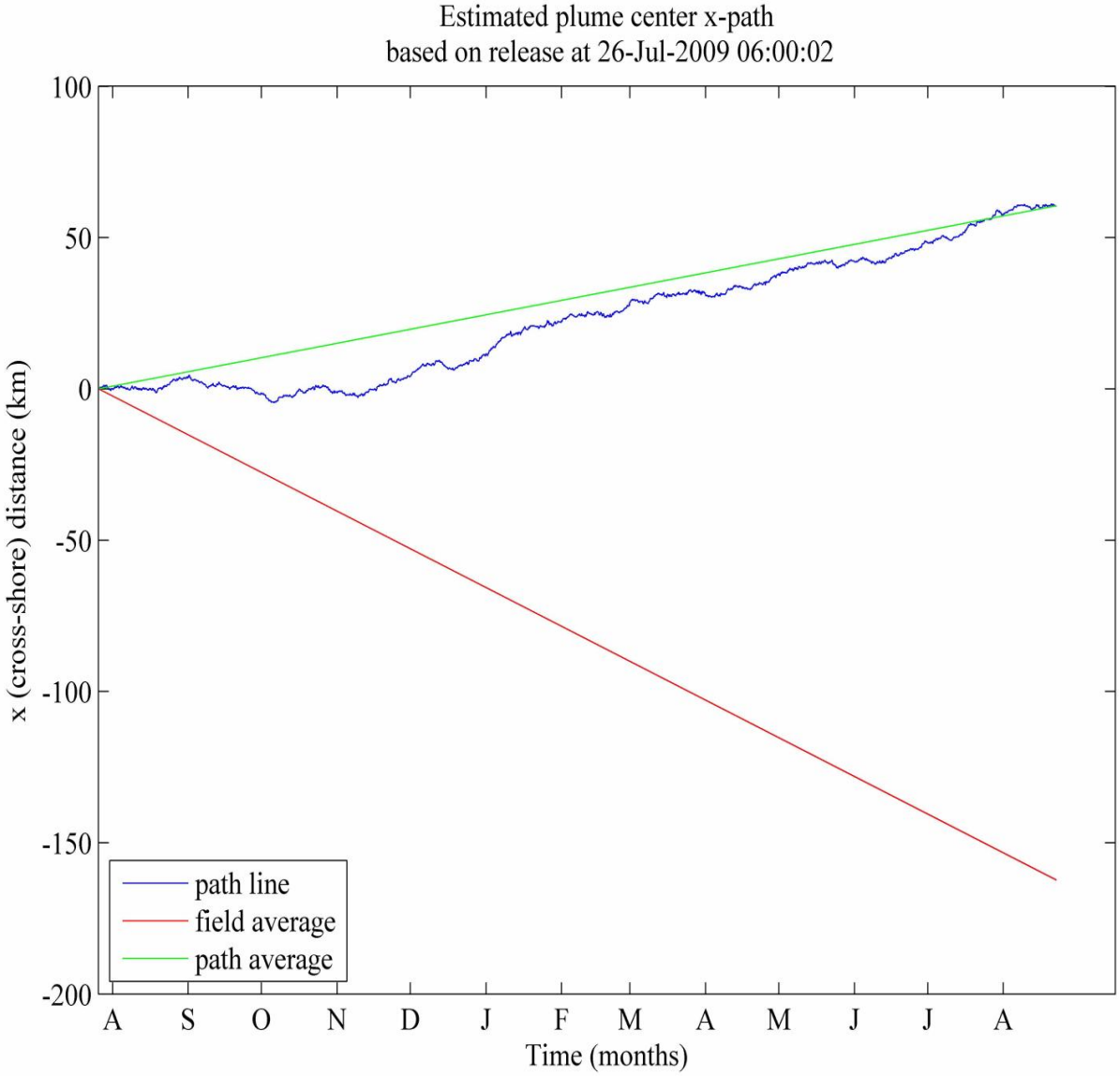

Figure 22: Example pathline y coordinate in time with averages.

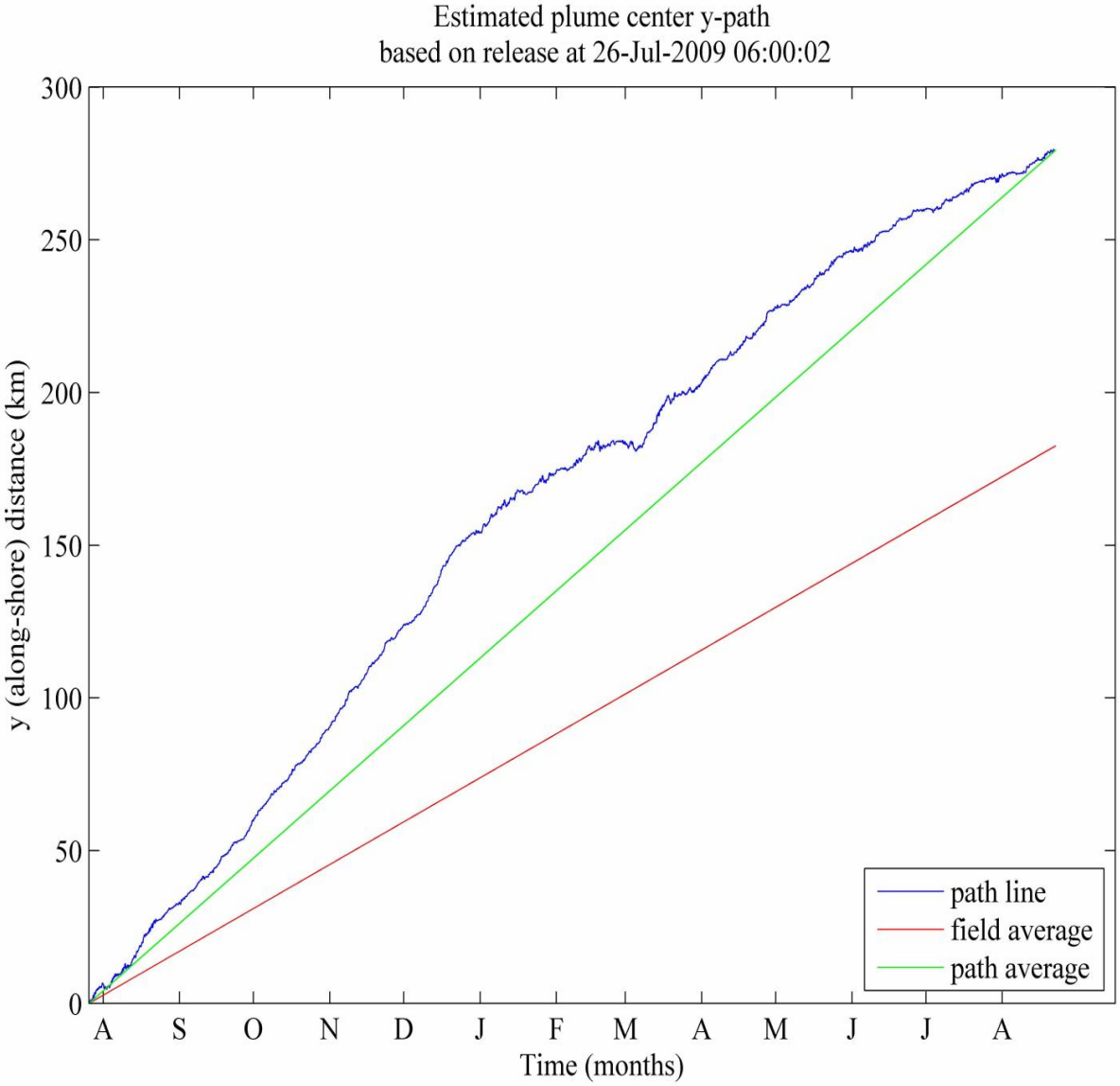

Figure 23 shows the estimated z (upward) coordinate of the pathline for a particle starting at the release site at the first time sample of the prepared velocity data set. The blue line is the z-component of the pathline in time and we can see that the pathline travels erratically up and down over a vertical distance of several hundred meters from the seafloor. This much vertical movement on the time scales indicated is probably not realistic. For example, in this particular pathline there are instances of vertical travel of over 200 m in a period of 6 hours. It may be that the measured velocities are too high, or that this large amount of vertical travel is a consequence of the continuity violation introduced by the assumption of horizontal homogeneity of the velocity field, or both.

The pathline and field averages of vertical travel are not shown because they are not very helpful in validating the pathline. Because we sometimes must limit the z travel of the pathline so that the z-coordinate does not become zero or negative, then the pathline average travel will not end in the same location as the pathline itself. The pathline average w velocity for the pathline shown was -0.007 cm/s and the field average w velocity (the average w velocity over all times and over all z values up to 278 mab) was -0.1036 cm/s.

Figure 24 shows the horizontal path taken by the pathline, which is the pathline x-coordinate versus the pathline y-coordinate, parameterized in time. As in several earlier figures, the blue line is the pathline itself and the green line is the path which would have been taken over the same time frame at a constant velocity corresponding to the average u and v velocities encountered along the pathline. As expected, these two paths end at the same location. The red line represents the path the particle would have taken if it had traveled at the field average u and v velocities which were explained above. A small X (on the x-axis) in figure 24 marks the approximate location of O'ahu. We can see that the stronger along-shore motion carries the pathline away from O'ahu, despite net motion in the positive cross-shore direction. To the extent that the red line may represent average motion more representative of a pathline that stays lower in the water column, we see that such a circumstance is even more favorable in that it would carry a chemical plume in direction more directly away from O'ahu. In fact, some preliminary computations were carried out with the w velocity artificially scaled down, which forced the pathlines to stay within 10 m or so of the bottom and in this case the u velocities were negative on average. Thus, whether the pathline stays closer to the bottom (as we expect is more physically reasonable) or behaves as the model predicts, and as show in these figures, the plume is not predicted to travel directly toward O'ahu. We will see shortly that this is also the case for pathlines originating at other times.

Figure 23: Example pathline z coordinate in time.

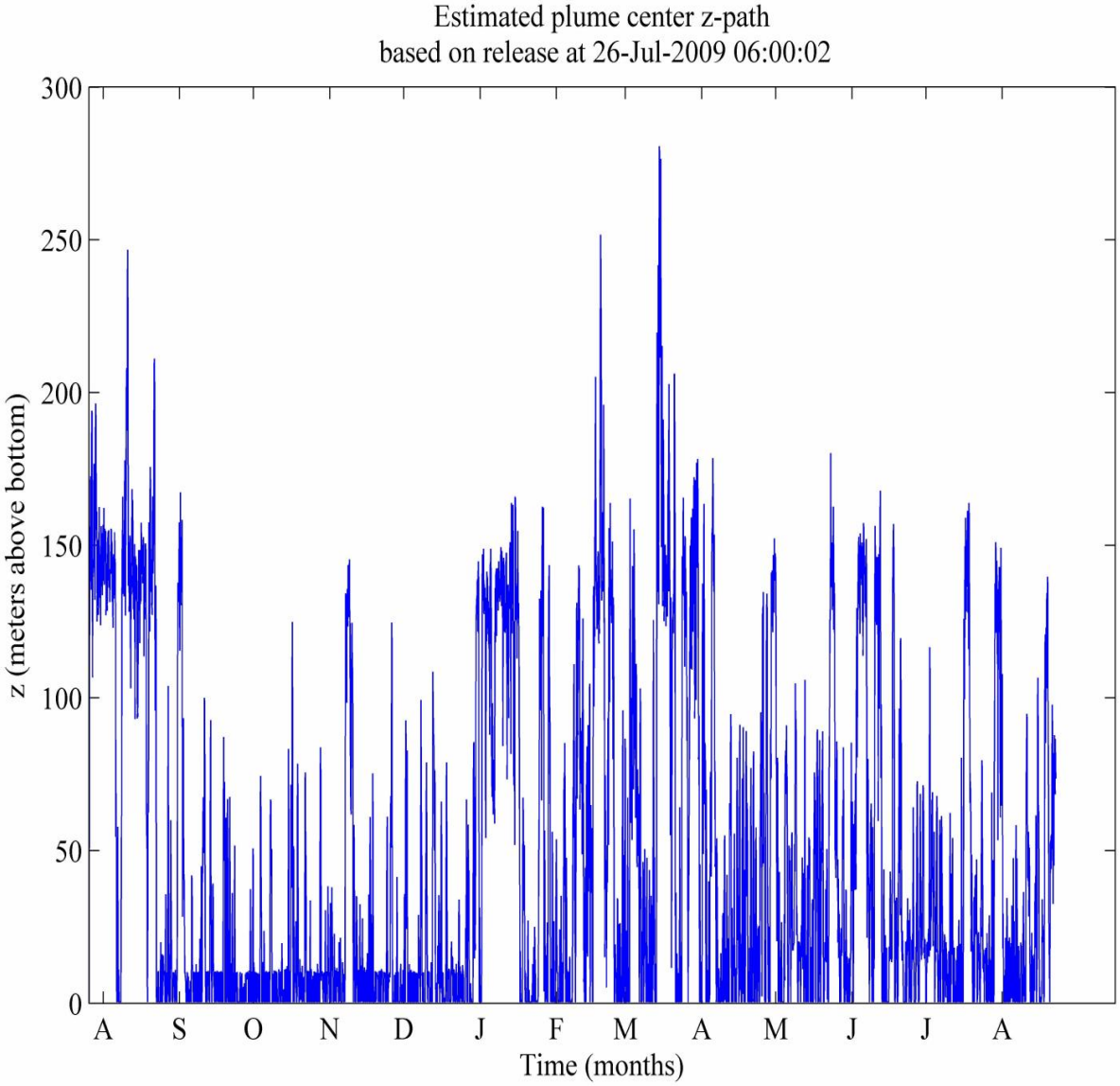

Figure 24: Example pathline x coordinate vs y coordinate over time.

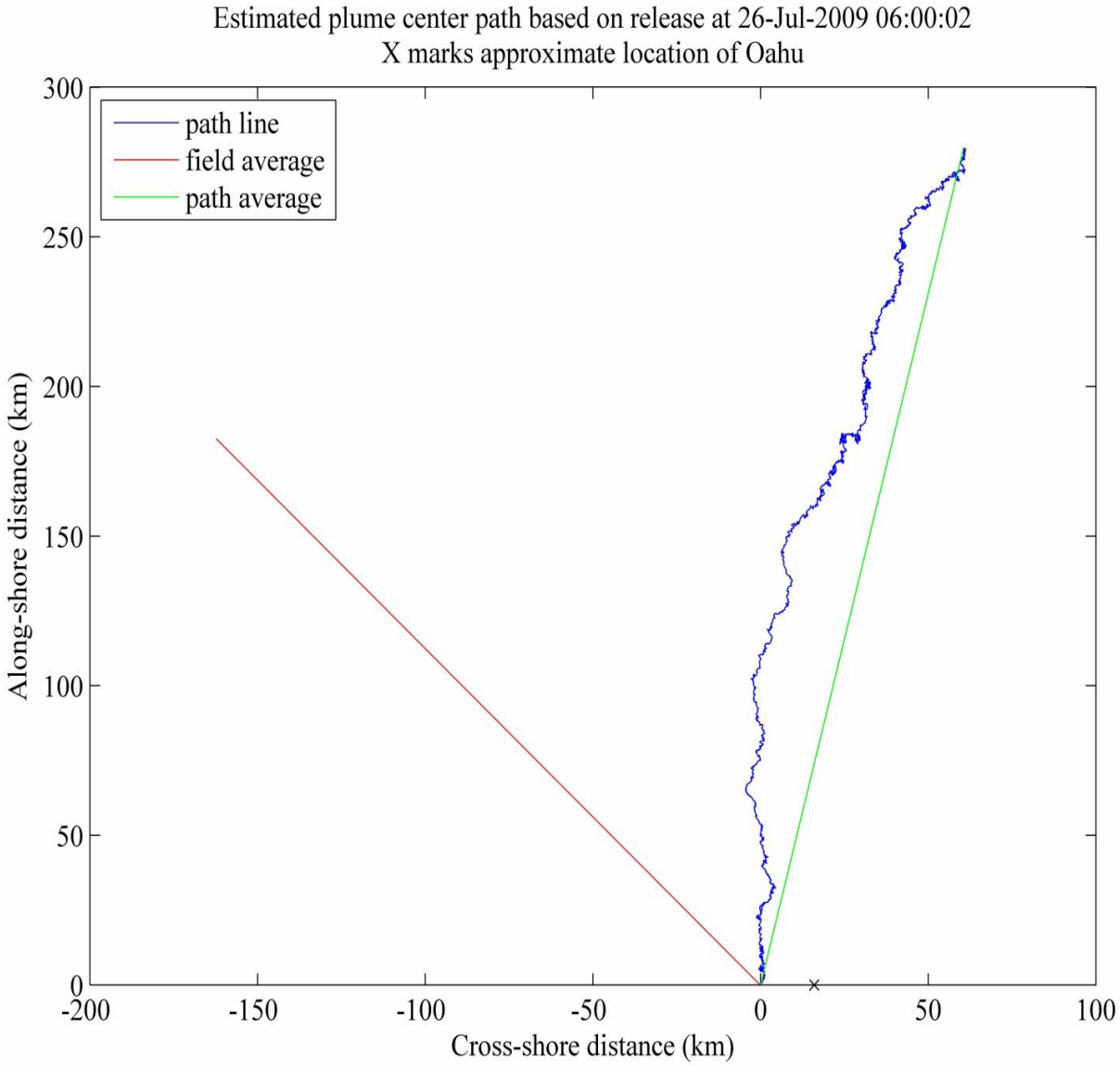

As an additional validation that the pathline computation is correct, figures 25–27 demonstrate the correlation between rate of change of position and velocity along the pathline. For example, in figure 25, the time rate of change in x along the pathline is approximated as

$$\left(\frac{dx}{dt}\right)_i \simeq \frac{x_i - x_{i-1}}{t_i - t_{i-1}} \tag{46}$$

where x_i is the x-coordinate of the i^{th} point on the pathline, corresponding to the x-location of the particle at time t_i and x_{i-1} is the x-coordinate of the $(i-1)^{st}$ point on the pathline, corresponding to the x-location of the particle at time t_{i-1}. This is plotted against u_i which is the value of $u(z_i(t_i), t_i)$ recorded along the pathline at the i^{th} point by interpolating the velocity data at (z_i, t_i) where $z_i(t_i)$ is the z-coordinate of the pathline in time. A dot is plotted for each point

$$\left(u_i\left(z_i(t_i), t_i\right), \left(\frac{dx}{dt}\right)_i\right). \tag{47}$$

Since we expect

$$u_i\left(z_i(t_i), t_i\right) \simeq \left(\frac{dx}{dt}\right)_i \tag{48}$$

then the dots should cluster around the line $y = x$. Similarly for figures 26 and 27. The approximation to position rates of change is crude, as this calculation was merely designed to detect gross errors in the pathline calculation. For a finer check, a centered approximation would be more appropriate but the present computation serves well enough to establish the validity of the pathline calculation.

Figure 25: Pathline approximate $\frac{dx}{dt}$ versus u.

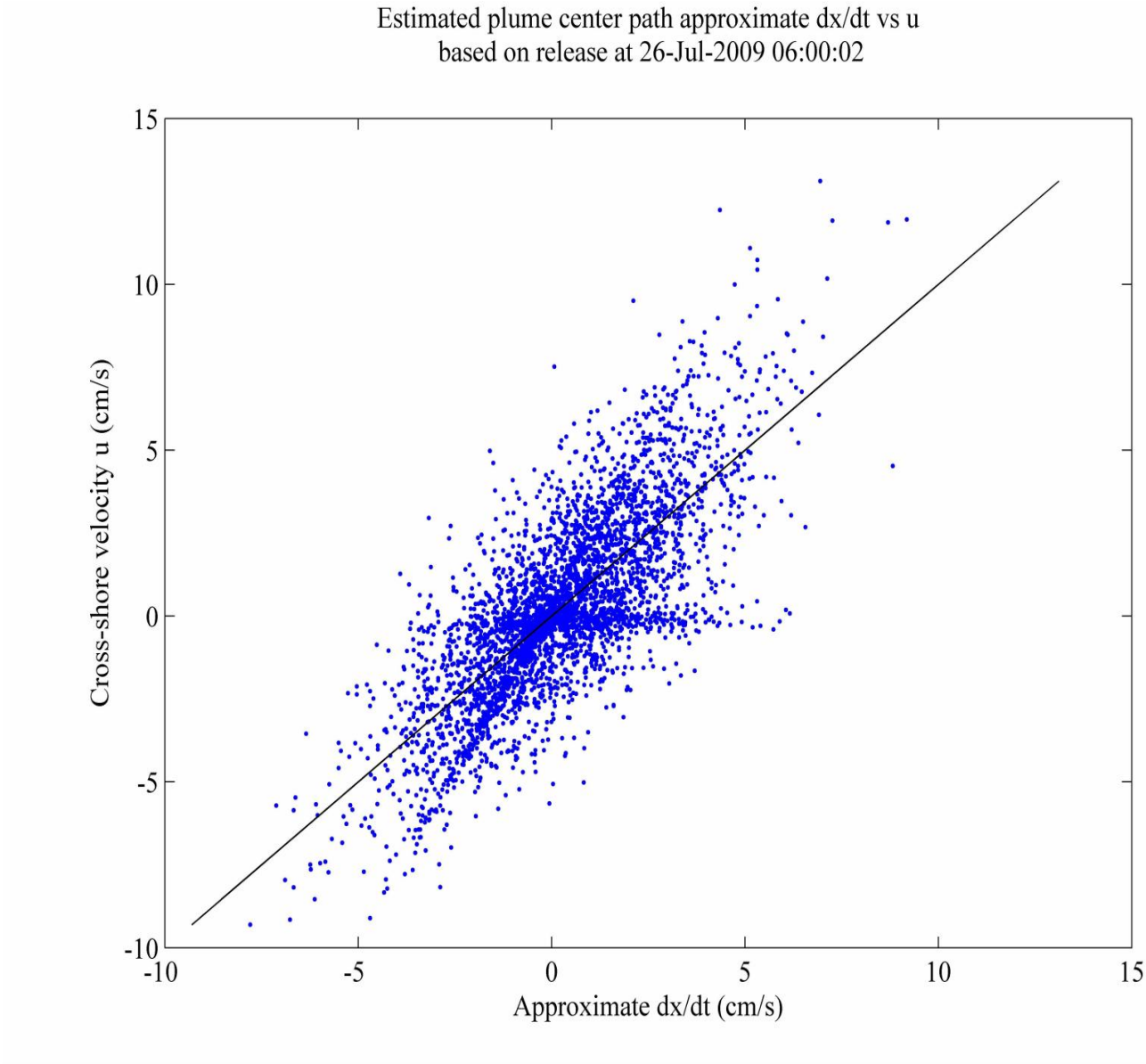

Figure 26: Pathline approximate $\frac{dy}{dt}$ versus v.

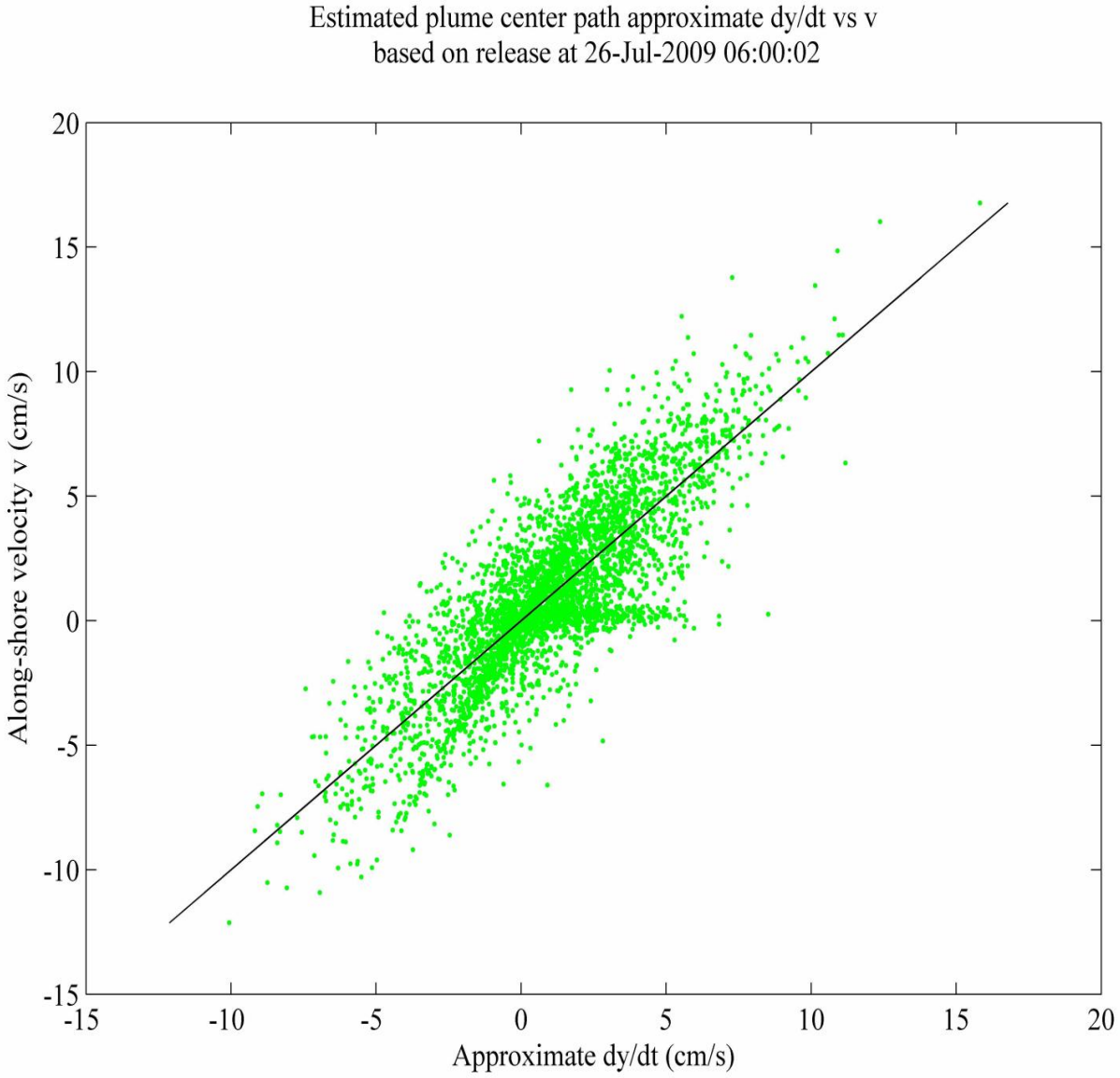

Figure 27: Pathline approximate $\frac{dz}{dt}$ versus w.

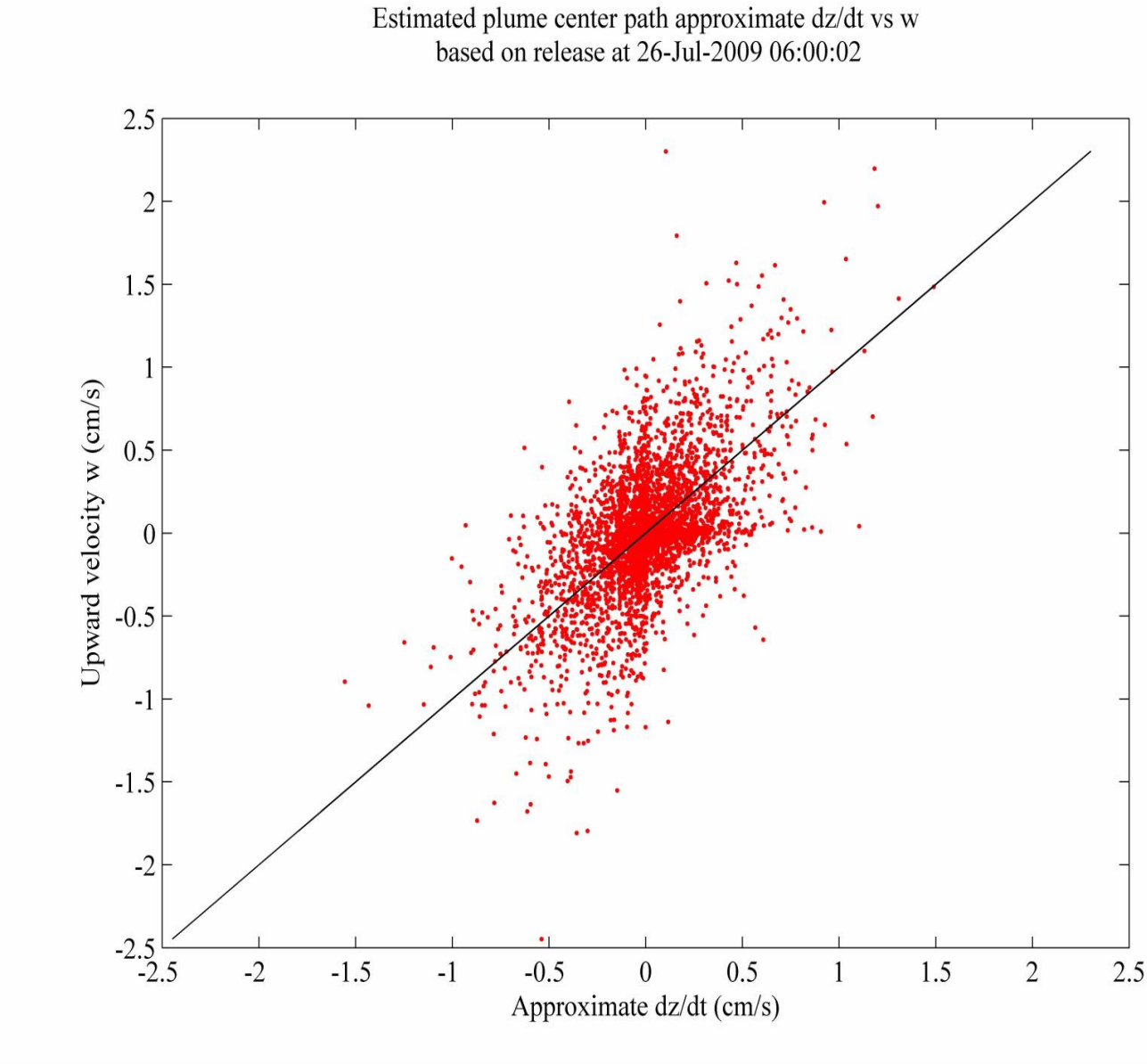

The next group of figures show information about an ensemble of pathlines. The pathline starting at the first time point in the prepared velocity data set was calculated, as shown in the previous group of figures. Next, 57 additional starting time points within the prepared velocity data set were randomly selected, excluding the last month of data, so that each pathline would be at least a month long. For each starting time point, a pathline was computed, yielding a total of 58 pathlines. These are referred to as the ensemble of pathlines. The purpose of working with an ensemble of pathlines is to represent a variety of different release times. Since we don't know when the chemicals might be released, we consider a variety of possible release times in case the currents tend to carry the plume in different directions depending on the release time.

Figure 28 shows the x-component of the pathline in time for each pathline in the ensemble. Each pathline starts at $x = 0$ (at the disposal site) but different pathlines start at different times. Adjacent pathlines are in different colors but there are fewer colors than pathlines so the colors eventually repeat.

Because we have assumed that velocities do not vary in the x or y directions, two pathlines which are far apart in space (vertically on the figure) still appear to execute similar motions in time. In other words, the pathlines look like they are roughly translated copies of each other. We may be tempted to assume that this suggests that temporal variation in velocity is more important than vertical variation in velocity in determining the pathline course. However, if different pathlines tended to follow the same z trajectory in time (as seems to be case as well) this would also produce the same effect.

The color-mapped velocity fields in figures 12–15 appear to show that temporal velocity variations are much more pronounced than velocity variations due to depth. However there are also a lot more samples in the temporal direction, which enhances that effect.

We can also note, in figure 28, that from August 2009 (on the left side of the plot) to roughly December 2009, the pathline tends to move in the negative x direction (away from O'ahu) on average while in 2010 the net x motion is in the positive x direction. This raises the same sort of question: is this primarily due to different current patterns between these two time periods, or to the pathline being at different depths during these time periods. There is evidence from some preliminary trials with an attenuated w velocity field that suggests that if the plume stays closer to the bottom then it moves in a net negative x direction throughout the year, and therefore, the initial negative x motion we see below in the earlier pathlines may be more directly related to the fact that the pathlines were closer to the bottom during this time period (see figure 30 below).

Figure 29 shows the y-component of the pathline in time for each pathline in the ensemble. The lines in this plot appear thinner than in figure 28 which is due to more back-and-forth motion in the x-direction (making the lines appear thicker) as compared to the steadier motion in the positive y-direction which can be seen in figure 29. The appearance of parallelism between the pathlines is even stronger in figure 29 than in figure 28.

Figure 30 shows the z component of the pathlines for the ensemble of paths. As before, each adjacent pathline is a different color, but the colors eventually repeat. However, this figure has a completely different appearance than the last two. Because the pathlines are making fairly steady net motion in a particular direction horizontally, they have the appearance of translated copies of each other in the figure. In contrast, the z motion of the pathlines consists of bouncing up and down primarily within the bottom 150 meters of the water column. As a result, one pathline tends to overwrite another. The pathlines were

Figure 28: Pathline ensemble x trajectories in time.

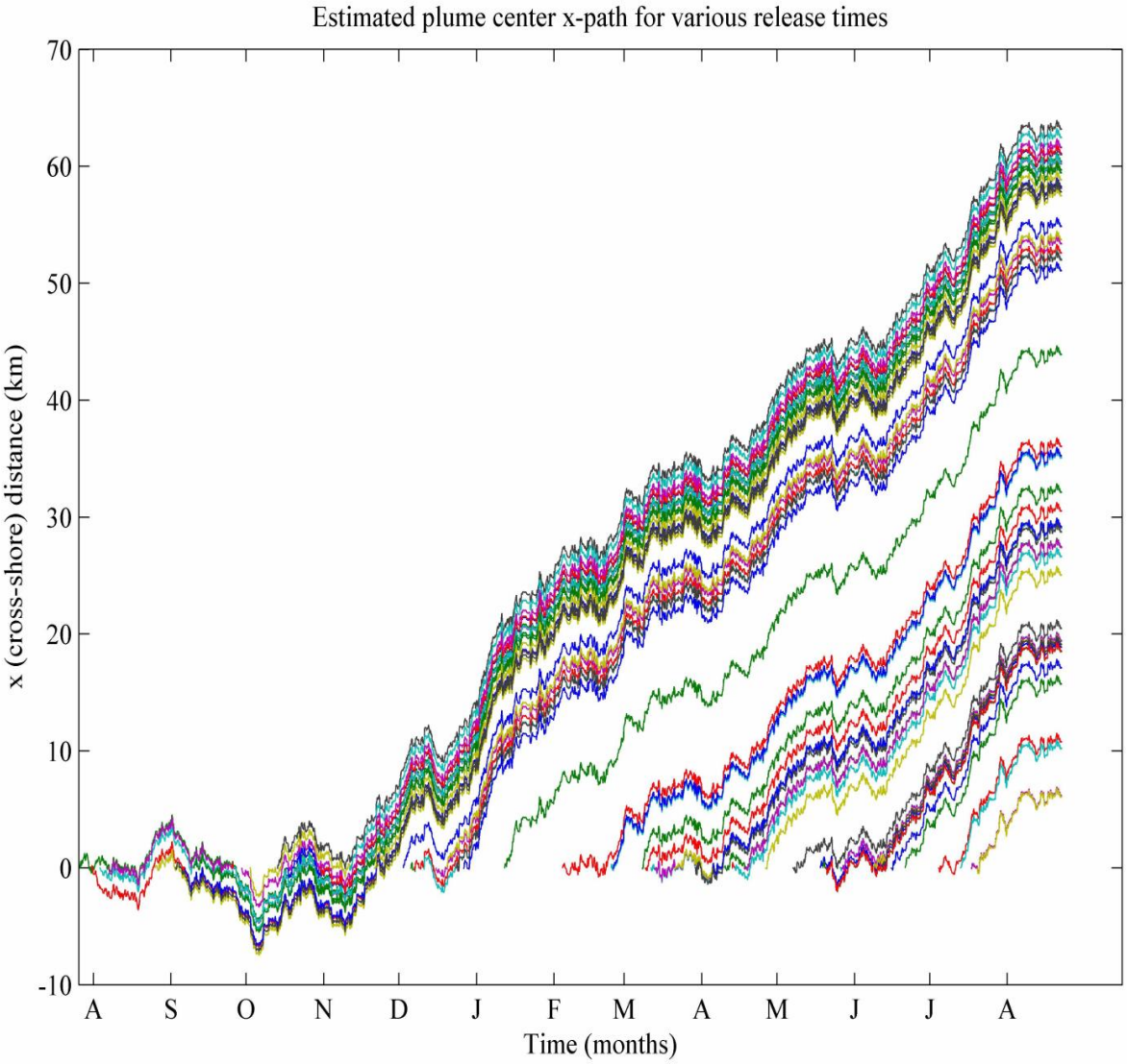

Figure 29: Pathline ensemble y trajectories in time.

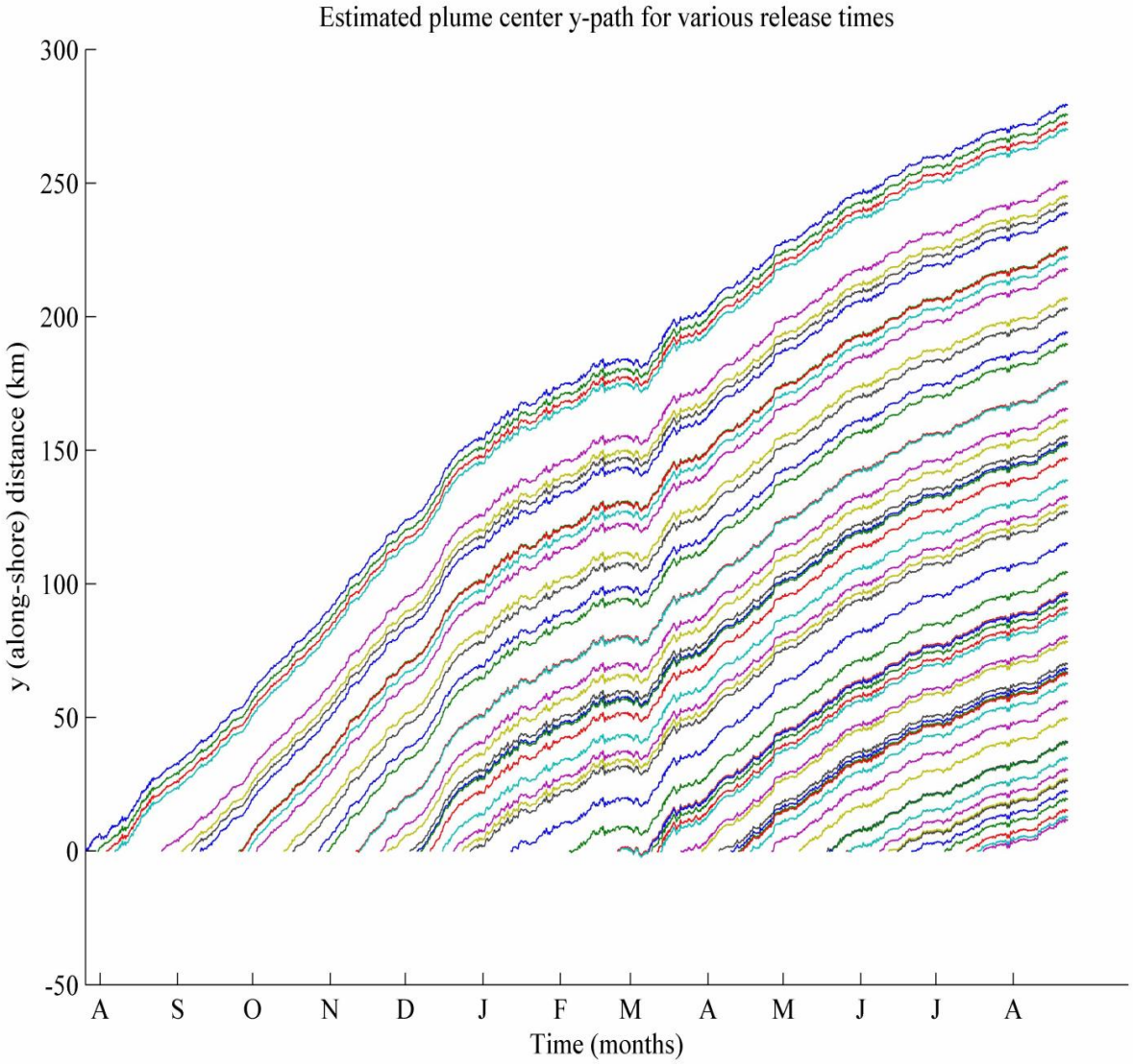

plotted in order of earliest release time to latest. The dark blue pathline is the first one plotted in this figure, followed by a green one and then a red one and then a cyan one. To the extent that the pathlines tend to follow the same trajectory, they will mostly overwrite each other. Thus, once the cyan pathline starts it appears to almost completely overwrite the earlier dark blue pathline. In places where two different colors occupy different vertical positions at the same time it indicates that two different pathlines were occupying different depths as a result of different release times. That is not seen very much in the figure below. We can see it in the beginning of the first blue pathline, where the blue pathline quickly ascends to around 150 mab and stays there for a while. The green pathline, which has a later release time, initially stays between 0 and 50 mab but eventually is overwritten by other pathlines, indicating that it is executing the same z motion as later pathlines. In fact, once the red pathline is released, it seems to overwrite the green, and when the cyan pathline is released it overwrites the earlier red, green, and blue pathlines, indicating that they are all now taking the same z path. This pattern continues throughout the figure, indicating that regardless of release time, we are getting very little variation in the z path of the particles (plume centers).

The z-direction is special in a number of regards. As mentioned above, it is characterized more by sloshing up and down than by net motion in a particular direction. Second, sustained net negative motion is not really possible since once the pathline gets near the seafloor, further negative motion is disallowed. In other words, the pathline is not allowed to go below a certain level (0.5 mab in these figures) because (a) it can't physically go below the seafloor, and (b) if the pathline goes to $z = 0$ it will stay there forever since the velocities are set to zero there. Thus, pathlines which are driven downward eventually all accumulate at $z = 0.5$ mab where they thereafter experience the same velocities and therefore travel the same paths. So any period of sustained negative w velocities will tend to synchronize the pathlines. This is an artifact of the model.

Finally, the z-direction is the direction in which we have to solve a differential equation to get the z-component of the pathline, which can introduce numerical artifacts or artifacts which result from errors in the velocity measurement. Near the bottom the measured velocities were suspiciously large and erratic, so we replaced this data with a linear boundary layer from the measured data at 6.5 mab to zero velocity at 0 mab. Despite the fact that velocities are going to zero near the bottom, the pathline still needs to be artificially prevented from going to or below 0 mab. Undoubtedly this reflects some combination of these factors: (1) numerical error, (2) errors in the measured velocities, (3) unrealistic assumption of velocities not depending on x and y, which violates continuity unless w is identically zero.

Another observation is that the scale of vertical motion exhibited by the pathlines is much larger and faster than expected. In the pathlines below we see vertical travel of over 200 m taking place in a span of 6 to 10 hours, which seems unlikely to be realistic. The factors mentioned in the previous paragraph are most likely responsible for this behavior as well. Since reducing tolerances in the ODE solver has no effect it is most likely that some of the larger measured velocities are in error and that not modeling any velocity variation in the x and y directions has removed spatial variation in w which is important to a more realistic pathline computation.

Figure 31 plots the x versus y components of the pathline to produce a visualization of the horizontal trajectory of the pathlines. A small X on the plot indicates the approximate location of O'ahu. The x and y axes are purposely scaled the same so as not to introduce

Figure 30: Pathline ensemble z trajectories in time.

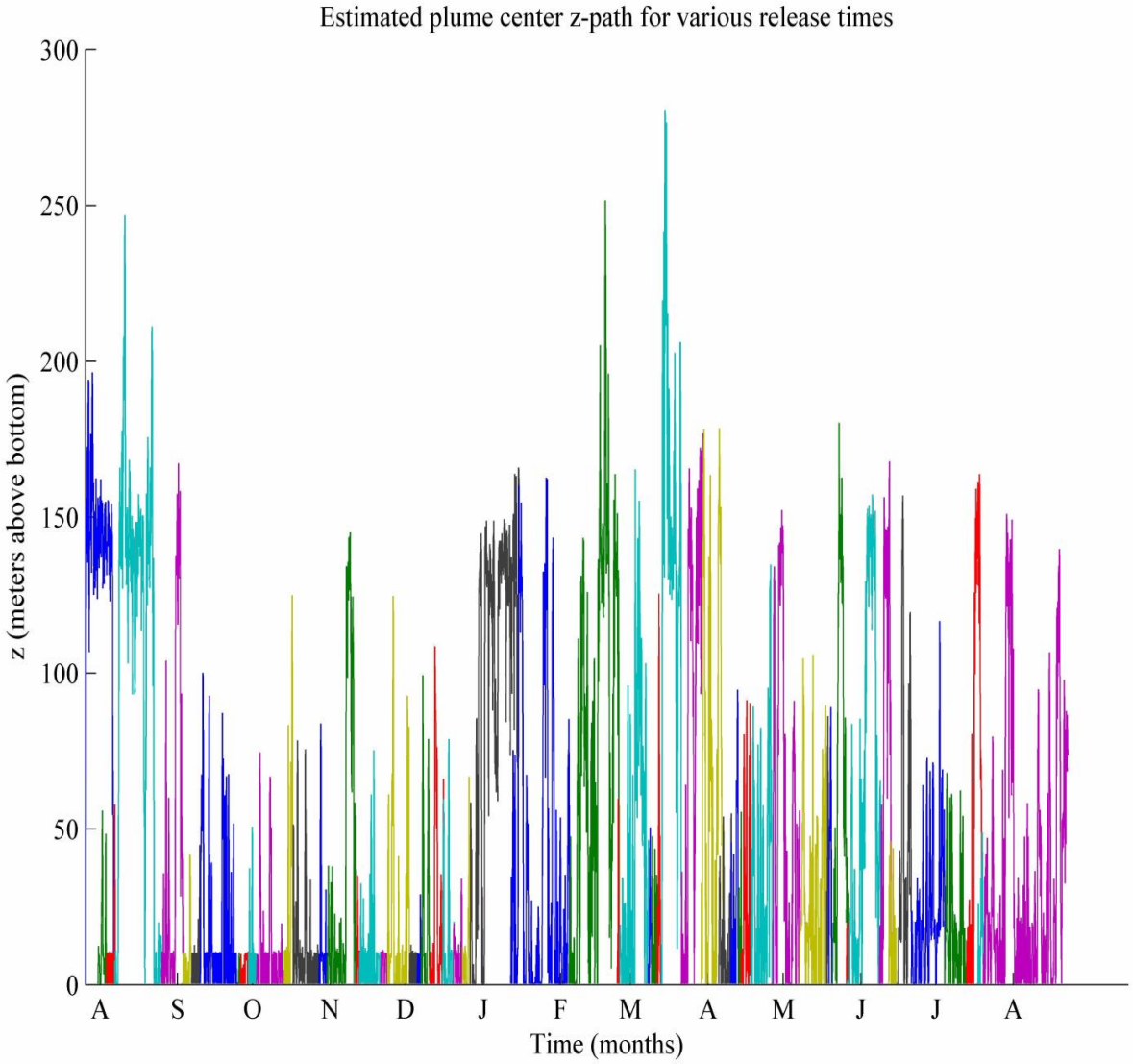

visual distortion. As can be seen, the pathlines are trending in a roughly northerly fashion. The longest pathlines represent approximately a year of travel. As will be seen later, a chemical plume is likely to be dispersed below the detection threshold long before a year. Therefore, the presence of pathlines should not be understood as necessarily suggesting the presence of detectable amounts of chemical.

The most interesting message from figure 31 is that the predicted pathlines are influenced by an along-shore current which is strong enough to take the pathlines away from O'ahu despite some cross-shore motion in the direction of O'ahu. Preliminary evidence using an attenuated w velocity field suggests that reduced w velocity causes the pathlines to stay closer to the bottom and to have a net negative x component which pushes the pathlines a little more westerly (even further from O'ahu than shown here). Thus, we may consider the present set of pathlines as a reasonable worst-case scenario.

Figure 31: Pathline ensemble x-y trajectories in time.

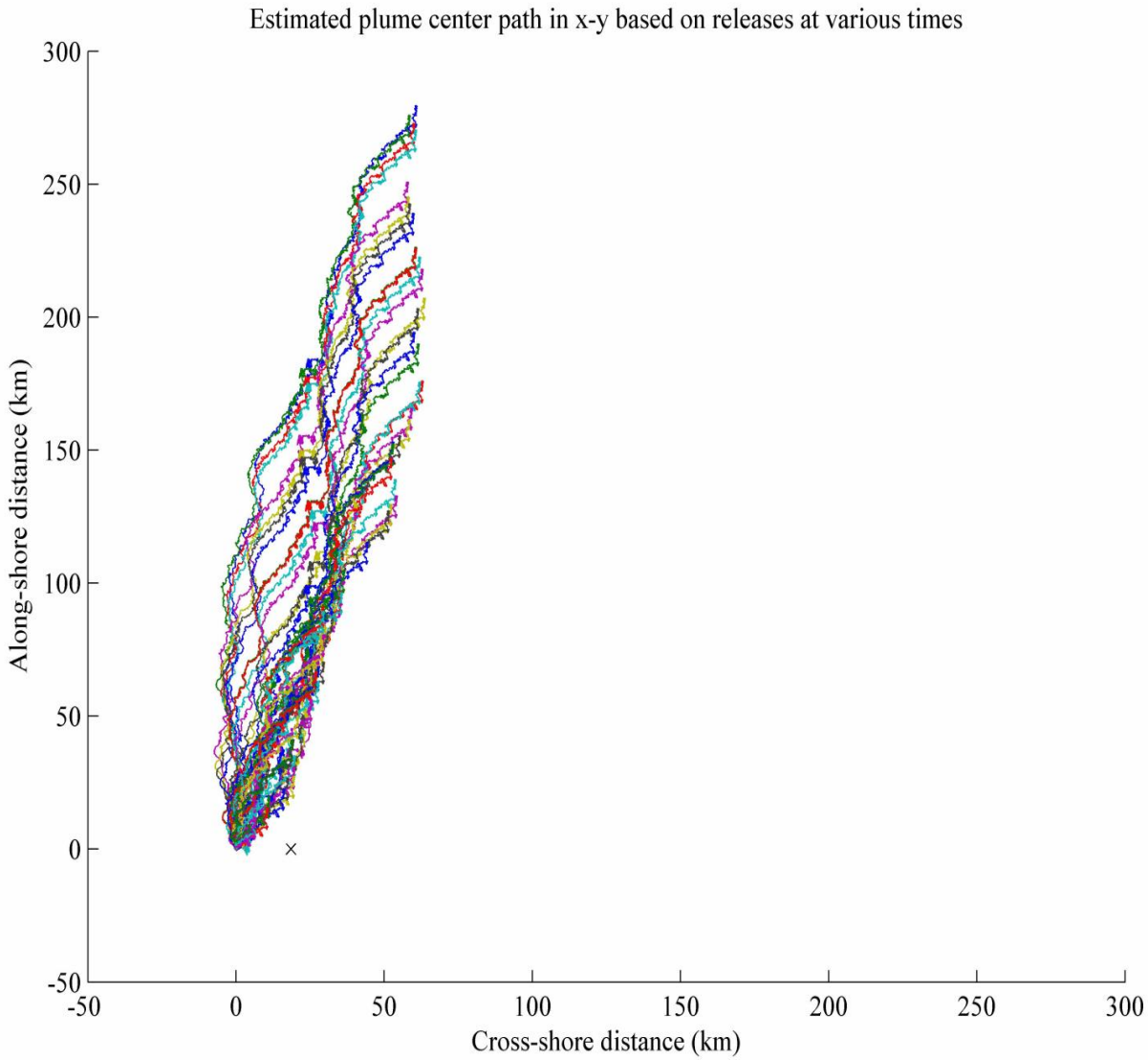

5.2 Footprints

Three types of footprint plot were produced: maximum concentration, exposure time, and exposure. We first discuss the maximum concentration plots as an introduction to this type of plot and to understand their implications. We then describe the computation of the footprint data in more detail, and finally, describe the exposure time and exposure footprint plots.

All footprint computations in this section are based on a release amount of 182 kg, which corresponds to the breach of two munitions, each holding 91 kg of hydrogen cyanide. The total amount of hydrogen cyanide known to have been disposed at this site is 1820 kg, but it is unlikely that all of it would be released simultaneously.

Nominal turbulent diffusivities of $K_H = 1$ m^2/s and $K_V = 1$ cm^2/s are assumed for all footprint plots in this section. In section 5.3 the effect of choosing lower or higher turbulent diffusivities is modeled.

5.2.1 Maximum Concentration

Figure 32 is an example of an x-y plot of the maximum concentration over all depths. To produce this plot, 58 different pathlines were computed by modeling the potential release of chemical at 58 different times during the window for which velocity data were available. Each pathline represents the estimated path which the center of the plume is predicted to take under the influence of the velocity field, which is assumed to vary with time and height above bottom. For each pathline, a maximum concentration footprint was computed which records the maximum concentration predicted by the model at each location on a grid of points in three-dimensional space. Such a footprint was created for each different pathline and then for each point in the spatial grid, the maximum concentration was computed across the full ensemble of footprints, each representing a different release time. This data can be visualized at different heights above bottom, as in figures 35–39, or as the maximum value over all heights, as shown in figure 32. All footprint plots presented here are for the ensemble of pathlines with different release times and therefore each footprint plot represents the range of expected advection patterns corresponding to a variety of release times.

Each plot has a red X in the approximate location of the nearest point of O'ahu to the disposal site, for reference. As can be seen in figure 32, the plume, as predicted by the model, does not come close to shore either horizontally (as is evident in the figure), nor vertically since the predicted plume remains more than a mile deep (see figure 40).

Recall that the coordinates are cross-shore and along-shore, so that north is roughly in the direction of the upper right corner of each plot. Each footprint which contributes to the ensemble data represents the predicted transport of a one-time instantaneous release of 182 kg of chemical (equivalent to two hydrogen cyanide ordnance, for instance) and assumes typical values of turbulent diffusivity ($K_H = 1$ m^2/s and $K_V = 1$ cm^2/s) for this setting. A larger release amount was selected for this section (as compared to section 5.3) in the spirit of a worst-case scenario. This amount of chemical, released instantaneously, is predicted by the model to disperse to a concentration everywhere less than 1 ppb within roughly 6.4 days. This is true regardless of the pathline because the nature of this model is that the diffusive processes are acting independently of advection, which determines only the center of the plume and not how rapidly the plume disperses.

The scale chosen for the color map is important in determining what sort of information can be discerned from the plot. For example, in figure 32, all x-y locations which are colored white are locations where a maximum concentration of 1 ppb, or more, is predicted to occur at some height in the water column. There are several things we cannot tell from this plot. We cannot tell, from this plot alone, at what depth the maximum value occurred. For that information, we must refer to the plots of maximum concentration for particular depths, such as figures 35–39. The second thing we cannot tell is how high the concentration might be at those x-y locations where a maximum concentration higher than 1ppb is predicted. For this information, we must plot the footprint on a different color scale. Figure 33 shows the same ensemble maximum concentration over all depths as was shown in figure 32, but this time plotted on a scale with a maximum of 10ppb. This brings out more detail in the regions where maximum concentration is predicted to be between 1 and 10 ppb, but we lose detail in regions where a maximum concentration of 1ppb or less is predicted. In the same way, we can plot this same data on a 100 ppb scale, as shown in figure 34, in order to see the detailed distribution of predicted maximum concentration values between 10 ppb and 100 ppb.

From figures 35–39, as well as from the earlier pathline data, we can see that the model predicts that vertical advection will transport the chemical several hundred meters upward in the water column. There are a number of reasons to be suspicious of such a large amount of vertical transport, as was discussed previously in sections 5.1 and 2.4.

Nevertheless, if there was this much vertical transport it would likely serve to increase the amount of water with which the chemical is mixed, resulting in increased dilution. For instance, as a very rough estimate, consider the area of the ensemble plume in figure 32 to be approximated by 10 km x 20 km and, based on figure 39, let us suppose that the plume extends to 320 mab. If 182 kg of chemical were evenly dispersed throughout a box of water of these dimensions the average concentration would be

$$\frac{182 \text{ kg}}{10000 \text{ m} \cdot 20000 \text{ m} \cdot 320 \text{ m}} \cdot \frac{1 \text{ m}^3}{1000 \text{ kg}} \simeq 2.8 \text{ parts per trillion} \tag{49}$$

where we assume the density of seawater is about 1000 kg/m^3 for the purpose of converting to parts per trillion. So, if the chemical plume stays close to the bottom, it will disperse primarily horizontally and will be unlikely to come in contact with humans by virtue of the depth of the water (on the order of 2500 m or more, which is in excess of 1.5 miles). If the chemical plume does travel as high as several hundred meters above bottom, then it ultimately mixes with a very large quantity of water and should dilute rapidly as a result. The present model does not directly capture all of the mixing processes because it uses turbulent diffusion as a surrogate for modeling mixing. In the event of vigorous vertical transport, the currently selected turbulent diffusivities likely underestimate mixing.

Preliminary modeling results in which vertical velocities were deliberately reduced so that the plume stayed within 10 m or so of the bottom resulted in pathlines which traveled in a more westerly direction, resulting in the chemical plume traveling almost directly away from the Hawai'ian Islands.

Figures 35–39 demonstrate, at the 1 ppb scale, how the maximum concentration behaves as we travel upward in the water column from $z = 0$ mab to $z = 320$ mab, and figure 39 demonstrates that the chemical concentration is below 1 ppb at this depth. Although not

shown in this sequence of figures, concentrations were computed at depths up to 600 mab and are confirmed to be below 1 part per trillion above 320 mab.

Figure 40 shows the ensemble maximum concentration in the x-z plane, maximized over all y locations.

Figure 32: Ensemble maximum concentration over all depths at 1 ppb scale

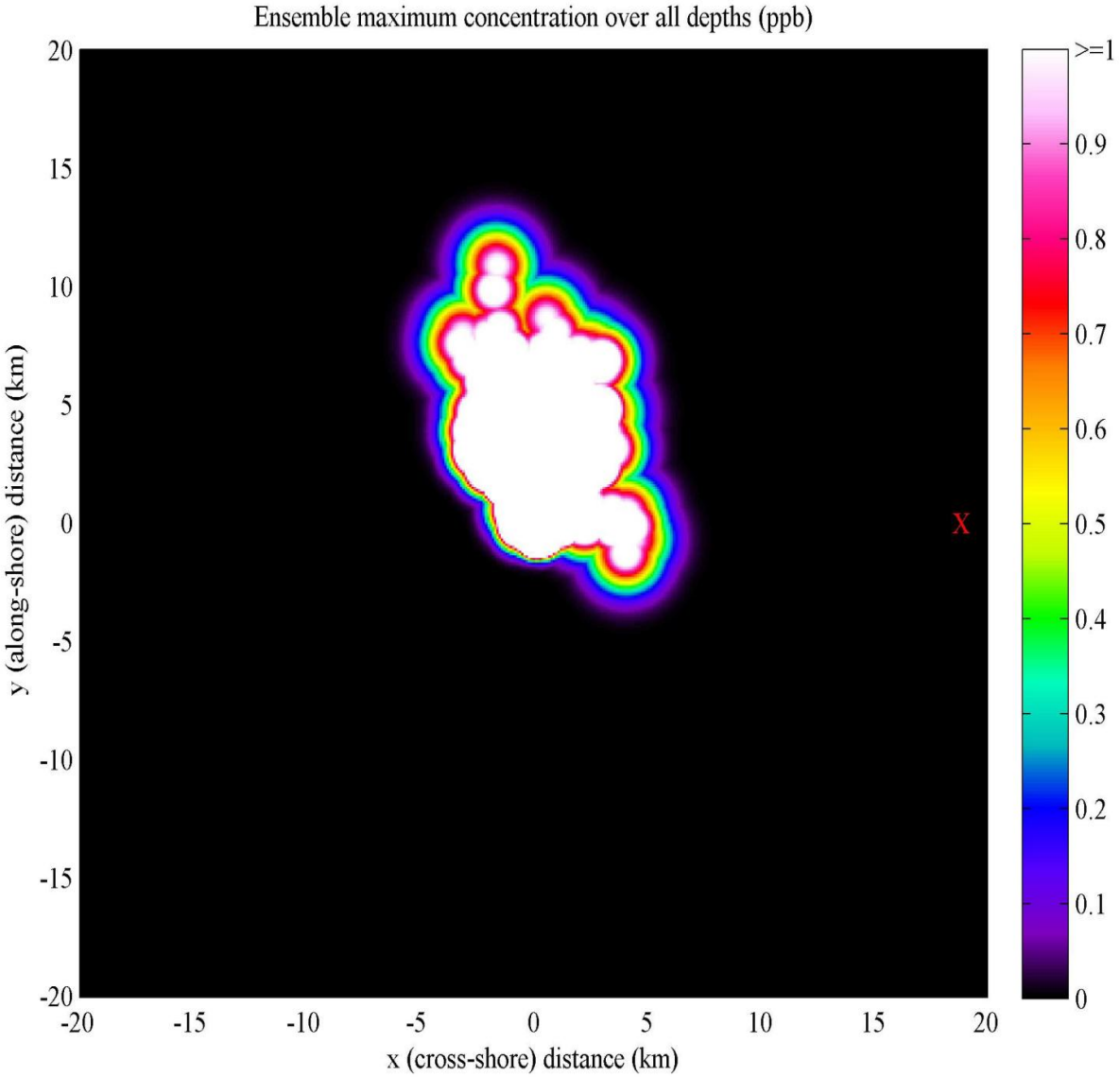

Figure 33: Ensemble maximum concentration over all depths at 10 ppb scale

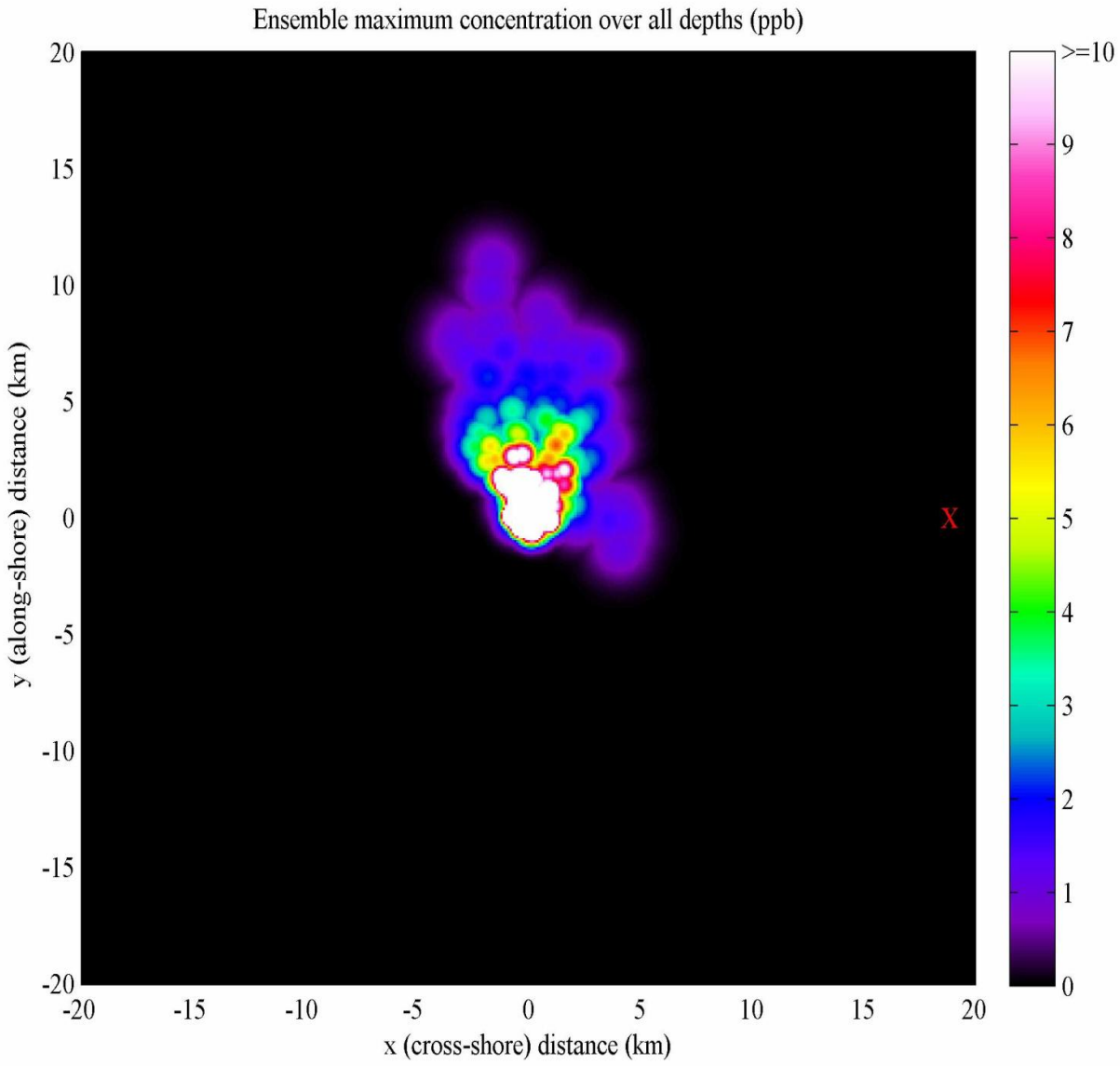

Figure 34: Ensemble maximum concentration over all depths at 100 ppb scale

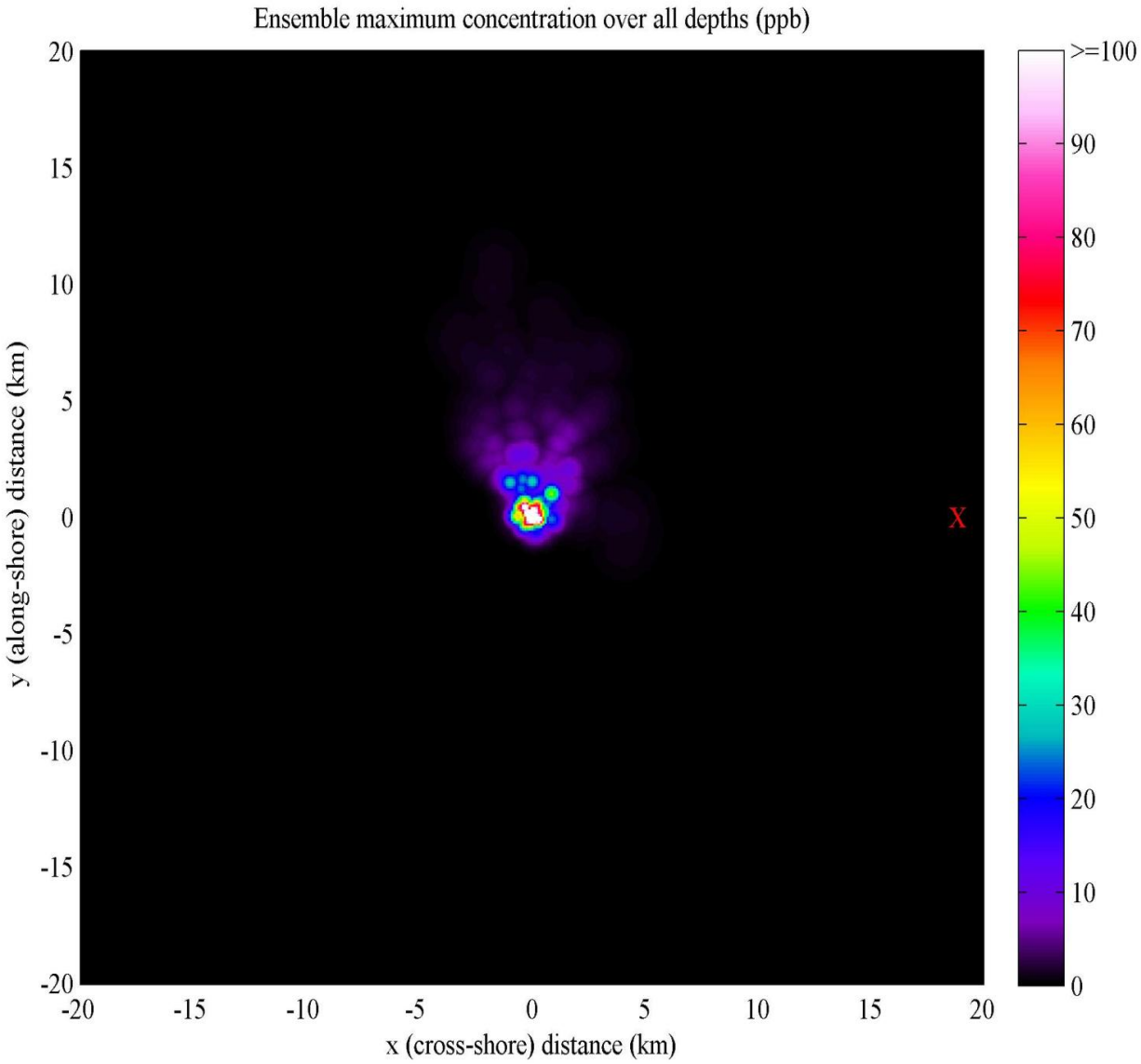

Figure 35: Ensemble maximum concentration at $z = 0$ mab

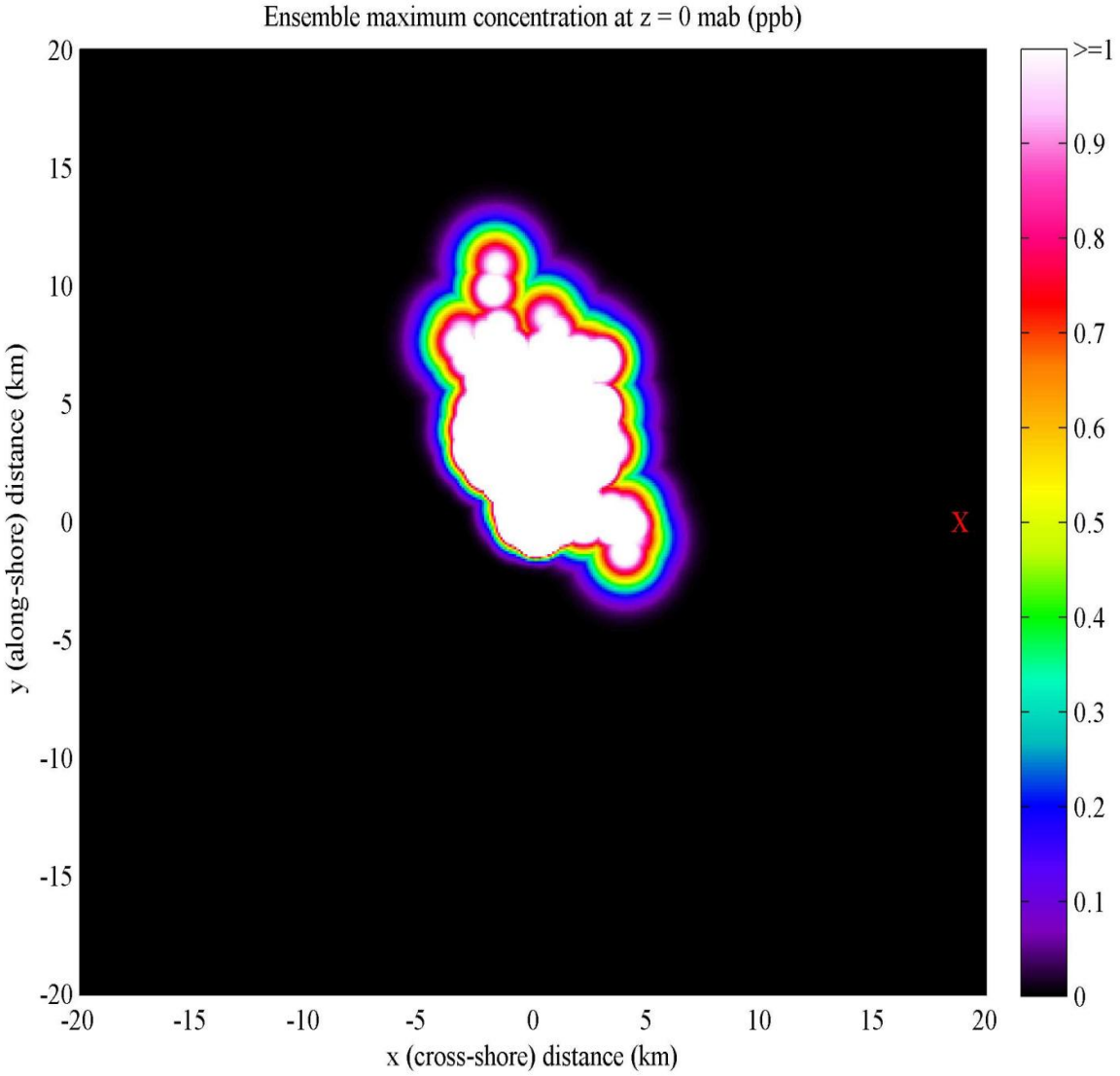

Figure 36: Ensemble maximum concentration at $z = 100$ mab

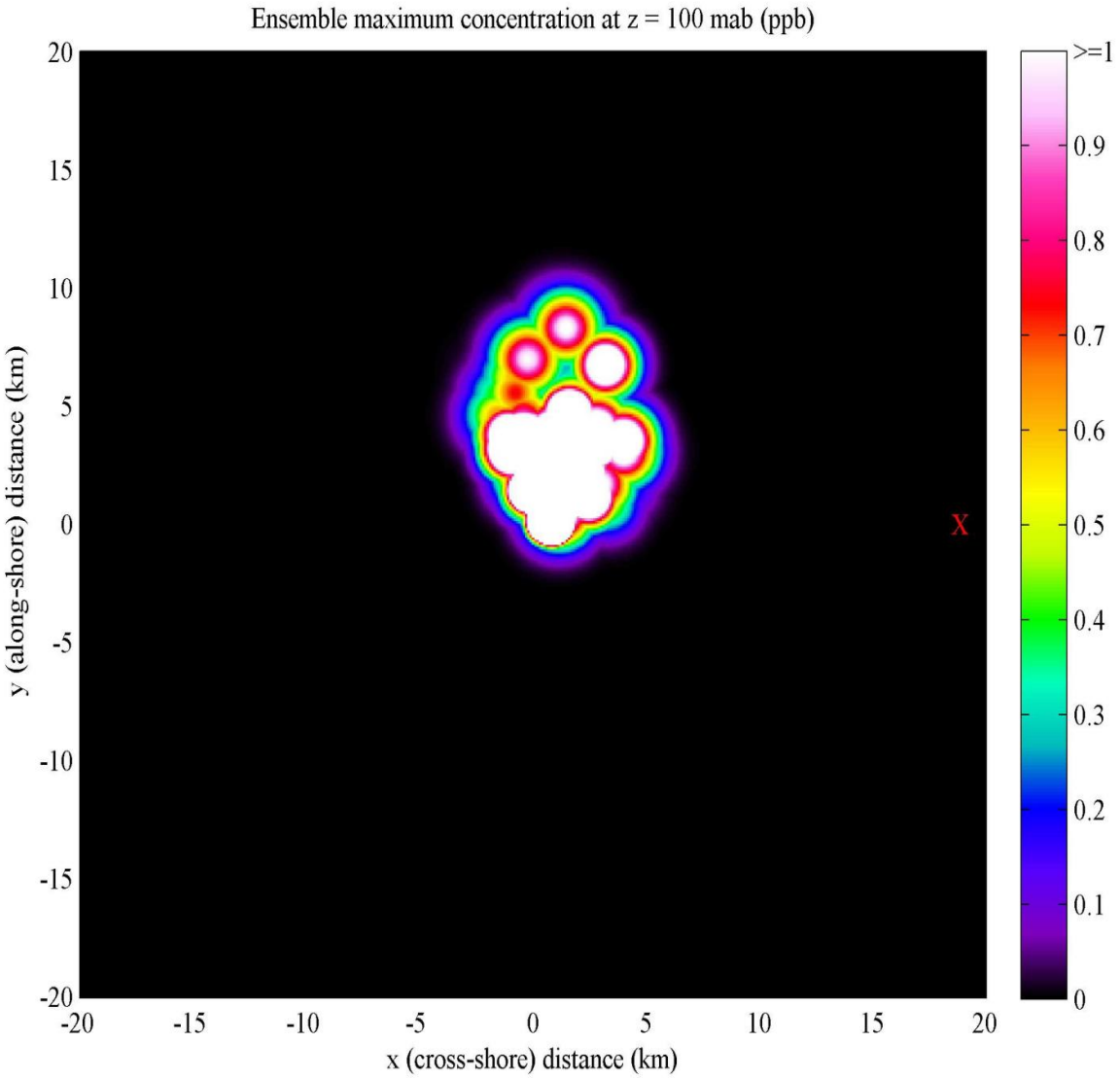

Figure 37: Ensemble naximum concentration at $z = 200$ mab

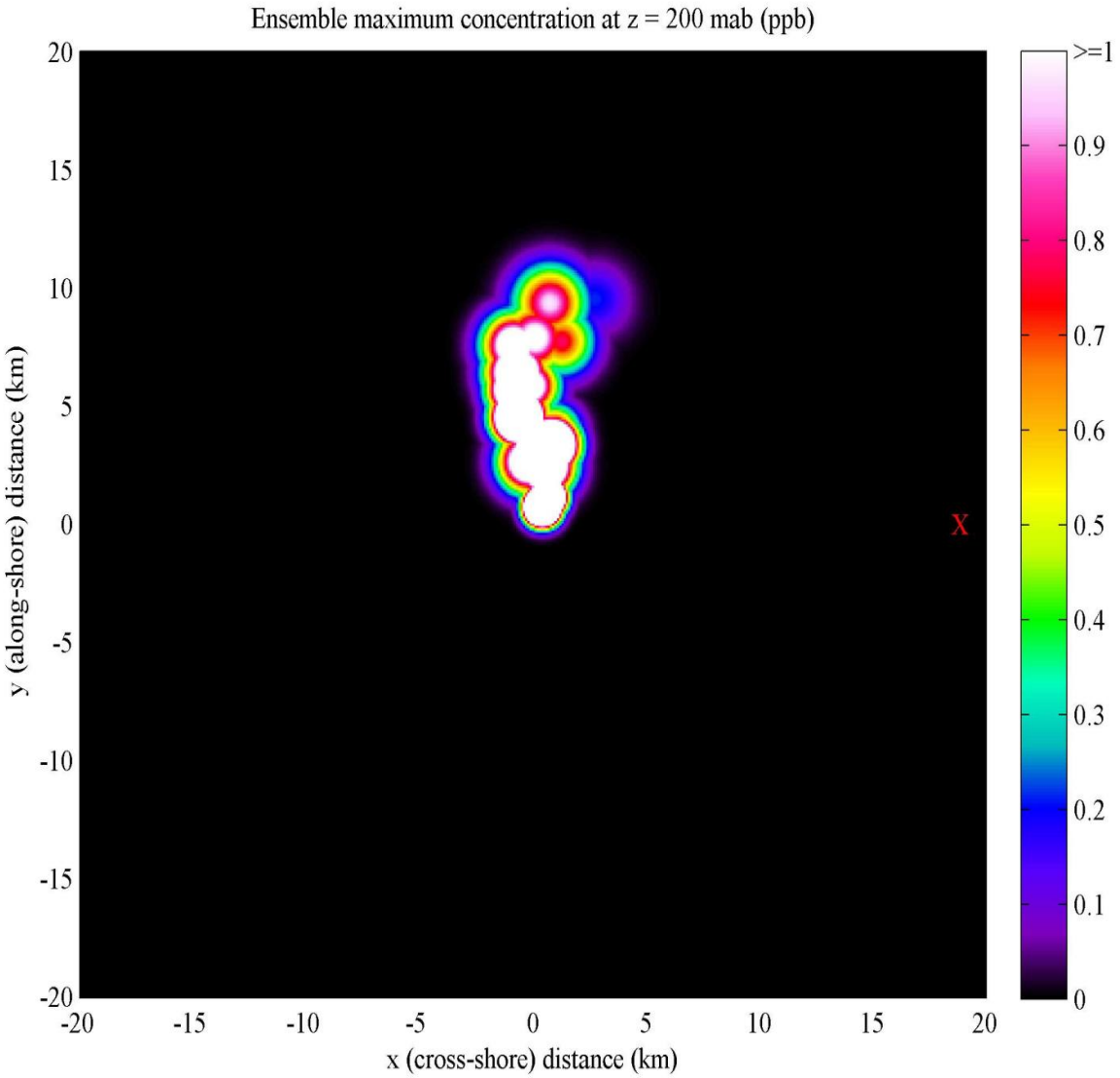

Figure 38: Ensemble maximum concentration at $z = 300$ mab

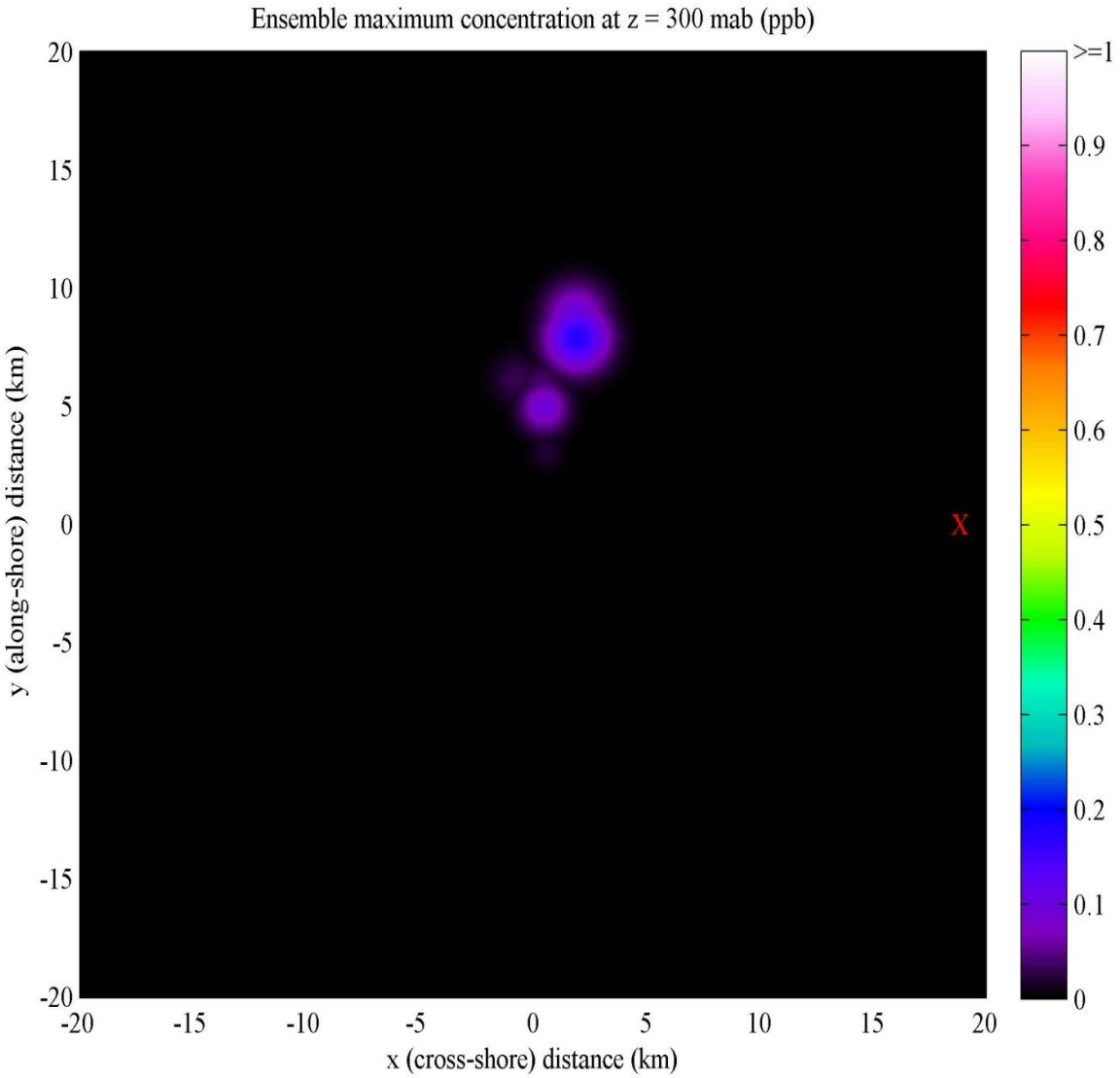

Figure 39: Ensemble maximum concentration at $z = 320$ mab

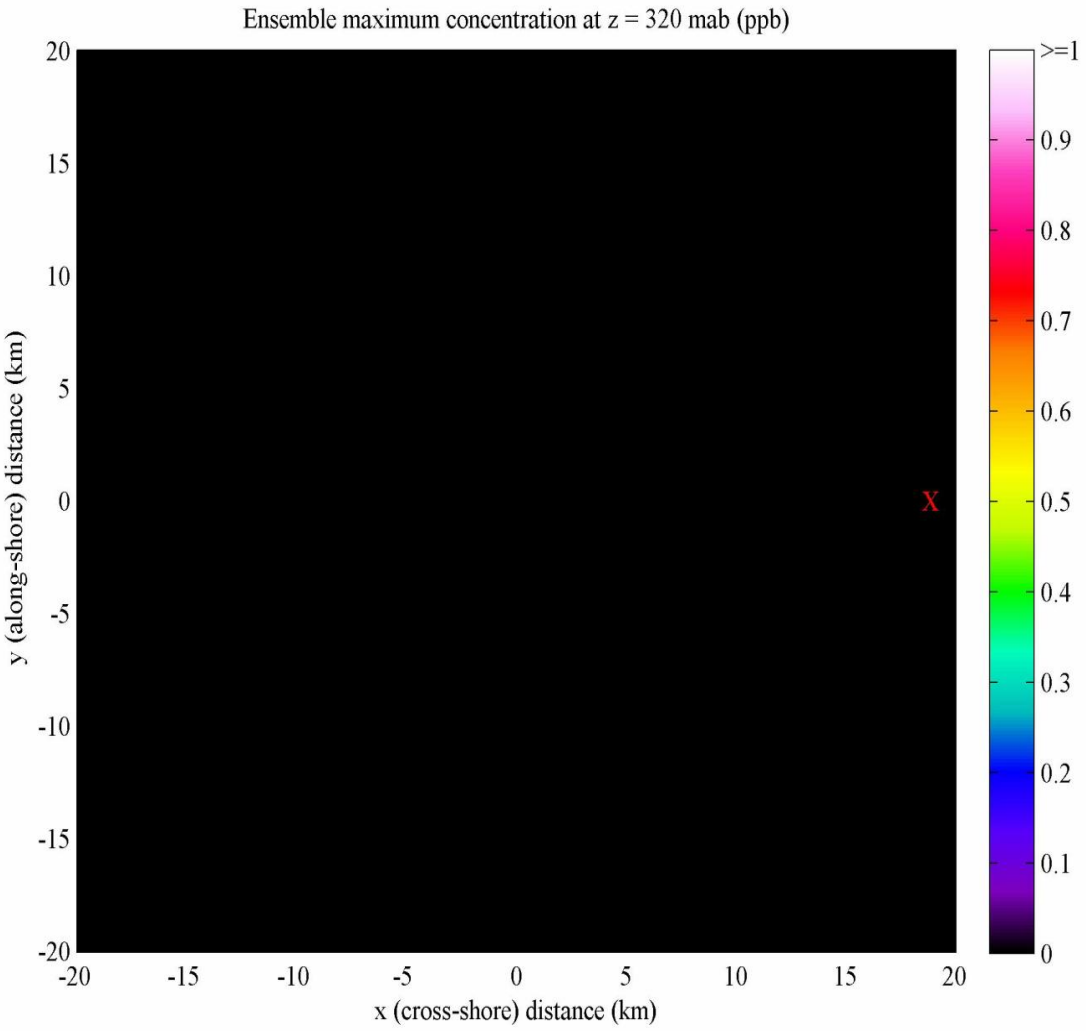

Figure 40: Ensemble maximum concentration in the x-z plane.

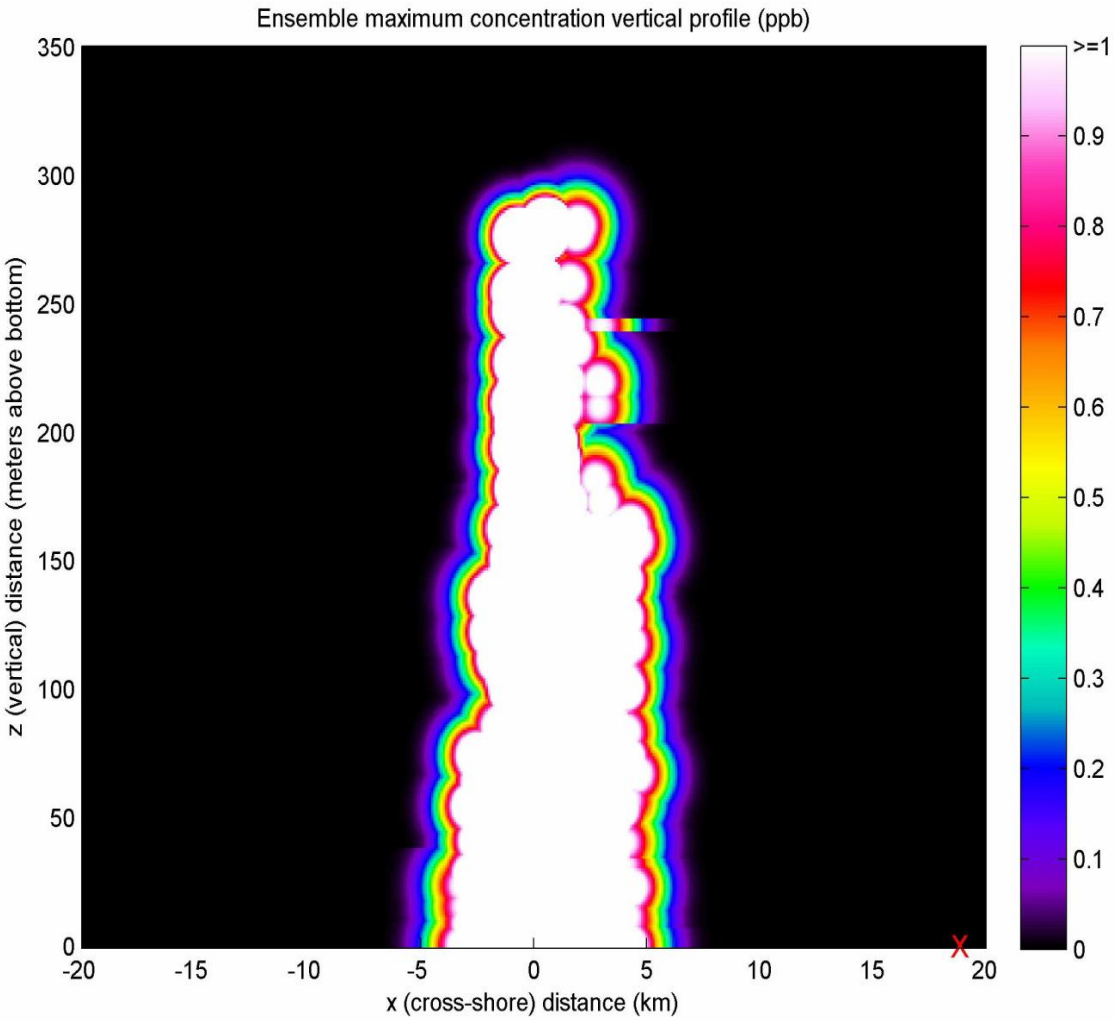

5.2.2 Details of Footprint Computation

A footprint computation was done separately for each pathline for the purpose of estimating maximum concentration, exposure time, and exposure, on a fixed, three-dimensional spatial grid in the region of interest. For the results shown in this section, computations initially covered a region 600 m deep (from 0 mab to 600 mab) and 100 km x 100 km horizontally, centered horizontally on the disposal site. When it became apparent that the plume would not extend above 320 mab, the upper bound of the region was reduced to 350 mab and the horizontal extent to within ± 20 km of the release site in the x and y directions. Grid points were placed 100 m apart horizontally and 1m apart vertically, because vertical diffusion is much slower.

Memory resources were the factor limiting refinement of this grid. In addition, the size of this grid made it impossible to keep information for different time steps, hence all information stored at these grid points consisted of either maxima or summations of quantities over the time steps.

The level of concern, or threshold, used in the calculations shown in this report was 1 ppb, but that is a parameter of the model and can be set to any desired value.

At each time point we compute the region where the concentration is expected to exceed the level of concern of 1 ppb. The time points are spaced 2 hours apart in the results shown here, corresponding to the sampling rate for ADCP1–ADCP4, but this is a parameter of the method and is not fixed, though it should be selected to match the sample period of the prepared velocity field and pathlines.

The region of the spatial grid to be updated is rectilinear and centered on the location of the pathline (the plume center) at that time. For each grid point in this region, we compute the concentration at that grid point and compare it to the stored maximum concentration for that same grid point, updating the stored maximum concentration as needed. In this way, we maintain an array containing maximum concentration over all times at each spatial grid point.

In addition, for each grid point where the concentration exceeds the level of concern (1 ppb) the exposure time at that grid point is increased by 2 hours (the size of the time step). Finally, we estimate total exposure at each grid point by multiplying the current concentration by the time period (2 hours) and keeping a running sum. This is (approximately) the integral of concentration over time, limited to the time when concentration exceeds the level of concern. Thus, we maintain three arrays, which are each the size of the spatial grid, which record maximum concentration, total exposure time, and total exposure, for each point in the spatial grid. Recall that we are describing the data for a single footprint calculation, corresponding to a single pathline, which corresponds to a single release of 182 kg of chemical at the location $(x, y, z) = (0\text{m}, 0\text{m}, 0.5\text{m})$ at a single release time.

First, the footprint data is calculated, as just described, for each pathline (corresponding to each release time) for a collection of randomly selected release times within the window of times where velocity data is available. Next, maxima are computed over all such footprint data to obtain ensemble footprint data which consists of maximum concentration, maximum exposure time, and maximum exposure at each spatial grid point. That is, depending on when the chemical is released, the plume might be transported in different directions because the currents patterns vary in time. So the purpose of the ensemble footprint data is to record the worst-case values at each point in the grid, over the range of different pathlines

corresponding to different release times. Finally, the ensemble data are available on a three-dimensional grid, but in some cases one is more concerned with the horizontal extent of the plume, so we also compute maxima of the ensemble data over depth or in other planes. It is important to recall, when viewing the depth-maximized data, that the lack of a specifically stated depth does not imply that the plume will be at the surface. In fact, the model is not showing concentration exceeding 1 ppb anywhere above about 300 mab or so.

5.2.3 Exposure time

As explained above, the exposure time is the estimated total time that concentration exceeds the level of concern (1 ppb for the figures shown here) at a point in the spatial grid. For the ensemble, we take the maximum exposure time at each point in the spatial grid, maximized over all footprints in the ensemble, where each footprint corresponds to a pathline with a different release time. Figure 41 shows the ensemble maximum exposure time which has additionally been maximized over all depths in the spatial grid. This is displayed in units of hours and the maximum value on the color scale (74 hours) corresponds to the maximum value achieved over the entire ensemble at all locations. Since the time step in the model is 2 hours, exposure time, as calculated here, is necessarily quantized in 2 hour increments.

Figures 42–46 show the ensemble maximum exposure time at particular depths, ranging from 0 mab to 320 mab. The exposure time is much reduced by 100 mab, increases a bit at 150 mab and then decreases again, which corresponds to the vertical excursion of the pathline. As discussed previously, there is probably not this much vertical motion. However, it should lend some confidence to note that even with these unexpected and probably unrealistically large vertical excursions, the model still predicts that by 320 mab, maximum exposure time is zero, as is suggested by 46 and confirmed by taking the maximum over all x-y locations at this height in the exposure array.

Figure 47 shows the ensemble maximum exposure time in the x-z plane, maximized over all y locations.

The longest exposure time experienced at any one point in space is 74 hours (a little over 3 days). The total dissipation time, which is the time elapsed from the release until concentrations are below the threshold of concern (1 ppb) at all locations, is about 6.4 days.

Figure 41: Ensemble maximum exposure time at all depths

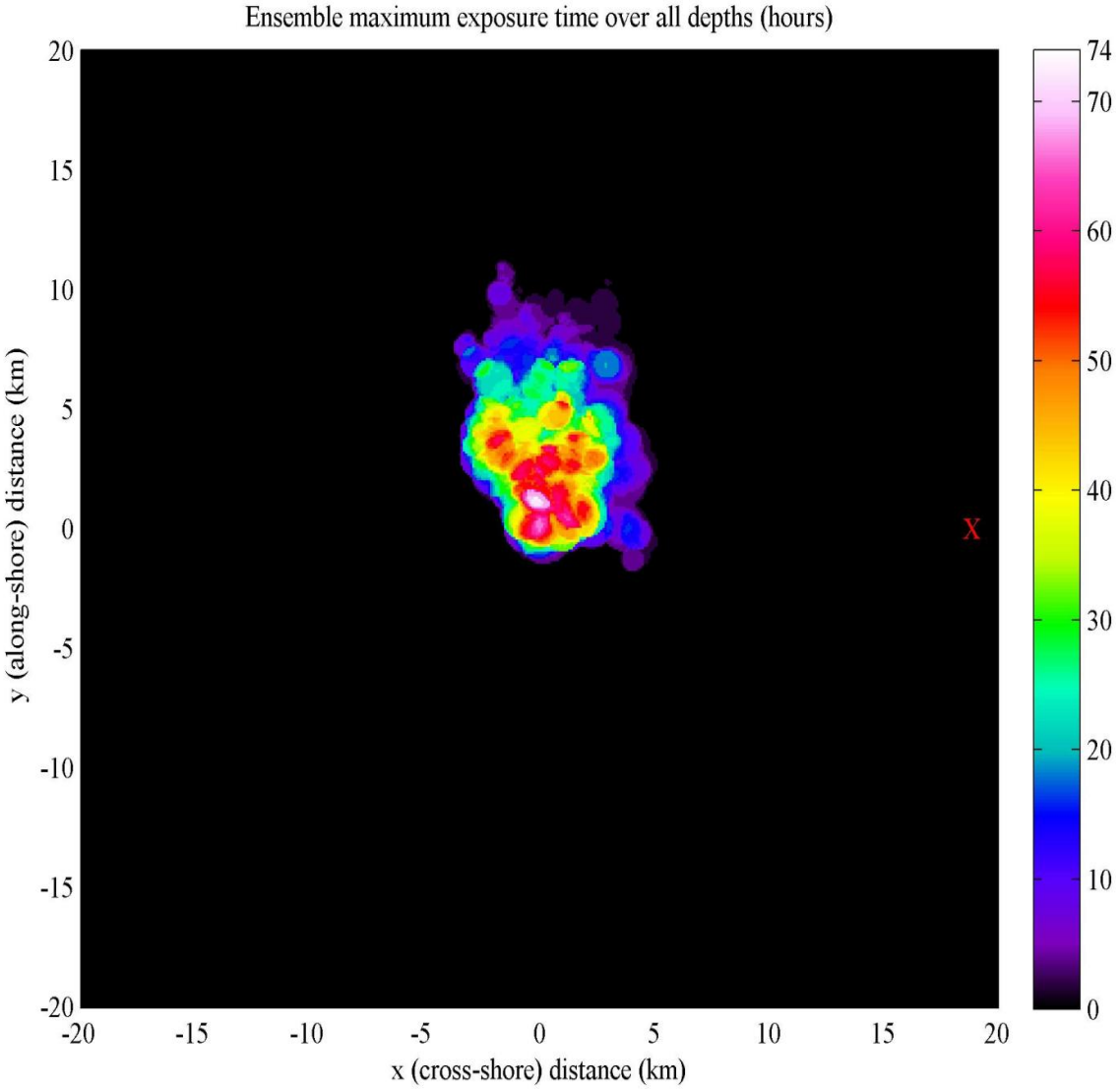

Figure 42: Ensemble maximum exposure time at $z = 0$ mab

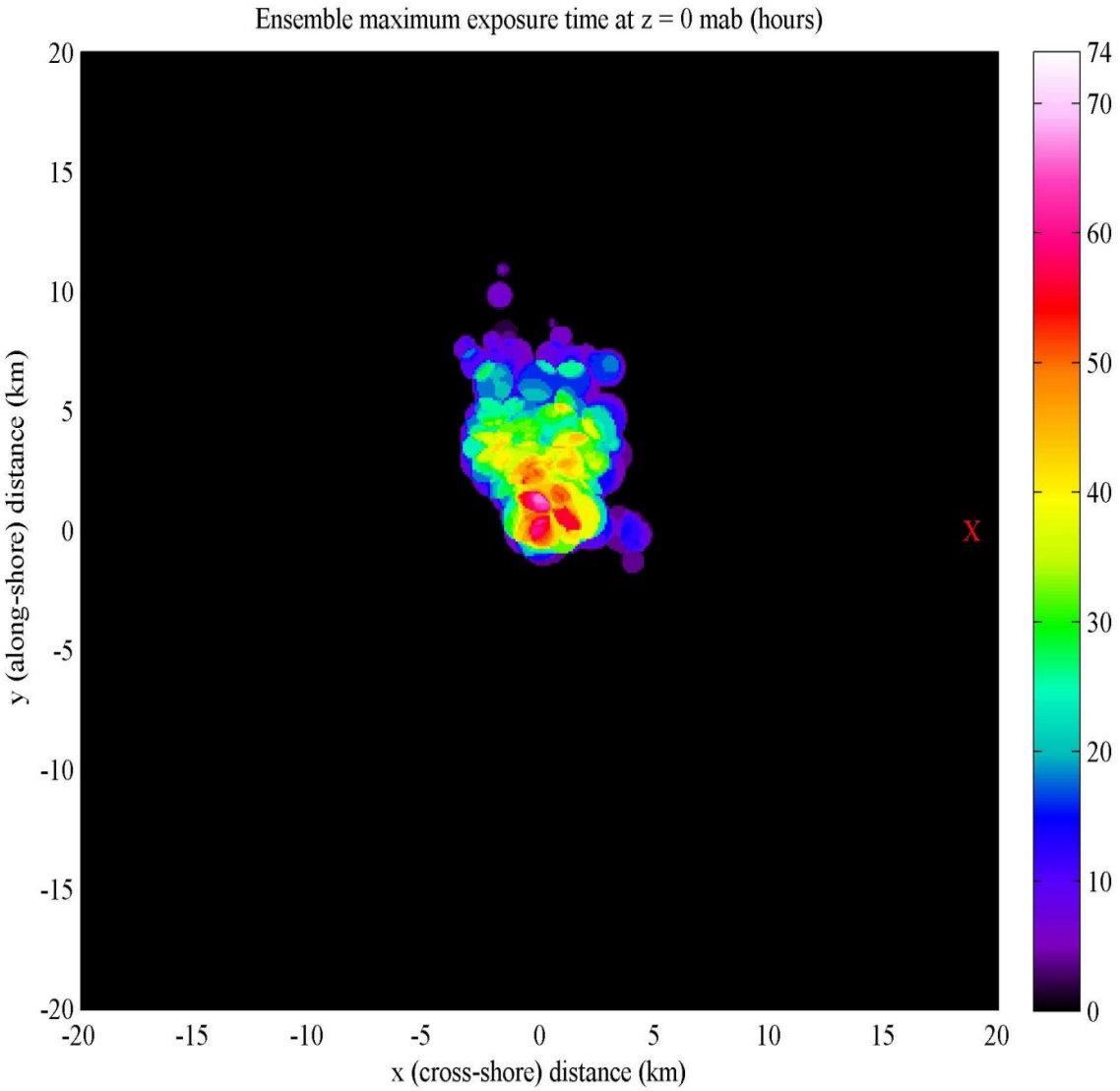

Figure 43: Ensemble maximum exposure time at $z = 100$ mab

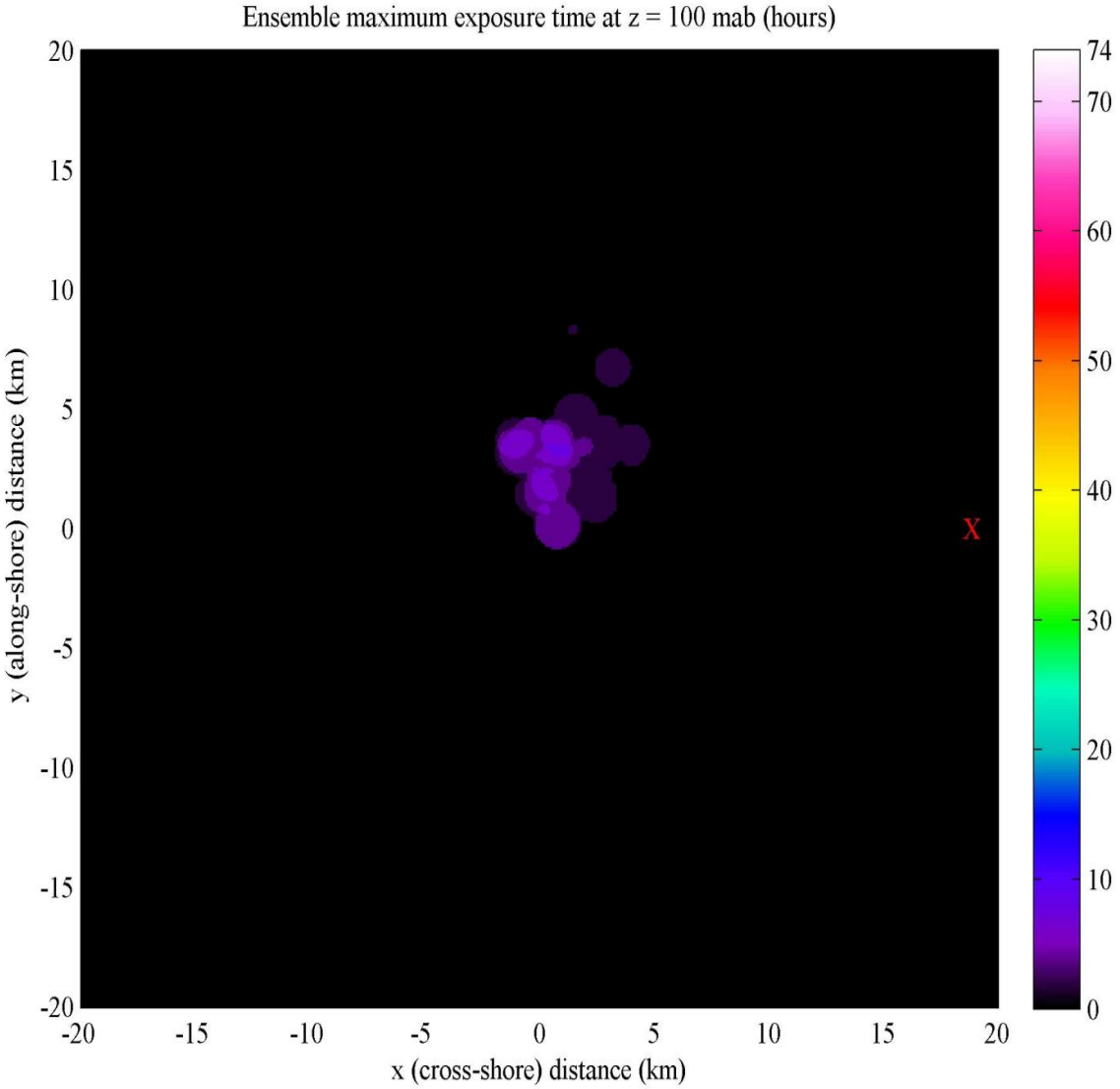

Figure 44: Ensemble maximum exposure time at $z = 150$ mab

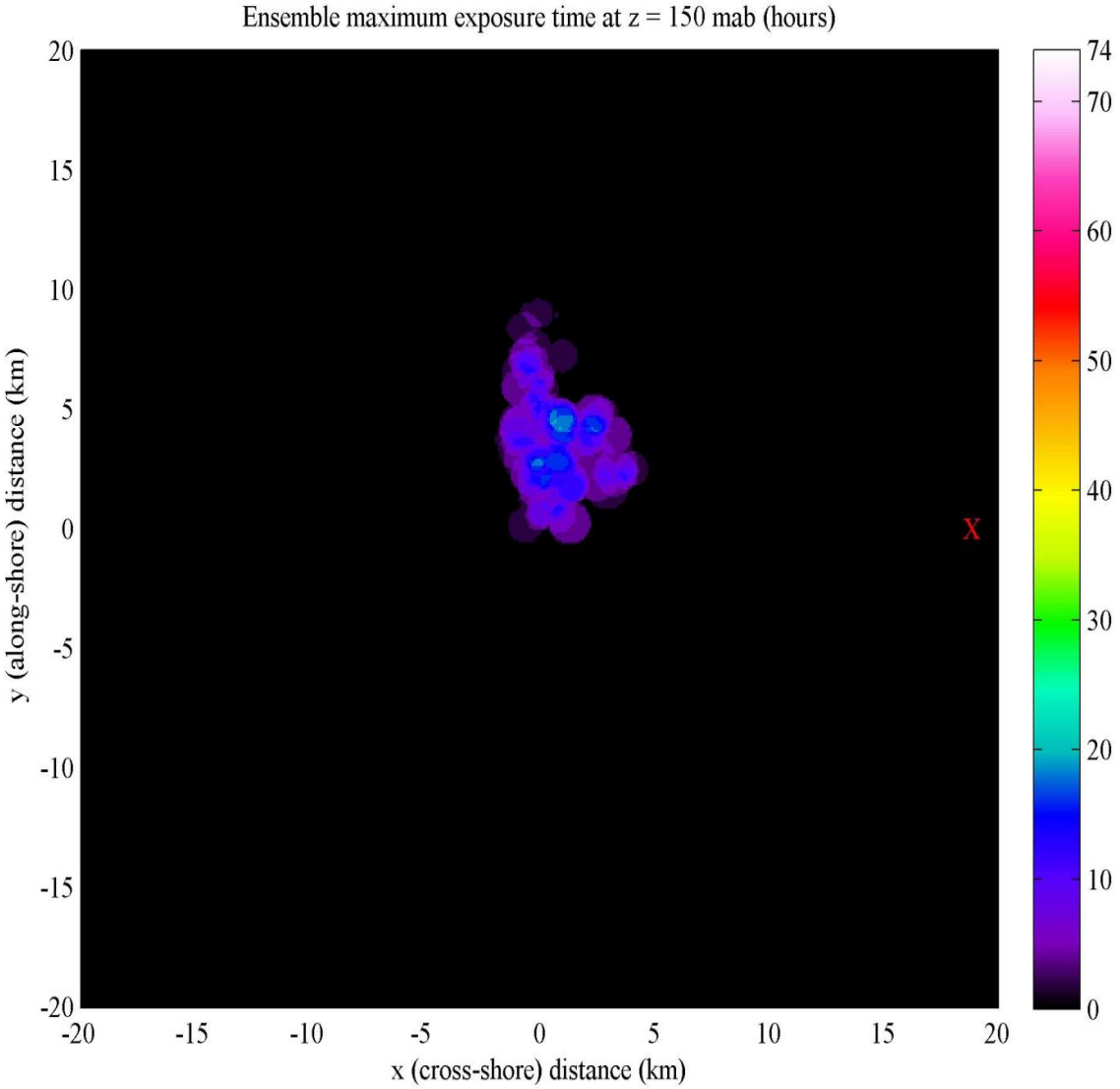

Figure 45: Ensemble maximum exposure time at $z = 250$ mab

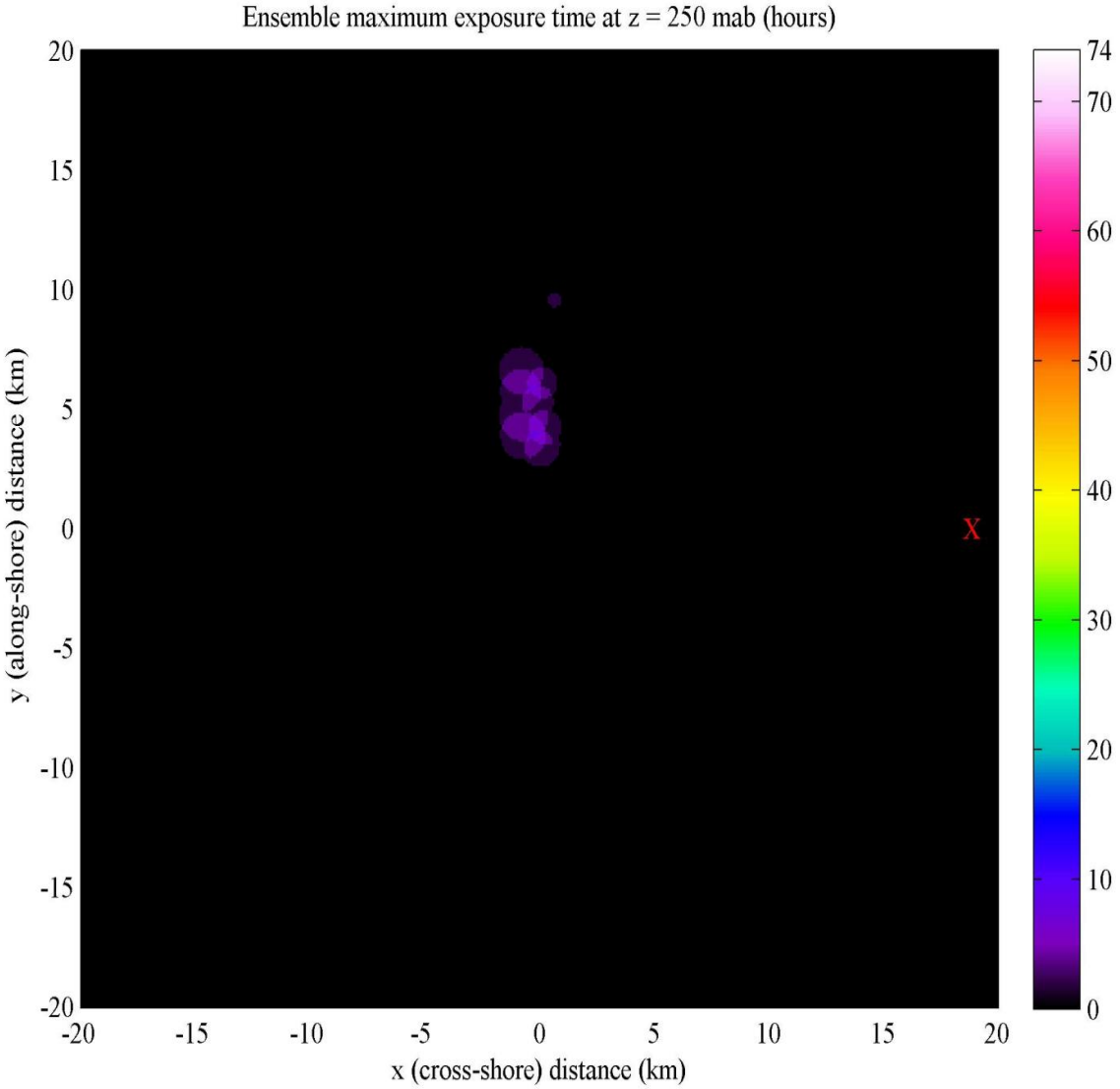

Figure 46: Ensemble maximum exposure time at $z = 320$ mab

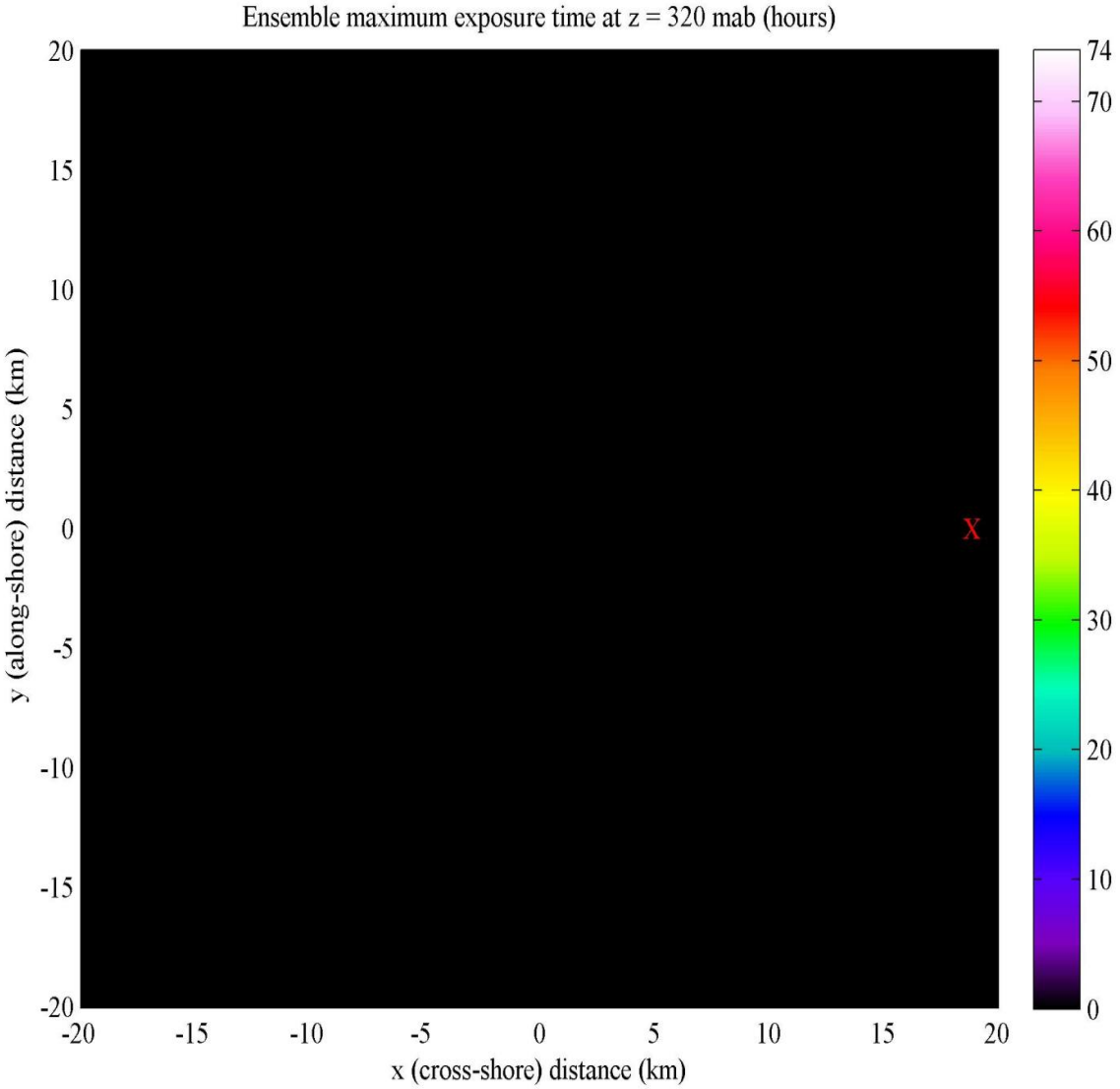

Figure 47: Ensemble maximum exposure time in the x-z plane.

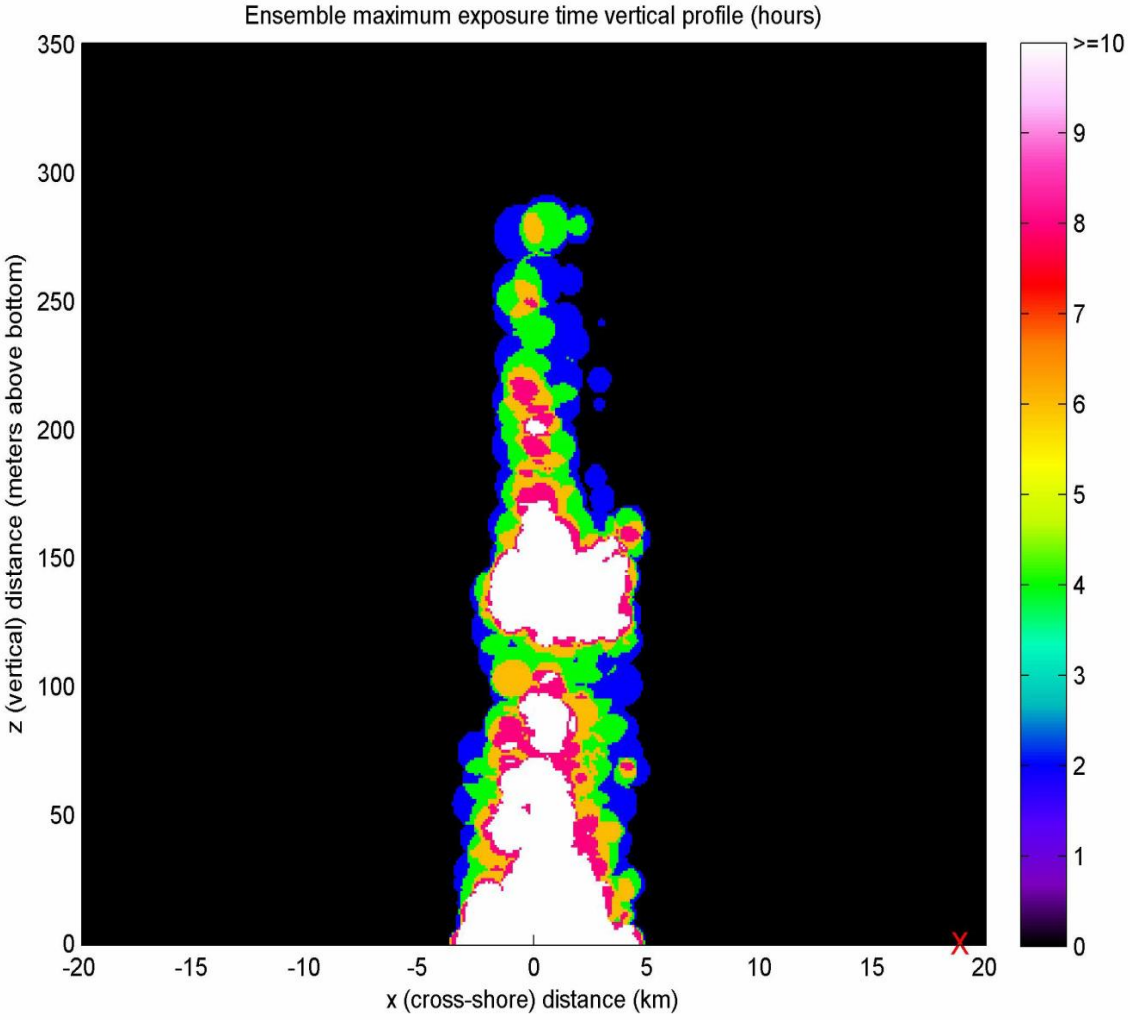

5.2.4 Exposure

Exposure is the integral, over time, of the concentration. In our computation this is approximated as the sum of concentration times the time period for each time step for which concentration exceeds the level of concern (1 ppb in the present plots). An exposure of 10 ppb*hours could therefore represent being exposed to 5 ppb concentration for two hours, or 1 ppb concentration for 10 hours.

Figure 48 shows the ensemble maximum exposure, maximized over all depths, in units of ppb*days with the color scale maximum set to 5 ppb*days. Viewing exposure on this scale makes clear that exposure falls off very rapidly away from the release location. Figure 49 presents the same ensemble maximum exposure data, maximized over all depths, but this time in units of ppb*hours with a maximum color scale of 10 ppb* hours. At this scale, we can't see the structure of the higher exposure areas, which are all white, but the structure of the lower exposure areas now is shown in more detail.

Figures 50–53 show the ensemble maximum exposure at various heights in the water column at this second scale in units of ppb*hours with a maximum color scale of 10 ppb*hours. It is clear that exposure falls off significantly away from the bottom and is predicted to be approximately zero above 320 mab.

Figure 54 shows the ensemble maximum exposure in the x-z plane, maximized over all y locations.

Figure 48: Ensemble maximum exposure at all depths

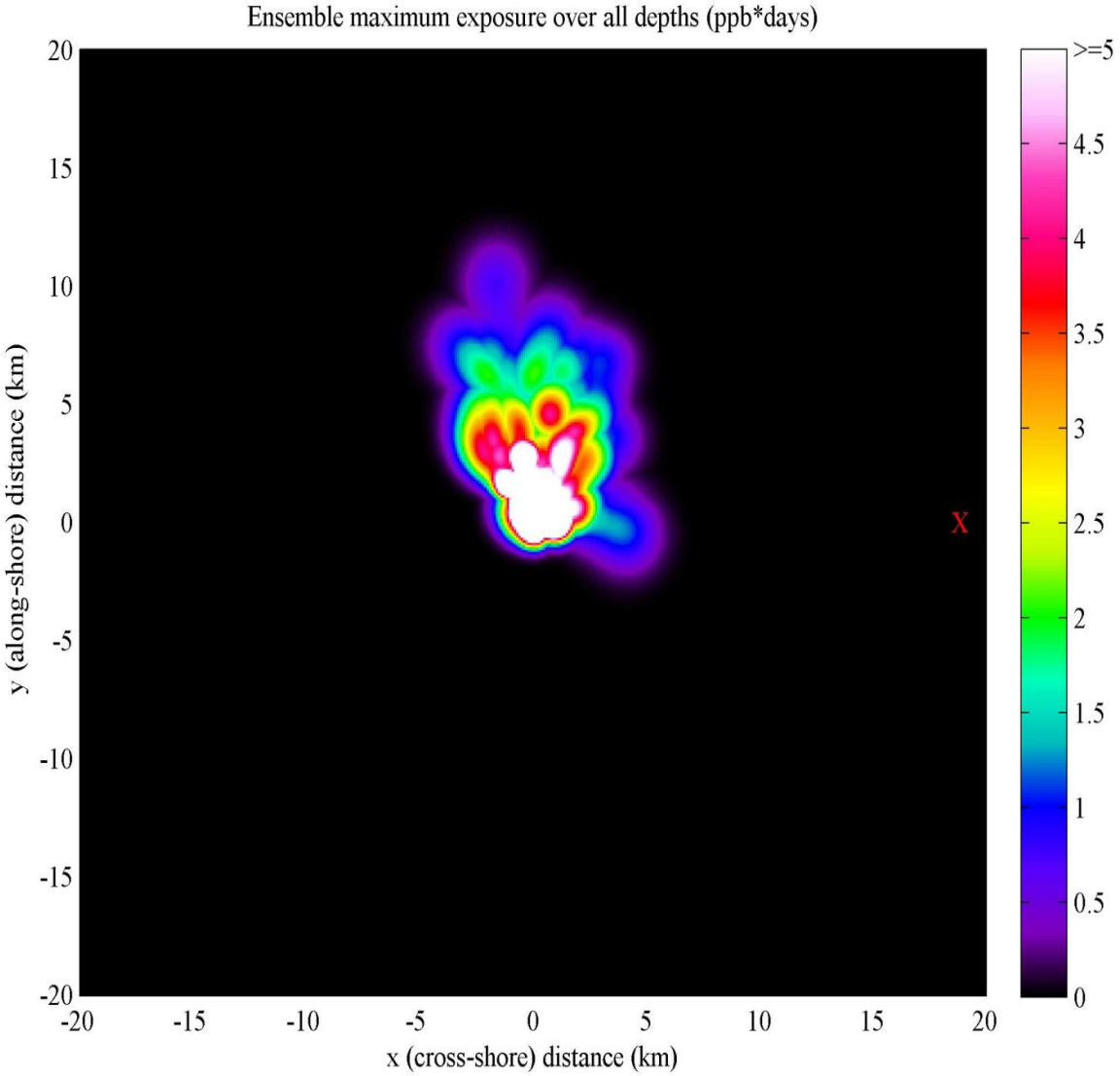

Figure 49: Ensemble maximum exposure at all depths

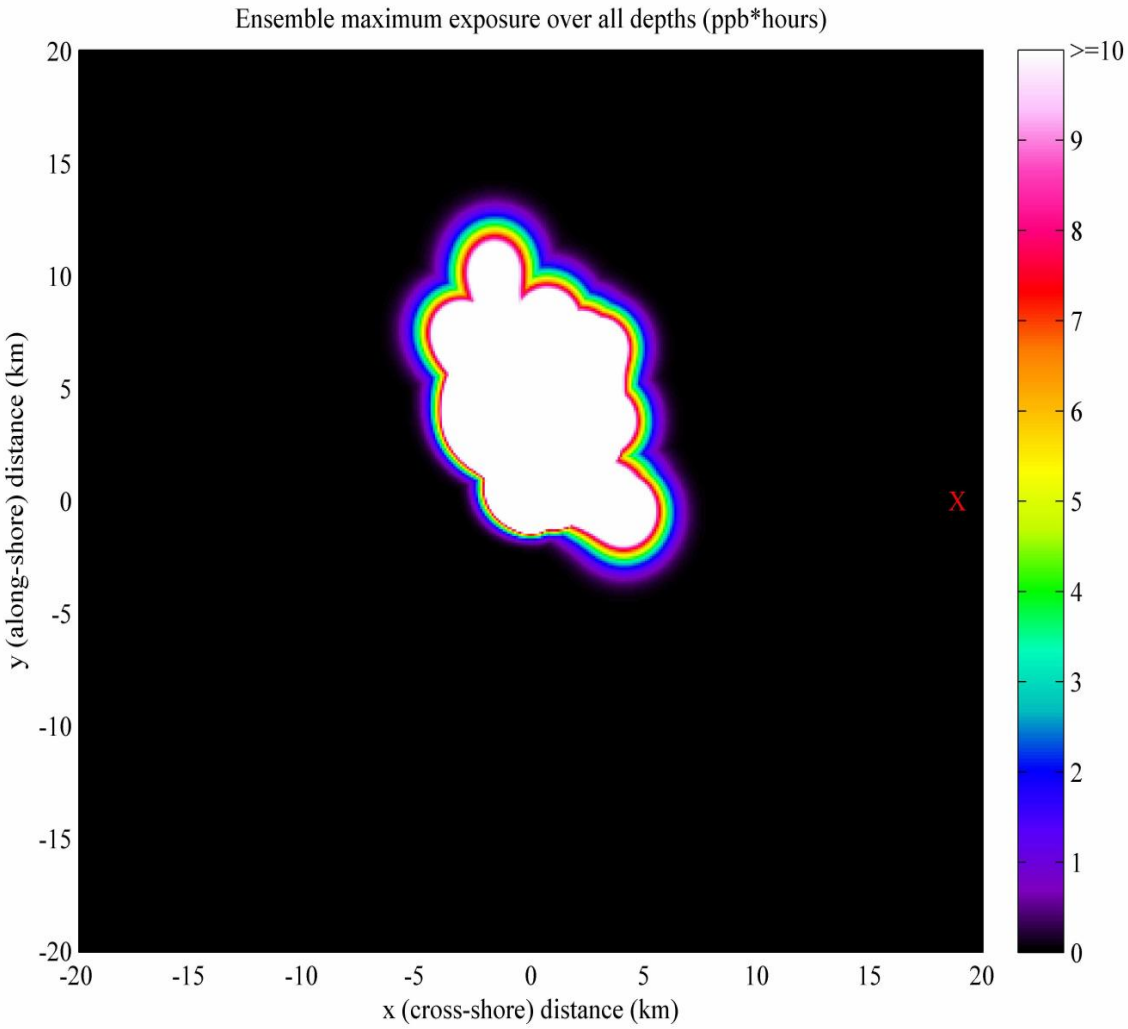

Figure 50: Ensemble maximum exposure at $z = 0$ mab

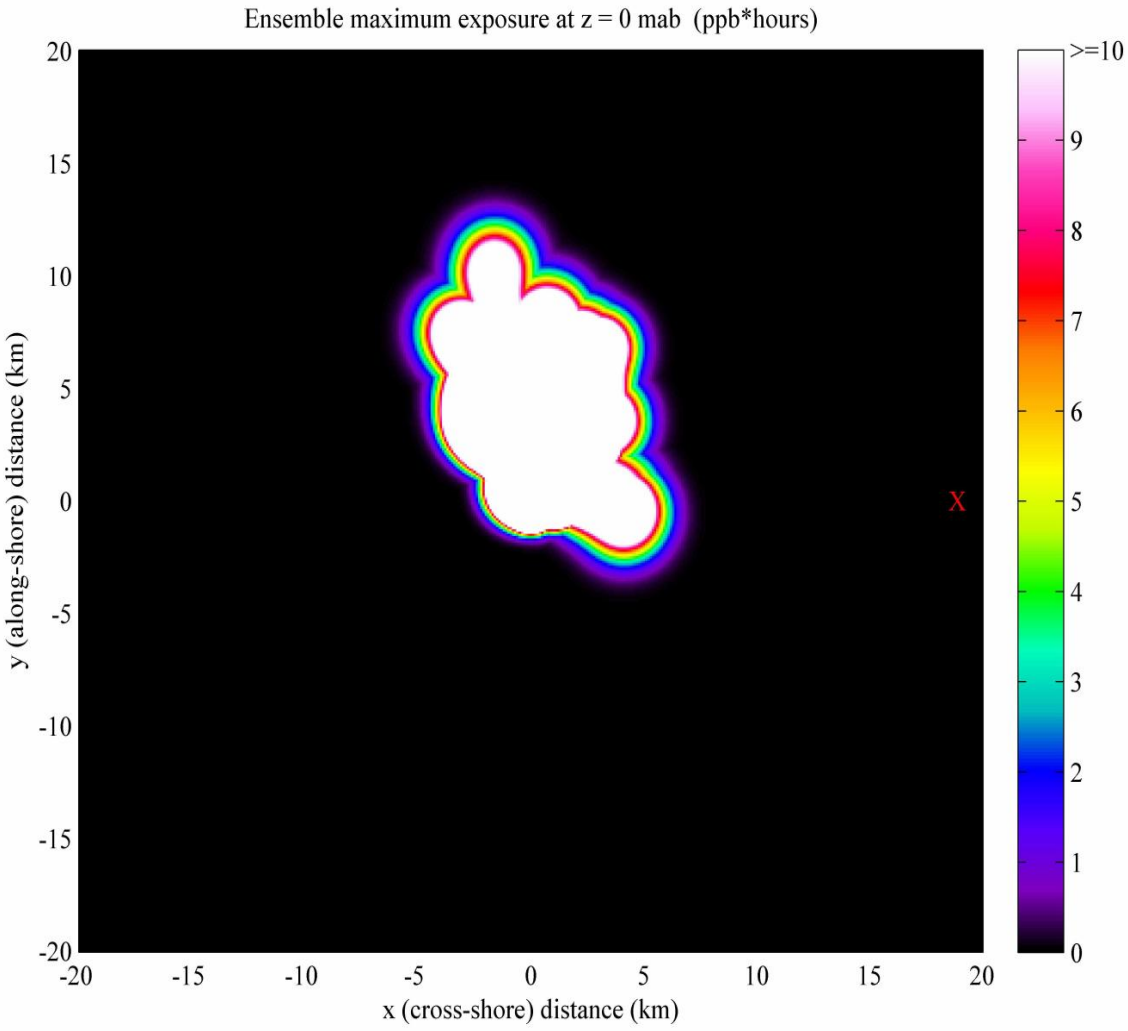

Figure 51: Ensemble maximum exposure at $z = 100$ mab

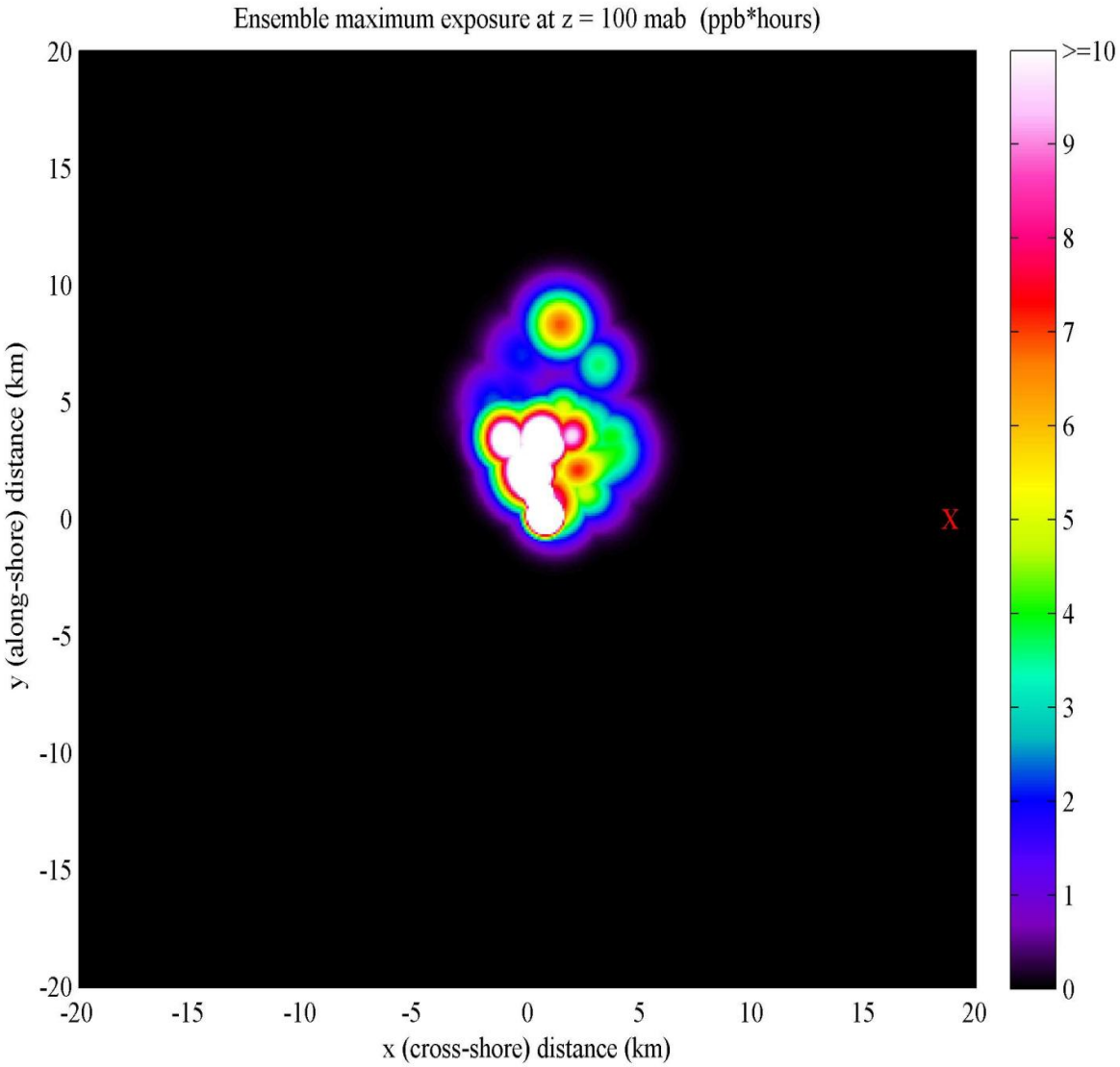

Figure 52: Ensemble eaximum exposure at $z = 200$ mab

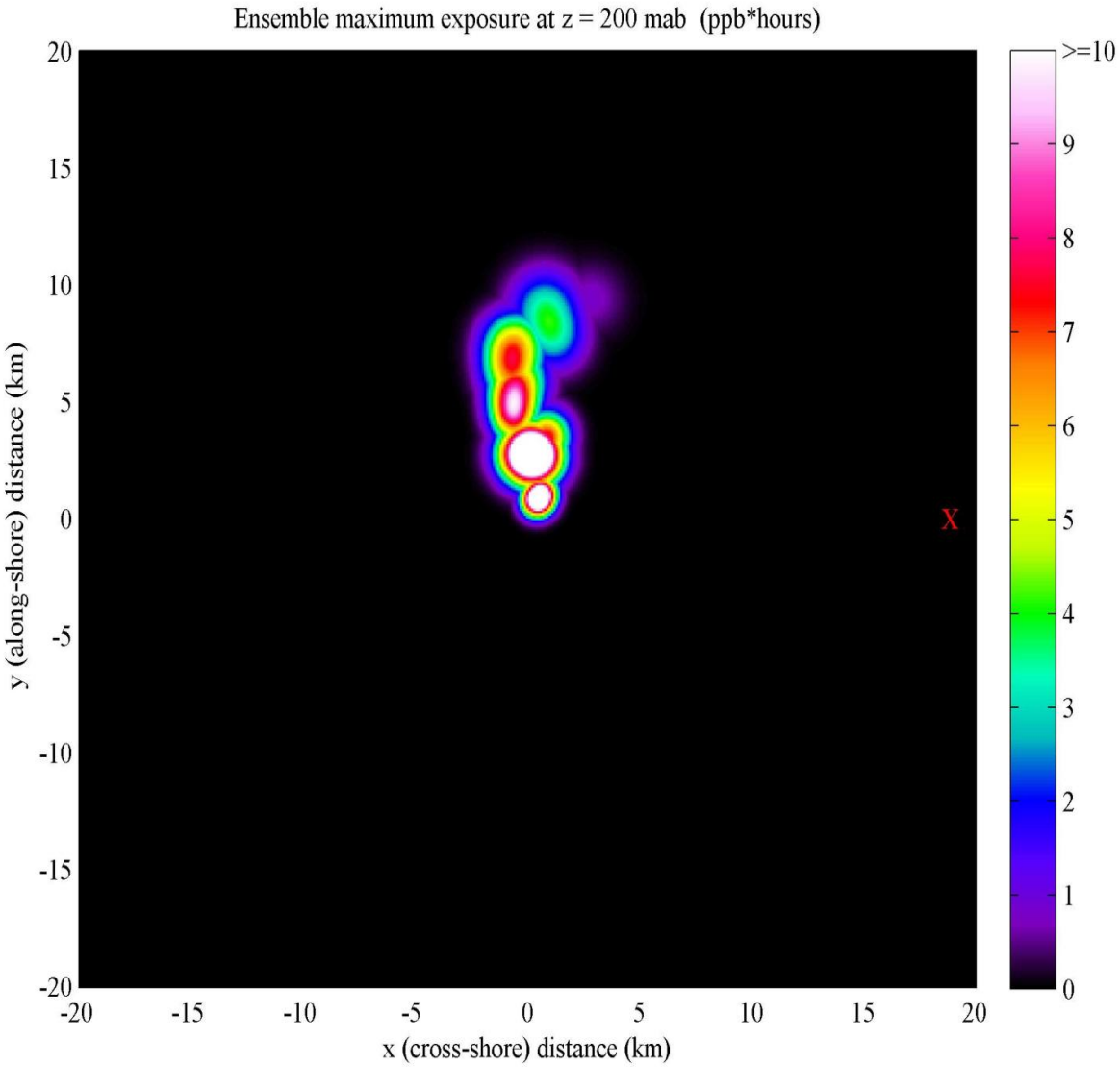

Figure 53: Ensemble maximum exposure at $z = 320$ mab

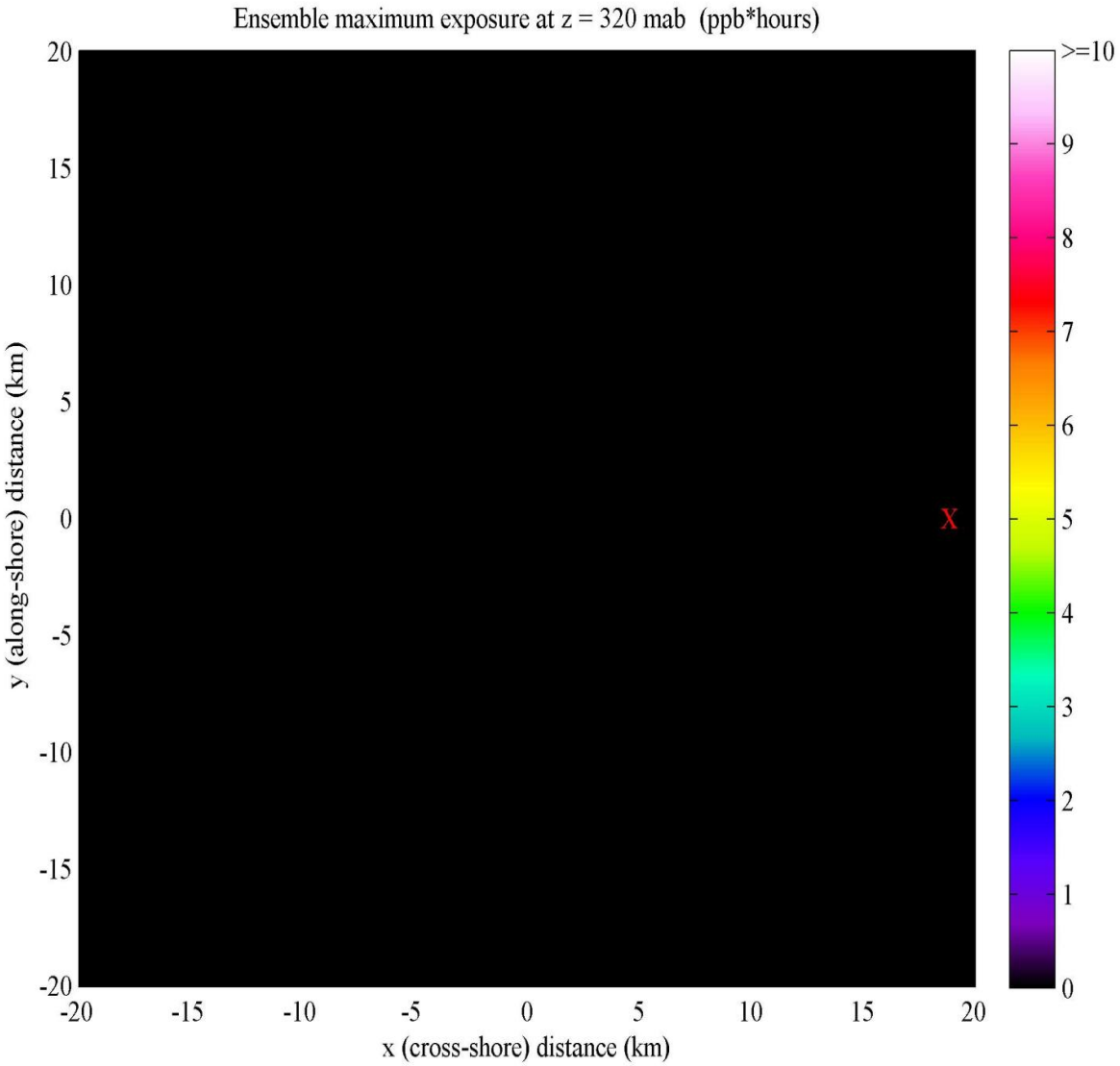

Figure 54: Ensemble maximum exposure in the x-z plane.

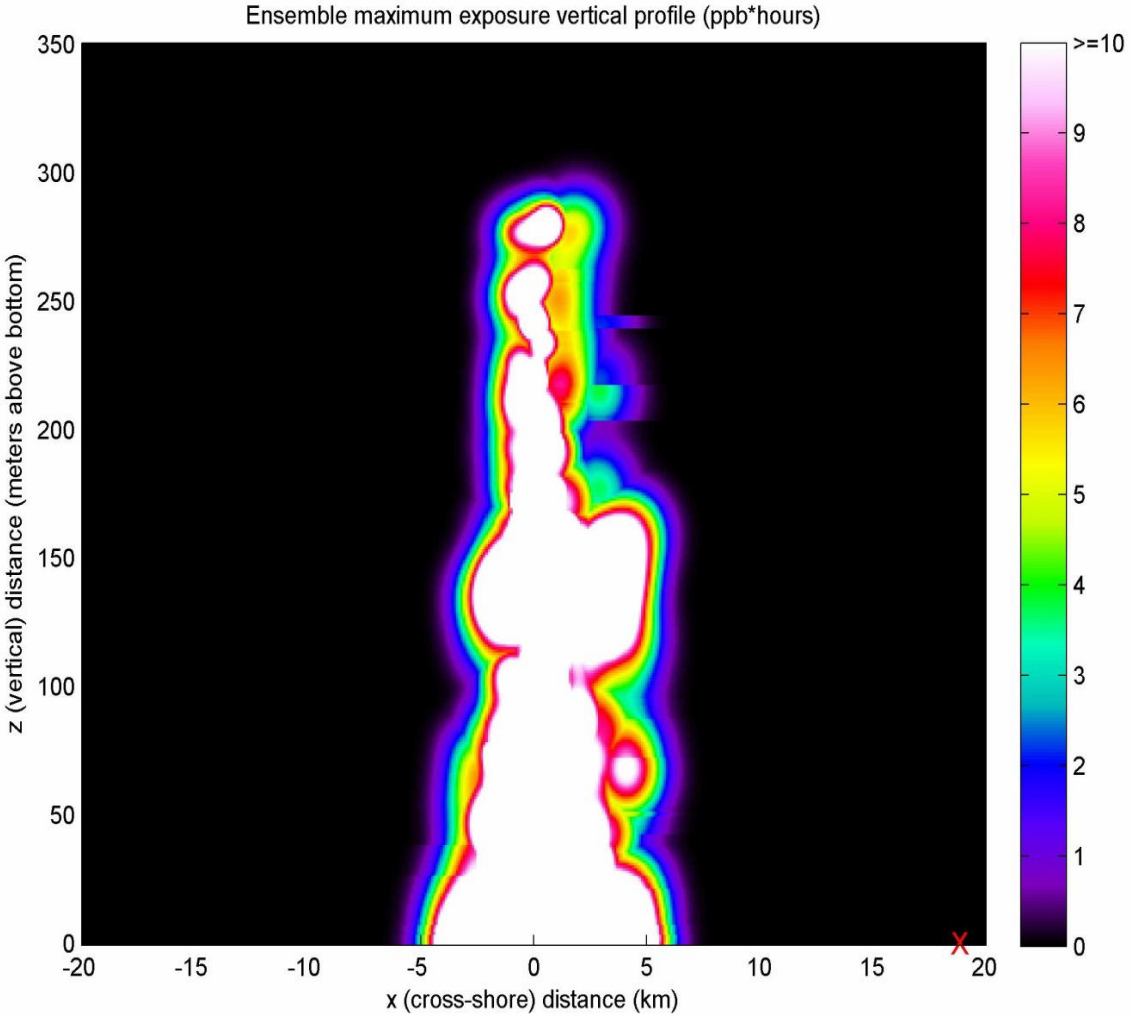

5.3 Effect of Turbulent Diffusivity Values

The analytical solution of the advection-diffusion equation which we are using to model chemical transport is

$$c(x,y,z,t) = \frac{Q}{4\pi K_H t\sqrt{4\pi K_V t}} e^{-((x-\tilde{x}(t))^2+(y-\tilde{y}(t))^2)/4K_H t-(z-\tilde{z}(t))^2/4K_V t}. \tag{50}$$

There are three parameters in the present model: Q, K_H, and K_V. Of these, Q (the initial mass of released chemical) is involved linearly in the expression for concentration, so doubling Q doubles the concentration and halving Q halves the concentration. As a result it is very easy to understand the impact of Q on the chemical plume.

The impact of the turbulent diffusivities K_H and K_V is non-linear and so not as simple. We can see that the diffusivities impact the height of the Gaussian through the instances that appear in the denominator of the multiplier outside the exponential, and they also appear within the exponential, in the role of standard deviations, if we think of the Gaussian as a normal distribution (since they have the same form). Therefore, the diffusivities affect the spread of the Gaussian. Smaller diffusivities should then correspond to less spread (a narrower Gaussian) and more height (higher peak concentrations) which persist longer in time.

To see exactly how different values of the diffusivities impact the chemical plume, we consider three cases: (1) the nominal diffusivity values of $K_H = 1$ m^2/s and $K_V = 1$ cm^2/s $= 0.0001$ m^2/s; (2) low diffusivity: $K_H = 0.1$ m^2/s and $K_V = 0.00001$ m^2/s; and (3) high diffusivity: $K_H = 10$ m^2/s and $K_V = 0.001$ m^2/s. For these computations we use $Q = 91$ kg for two reasons: first, this is a reasonable instantaneous release amount, and second, because the low diffusivity calculations take a long time for larger Q values. Since Q is linearly involved, we can always scale up concentrations to get an idea of the impact of a larger release.

As in the previous section, we will examine ensemble maximum concentration, ensemble maximum exposure time, and ensemble maximum exposure, comparing the nominal diffusivity to both the high and low diffusivity cases. In this way we can better understand the impact of diffusivity as well as bracketing the range of mixing which might occur and its impact on the plume evolution.

Recall the difference between maximum exposure time and total dissipation time. Ensemble maximum exposure time is the longest time that any one location is exposed to concentrations at or above the threshold of concern (1 ppb). Total dissipation time is the time elapsed from release until the concentration everywhere is below the threshold of concern. If there were no advection, these would be the same. With advection, the total dissipation time is longer than the maxium exposure time because the plume moves, resulting in shorter exposure times at any particular location.

Figure 55 shows the ensemble maximum concentration footprint in the x-y plane (maximized over all heights) in the case of higher diffusivity on the left and nominal diffusivity on the right. The plume on the left is less extensive because it has diffused more rapidly. Figure 56 shows the ensemble maximum concentration footprint in the x-z plane (maximized over all along-shore y values) for both nominal and higher diffusivities. In the case of higher diffusivity, the plume has dissipated below the level of concern before the pathline reaches above 200 mab, with a maximum exposure time of 8 hours and total dissipation time of 9.6

hours. In the nominal diffusivity case, the maximum exposure time of 2.4 days and the total dissipation time is about 4 days.

Figures 57 and 58 show ensemble maximum exposure time in the x-y and x-z planes, respectively, for both nominal and higher diffusivities. The red X in all of these figures represents the nearest point of Oahu to the release site. Note that the minimum positive value for exposure time is 2 hours because that is the sampling period, which is why the value of 1 hour (corresponding to purple in the colormap) does not appear in the exposure time figures.

Figures 59 and 60 show ensemble maximum exposure in the x-y and x-z planes, respectively, for both nominal and higher diffusivities.

The next group of figures compare footprints for low diffusivity to those for nominal diffusivity. In the low diffusivity case, the maximum exposure time is 100 hours (just over 4 days), and the total dissipation time is about 40 days. In this time, advection carries the plume much farther than in the nominal diffusivity case, where the plume dissipates below 1 ppb everywhere within about 4 days.

In figures 61 and 62 we see ensemble maximum concentration compared in the low and nominal diffusivity cases. In the low diffusivity case the plumes travel far enough that we can start to see individual pathlines resolved. Note that any single plume (from a single release) would be relatively thin (like one of the fingers in the left side of figure 61) but the ensemble includes pathlines for many different release times and therefore indicates the entire region which might be visited by a plume. In figure 62 the wide coverage seen in the x-direction of the ensemble of plumes is the result of the plume moving in the x-direction as it is carried along in the positive y-direction. That is, in some cases, the plume has passed O'ahu in the y-direction before it heads in positive x-direction. Thus, proximity to the red X in this figure does not necessarily imply proximity to O'ahu because the amount of travel in the y-direction must be considered. It is helpful to look at the pathlines in the x-y plane in figure 31 to develop a clearer picture of this.

Figures 63 and 64 show ensemble maximum exposure time in the x-y and x-z planes, respectively, for both nominal and lower diffusivities. Figures 65 and 66 show ensemble maximum exposure in the x-y and x-z planes, respectively, for both nominal and lower diffusivities.

Lowering both the horizontal and vertical diffusivities by an order of magnitude from the nominal values makes the transport advection-dominated. We note the plumes being carried much farther before ultimately dissipating but we also note that they are carried in a direction which takes them generally away from land and that they still remain below 320 mab.

Figure 55: Ensemble maximum concentration at high and nominal diffusivities in the x-y plane.

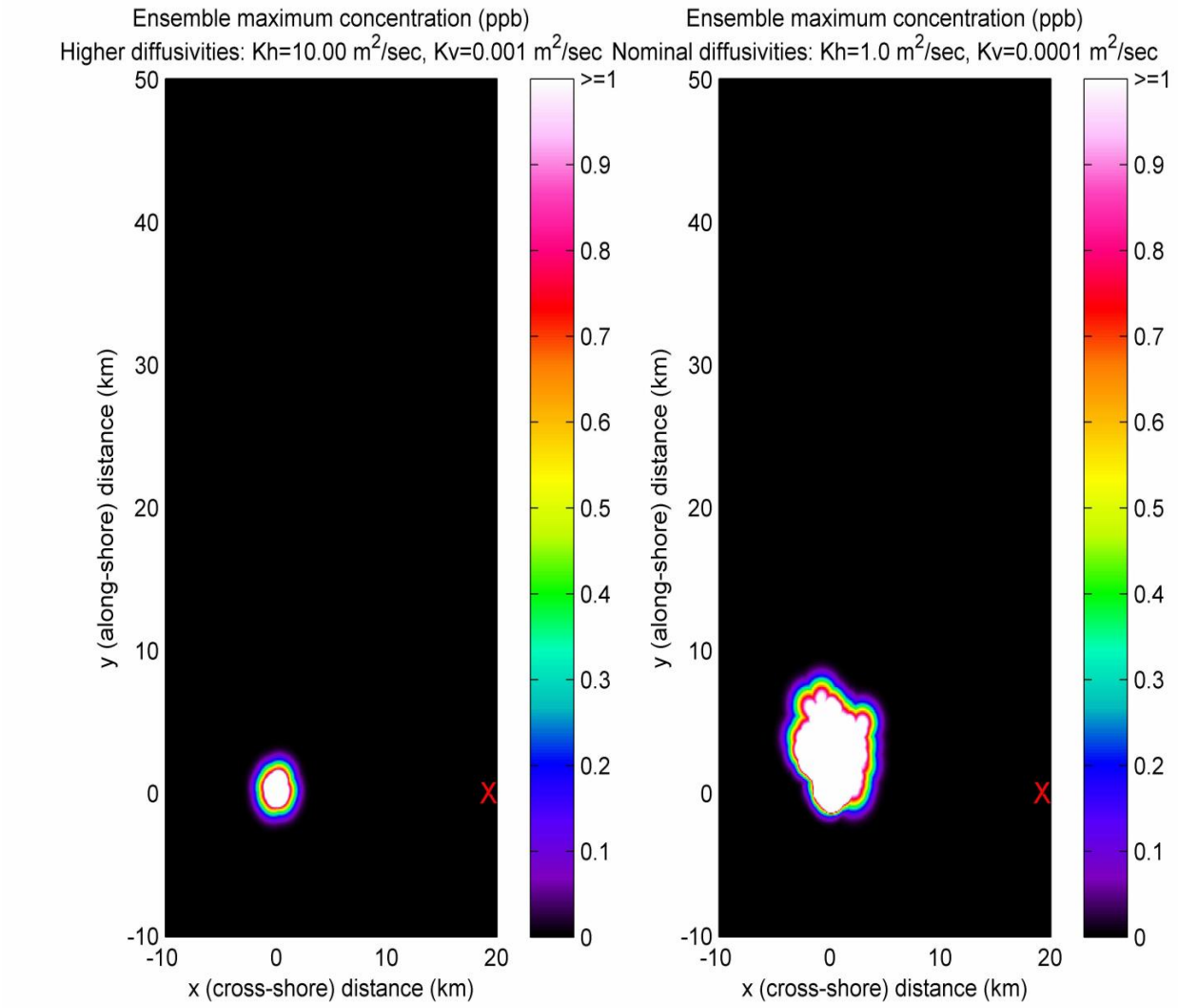

Figure 56: Ensemble maximum concentration at high and nominal diffusivities in the x-z plane.

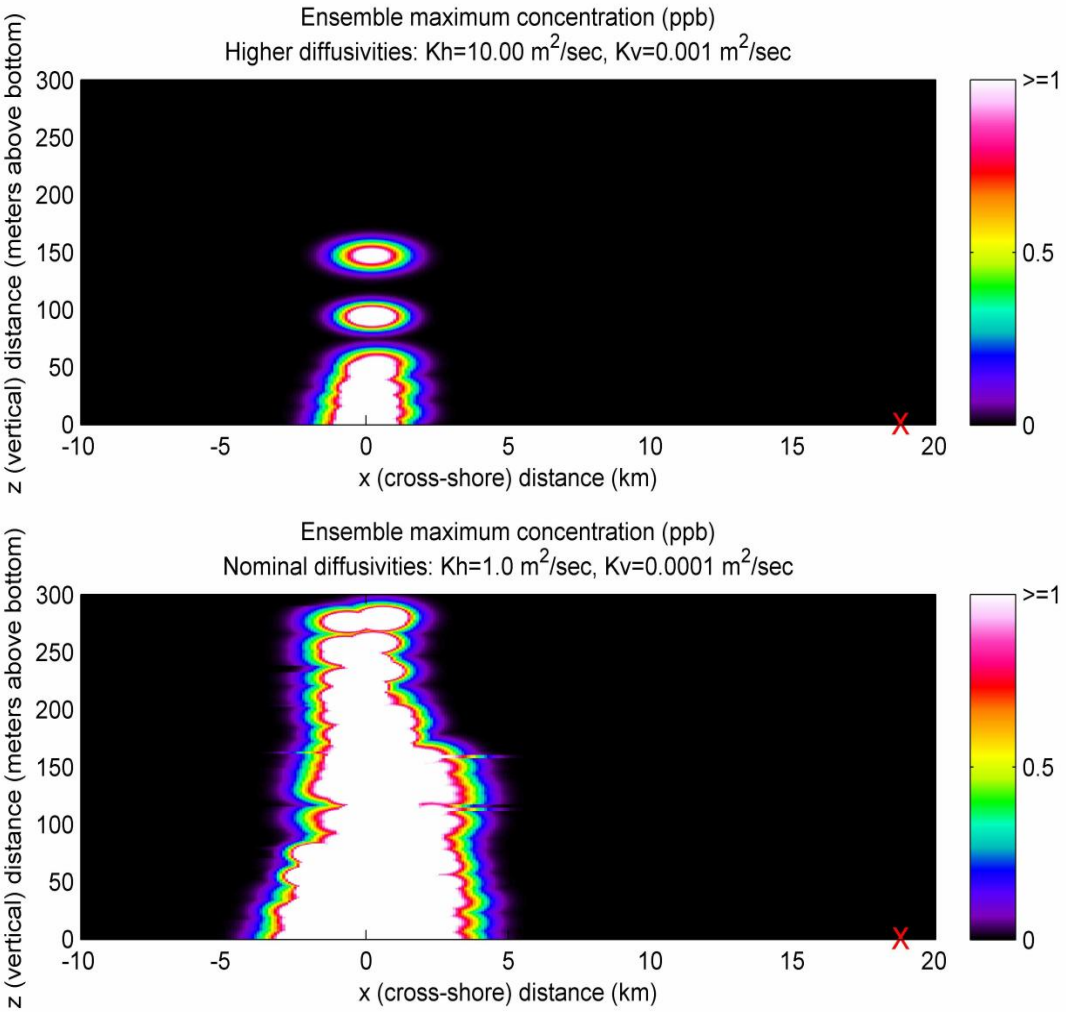

Figure 57: Ensemble maximum exposure time at high and nominal diffusivities in the x-y plane.

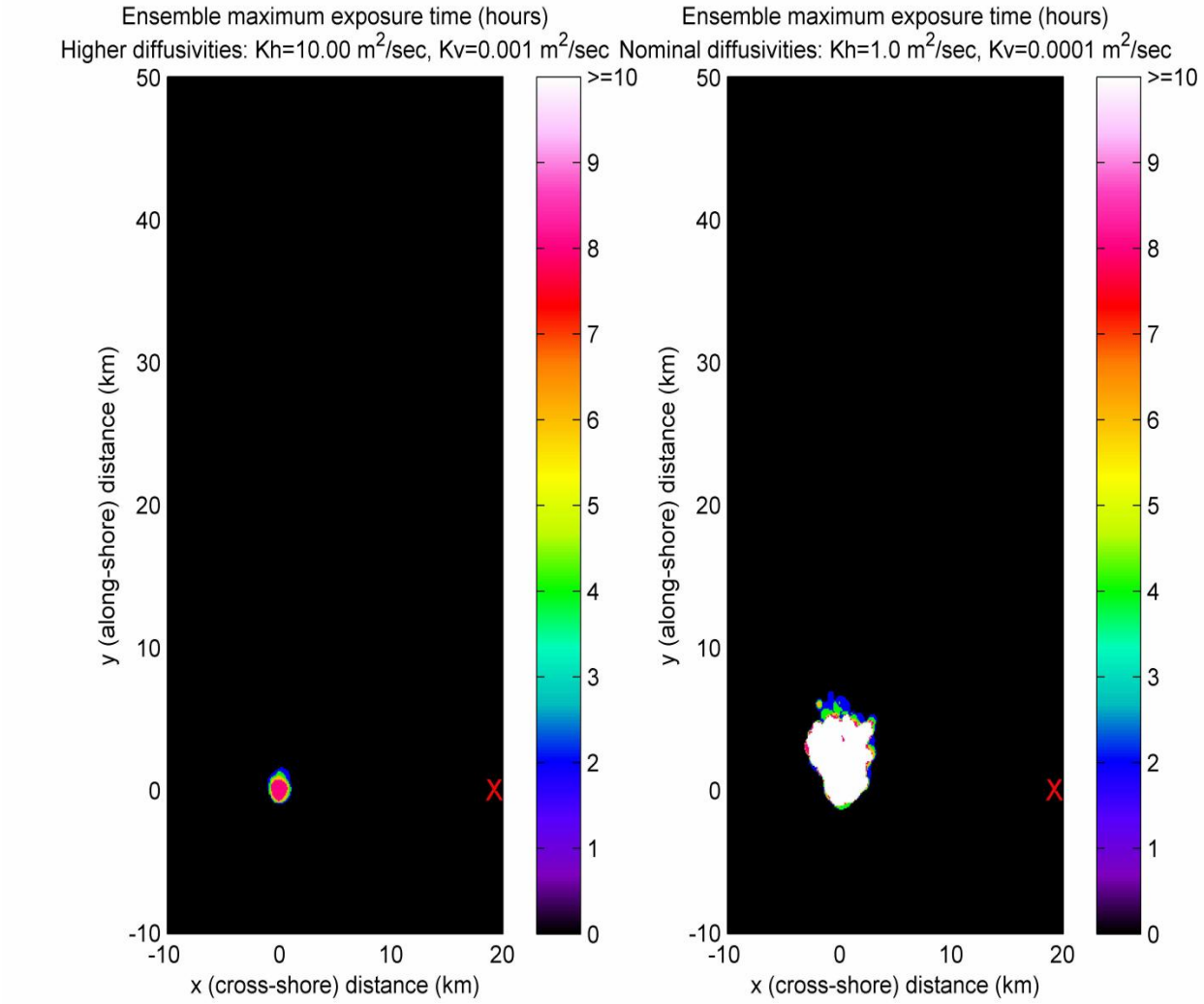

Figure 58: Ensemble maximum exposure time at high and nominal diffusivities in the x-z plane.

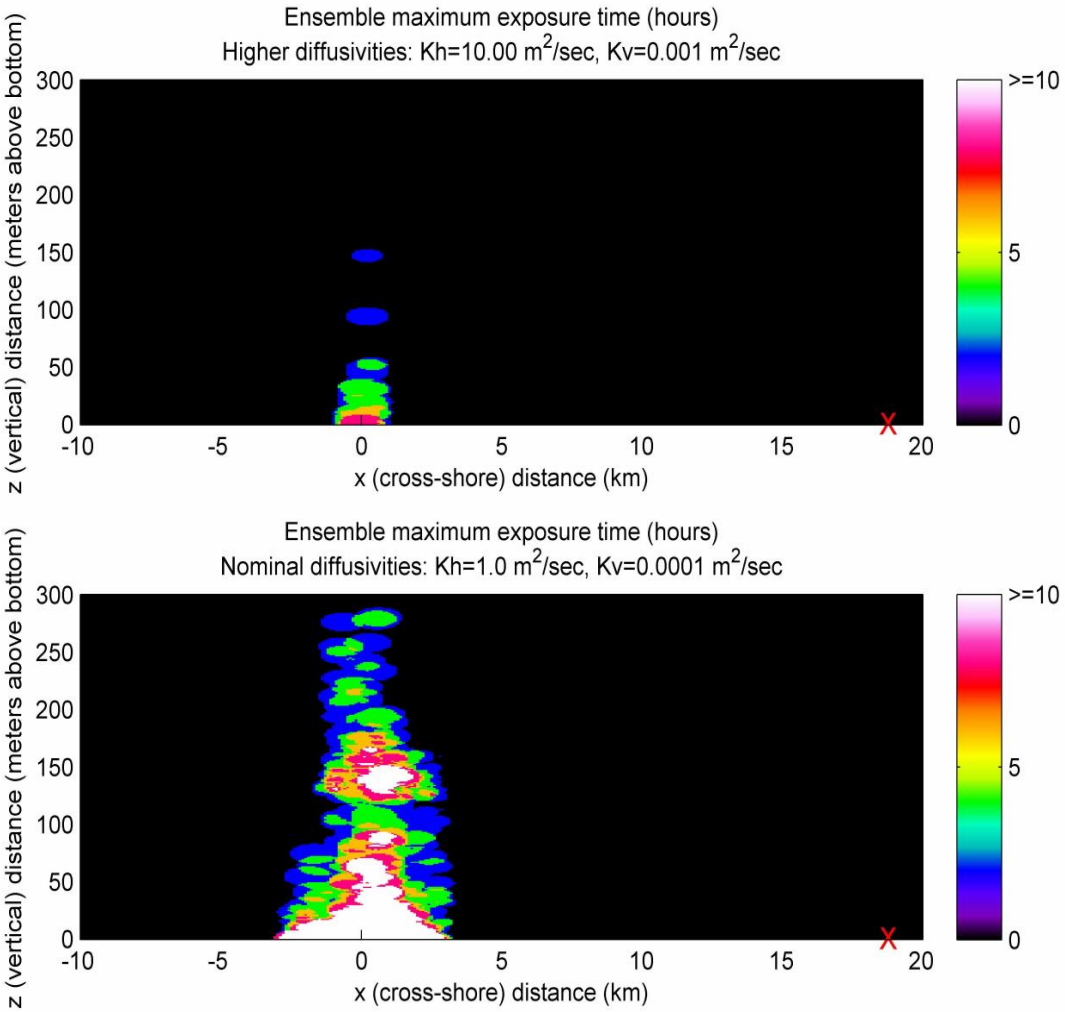

Figure 59: Ensemble maximum exposure at high and nominal diffusivities in the x-y plane.

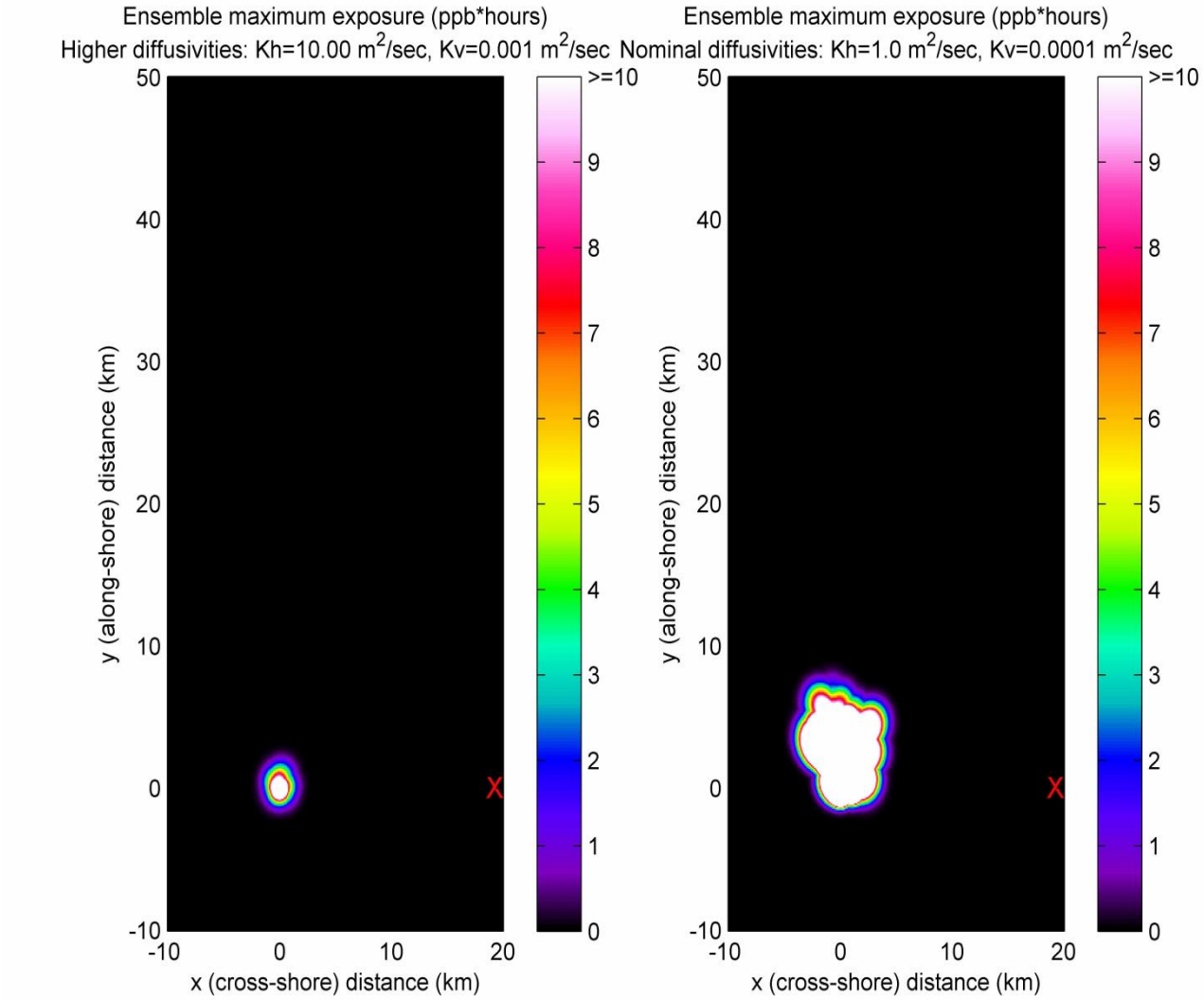

Figure 60: Ensemble maximum exposure at high and nominal diffusivities in the x-z plane.

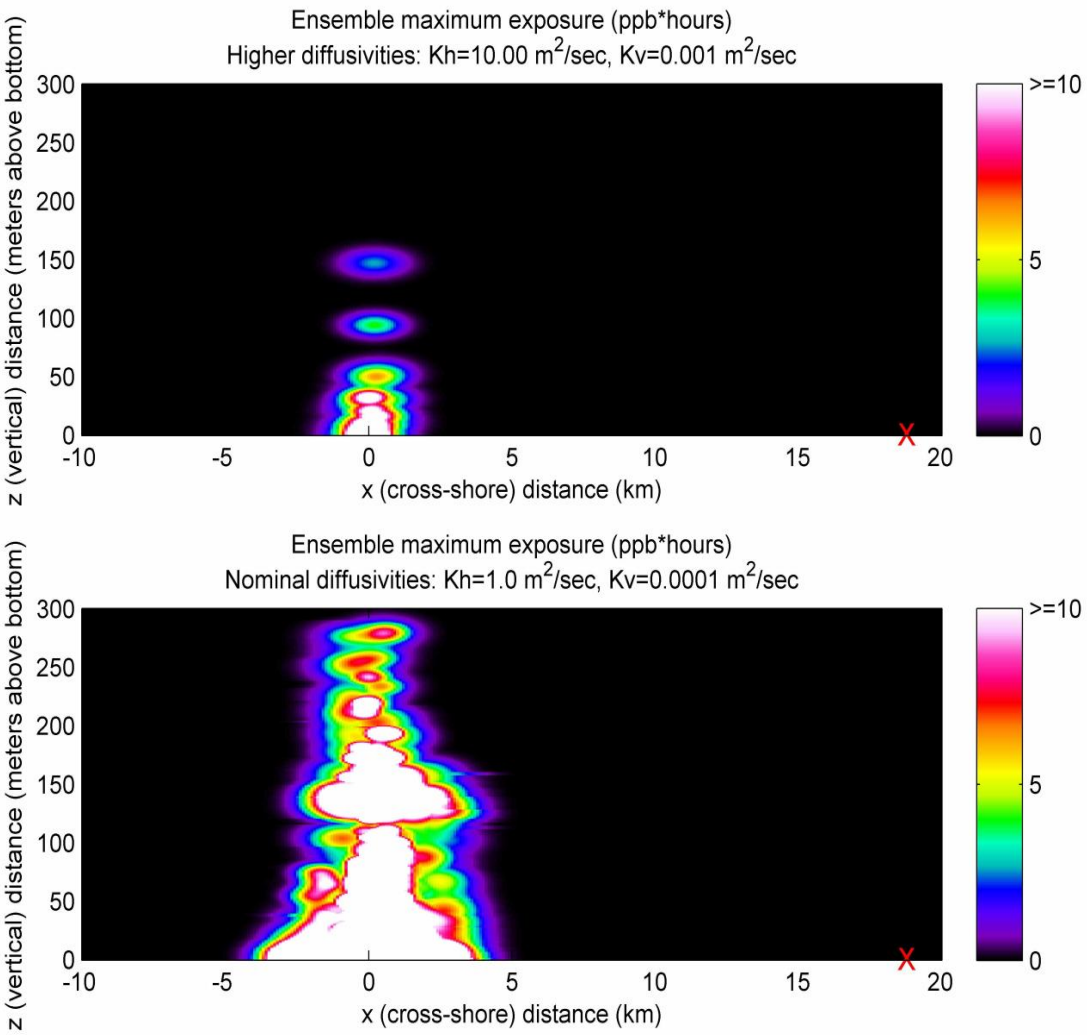

Figure 61: Ensemble maximum concentration at low and nominal diffusivities in the x-y plane.

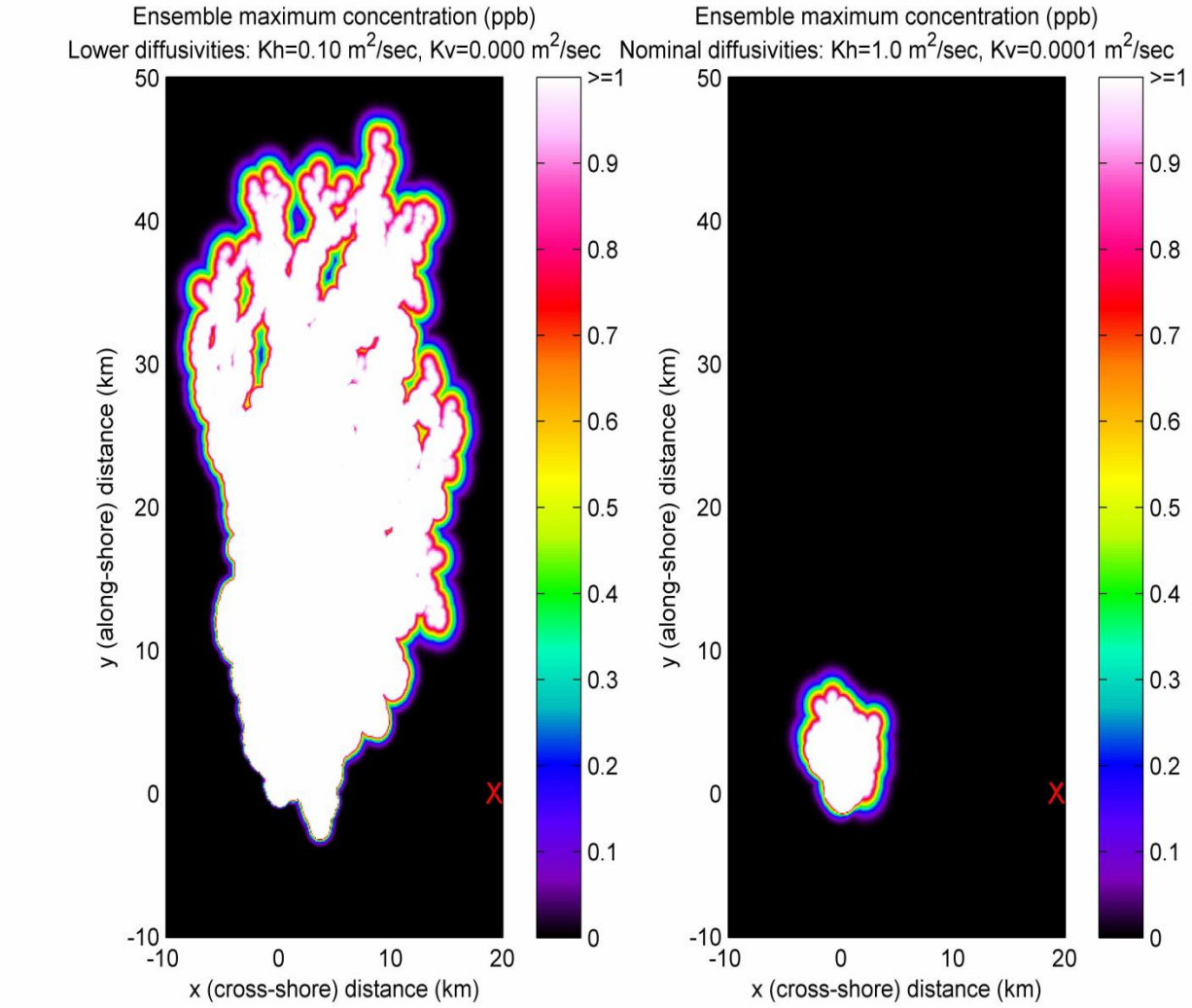

Figure 62: Ensemble maximum concentration at low and nominal diffusivities in the x-z plane.

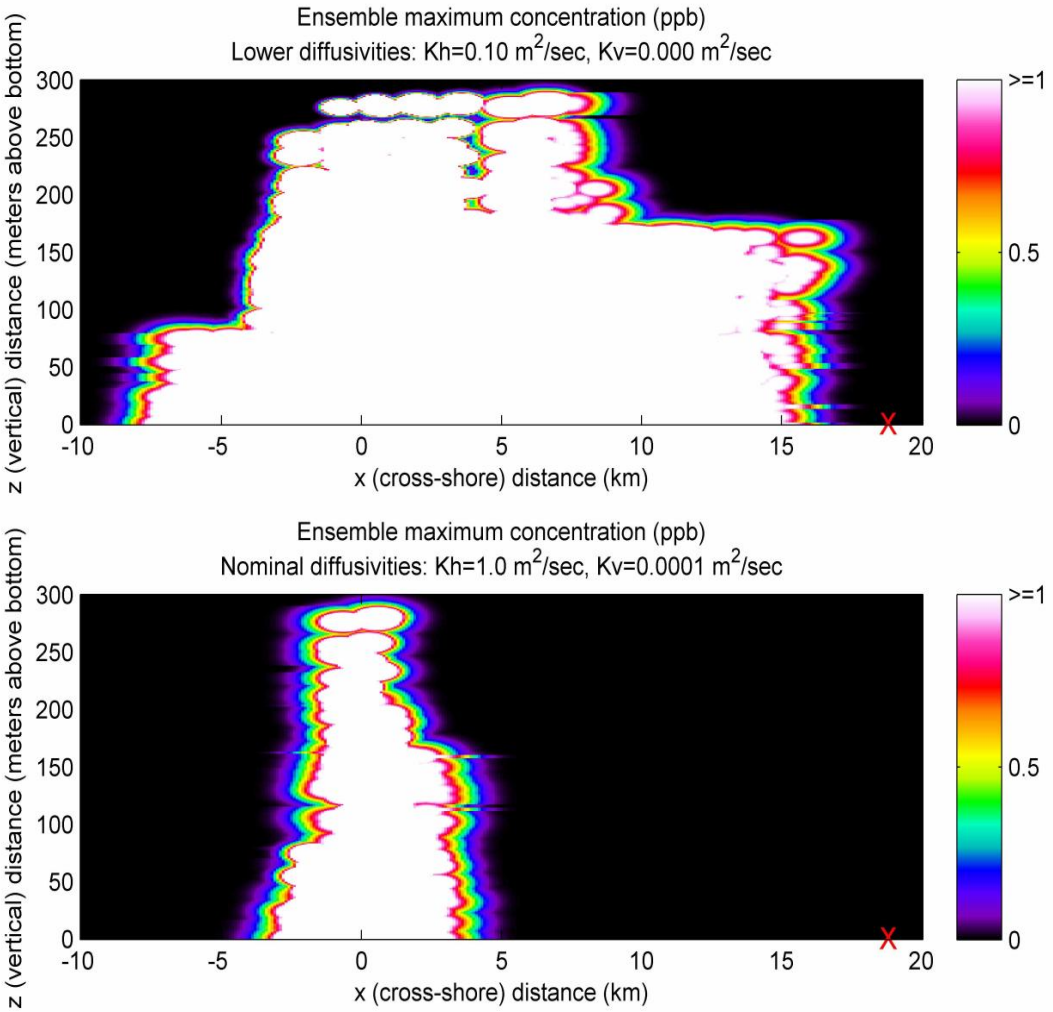

Figure 63: Ensemble maximum exposure time at low and nominal diffusivities in the x-y plane.

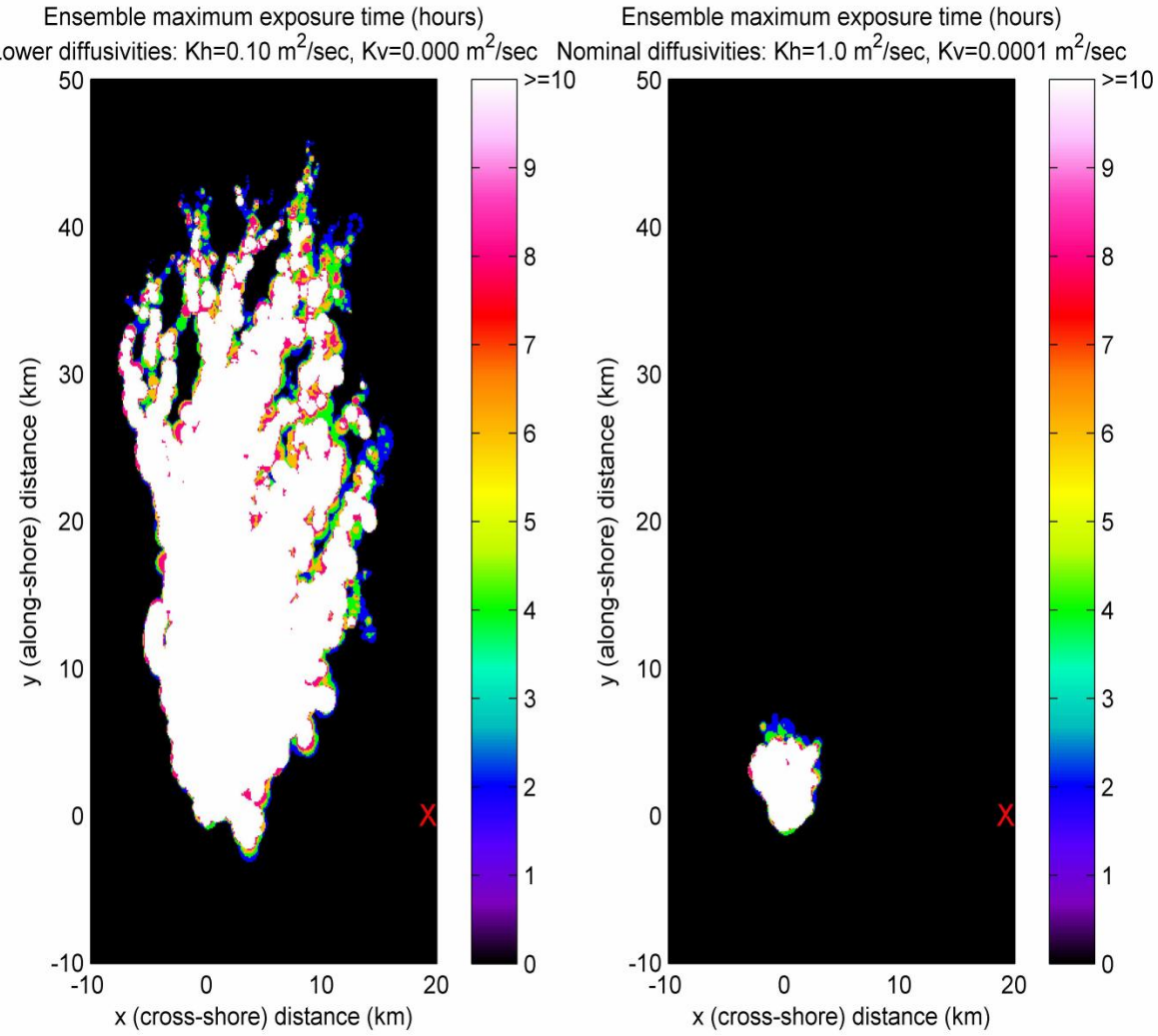

Figure 64: Ensemble maximum exposure time at low and nominal diffusivities in the x-z plane.

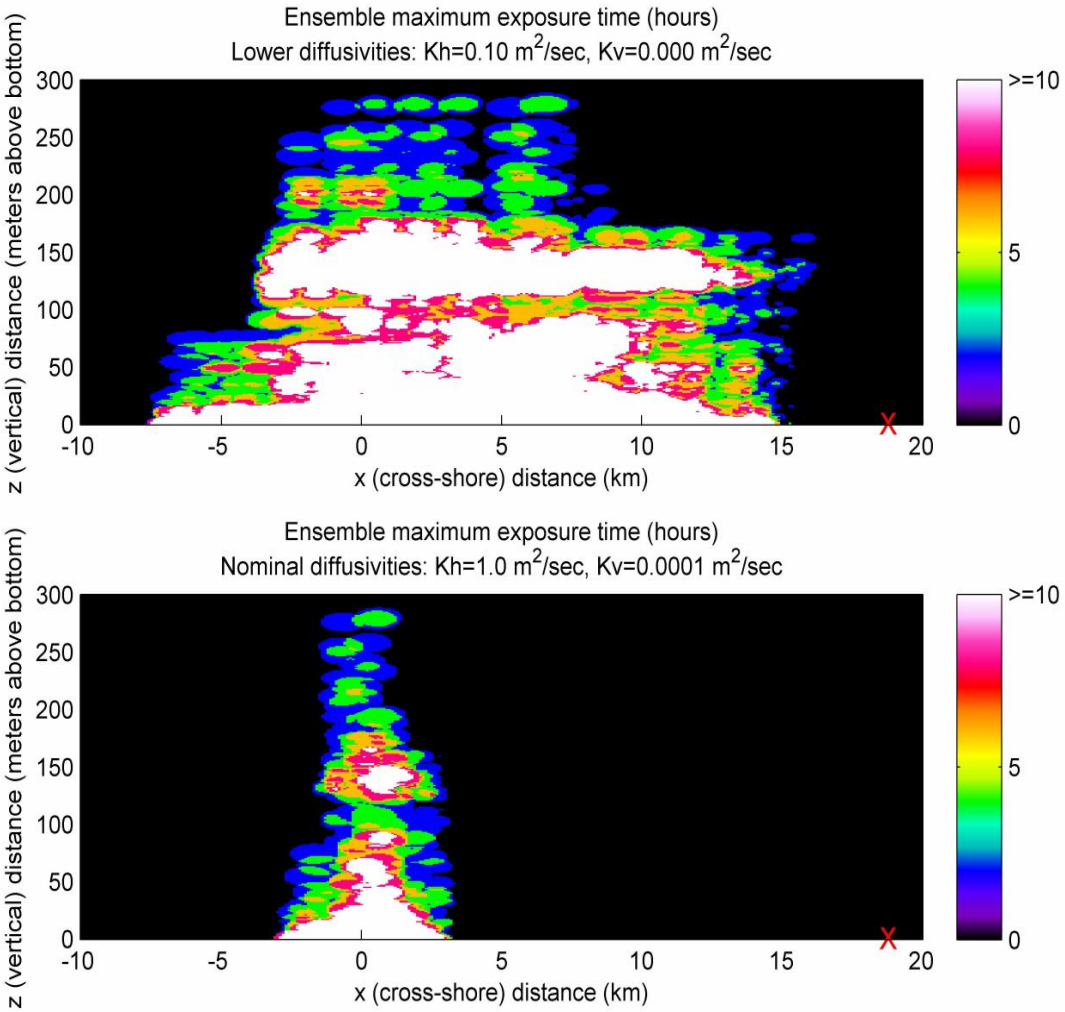

Figure 65: Ensemble maximum exposure at low and nominal diffusivities in the x-y plane.

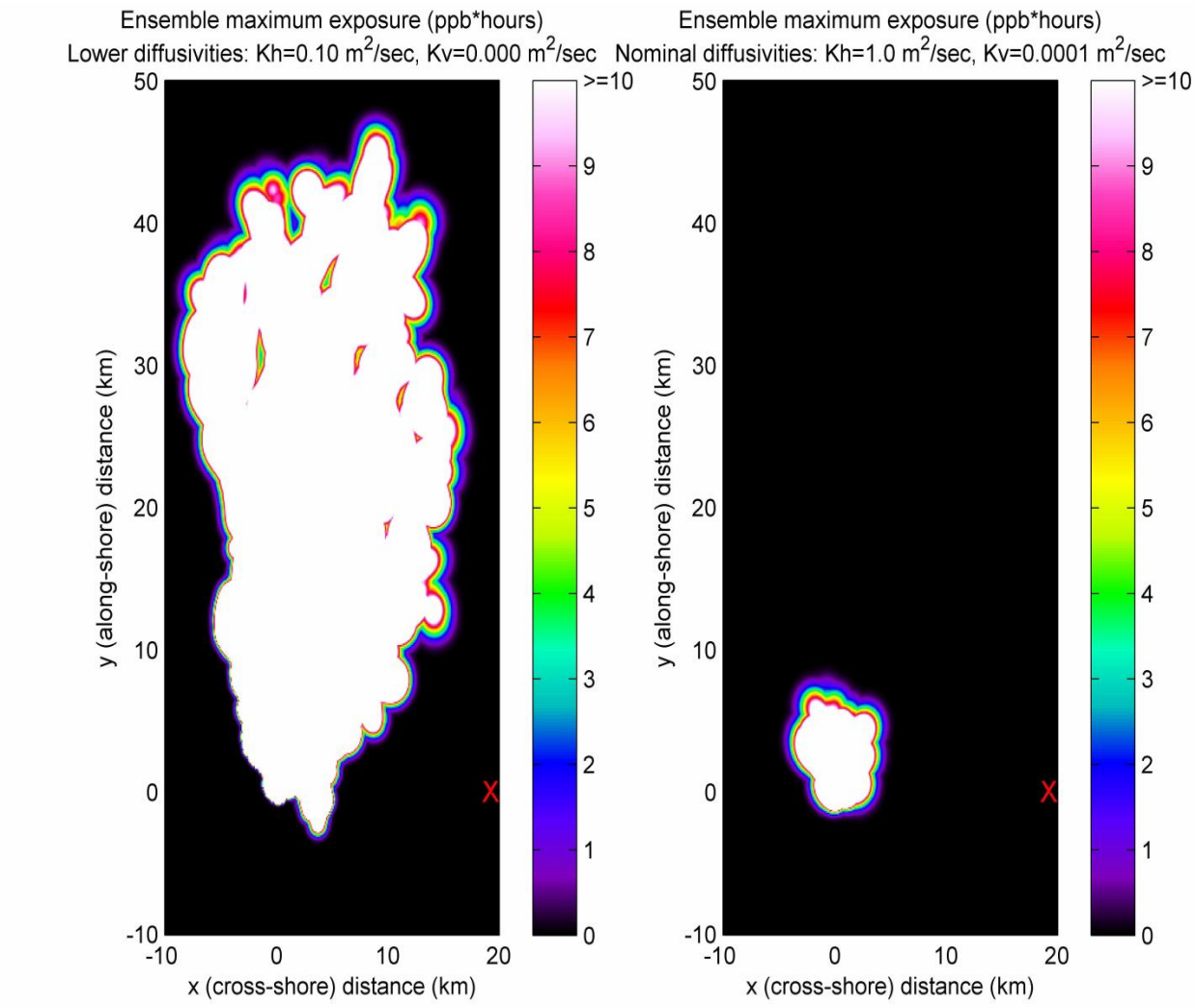

Figure 66: Ensemble maximum exposure at low and nominal diffusivities in the x-z plane.

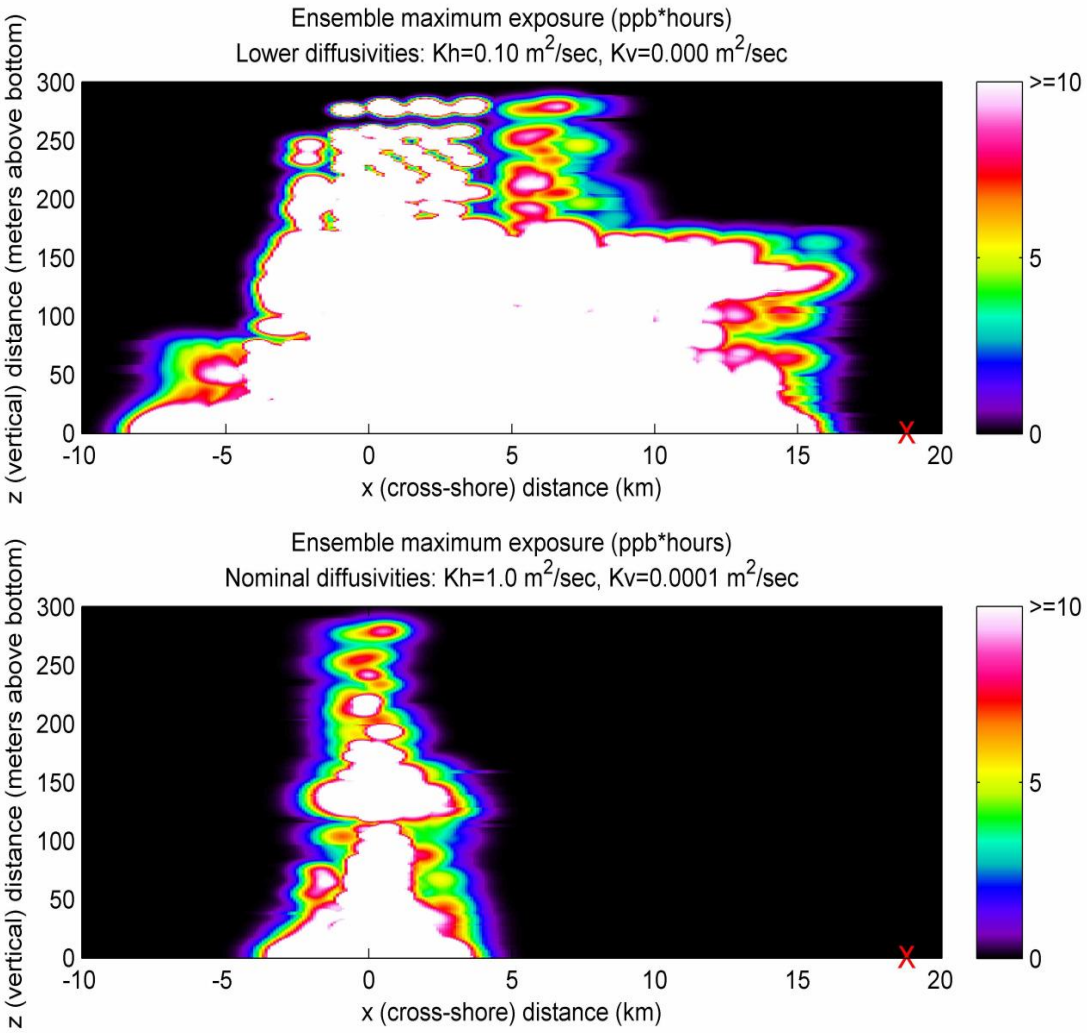

6 Conclusions

The overall conclusion of this work is that in the event that chemicals are released from the deep water disposal site, they are likely to dissipate to concentrations below 1 ppb within a period of 8 hours to 40 days of the release (depending on the amount released and on the actual mixing rates), during which time chemicals are not likely to reach detectable quantities except in the bottom several hundred meters of the water column, at worst. Maximum exposure time for any one location was, at most, 4 days in the circumstances modeled. During the several days or weeks when concentrations in the deep water may exceed 1 ppb in places, the chemical plume is likely to travel past O'ahu, mostly in an along-shore direction, with some cross-shore motion, the magnitude and direction of which depends on the depth at which the plume travels. Near the disposal site, concentrations are predicted to exceed 1 ppb for less than 4 days, with exposure times rapidly decreasing away from the release site and upward through the bottom several hundred meters of the water column. Exposures are expected to be essentially zero at all depths within a few kilometers of O'ahu, and everywhere else except in the bottom 300 meters of the water column, where they are highest near the disposal site.

Based on a worst-case scenario of the instantaneous release of 182 kg of chemical, the model predicts that concentrations would be everywhere less than 1 ppb within 6.4 days. Hydrogen cyanide (AC) is the chemical which causes the most concern because it is completely miscible with water. However, 182 kg represents a tenth of the total amount of disposed hydrogen cyanide, which is packaged in munitions which each contain about 91 kg of hydrogen cyanide. Thus, an instantaneous release of 182 kg represents the simultaneous breach of 2 of the 20 munitions disposed which contain hydrogen cyanide. Even if all 20 of the munitions containing hydrogen cyanide were simultaneously breached, the model predicts concentrations would be everywhere below roughly 10 ppb within about 6.4 days (using the linearity of the model in Q).

The same dissipation rate is predicted in the event of a release of any of the chemicals, but breakdown of the chemicals is not modeled. Cyanogen chloride is not of as much concern since its breakdown products are not considered dangerous. Lewisite and sulfur mustard are only sparingly soluble, so it is difficult to imagine an instantaneous release of either in a quantity as large as 182 kg. Nevertheless, if we consider a release of this magnitude, the result is still that the concentration everywhere would be below 1ppb within about 6.4 days. More realistic predictions suggest mustard or Lewisite is not likely to be transported more than a matter of feet from the disposal site in concentrations of concern for human health based on the slow rate at which these dissolve in water [see NOAA Chemical Warfare Agents Summary, 2011].

Ensemble footprint plots for maximum concentration (see figure 32) based on the instantaneous release of 182 kg of chemical and using the measured velocity field to estimate the path of the plume center suggest that concentrations in excess of 0.05 ppb are unlikely to come closer than 10 kilometers to O'ahu horizontally, and would not be noted in surface waters, but only within several hundred meters of the bottom. Kauai is more than 100 km away and hence would be even farther from the plume. If we consider a 91 kg release with lower diffusivities, concentrations exceeding 0.5 ppb are unlikely within a kilometer of O'ahu horizontally, and concentrations in this vicinity only deeper than 320 mab, not near the surface.

The ensemble maximum exposure time (figure 41) prediction reaches a maximum of 74 hours (just over 3 days) near the disposal site for a release of 182 kg. At 290 mab the ensemble maximum exposure time is predicted to be at most about 2 hours and by 320 mab the ensemble maximum exposure time is zero, which means that no locations above 320 mab are expected to be exposed to concentrations at or above 1 ppb (figures 45 and 46). Exposure times in the vicinity of O'ahu should be zero since the ensemble maximum exposure time for any location with an x coordinate of more than 5.2 km (in the positive cross-shore direction from the disposal site) is zero (based on direct computation from the model).

Ensemble maximum exposures are also presented but exposures are zero in the vicinity of O'ahu because exposure times are zero there. Above 200 mab, ensemble maximum exposures are everywhere less than 36 ppb*hours, which is equivalent to being exposed to 36 ppb for 1 hour or 1 ppb for 36 hours, for example. Above 320 mab, exposures are everywhere essentially zero.

Investigations of transport after a 91 kg release in the event that diffusivities are higher than nominal (see figure 55) show very rapid dissipation to below 1 ppb everywhere (under 10 hours versus 4 days for nominal values of diffusivity). In the event that diffusivities are lower than expected, plumes will take longer to completely dissipate (40 days for 91 kg) and will therefore travel considerably further (see figure 61) but are still predicted to remain below approximately 320 mab and to travel principally in the along-shore direction.

7 References

References

L. Alves, R. M. Cotta, and M. D. Mikhailov. Covalidation of integral transforms and method of lines in nonlinear convection-diffusion with mathematica. *Journal of the Brazilian Society of Mechanical Sciences*, 23(3), 2001.

J. Beddington and A. Kinloch. Munitions dumped at sea: A literature review. Technical report, Imperial College London Consultants, 2005. URL http://www.mod.uk/NR/rdonlyres/77CEDBCA-813A-4A6C-8E59-16B9E260E27A/0/ic_munitions_seabed_rep.pdf.

Danish Environmental Protection Agency. Report on chemical munitions dumped in the baltic sea. Technical report, Report to the 15th Meeting of Helsinki Commission 8–11 March 1994 from the Ad Hoc Working Group on Dumped Chemical Munition (HELCOM CHEMU), 1994. URL http://www.helcom.fi/stc/files/Publications/OtherPublications/1994Report-ChemicalMunitionsDumpedInTheBalticSea.pdf.

T. Decloedt and D. S. Luther. On a simple empirical parameterization of topography-catalyzed diapycnal mixing in the abyssal ocean. *Journal of Physical Oceanography*, 40: 487–508, March 2010. note.

R. A. Fine, J. L. Reid, and H. G. Östlund. Circulation of tritium in the pacific. *Journal of Physical Oceanography*, 11:3–14, 1981.

T. D. Finnigan, D. S. Luther, and R. Lukas. Observations of enhanced diapycnal mixing near the hawaiian ridge. *Journal of Physical Oceanography*, 32:2988–3002, November 2002. note.

H. B. Fischer, E. J. List, R. C. Y. Koh, J. Imberger, and N. H. Brooks. *Mixing in Inland and Coastal Waters*. Academic Press, San Diego, CA, 1979.

C. Garrett. Turbulent dispersion in the ocean. *Progress in Oceanography*, 70:113–125, 2006.

D. M. Glover, W. J. Jenkins, and S. C. Doney. *Modeling Methods for Marine Science*. Cambridge University Pres, New York, 2011.

M. Holtappels and A. Lorke. Estimating turbulent diffusion in a benthic boundary layer. *Limnology and Oceanography*, 9:29–41, 2011. note.

W. C. Jackson, K. E. Jackson, E. L. Fasanella, and J. Kelley. Analysis of the effects of sea disposal on a one-ton container. STI TM-2007-214881, ARL-TR-3883, NASA, Hanover, MD, July 2007. URL https://trac.orr.noaa.gov/trac/UXO/attachment/wiki/BackgroundMaterial/NASA-tm-2007-214881.pdf. This document is from the NOAA TRAC site.

J. C. J. Nihoul, editor. *Modelling of Marine Systems*, volume 10 of *Elsevier Oceanography Series*. Elsevier, New York, 1975.

NOAA ADCP Data. Noaa ordnance transport 12-month ADCP data set (deep string). https://trac.orr.noaa.gov/trac/UXO/attachment/wiki/ADCP/, 2010.

NOAA ADCP Report. Noaa ordnance transport 12-month ADCP data summary. https://trac.orr.noaa.gov/trac/UXO/attachment/wiki/ADCP/12monthDataSumm.pdf, 2010.

NOAA Chemical Warfare Agents Summary. Chemical warfare agents at ordnance reef. https://trac.orr.noaa.gov/trac/UXO/attachment/wiki/CWSec/Summary_of_Noblis_Chemical_weapons_v1.doc, 2011.

NOAA DMM Chemicals. Detail of CWC schedule disposals and other materials co-disposed. This document is from the NOAA TRAC site., 2010. URL https://trac.orr.noaa.gov/trac/UXO/attachment/wiki/TechnicalDocuments/Deep%20CWM%20disposal%20site.doc.

Noblis Chemical Munitions Report. Physicochemical properties for compounds in chemical munitions in the deep water site of ordnance reef, O'ahu, hawaii. https://trac.orr.noaa.gov/trac/UXO/attachment/wiki/BGChem/NOAA%20draft%20CWM%20deepsite%20Report_Final3.pdf, 2011.

Ordnance Reef Hawaii. Ordnance reef (site HI-06) history. http://www.ordnancereefhawaii.org/history.htm, 2011.

W. H. Press, S. A. Teukolsky, W. T. Vetterling, and B. P. Flannery. *Numerical Recipes*. Cambridge University Press, New York, 3rd edition, 2007.

J.-L. Thiffeault, C. R. Doering, and J. D. Gibbon. A bound on mixing efficiency for the advection-diffusion equation. *Journal of Fluid Mechanics*, 521(1):105–14, 2004. ThiffeaultDoeringGibbon-2004-ADEMixingEfficiencyBound.pdf.

H. V. Thurman. *Introductory Oceanography*. Charles E. Merrill Pub. Co., Columbus, 3rd edition, 1981.

Calculating Three-Dimensional Concentrations from Particle Trajectories Modeled via GNOME at Ordnance Reef–HI-06

Introduction

GridPlume is a computer program which takes the particle trajectories forecast by the General NOAA Operational Modeling Environment (GNOME) model and uses them to estimate concentration of a pollutant in three dimensions (3D). For the Ordnance Reef munitions disposal site (HI-06) off the west coast of O'ahu, Hawai'i, GridPlume was used to estimate the concentration of ammonium picrate that would result from an instantaneous 10 kg release of this chemical from munitions on the seafloor. The results from GridPlume showed such a release of ammonium picrate would become extremely dilute, with concentrations never reaching 1 ppb at the beaches nearby.

Approach

Output from the GNOME model used by GridPlume consisted of a set of latitude, longitude, and depth coordinates for 1,000 particles ("Lagrangian elements," a.k.a LEs), with these 3D positions recorded every 15 minutes for three days. The 10 kg mass of ammonium picrate was considered by GNOME to be divided evenly among the LEs and this mass was conserved, such that the total of 10 kg remained fixed over time. Therefore for each LE the following were known:

x,y,z	=	the coordinates of the LE
t	=	time
M	=	the total mass within the LE

These LEs were used by the GridPlume code to determine the chemical concentration their distribution would represent in the ocean. The following were also defined via GridPlume:

t_{0x},t_{0y},t_{0z}	=	the virtual start time for the original point source
$\sigma_{0x},\sigma_{0y},\sigma_{0z}$	=	the variance components – dimensions – of the patch leaving the source

For all t the spreading behavior of the LEs was modeled as a Gaussian distribution. Thus each LE was treated as a continuous, rather than discrete, element with its center at x_0,y_0,z_0 considered to be the mid-point of a Gaussian distribution of concentration $\varphi((x-x_0), (y-y_0), (z-z_0))$:

$$\varphi = \frac{c_0}{(2\pi)^{\frac{3}{2}}} e^{-\frac{1}{2}\left(\frac{x-x_0}{\sigma_x}\right)^2} e^{-\frac{1}{2}\left(\frac{y-y_0}{\sigma_y}\right)^2} e^{-\frac{1}{2}\left(\frac{z-z_0}{\sigma_z}\right)^2} \qquad [1]$$

Here concentration C_0 was given by the integral constraint on the total mass of the LE:

$$C_0 = \frac{M}{\sigma_x \sigma_y \sigma_z} \quad [2]$$

and σ_x, σ_y, and σ_z were standard deviation functions of time that obeyed the following power law:

$$\sigma_x(t) = \sigma_{0x}\left(\frac{t}{t_{0x}}\right)^{\frac{3}{2}} \qquad [3]$$

In [3] σ_{0x} was the x dimension of the chemical plume and the value t_{0x} was a virtual start time defined by:

$$t_{0x} = \frac{\sigma_{0x}^{\frac{1}{\alpha}}}{D_x} \qquad [4]$$

with the exponent of spreading $\alpha = 0.5$ and the horizontal diffusion coefficient $D_x = 0.01\ m^2\ s^{-1}$. Equations equivalent to [3] and [4] were used for the sigma components in the y and z directions; with a vertical diffusion coefficient of $D_z = 0.001\ m^2\ s^{-1}$ for z.

GridPlume created an x-y-z grid that spanned the space covered by the LEs. All grid points were initially set to zero concentration. GridPlume's algorithm's main computational loop considered each LE and, based on equation [1], added a concentration value to the given grid point if the distance between the center of the LE and the grid points was less the 3σ in any direction. At the end of the computational loop the concentrations were transferred to the grid and values from the grid contoured.